Ti-V-Mn BASED METAL HYDRIDES FOR HYDROGEN STORAGE AND COMPRESSION APPLICATIONS

by

Lydia Anne Pickering

A thesis submitted to the University of Birmingham
For the degree of
Doctor of Philosophy

School of Metallurgy and Materials
College of Engineering and Physical Sciences
University of Birmingham
September 2013

Synopsis

The synthesis of Laves phase-related BCC solid solution Ti-V-Mn based alloys for use in hydrogen storage and hydrogen compression applications, was investigated. In $Ti_{0.5}V_{0.5}Mn$ based alloys, the effects of composition, microstructure, and crystallography on the hydrogen sorption properties were examined using SEM-EDS, XRD and Sievert's-type PCT measurements. Alloys were synthesised by arc melting, after which heat treatment was performed at 1233 K for 6 hours in a vacuum furnace ($< 10^{-6}$ mbar).

Three $Ti_{0.5}V_{0.5}Mn$ alloys were investigated and it was found that small compositional variations, $Ti_{0.5}V_{0.5\pm x}Mn$ (x = - 0.04 and 0.01), resulted in differing C14 Laves phase unit cell volumes. This resulted in a significant change in the plateau pressure and hysteresis between the alloys: compositional variation of 0.5 at% led to a shift of the plateau pressure by almost a third, from 42 – 52 bar to 60 – 70 bar for absorption and 25 – 15 bar to 40 - 30 bar for desorption.

After studying seven novel compositions based on Ti-V-Mn (i.e. $Ti_{0.5}V_{0.4}TM_{0.1}Mn$, where TM = Nb, Cr, Mo, Ta and $Ti_{0.5}V_{0.5-x}Nb_xMn$, where x = 0.05, 0.2 and 0.5) it was found that small amounts (0.05 - 0.1 at%) of Nb substituted for V resulted in a reduction in hysteresis between hydrogen absorption and desorption, as well as higher hydrogen dissociation pressures: from 40 to 45 bar. This finding led to the successful development of a two-stage metal hydride compressor utilising the Ti-V-Nb-Mn (Nb = 0.05) alloy. Trials on the compressor system have shown that output pressures of 650 bar can be achieved from an input pressure of less than 10 bar, at a filling rate of 0.5 g H_2/min.

Correlations were also observed between the unit cell volume and the enthalpy of hydride decomposition in the different alloy systems. Firstly, niobium substitutions appear to stabilise the C14 Laves phase hydride, thereby allowing the hydride to form at lower pressures: the absorption plateau pressure is reduced from 60 – 70 bar to 42 – 62 bar in Nb = 0.05. Secondly, transition metal substitutions destabilise the BCC phase, which resulted in an increase in the desorption plateau pressure from 40 – 30 bar to 50 – 25 bar, when 0.1 at% V was substituted for Mo. This indicates that the enthalpy of desorption in Ti-V-TM-Mn and Ti-V-Nb-Mn alloys is influenced by more factors than unit cell and interstitial volume.

In summary, it has been demonstrated that the plateau pressure and enthalpy of desorption of the Ti-V-Mn alloy hydride system can be tailored, through the careful addition of transition metals such as Nb.

Acknowledgements

Firstly I would like to thank my supervisor Dr. David Book for his continued support and guidance throughout my PhD.

I would like to thank members of the Hydrogen Materials Group, both past and present, for their friendship and support throughout my time in the department. In particular, a special thank you to Dr. Daniel Reed for his continuous assistance with the equipment and advice with data analysis and thesis writing.

Thanks to my co-supervisor Dr. Alex Bevan for encouraging me to do a PhD and his endless enthusiastic ideas and suggestions; Andy Bradshaw for technical assistance with alloy synthesis; and members of the Magnetic Materials group for their friendship, support and even the odd game of squash/badminton over the years.

I wish to gratefully acknowledge the financial support I have received from the EPSRC which enabled me to continue my studies after my undergraduate degree.

I am eternally grateful to my friends and family for all their love and encouragement over the course of my studies. A special mention must go to Andrew for putting up with my moaning in recent months and always believing in me.

Finally, I wish to thank my Mum and Dad for their continued love and support over the last 25 years – without you, none of this would have been possible.

Table of Contents

Chapter 1

INTRODUCTION TO THE HYDROGEN ECONOMY

This thesis will investigate the use of metal hydrides for applications including hydrogen storage for fuel cell vehicles and metal hydride hydrogen compressors. The following chapter provides the background to, and some context for, the project.

1.1 Introduction

There is increasing demand for the development of a low carbon emission economy. Continuing growth in population coupled with ever-increasing fears over the environmental and health effects of climate change has meant that reducing our dependency on fossil fuels is one of the greatest challenges over the coming decades: a comprehensive review of this topic has been given by Armaroli & Balzani (2010).

With the need for energy ever-increasing – in a recent report the International Energy Agency (IEA) estimated that the long-term global energy demand is projected to increase by a third from 2010 to 2035 (IEA, 2012) – and known conventional oil and coal resources becoming more scarce, a long-term solution is needed.

The uneven distribution of existing fossil fuel supplies along with political instability in many oil-producing and consuming countries has meant that the diminishing oil reserves are becoming ever more undependable and inaccessible. Recently, there has been interest in gas formed from unconventional sources such as shale formations. In the United States, shale gas

increased from less than 1% of domestic gas production in 2000 to over 20% by 2010 (Stevens, 2012) . However, in spite of this there is still uncertainty over the negative environmental impact of the hydraulic fracturing process required to extract the natural gas (Howarth et al., 2011)

This has all contributed to growing fears over future energy security (Bauen, 2006). The use of hydrogen as an energy vector may form part of the solution to this mounting energy challenge.

1.2 Hydrogen as an Energy System

Elemental hydrogen is made up of a single proton and electron making it the simplest and most abundant element in the universe. Although less than 1 ppm (by volume) of molecular hydrogen occurs naturally within the atmosphere of Earth in a gaseous state (Lide, 2004), substantial amounts of hydrogen are contained within water and hydrocarbons, and so molecular hydrogen can be produced on-site in many locations as long as there is sufficient energy available for processing (i.e. electrolysis, reformation, etc). Hydrogen burns cleanly in air and when reacted with oxygen in a fuel cell the only by-product is water. It also possesses the highest known energy density per unit mass: on a weight basis hydrogen has almost three times the energy content of other chemical fuels based on liquid hydrocarbons; 120 MJ kg^{-1} vs. 44 MJ kg^{-1} (Harris et al., 2004).

The concept of a 'Hydrogen Economy', whereby energy needs are predominantly met by hydrogen as a energy vector, has been suggested as a means to overcome dependency on fossil fuels (Crabtree et al., 2004). A hydrogen economy would lead to a reduction in green house gas emissions and result in reducing fears over energy security.

Despite the advantages of adopting the use of hydrogen to meet our future energy needs, there are still several technical, political and socio-economic barriers that need to be overcome before hydrogen can be seen as a safe, efficient energy vector of the future.

Many of the OECD economies have large hydrogen-based research and development programmes in place, e.g. the US Department of Energy (DOE) and the Japanese National Institute of Advanced Industrial Science and Technology (AIST).

The transition over to a hydrogen economy will require significant technological advances in: production; distribution & delivery; storage; and conversion & use.

1.2.1 Hydrogen Production

Currently, the majority of hydrogen production comes from natural gas reformation. In this process, steam reacts with methane at temperatures in excess of 800 °C to produce a gas stream containing carbon monoxide and hydrogen (Xu & Froment, 1989).

$$CH_4 + H_2O + heat \rightarrow 3H_2 + CO \ (\Delta H = 206 \text{ kJ/mol})$$

This hydrogen can then be separated and purified. In a second stage, additional hydrogen can be generated through a lower-temperature (200 °C) water gas shift reaction:

$$CO + H_2O \leftrightarrow CO_2 + H_2 + heat \ (\Delta H = -41 \text{ kJ/mol})$$

In the final process stage, known as pressure-swing adsorption, carbon dioxide and other impurities are removed from the gas stream, resulting in very pure hydrogen.

The production of hydrogen from gas reformation results in the release of CO_2. Research into carbon capture and storage techniques, such as in underground geological formations, is being

carried out to try to reduce the amount of CO_2 emitted into the atmosphere (Winter, 2009). However, there are concerns over leakage of this stored CO_2 so production of hydrogen from gas reformation cannot be considered a sustainable long-term solution.

The electrolysis of water is another well-established technology used for hydrogen production (Turner, 2004). During electrolysis, an electric current is used to split water into hydrogen and oxygen.

$$2\ H_2O(l) \rightarrow 2\ H_2(g) + O_2(g)$$

The electricity used for this reaction can be produced in a number of ways, however, in order to address the issues of climate change and sustainability, renewable energy resources such as solar and wind would be preferable.

In addition there are a number of alternative technologies, including biological and photo-electrochemical methods, which can be used to produce hydrogen that offer several potential solutions in terms of improving efficiency and reducing CO_2 emissions (Hawkes et al., 2002).

1.2.2 Hydrogen Distribution & Delivery

Before a transition to a hydrogen economy can occur, infrastructure needs to be developed to allow for hydrogen to be transmitted from its point of production to end use, with the capability of meeting the demand on hourly, daily, and seasonal basis.

Pipelines provide a safe, cost-effective and environmentally friendly way of transporting and distributing hydrogen in large quantities. Existing natural gas pipelines for industrial uses are already present in parts of the US, UK and Europe so attention has been focused on

investigating the extent to which existing pipelines can be used for hydrogen delivery (Dodds & Demoullin, 2013).

For existing pipelines to carry pure hydrogen a number of issues need to be addressed, including the low volumetric energy density of hydrogen and the potential for embrittlement in pipe materials based on steel. It has been shown that to compensate for hydrogen's low volumetric energy density, hydrogen would need to be pumped at 2.8 times the rate of natural gas to deliver the same energy through existing pipeline (Bjørnar et al., 2002).

To ease the technical and logistical problems associated with distributing hydrogen via existing and/or new pipelines, the production of hydrogen on-site where it will be utilised i.e. placing electrolysers at hydrogen filling stations, offers significant advantages (Symes et al., 2012).

Another important component for large-scale hydrogen distribution is hydrogen compression. Several methods employed for storing hydrogen (which will be discussed further in section 1.2.3 and subsequent chapters) require the use of high pressures. This means that at hydrogen distribution sites and filling stations hydrogen compression techniques, which are efficient, economic and safe, are required to deliver high pressures of hydrogen to storage tanks.

There are several different ways of compressing gas and as such there are a number of types of compressors commercially available. Traditionally, compressors are mechanical devices which utilise a piston driven by a crankshaft powered by either a combustible fuel or electricity to compress the gas.

Despite their advantages, mechanical compressors cannot be considered a long-term solution for hydrogen compression because when operating on a combustible fuel they release environmentally harmful gases into the atmosphere, they require regular servicing - which is

both financially and labour expensive - and they are susceptible to the same failure as any other mechanical device.

A metal hydride compressor takes advantage of the thermodynamic properties of metal hydrides. Hydrogen is absorbed into an alloy bed at ambient temperatures and is released at elevated pressures when the bed is heated. Compression energy can therefore be supplied by heat (for example hot water, oil or electrical resistance).

Some of the benefits of using metal hydride compression include: the provision of ultra-high purity hydrogen; no gaseous emissions associated with lubricants; contains no moving parts so servicing is minimised; and allows for silent operation (Muthukumar et al., 2005).

However, to date researchers have not yet been able to optimise the overall energy efficiency of such a system and the capital cost is still too high to be considered commercially viable (Lototskyy et al., 2012). Appropriate metal hydride selection is therefore essential in order to realise the full potential for metal hydride compressors (Popeneciu et al., 2009). This will therefore be one of the focuses of the current work.

1.2.3 Hydrogen Storage

From a technical perspective, the major limitation to the use of hydrogen is that as a gas it possesses a low energy density per unit volume; at 0.08988 g/L at atmospheric pressure, it has only $1/10^{th}$ of the energy compared with gasoline from the same volume (Züttel, 2004). Economic, efficient and safe hydrogen storage is therefore required before the vision of a hydrogen economy can be fully realised.

Ultimately, it is the end use of the hydrogen which will dictate the requirements for the storage system.

For mobile applications such as passenger vehicles, it is important to find a storage solution that offers both a high: volumetric (due to onboard physical space requirements), and gravimetric hydrogen storage densities (low weight requirement for vehicles) to achieve an acceptable driving range. On the other hand, for stationary and static applications such as auxiliary power units, where the main objectives are an acceptable duration of operation between refuelling and adequate power outputs, the weight of the storage solution is not as significant.

Currently, hydrogen can be stored as a compressed gas, a cryogenic liquid or a solid-state compound. To determine which method is appropriate for specific applications, the cost and volumetric requirements of the system must be taken into account.

To date, no single storage technology is capable of fully meeting the storage requirements for on board vehicle applications. As a result, the global research community is investigating ways to optimise the performance of current technologies to both improve efficiency and lower cost through the exploration of new and advanced materials. This is the second focus for the current work.

1.2.4 Hydrogen Conversion

Hydrogen can be used to generate power in two main ways:

- Through direct combustion with air in combustion engines.
- Through an electrochemical reaction with oxygen to produce electrical energy in a fuel cell.

Combustion Engines

Hydrogen can be used as a substitute fuel in conventional engines (Prasath et al., 2012). It is widely used within gas turbines for electrical power generation and offers several advantages over fossil fuel based turbines including lower maintenance and longer life because sediment and fuel-associated corrosion are reduced. When hydrogen is used within internal combustion engines, fewer harmful emissions are released into the atmosphere with only low levels of nitrogen oxide being produced.

Fuel Cells

Hydrogen can be used within fuel cells to produce electricity in an electrochemical reaction with oxygen. The technology behind fuel cells was demonstrated back in 1893 (Grove, 1839) but remained largely dormant until the 1960's when NASA used precursors of today's proton exchange membrane (PEM) fuel cells to generate power and produce pure water for spacecraft (Burke, 2003).

There are several types of fuel cells available and typically they are categorised by both their operating temperature and the type of electrolyte used. The selection of an appropriate fuel cell is therefore largely dependent on the end use.

The operating principle behind the process which takes place within fuel cells is the inverse of electrolysis. In this process hydrogen is fed into the anode and oxygen to the cathode. At the anode the hydrogen is split into positively charged ions (protons) and negatively charged electrons by a catalyst. At the cathode, the protons and electrons combine to form water and heat – the two by-products of the reaction. This reaction is illustrated in Figure 1.1.

Figure 1.1 Schematic of a hydrogen fuel cell showing the chemical reactions which take place at each section (Alternative Energy, 2009).

The current development of fuel cell technology is focused around three main areas: hydrogen for static applications, stationary applications and mobile applications. This work will focus

on the use of hydrogen for mobile applications, and more specifically the challenges facing the transport sector.

Hydrogen for Mobile Applications

In developed countries, there is a major dependence on fossil fuels for transport. Globally, the transportation sector represents 23 % of overall CO_2 emissions from fossil fuels and approximately 15 % of overall green house gas emissions (International Transport Forum, 2010). In the UK alone, road transport makes up just over 90 % of all domestic transport emissions of which 62.7 % of CO_2 emissions from vehicles in 2009 were produced from passenger road vehicles (DfT, 2010).

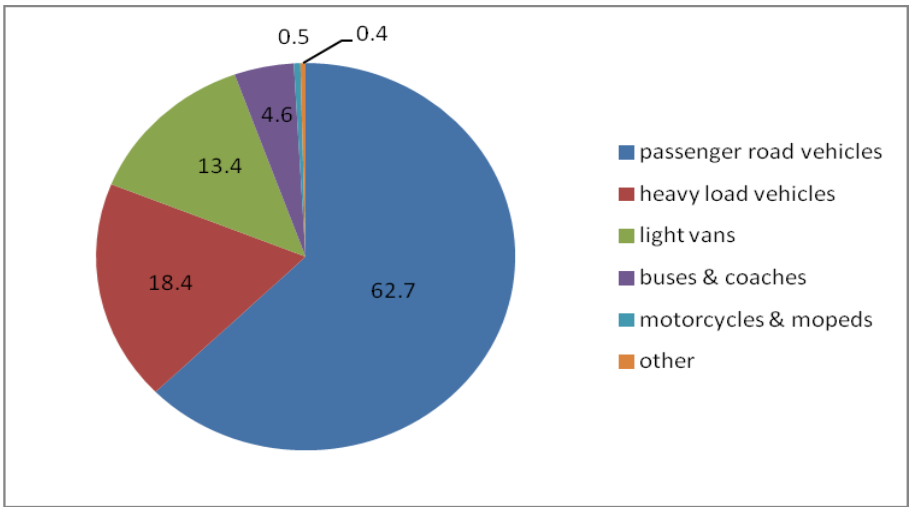

Figure 1.2 UK road emissions by vehicle type in 2009 (chart constructed from data adapted from DfT, 2010).

Hydrogen fuel cell vehicles are seen as an attractive alternative to other zero-emission vehicles, such as battery electric vehicles, due to their high energy densities (Winter & Brodd, 2004). The cruising range of battery electric vehicles, when based on lithium-ion batteries, is therefore lower when compared to hydrogen fuel vehicles (Hirose, 2010).

Over the last fifteen years PEM fuel cells have emerged as a promising contender for use in zero emission vehicles, largely due to their rapid start-up times and ability to operate at low temperatures (Burns et al., 2002).

It has been shown that PEM fuel cells have an efficiency of 60 % (Schlapbach & Züttel, 2001) which is about 2-3 times more efficient than standard internal combustion engines running on petrol (Crabtree et al., 2004).

Despite their advantages, the high cost of PEM fuel cells along with their susceptibility to CO poisoning has meant they cannot be considered commercially viable on a large-scale (Pollet et al., 2012).

At present there are only a handful of hydrogen-powered vehicles commercially available, including the Honda FCX Clarity, shown in Figure 1.3.

Figure 1.3 The Honda FCX Clarity (Honda, 2013).

The FCX Clarity is currently only available to lease in the US, Japan and only recently in some European countries. The vehicle operates using a 100 kW PEM fuel cell combined with a lithium ion battery for regenerative breaking. On-board, 4.1 kg of hydrogen is stored using compressed gaseous storage (see Chapter 2) at 350 bar, which gives an average range of 240 miles (~ 386 km) (Honda, 2013).

The lack of hydrogen refuelling stations, both on a national and international level, has also acted as a limiting factor to the technology behind hydrogen fuel cell vehicles (Winter, 2009). Until governments are committed to investing in the necessary infrastructure for hydrogen refuelling, end users are unable to take full advantage of this technology.

Chapter 2

HYDROGEN STORAGE

This chapter will examine the current status and limitations of hydrogen storage technologies. In doing so it will present information on the target criteria for potential storage media as well as providing a greater understanding of suitable materials.

2.1 Introduction

Based upon current efficiencies, a medium sized family vehicle utilising a PEM fuel cell would require approximately 4 kg of hydrogen for a range of around 400 km (Schlapbach & Züttel, 2001). This mass of hydrogen equates to a volume of 44 m^3 at atmospheric pressure, which for practical use in cars would require a significant reduction in volume. Efficient and effective hydrogen storage is therefore required for applications such as hydrogen-powered vehicles.

Figure 2.1 shows the tank volumes required to store 4 kg of hydrogen in relation to the size of a standard passenger vehicle, using several storage mediums.

Figure 2.1 Relative volume required to store 4 kg of hydrogen using compressed hydrogen, liquid hydrogen and hydrogen absorbing alloys in relation to the size of a standard passenger vehicle (Schlapbach & Züttel, 2001).

Hydrogen can currently be stored in three states of matter: as a gas, liquid or sorbed in/on a solid material. These systems can broadly be categorised as (Züttel, 2003) :

1. Compressed gaseous hydrogen. } Gas State Storage
2. Cryogenic liquid hydrogen. } Liquid State Storage
3. Irreversible reactions with water.
4. Hydrogen adsorption (physisorption) } Solid State Storage
5. Complex Hydrides.
6. Hydrogen absorption (chemisorption)

For mobile applications, car manufacturers and national bodies have set targets for on-board hydrogen storage systems. The U.S Department of Energy (DOE) has established several on-board vehicular hydrogen storage targets over the last decade. The following table summarises the DOE system gravimetric and volumetric targets which have previously been set, along with the current requirements (DOE, 2010).

Table 2.1 Summary of previous and current DOE target values for system gravimetric and volumetric density. Note these are system targets and therefore include the weight of the complete storage system (storage container and all the necessary components).

Storage Parameter	2010	2015	Ultimate
System Gravimetric Density (wt%)	4.5 (1.5 kWh/kg)	5.5 (1.8 kWh/kg)	7.5 (2.5 kWh/kg)
System Volumetric Density (kg/m^3 H_2)	28 (0.9 kWh/L)	40 (1.3 kWh/L)	70 (2.3 kWh/L)

In addition to the DOE target values, when considering appropriate hydrogen storage methods or materials, there are several factors that need to be considered. These can be broadly categorised into the following areas (Hirose, 2010; Satyapal et al., 2007):

- System Weight,
- Cost,
- Safety,

- Uptake and discharge kinetics; the rate at which hydrogen can be taken up and released from the system,
- Operating temperature and pressure,
- Degradation of properties over its lifetime (cyclability), and
- Release hydrogen with the required purity.

Figure 2.2 is a graphical representation of the current status of a number of hydrogen storage methods which are being investigated at present. It shows several storage options and their relative capacities in relation to the DOE system targets for gravimetric and volumetric capacity.

*N.B 'Learning Demo' data shows range across 138 vehicles with 350 bar and 700 bar systems.

Figure 2.2 Current status of hydrogen storage based on system targets for gravimetric and volumetric capacities for the different storage methods (DOE, 2010).

As highlighted in the top right corner of the figure, a material which exhibits a high gravimetric and volumetric hydrogen density is required.

At present, no single storage technology is capable of satisfying these target values (Ahluwalia et al., 2012). It is expected that through development and innovation, vehicular targets for hydrogen storage will be met in the coming years.

2.2 Storage Methods

2.2.1 Compressed Gaseous Hydrogen

Hydrogen is a gas at room temperature and atmospheric pressure so can be compressed and stored in cylinders up to 200 bar relatively easily. The main benefit of compression is that it allows for fast refuelling and discharge rates: filling rates similar to conventional internal combustion engine (ICE) vehicles are possible by pre-cooling the hydrogen (Maus et al., 2008). As a result, compressed gas cylinders are the most common hydrogen storage method currently employed on vehicles (Züttel, 2003).

Appropriate selection of cylinder material is of great importance because safety is a large concern when high pressures are concerned, especially for vehicle applications where there is always an inherent risk of impact. A low-mass material which possesses a high tensile strength, does not react with hydrogen and is able to prevent hydrogen from leaking is therefore required. Such pressure vessels are composed of several layers: an inner polymer liner which prevents gas leakage, over-wrapped with a carbon-fibre shell which acts as the stress bearing component, and finally an outer layer made from a corrosion-resistant material which is able to withstand mechanical impact.

Despite being a well-established technology, there are several drawbacks to the use of compressed hydrogen gas.

There is considerable energy loss during the pressurisation of hydrogen, which reduces the overall efficiency of this technology. For example, for compression to 800 bar, energy loss is typically in the order of 12 – 16 % (Westerwaal & Haije, 2008). In addition for vehicular applications, PEM fuel cells require high-purity hydrogen to prevent damaging the expensive membrane material (Yang et al., 2010).

Both of these issues can be overcome by the use of safe, efficient hydrogen compressors. This highlights the need for new compression techniques, which will be discussed further in Chapters 5 and 11.

Ahluwalia et al., (2010) have shown that 350 bar storage tanks can meet the DOE 2010 and 2015 system targets for gravimetric capacity and have the potential to meet the ultimate target of 7.5 wt% by substituting the outer shell material with a lighter density alloy. In terms of the volumetric capacity, it is possible to meet both the 2010 and 2015 system targets by reducing the thickness of the inner liner material but it is unlikely to meet the ultimate target of 70 kg/m^3 H_2. In addition 350 bar storage tanks have high manufacturing costs, which limit them to high end vehicle applications.

Ultimately, the low volumetric hydrogen density of high pressure gas cylinders, coupled with high cost and poor conformability mean that compressed gaseous hydrogen cannot be consider a long-term storage solution.

2.2.2 Cryogenic Liquid Hydrogen

Liquid hydrogen is stored in cryogenic tanks at 21.2 K at ambient pressures. Open systems (vessels containing free space) are employed for this method of storage because hydrogen has a low critical temperature (33 K), above which no liquid phase exists.

For vehicle applications, double-wall cylindrical stainless steel or aluminium tanks are used because they are very resistant against hydrogen embrittlement and show negligible hydrogen permeation (Krainz, 2004).

This storage method is currently employed for transporting large amounts of hydrogen for industrial applications. Despite this, there are several drawbacks associated with the use of cryogenic liquid hydrogen.

The liquification process is very energy intensive (up to 15 kWh/kg) which reduces the overall efficiency of a system employing liquid hydrogen storage (Wolf, 2002). In addition, it is susceptible to 'boil off' losses as a result of heat leaks within the system - the rate of which is dependent on the size and shape of the vessel. For double-walled insulated spherical tanks with a storage volume of 50 m^3 boil off losses are typically around 0.4 % per day (Züttel, 2004).

Liquid hydrogen storage is therefore limited to applications where the cost of hydrogen is not an issue and the gas is used within short periods of time, for example in air and space applications (Schlapbach & Züttel, 2001).

2.2.3 Irreversible Reaction with Water

Hydrogen can be generated through a chemical reaction of metals and chemical compounds with water. A common experiment, often demonstrated in chemistry lessons, where hydrogen is produced by a piece of sodium floating on top of water, is one example of this method of storage.

During this reaction two sodium atoms react with two water molecules and produce one hydrogen molecule and two sodium hydroxide molecules (NaOH). Using Na, this process yields a gravimetric hydrogen density of 3 wt%. Although the reaction is not directly reversible, NaOH can be removed and reduced back to metallic Na using a solar furnace.

This storage method has also been successfully demonstrated with Li, substituted for Na, and results in a higher gravimetric hydrogen density of 6.3 wt%, taking into account the mass of water required for the reaction (Züttel, 2004). However, a major drawback to this is difficulties surrounding the reduction and recovery of the metal hydroxide (Züttel, 2003).

The reaction of sodium borohydride with water also offers advantages, including high gravimetric capacity of 10.9 wt% and fast kinetics (Züttel, 2004) :

$$NaBH_4 + 2H_2O \Rightarrow NaBO_2 + 4H_2$$

Unfortunately, it is not possible for regeneration to take place on-board mobile vehicle applications so external regeneration is required - limiting the commercial viability of this storage medium.

2.2.4 Adsorbed Hydrogen (physisorption of molecular hydrogen onto materials with high surface areas)

The physical adsorption of a gas onto the surface of a solid is achieved through van der Waals interactions between a gas molecule and atoms on the material surface. Significant physisorption is only observed in materials with very high surface areas (> 1000 m^2/g) and small pore sizes. Due to the low enthalpy of adsorption associated with these weak van der Walls interactions (5-10 kJ/mol H_2), the bonding of these materials require low temperatures, typically < 273 K, for hydrogen (Züttel, 2003).

There are several different mechanisms of adsorption, which are largely dependent on the geometry of the adsorbent. For hydrogen storage applications, a wide range of high surface area materials have therefore been investigated.

Materials based on graphite, such as activated carbons have been widely investigated about their hydrogen storage properties. It has been shown that using activated carbon, with a specific surface area of 1,315 m^2g^{-1}, 2 wt% can be reversibly adsorbed at 77 K (Nellis et al., 1998). The amount of reversibly adsorbed hydrogen is proportional to the specific surface area of the adsorbent.

Another category of high surface area materials which has been investigated are supramolecule metal organic frameworks (MOF). MOFs are compounds consisting of metal ions which are connected by ligands to form ordered one-, two- or three-dimensional structures. In particular MOF-5 with the composition Zn_4O(1.4-benzenedicarboxylate)$_3$ is capable of storing 4.5 wt% at 77 K and 1 wt% at room temperature (298 K) under 20 bar H_2 (Rosi et al., 2003). Despite the promising gravimetric storage capacities, the volumetric capacities of MOFs are only slightly above the DOE 2010 system target of 28 kg/m^2. For

example, MOF-177 which shows the highest gravimetric capacity (7.5 wt% at 77 K) has a volumetric density of just 32 kg/m^2 (Wong-Foy et al., 2006).

Some of the advantages of storing hydrogen through physisorption are rapid sorption kinetics, low operating pressure, it results in a high purity of desorbed hydrogen and it involves relatively low material cost. However, the low operating temperatures and small volumetric densities of these materials are significant drawbacks to this class of materials and have hindered their practical application.

2.2.5 Complex Hydrides

Group I, II and III metals, such as lithium and sodium, are capable of forming stable and ionic compounds with hydrogen. In these complex compounds hydrogen is bound into the bulk of the material and is absorbed and released through a series of recombination and decomposition reactions. Complex hydrides differ from metal hydrides (which will be discussed in the following section) because ionic or covalent bonds form during hydrogen absorption.

Complex compounds exhibit some of the highest volumetric and gravimetric densities of any hydrogen storage media. For example, $LiBH_4$ possesses a gravimetric hydrogen density of 18.5 wt% (Züttel et al., 2003). However, due to the strong ionic and covalent bonding of these materials, high desorption temperatures are required to release the hydrogen: in $LiBH_4$, heating up to 553 K is required to desorb three of the four hydrogen atoms – representing a gravimetric storage capacity of 13.6 wt% (Vajo et al., 2005). Once the hydrogen is liberated temperatures of up to 873 K and pressures of 350 bar are then required for the recombination

reaction of $LiBH_4$ (Eberle et al., 2009) which is a significant drawback to this type of material.

It has been shown that the addition of MgH_2 to the $LiBH_4$ system enables a reversible capacity of 8 – 10 wt% between 588 and 673 K (Vajo et al., 2005). However, this process is hindered by slow kinetics: it takes up to 100 hrs to reach equilibrium during absorption.

The main disadvantage of complex hydrides is that they show little or no reversibility so high desorption temperatures are required which often results in slow desorption kinetics. In addition they are highly sensitive to air and moisture which makes handling difficult. This means that complex compounds cannot be considered as suitable materials for practical applications.

2.2.6 Absorbed Hydrogen (chemisorption of atomic hydrogen into the lattice of host metals)

Many metals and alloys are capable of reversibly absorbing hydrogen. When this occurs, the alloys are termed 'metal hydride compounds'. Unlike some of the previously discussed materials, metal hydrides absorb hydrogen within interstitial sites in the crystal lattice rather than directly into a crystal structure (Shriver & Atkins, 1999). The capacity of metal hydrides is subsequently related to the number of interstitial sites within the lattice.

The general reaction of H_2 with a metal/alloy (M) to form a metal hydride (MH_x) can be expressed as (Sandrock & Bowman, 2003):

$$M + (x/2)\ H_2 \leftrightarrow MH_x + \text{heat}$$

The study of metal hydrides began nearly 150 years ago by Tomas Graham with the discovery of the hydrogen absorbing properties of palladium (Graham, 1866). It has since been shown that hydrogen can reversibly react with several other intermetallic alloys at moderate temperatures and pressures.

The desired reaction for the formation of an intermetallic alloy A_yB_z with hydrogen can be expressed as:

$$A_yB_z + xH_2 \leftrightarrow A_yB_zH_{2x} + \Delta Q$$

Where, A is usually a group III or IV or a rare-earth metal, forming a stable hydride, B is a transition metal and does not form a stable hydride but helps to catalyse the dissociation of the H_2 molecule and ΔQ is the heat related upon absorption of hydrogen (Züttel, 2003).

To date, one of the most promising reversible metal hydrides is MgH_2 which has the highest energy density of any studied material; 9 MJ/kg Mg, it can store 7.7 wt% of hydrogen and is low in cost (Zhu et al., 2006). The main disadvantage of MgH_2 is that it has high thermal stability so requires a high temperature for hydrogen discharge, which results in slow desorption kinetics (Sakintuna et al., 2007). It also has a high enthalpy of formation making thermal control difficult (Bohmhammel et al., 1999).

Intermetallic compounds, such as binary AB_5 alloys like $LaNi_5$, have high volumetric hydrogen densities (115 kg/m^3) and good cycling ability (Schlapbach & Züttel, 2001). However, they are comprised of heavy transition and rare earth elements so, like several other intermetallic hydrides, at 1.4 wt% their gravimetric capacity is considered too low for on-board hydrogen storage for mobile applications.

In the last 30 years, AB_2 alloys, based on compounds containing titanium and manganese (e.g. $TiMn_2$) have been investigated because they possess a number of advantages over AB_5 alloys, including: being cheaper, lighter, possessing higher dissociation pressures and have the capability of volumetrically storing 20-50% more hydrogen than $LaNi_5$ (Dehouche et al., 2005). In addition, small variations of the elements within such systems allow the properties to be tailored to meet the specific requirements of the system.

A more thorough review of the different metal hydride systems is provided in Chapter 4.

In comparison with other methods of hydrogen storage, metal hydrides are very effective at reversibly storing large amounts of hydrogen in a safe and compact way. Although there has been much pressure to discover a metal hydride which is capable of meeting, or indeed exceeding, the DOE target values, one must realise the importance of taking into consideration both the material itself and the end term use for application-specific targets.

For hybrid hydrogen storage applications, metal hydrides with fast kinetics and a hydrogen dissociation pressure greater than 10 bar are required (Shibuya et al., 2008).

For compression applications, depending on the requirements of the system, metal hydrides are required with: a good hydrogen absorption capacity, small enthalpy of formation, fast hydrogen sorption reaction kinetics and structural stability during cycling (Popeneciu et al., 2009).

These applications will be discussed further in Chapter 5.

2.3 Summary of Hydrogen Storage Methods

Figure 2.3 shows examples of the six storage methods in relation to the DOE system targets for volumetric and gravimetric densities.

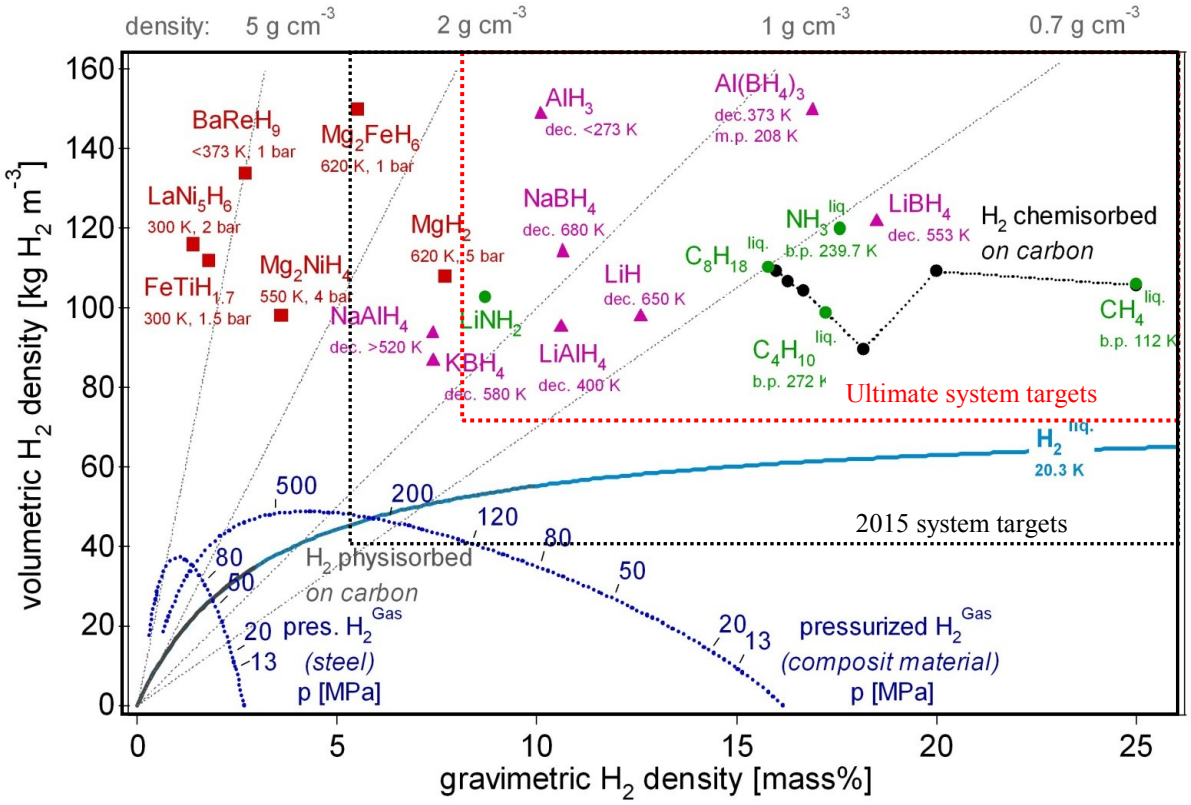

Figure 2.3 Volumetric and gravimetric hydrogen density of several hydrogen storage materials in relation to the DOE system targets. Modified from Züttel (2003).

From Figure 2.3 it can be seen that methane (CH_4) has the highest gravimetric density of all the storage methods which are displayed. The steam methane reformation process requires high temperatures (> 700 ^{o}C) and results in the release of CO_2 which limits the practical application of methane as a hydrogen storage medium.

Materials based on $BaReH_9$ and $LaNi_5H_6$ show the highest volumetric densities but suffer from poor gravimetric densities due to the heavy weight of the metals.

A summary of the six different storage methods against several performance criteria, including gravimetric and volumetric hydrogen densities amongst others, is shown in Table 2.2.

From this it can be seen that despite being well-established technologies, conventional storage solutions based on compressed gas and liquid hydrogen do not provide sufficient storage densities at the required temperatures and pressures for vehicle applications.

Disadvantages of the irreversible reaction with water include that it is not fully reversible and does not yield high purity hydrogen, thus rendering it not cost effective.

The use of adsorbed hydrogen onto high surface area materials through physisorption requires very low temperatures and fails to meet the criteria for system gravimetric and volumetric densities.

Complex hydrides show promising gravimetric and volumetric capacities but require high temperatures for desorption and high pressures for absorption. In addition they are not fully reversible so have to be regenerated off board.

Finally, in spite of their low gravimetric storage densities, metal hydrides offer promising volumetric capacities at ambient temperatures and pressures, making them suitable for a range of practical applications. Metal hydrides will therefore be the focus of the current work.

The next chapter will provide an overview of the fundamentals of the metal-hydrogen interactions which takes place within interstitial metal hydrides.

Table 2.2 Summary of the six different hydrogen storage methods. Adapted from Züttel (2003), Züttel (2004) and Harris et al., (2004).

	Gravimetric Density (wt%)	Volumetric Density (kg/m^3 H_2)	Operating Temperature (°C)	Operating Pressure (bar)	Fully Reversible	Cost Effective	Results in high purity hydrogen	Comments
Compressed Hydrogen	13	< 40	25	200-800	Yes	Yes	Yes	Well established but energy intensive.
Liquid Hydrogen	Depends on tank size	71	-252	1	Yes	No	Yes	Well established but susceptible to "boil off".
Irreversible reaction with water	< 40	> 150	25	1	No	No	No	Complicated and not directly reversible.
Adsorbed Hydrogen (physisorption)	~ 2	20	-80	100	Yes	Medium	Yes	Require very low temperatures.
Complex Hydrides	< 18	150	> 100	1	No	Medium	No	Require low pressures and high temperatures for desorption and high pressures for absorption.
Absorbed hydrogen (metal hydrides)	~ 2	150	25	1	Yes	Medium	Yes	Inherently safe but comparatively low wt% (due to heavy metals)

Chapter 3

FUNDAMENTALS OF METAL/HYDROGEN INTERACTIONS

This chapter will examine the fundamentals of metal hydrogen interactions within interstitial metal hydrides. In doing so it will firstly introduce the underlying principles, followed by a discussion in to the typical experimental method employed to observe metal/hydrogen interactions and some of the errors associated with these types of measurement.

3.1 Introduction

The reaction of hydrogen with a metal is known as the absorption process. In order for hydrogen to combine with a metal several reactions must take place. A simplified schematic of the process is shown in Figure 3.1.

In 3.1(a) a hydrogen molecule (H_2) is **approaching** the metal surface. 3.1(b) shows the H_2 interacting with the atoms at the surface of the metal, leading to a **physisorbed** state. 3.1(c) shows the hydrogen **disassociation** to form a chemisorbed state forming a bond with the metal. In the final stage, 3.1(d) the chemisorbed hydrogen has moved into the subsurface and

occupied an interstitial site with the host lattice and then through solid state **diffusion** the hydrogen (screened proton) travels into the bulk forming a M-H solid solution.

This process can also be described in terms of a simplified one dimensional potential energy curve (Lennard-Jones, 1932). Figure 3.2 shows the potential energy curve for a hydrogen molecule as a function of the distance from a metal, for molecular absorption i.e. physisorption and dissociative absorption i.e. chemisorption, with reference to the four fundamental stages of the metal/hydrogen interactions.

Figure 3.2 Simplified one-dimensional potential energy curve of hydrogen approaching a metal in molecular and atomic form (Züttel, 2003) with reference to the four fundamental stages of the metal/hydrogen interactions provided in Figure 3.1.

Away from the metal surface the potential energy of the hydrogen molecule and the two hydrogen atoms are separated by the dissociation energy. The first attractive interaction of the hydrogen molecule as it approaches the surface of the metal is achieved through Van der Waals forces and results in the physisorbed state. In order for dissociation and the formation of the hydrogen metal bond to occur, the hydrogen has to overcome an activation barrier

closer to the surface. Hydrogen atoms which share their electrons with the atoms at the surface of the metal are in the chemisorbed state. The chemisorbed hydrogen atoms are then free to move in the subsurface layer where they diffuse through the host metal lattice and into the interstitial sites.

In terms of the physical changes that occur during the hydrogen/metal interaction, the action of hydrogen atoms moving to interstitial sites within the lattice through solid state diffusion results in a volume expansion of the lattice. This volume expansion generates internal stresses within the material, causing intergranular (brittle) fracture, which is known as decrepitation. The process of decrepitation generates smaller particles with clean (non-oxidised/contaminated) surfaces, which allows for faster kinetics, due to increased surface areas.

3.2 Pressure-Composition Isotherms

From a thermodynamic aspect, the formation of metal hydride from gaseous hydrogen can be described by pressure-composition isotherms (PCT curves). PCT curves are formed by measuring the change in hydrogen concentration with pressure at a given temperature. The types of measurements involved for this will be explained in the following section. A typical PCT curve is shown in Figure 3.3 and it can be seen that there are three distinct regions: α-phase region, α + β two phase region and β-phase region.

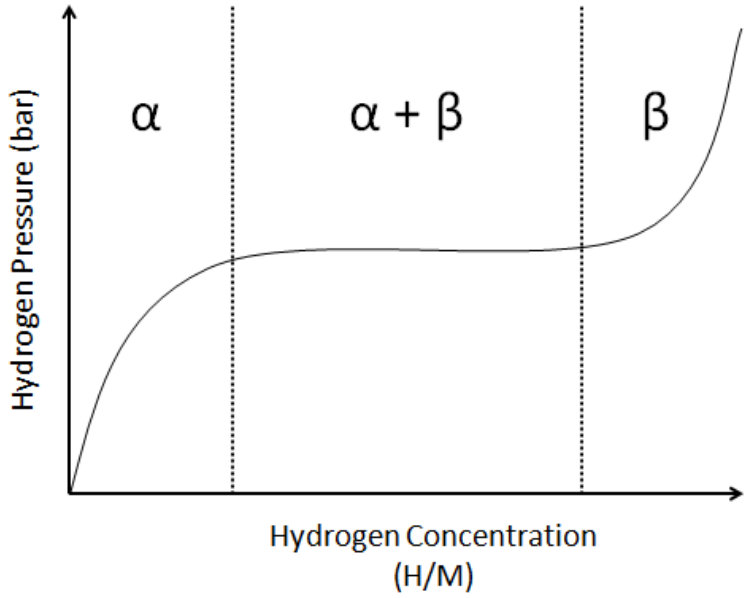

Figure 3.3 A typical pressure-composition isothermal (PCT) plot.

At the start of the PCT curve when a metal lattice and hydrogen initially combine, only a small amount of hydrogen dissolves into the metal. This creates a solid solution α-phase at which only some of the hydrogen is absorbed. As the hydrogen pressure and concentration of hydrogen in the metal increases more interactions take place between the metal atoms and hydrogen which leads to the nucleation and growth of a new hydride, the β-phase. At this stage the hydride is fully formed and as the pressure increases any further hydrogen is dissolved within the metal.

In the region in which both the solid solution α-phase and metal hydride β-phase co-exist a plateau is present in the isotherm.

3.2.1 Characteristics of PCT Curves

When describing a PCT measurement there are several features which can be explained. Figure 3.4 shows some of the key characteristics of PCT curve.

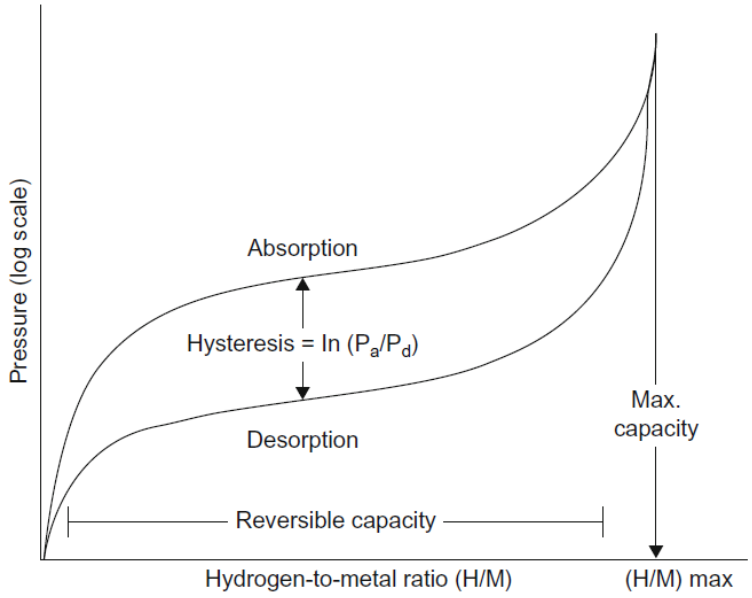

Figure 3.4 A typical PCT curve showing absorption and desorption.

Absorption and desorption curves of metal hydride systems vary because most metal hydrides do not go through the same absorption/desorption path. This difference between the absorption and desorption path in an isotherm is known as *hysteresis* (Sandrock, 1999). For successful hydride formation, the plateau pressure for absorption, P_a, must be greater than the plateau pressure for desorption, P_d. The ratio of P_a/P_d is used to calculate hysteresis loss which gives a measure of the energy loss during each hydriding and dehydriding cycle.

Capacity is another important feature of a PCT curve. The *maximum capacity* is defined as the amount of hydrogen that an alloy can absorb until it is fully saturated. Typically, this

quantity of hydrogen cannot be completely removed from a metal hydride without substantial heating and often requires the use of a vacuum.

On the other hand, the *reversible capacity* of a metal hydride refers to the width of the plateau section and is the hydrogen storage capacity of the hydride under practical operating pressures.

When evaluating the fundamental properties of a given hydride the atomic H/M ratio is considered, however, a more applicable measure is weight percent (wt%), where the mass of the host lattice is considered (Sandrock, 1999). In the case of hydrogen storage, the capacity of a metal hydride is calculated using the following equation:

$$wt\% = 100 \times \left(\frac{M_H}{M_S \times M_H}\right)$$

Where, M_H is mass of hydrogen and M_S is the mass of the sample.

3.2.2 Thermodynamic Considerations

Figure 3.5 shows the effect of temperature on PCT curves. As the temperature is increased, from T_1 to T_3, the plateau during the α + β two phase region is reduced in length until it reaches the critical temperature, T_C. Above T_C there is a continuous transition between the α-phase and β-phase in which no plateau is present.

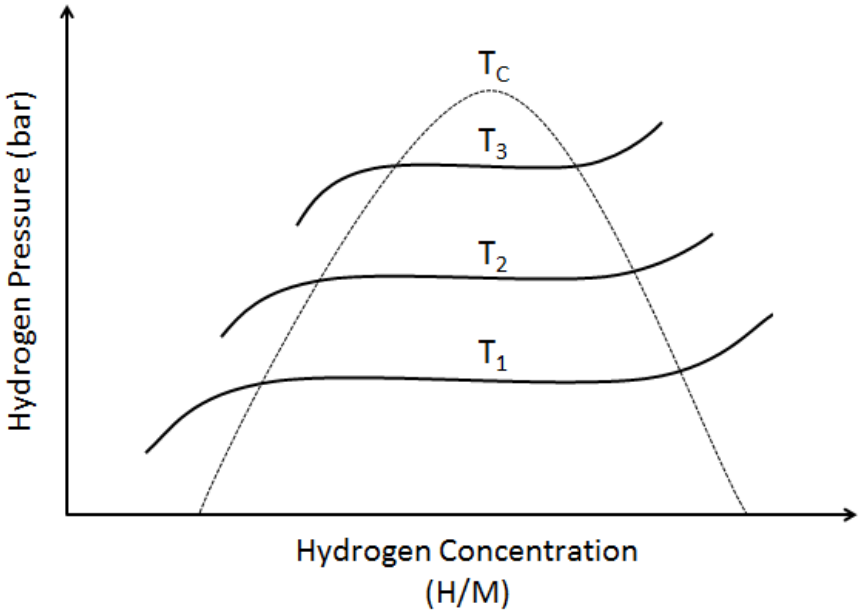

Figure 3.5 Variation of plateau pressure with temperature in a PCT plot.

The relationship between plateau pressure and temperature can be expressed by the van't Hoff equation:

$$\ln \mathrm{P} = \frac{\Delta H}{RT} - \frac{\Delta S}{R}$$

Where, P is the equilibrium pressure at temperature, T, ΔH and ΔS are standard enthalpy and entropy changes of the hydriding/dehydriding reaction and R is the gas constant (8.3145 J/mol K).

The ΔS is generally considered to be a relatively constant value because it corresponds to the entropy of a gaseous hydrogen molecule and two hydrogen atoms: - 130 J/K mol H_2. It therefore does not significantly vary between different metal hydrides (Züttel, 2004).

The ΔH is used to characterise the strength of the M-H bond so values vary amongst metal hydrides. To reach a plateau pressure of 1 bar at 300 K, ΔH should amount to 39.2 kJ mol^{-1} (Züttel, 2003).

The ΔH of metal hydrides is also an important consideration for applications in which thermal management is required - generally a small ΔH is needed.

The derivation of ΔH and ΔS values for hydride formation or decomposition can be achieved through the measurement of several PCT isotherms, evaluating the change in the plateau pressure (lnP) versus the inverse temperature (1/T); known as a van't hoff plot. Using the van't hoff equation (Equation 2) the gradient of the line is used to give ΔH and the intercept (when, 1/T = 0) the ΔS.

3.3 Gas Sorption Measurements

There are two main methods of performing gas sorption measurements. Gravimetric techniques are used to determine the amount of hydrogen absorbed or desorbed by a sample through calculating the change in its mass (Benham & Ross, 1989). On the other hand, volumetric techniques determine the amount of hydrogen absorbed or desorbed by a sample by calculating the change in pressure of a fixed volume (Checchetto et al., 2004).

For metal hydrides, the most frequently used measurement technique is the volumetric method involving Sievert's type apparatus. The basic operating principle behind a Sieverts type system relies on the fundamental idea that pressure is proportional to the number of moles, as derived from the real gas law:

$$PV = nZRT$$

Where, P is pressure, V is volume, *n* is the number of moles, Z is the gas compressibility, R is the universal gas constant (8.3145 J/mol K) and T is the temperature. Where V, Z, R and T are kept constant, P is varied and *n* determined.

Unfortunately, the real gas law does not take into consideration volume occupied by the gas and the interaction forces of different gases. To overcome this, a modification was proposed by Johannes D. van der Waals in 1873 which includes two constants, *a* and *b* to account for deviations from real gas behaviour at higher pressures. The van der Waals equation of state model is now widely accepted as the most accurate way of calculating gas sorption:

$$nRT = \left(P + \frac{n^2 a}{V^2}\right)(V - nb)$$

Again where, P is pressure, V is volume, *n* is the number of moles, R is the universal gas constant and T is the temperature.

3.3.1 The Sieverts Method

A schematic diagram of a basic Sieverts system is shown in Figure 3.6. Within the system, known volumes V1 (dose volume) and V2 (reactor volume) are accurately determined. Valves A and B allow control of the gas pressure set in V1. Valve C is a fast opening valve used to vary the pressure in V2. The pressure in V1 is continually monitored by a pressure gauge.

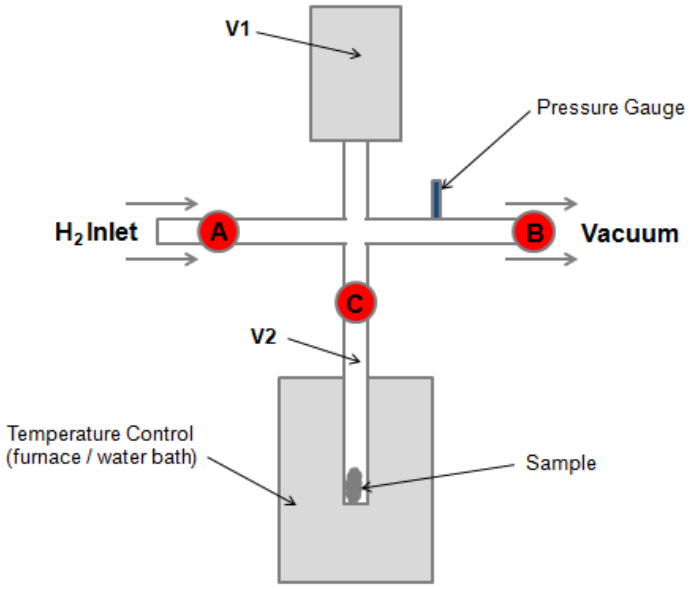

Figure 3.6 Schematic diagram of basic sieverts system.

The dose volume (V1) is maintained at a constant temperature (e.g. 303 K), the reactor volume (V2), which contains the sample, can be set to the desired temperature, using either a furnace or water bath. Thermocouples are placed both within the furnace and sample holder to ensure the temperature can be controlled and measured accurately.

During an absorption measurement, an initial pressure (P_i) is set in V1, via valves A and B with valve C closed, the pressure is allowed to stabilise, with Pi then accurately recorded (with valves A and B closed). Valve C is then opened and the pressure is allowed to reach equilibrium, before valve C is closed; the equilibrium pressure (P_f) is measured in V1 only.

The number of hydrogen moles (uptake) sorbed by a sample at any given pressure step is given by the following equation:

$$\Delta n = \frac{\mathrm{P}_i \mathrm{V}_i}{Z_i T\ \mathrm{RT}} - \frac{P_f(\mathrm{V1} + \mathrm{V2})}{Z_f T\ \mathrm{RT}}$$

Where, *ZiT* and *ZfT* are hydrogen compressibility factors at the measurement temperature, T, and P*i* and P*f* are the initial pressure and final measured pressure respectively. This process is then repeated until a complete isotherm is mapped out.

Once the number of moles (therefore mass) of hydrogen has been determined with knowledge of the sample mass the wt% of hydrogen can be calculated.

A limitation in this approach is that the total measured uptake is the sum of the individual uptakes measured at each step. This results in a compounding of errors, where any error in determining the uptake of a given pressure is carried forward to all subsequent stages. Sources of errors during measurement will be discussed in Chapter 6.

3.4 Summary

This chapter has illustrated the four fundamental stages of metal/hydrogen interactions:

- Physisorption of H_2 on the surface,
- Dissociation to form two hydrogen atoms,
- Chemisorption into an interstitial site,
- Diffusion through the lattice, via interstitial sites, resulting in a solid solution (β phase),

The act of hydrogen atoms residing within interstitial sites within the lattice results in a volume expansion of the unit cell and therefore the lattice as a whole. This volume expansion generates stressed within the material, causing intergranular fracture (decrepitation). The process of decrepitation yields smaller particles with cleans (non-oxidised/contaminated) surfaces, allowing faster kinetics, due to reduced diffusion lengths and high surface areas.

This chapter has also highlighted the significance of PCT isotherms in determining the performance of hydrogen storage materials. Chapter 6 will detail further the experimental conditions used to acquire the PCT isotherms in this thesis.

Chapter 4

METAL HYDRIDES: A REVIEW

This chapter will provide a critical literature review of the different metal hydride systems. The aim of this review is to enable understanding of the alloy choices made throughout this project.

4.1 Introduction to Metal Hydride Systems

Since the discovery of the hydrogen absorbing properties of palladium (Graham, 1866), it has been found that several intermetallic compounds are capable of reversibly reacting with hydrogen under moderate temperatures and pressures.

Promising metal hydrides are grouped by alloy type into families of hydriding-forming intermetallic compounds and include; AB_5, AB_2, AB and A_2B amongst others, where A is a stable hydride-forming element and B is an element with a low affinity for hydrogen (Züttel, 2004). This is in agreement with the Miedema model of reversed stability (Miedema, 1973) which states that the more stable an intermetallic compound is, the less stable the corresponding hydride and vice versa (Van Mal et al., 1974). Solid solution alloys are also of interest as hydrogen storage alloys.

The 'family tree' of hydriding alloys and complexes can be seen in Figure 4.1, with intermetallic compounds and solid solution alloys shown to the left, under the 'Alloy' side of the figure (Sandrock, 1999). As previously discussed (Chapter 2) complex hydrides (shown in red) will not be considered due to the limitations of operating temperatures.

Figure 4.1 Metal hydride family tree (Sandrock, 1999).

The thermal properties of metal hydrides (discussed in Chapter 3) are an important consideration because most of the natural elements will hydride under appropriate conditions. Unfortunately, in their natural form most elements do not fulfil the requirements of practical use (1 – 10 bar, 0 – 100 ^{o}C) as shown by the box in Figure 4.2.

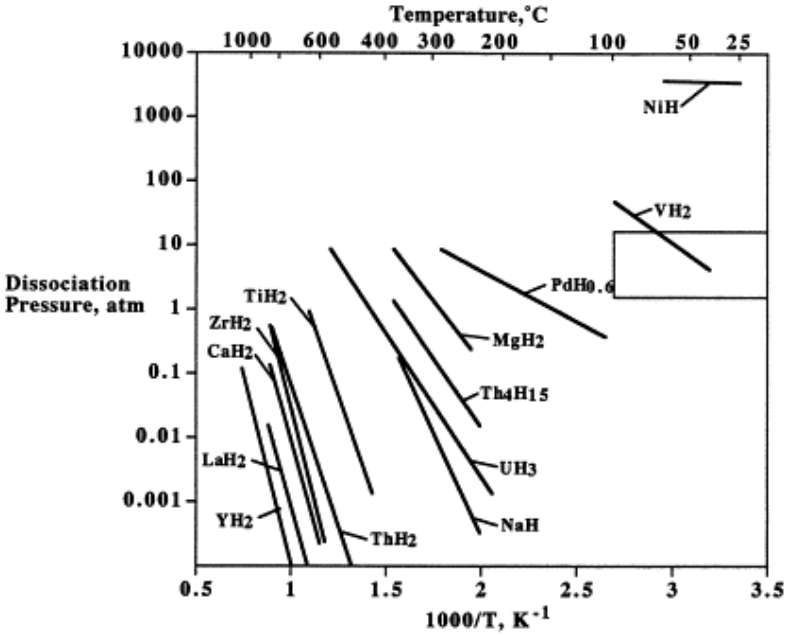

Figure 4.2 Desorption Van't Hoff lines for several known elemental hydrides. The box on the right indicates the 1–10 atm, 0–100°C range (Note : 1 atm = 1.01 bar) (Sandrock, 1999).

From Figure 4.2 it can be seen that only vanadium is within the desired temperature and pressure range which is why there is interest in solid solution alloys based on V for hydrogen storage applications. This will be discussed after a review of Intermetallic Compound.

4.2 Intermetallic Compounds

4.2.1 AB_5

The AB_5 family of alloys are known to have exceptional versatility because many different elemental species can be substituted, at least partially, into the A and B lattice sites. In these alloys the A elements tend to be based on elements such as La, Ca, Y or Zr and the B elements are mostly based on Ni, with many other possible full or partial substitution elements such as Co, Al, Mn, Ti etc (Chandra et al., 2006).

One of the most common examples of an AB_5 type alloy is $LaNi_5$ which has a hexagonal $CaCu_5$ (*P6/mmm*) crystal structure, as shown in Figure 4.3.

Figure 4.3 Crystal Structure of $LaNi_5$ (Gross et al., 1998).

The reaction of $LaNi_5$ with hydrogen can be written as:

$$3H_2 + LaNi_5 \leftrightarrow LaNi_5H_6$$

Hydrogen has been shown to occupy interstitial sites within alloys which have a spherical radii of at least 0.4 Å. If the interstitial sites are larger the hydrogen atom often sits off centre.

The logarithm of the plateau pressure has been shown to vary linearly with the unit cell volume of the host lattice for AB_5 alloys, as seen in Figure 4.4. This was first investigated by Mendelsohn & Gruen in 1977 and later supported by Reilly et al., (1999). A reduction in unit cell volume will result in a reduction in the spherical radii on any interstitial sites, giving rise to a larger enthalpy of reaction (Mendelsohn & Gruen, 1977; Reilly et al., 1999).

This correlation between unit cell volume and ΔH has been widely utilised in the development of AB_5 alloys, which form hydrides with stabilities within the required range for battery applications.

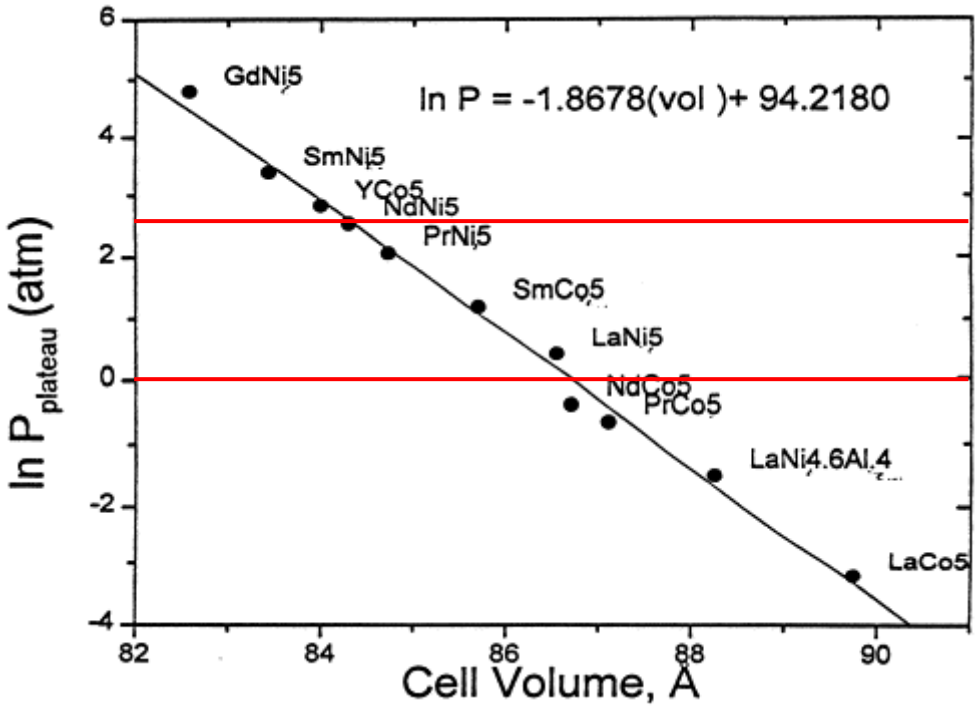

Figure 4.4 Alloy cell volume vs. ln $P_{plateau}$ for various AB_5 type hydrides at room temperature, with the red lines representing 1 and 10 atmospheres. Adapted from Reilly et al., (1999).

The high number of alloys with near-ambient PCT properties makes AB_5 alloys ideal for both PEM fuel cell and metal hydride battery applications, with the ability of tuning the alloy composition to meet the desired properties for a given application possible.

Unlike other systems, AB_5 alloys are easy to activate and because these alloys do not form protective oxide layers they have a good tolerance to small amounts of O_2 and H_2O impurities in the hydrogen stream (Sandrock & Goodell, 1984) .

Despite the promising volumetric hydrogen densities that these alloys possess, their gravimetric densities are limited to 1 – 1.25 wt% reversible capacity (Sandrock, 1999). In addition, the raw material cost is high in comparison to alternative systems (which will be explained in the following sections).

4.2.2 AB_2

The AB_2 family of intermetallic compounds, like the AB_5 alloys, represents a large and versatile group of hydriding materials with PCT properties suitable for ambient temperature applications. The first AB_2 intermetallic alloy was reported in 1967 by Pebler and Gulbransen in their investigation of the binary alloys ZrM_2, where, M = V, Cr, Fe, Co and Mo (Pebler & Gulbransen, 1967). In these alloys, the A-elements tend to be from the IVA group, such as Ti, Zr, Hf and/or the lanthanides (La, Ce Pr, etc). The B-elements can be a variety of transition or non-transition metals with a preference for V, Cr, Mn or Fe (Sandrock, 1999).

Similar to the AB_5 family, a wide variety of substitutions are possible for both A and B elements which allows for fine tuning of the PCT properties. An example of this is provided in a review article by Bowman & Fultz (2002) which illustrates that the midpoint plateau pressure for absorption in the AB_2 alloy $ZrMn_x$ ($1.8 < x < 3$), can vary by nearly a factor of fifty over the different compositions.

Almost all AB_2 alloys are based on two related Laves phase crystal structures, which are shown in Figure 4.5.

Figure 4.5 (a) The C14 Laves (Barrett, 1973) and (b) C15 Laves (Wernik, 1967) crystal structure.

- C14 Laves: Hexagonal, $MgZn_2$ structure (*P63/mmc*)
- C15 Laves: Cubic, $MgCu_2$ structure (*Fd3m*)

These two crystal structures are related to each other as the basic unit layer of the phases is the same, with the major difference being the stacking sequence of the unit layer (Edwards, 1972).

As with the AB_5 system, it has been found that there is a correlation between unit cell volume and plateau pressure and subsequently enthalpy values in Laves based AB_2 alloys. This was first experimentally demonstrated on the C15 phase, and later on the C14 phase by Nakano & Wakao (1995) and Nakano et al., (1997) . The relationship between the unit cell volume of the C14 Laves phase and enthalpy is shown in Figure 4.6.

Figure 4.6 C14 Laves unit cell volume vs. $-\Delta H$ for Zr-Ti-V-Mn-Ni-E (Co, Fe, Mo) AB_2 type hydrides with varying compositions at room temperature (Nakano et al., 1997).

There can be difficulties surrounding the activation of AB_2 alloys, although some can do so without heating; such as those based on Zr or Mn. To overcome some of these issues, it has been shown that the presence of a second phase often greatly improves activation behaviour, along with reaction kinetics during hydrogen charging in AB_2 alloys (Bououdina et al., 1998)

One example of a commercial use of an AB_2 system was demonstrated by GfE who developed a Ti-Zr(V-Fe-Cr-Mn) alloy which exhibited a storage capacity of 1.8 wt% and rapid kinetics. A similar alloy has also been successfully demonstrated for use as a hydrogen storage material onboard the first hydrogen powered canal boat - The Ross Barlow (Bevan et al., 2011).

Once activated AB_2 alloys are relatively sensitive to impurities in the hydrogen stream and, when based on Zr or Mn, they are also highly pyrophoric which is a major safety concern.

The reversible capacities of AB_2 alloys are comparable to AB_5 alloys but they generally have higher maximum capacities. In addition, they offer significant advantages over AB_5 type alloys in cost.

4.2.3 AB

The first practical AB alloy was demonstrated by Reilly & Wiswall (1974) who investigated TiFe and the effects of substitution on the system, such as replacing Fe with Mn or Ni. These Ti-Fe-based alloys are generally based on an ordered BCC, CsCl structure (*Pm3m*) and can be seen in Figure 4.7

Figure 4.7 The CsCl structure (Sirdeshmukh et al., 2011).

Similar to the other families of intermetallics, the PCT properties of these alloys can be modified by substitution of Ti and Fe. From a hydrogen sorption perspective, the hydrogen capacities of TiFe-based AB alloys are comparable with AB_5 and AB_2 type alloys, achieving a maximum capacity of 1.86 wt% and with a reversible capacity of 1.5 wt% (Sandrock, 1999).

Although these alloys are relatively low in raw material cost, the difficulties associated with activation, coupled with their low tolerance to gaseous impurities have prevented the widespread commercial use of TiFe-based AB alloys for hydrogen storage applications.

4.2.4 A_2B

The A_2B family represents the fourth group of intermetallic compounds. In these compounds A is typically a Group IVA element, such as Ti, Zr, Mg or Hf and the B-element is a transition metal, often Ni. As a result of this, various crystal structures are possible within A_2B compounds.

A typical example of an A_2B type alloy is Mg_2Ni, shown in Figure 4.8, which has been extensively investigated from both a fundamental and application perspective due to it possessing an attractive hydrogen capacity as well as cheap raw materials.

Unlike other intermetallic alloys Mg_2Ni transforms to a transition metal complex when exposed to hydrogen. During this reaction, four hydrogen atoms bond with a Ni atom and the two Mg atoms donate electrons to stabilise the bond – forming Mg_2NiH_4 (Sandrock, 1999). This results in a reversible capacity of 3.6 wt% which is significantly higher than any other alloy system.

Unfortunately, due to the high stability of the bonding in the Mg_2NiH_4 complex, the enthalpy of hydride decomposition is very high, -63.5 kJ/mol H_2. This requires temperatures of up to 300 ^oC for desorption at 2.5 bar (Westerwaal & Haije, 2008). Both the low operating pressure at ambient temperature and high temperature required for desorption make Mg_2Ni unsuitable for most practical applications.

Additionally, in contrast to the other intermetallic alloy systems, Mg_2Ni is also not very amenable to modification of PCT properties by elemental substitution.

Figure 4.8 The Mg_2Ni (P6222) crystal structure (Zhang et al., 2011).

4.2.5 Other

As well as the AB_5, AB_2, AB and A_2B intermetallic compounds which have been discussed, several other families of intermetallic alloys have been shown to be capable of reversibly reacting with hydrogen. Examples include AB_3, A_3B, A_2B_7, A_6B_{23}, amongst others.

Most of these structures involve long-range AB_5 and AB_2 stacking sequences so they are therefore crystallographically related to these classic structures.

Although to date there has been little commercial interest in such alloys, AB_3 and A_2B_7 alloys have PCT properties which are of interest for ambient temperature applications.

4.3 Solid Solution Alloys

From a metallurgical perspective, the term solid solution alloy comprises of a primary element (solvent) into which one or more minor elements (solutes) are dissolved (Callister, 2003). The main difference between solid solution alloys and intermetallic compounds is that in solid solution alloys, the solute does not need to be present at a stoichiometric relationship to the solvent.

In the case of hydrogen storage alloys, solid solutions are largely based on AB_2 and AB_5 intermetallic compounds and involve a substitution-reaction mechanism whereby atoms in the crystal lattice are replaced in a disordered manner.

The main advantage of solid solution alloys is that because they are non-stoichiometric compounds, it provides a good opportunity to modify the properties of intermetallic alloys by means of substitution rather than additions of another component to the alloy. This allows for comparatively easy processing during alloy synthesis.

4.3.1 Vanadium Based Solid Solution Alloys

One family of solid solution alloys that has attracted a large amount of interest as ambient temperature hydrogen storage media are those based on V. Before we consider V-based solid solution alloys we first need to consider V alloys.

An advantage of V is that it forms a di-hydride so is capable of absorbing 2 hydrogen atoms per molecule, resulting in promising gravimetric hydrogen capacities.

An x-ray diffraction study on the V-hydride system found the existence of three crystalline phases; the primary solid solution, BCC α-phase, at a hydrogen concentration between VH_0-$VH_{0.05,}$ a body-centered tetragonal β-phase at $VH_{0.05}$ and an FCC γ-phase appears at $VH_{0.90}$ (Maeland, 1964). The di-hydride properties of V are presented by two plateaus at different equilibrium pressures in the PCT measurements. Figure 4.9 shows a PCT measurement of V-hydride, showing the plateau between $VH_{\sim1}$ and $VH_{\sim2}$, which is responsible for the majority of the reversible uptake.

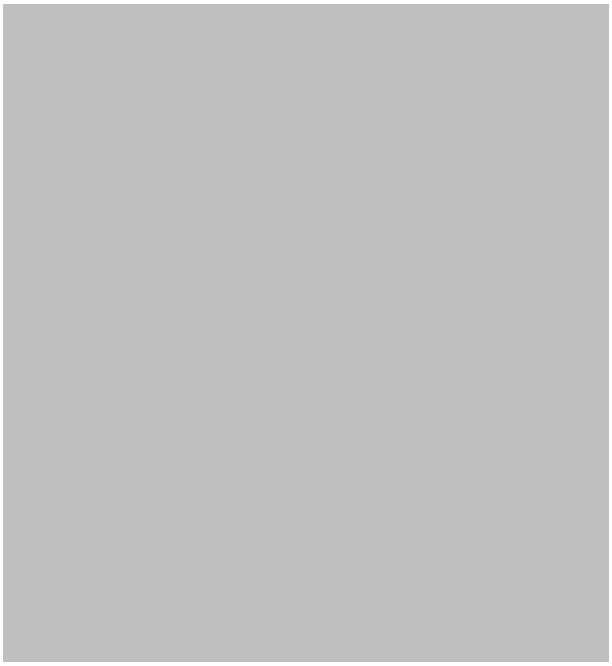

Figure 4.9 PCT diagram of $VH_{\sim1}$ and $VH_{\sim2}$ (Reilly & Wiswall, 1970).

The equilibrium pressures of the two plateau regions shown in the PCT measurement of V was measured by Papathanassopoulos & Wenzl (1982). The authors found that the lower desorption equilibrium pressure was at 10^{-1} Pa (0.00001 bar) at 353 K and the upper was 10^{5} Pa (10 bar) at 263 K.

The plateau region in BCC alloys often exhibit sloping behaviour which is undesirable for hydrogen storage applications because it reduces the effective hydrogen capacity (Hagström et al., 1998; Park et al., 2002; Yang et al., 2010). Although solid solution BCC alloys based on V are capable of absorbing up to 3.8 wt% hydrogen (H/M ~2), only half of the absorbed hydrogen can be desorbed at room temperature (Reilly & Wiswall, 1970). Subsequently, despite the intrinsically large hydrogen capacities V-alloys exhibit, there have only been a limited number of studies on their hydrogen-absorbing properties.

Some of the other reported disadvantages of BCC phase metals and alloys used as hydrogen storage materials include slow kinetics, difficulties in activation and cost – particularly when V is used.

To overcome some of the issues surrounding the slope of the plateau in BCC alloys, several groups have studied the effect of alloying additions to V-based solid solution alloys. This is because, based on the properties of the V di-hydride, it is logical that binary and higher component solid solution alloys based on V offer large potential for applications involving hydrogen storage at ambient temperatures.

Ono et al. (1980) investigated the effect of using Ti as an alloying additive to the V-H_2 system as a method of controlling the dissociation pressure and to reduce cost. The results obtained show that the addition of Ti to V lowers the plateau pressure and lowers the enthalpy of

hydride formation and decomposition from previous work reported on the V-H_2 system reported by Reilly & Wiswall (1970): from - 40.17 kJ/mol H_2 to - 48.12 kJ/mol H_2.

The reaction rates of V and other group V BCC metals were later investigated by Libowitz and Maeland in 1984. Their first study highlighted that adding a second element to BCC metals results in alloys that rapidly react with hydrogen at room temperature without the need for prior high temperature activation. In order for this to occur the authors found that the second element had to possess an atomic radii 5 % smaller than the BCC metal (Maeland et al., 1984). In addition, the authors found that this effect was not just limited to binary alloys. In their later study Maeland et al., (1984) found that V-Ti alloys prepared by quenching at high temperature exhibit rapid hydriding behaviour with small additions of a third element - again provided that the atomic radii of the element is at least 5% smaller than the average radii for the V-Ti. Suitable elements with smaller atomic radii include Fe, Mn, Cr and Co.

Following on from these findings, Lynch et al., (1985) studied the effect of alloy composition on the PCT properties of V-Ti-Fe alloy systems, as Fe was substituted for Ti. It was found that small additions of Fe resulted in an increase in the desorption plateau pressure during PCT measurements. This led to a significant change in the enthalpy of hydride decomposition: a linear decrease was observed in ΔH with increasing Fe, as shown in Figure 4.10.

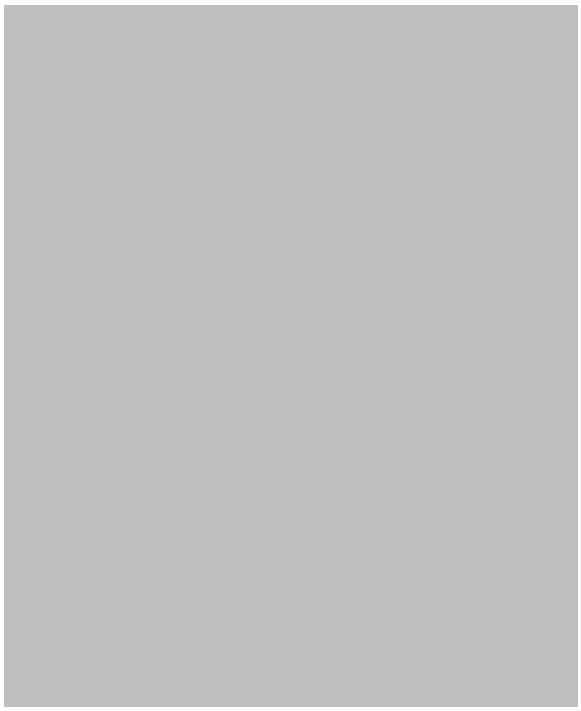

Figure 4.10 Variation in the enthalpy of hydride decomposition as a function of Fe content in V-Ti-Fe alloy (Lynch et al., 1985).

The authors suggested that this relationship was due to the decrease in lattice parameters and atomic radius of the tetragonal site occupied by hydrogen within the dihydride lattice. This study therefore provides evidence for the correlation between atomic radii with plateau pressure and enthalpy values in BCC solid solution alloys.

A similar V-Ti-Fe system was later investigated by Nomura & Akiba (1995) who were developing high capacity hydrogen absorbing alloys to recover hydrogen from a nuclear fusion reactor. During the investigation alloys with varying Ti, V and Fe content were produced by arc-melting. The PCT measurements were carried out at the working temperature of the reactors; 253 K for absorption and 573 K for desorption. It was found that a $Ti_{0.435}V_{0.49}Fe_{0.075}$ alloy had a maximum hydrogen capacity of 3.9 wt% and reversible capacity of 2.4 wt% at 253 K under 70 bar H_2. Furthermore, the hydrogen absorption rate was faster than the conventional $LaNi_5$ system and the hydrogen capacity did not reduce after

fifty hydrogen absorption-desorption cycles, making it a suitable candidate as a hydrogen storage alloy.

A group led by Tsukaha reported on AB_2 V-based multiphase alloys to be used as electrode material in Ni-metal hydride batteries (Tsukahara et al., 1995; Tsukahara et al., 1995; Tsukahara et al., 1996). They found a $TiV_3Ni_{0.56}$ alloy consisted of two phases which each had a different function: the first phase was a Ti-V based solid solution with a BCC structure that absorbed large amounts of hydrogen and the second phase was a TiNi-based compound with a BCC structure, which acted as a catalyst during the reaction with hydrogen.

The authors went on to report on $TiV_3Ni_{0.56}$ alloys with Hf additions (0.046 and 0.24 at%) which were developed in order to improve the kinetic properties of these alloys (Tsukahara et al., 1996). XRD analysis identified that these alloys consisted mainly of a BCC solid solution phase but also a $MgZn_2$-type C14 Laves phase structure. After five hydrogen absorption-desorption cycles cracking was observed in and around the C14 Laves phase. It was suggested that the cracking occurred due to the two phases absorbing different amounts of hydrogen during the absorption-desorption cycles, leading to stress induced by the different expansion ratios. This cracking resulted in an improvement in the reaction rate as it increased the fresh surface area of the alloys. It was concluded that the combined effect of the two phases provided a higher electrode capacity than those previously reported in single-phase intermetallic compounds.

4.3.2 Multiphase Solid Solution Alloys

Akiba et al., (1994) formed multi-component AB_2 alloys (consisting of Zr and Ti for the A site and V, VI and VII transition metals for the B site) that contained multiple phases

including: C14 Laves, C15 Laves, BCC based solid solution and a Zr_3V_3O oxide phase. These alloys were subsequently described as *"*Laves phase related BCC solid solution alloys*"*.

PCT measurements showed that all the multi-phase alloys had single step isotherms, as shown in Figure 4.11. This indicates that during hydrogen absorption-desorption these multi-phase alloys behaved like single phase alloys.

Figure 4.11 PCT diagram of the $Zr_{1-x}Ti_xM_2$-H_2 systems at 313 K (Akiba et al., 1994).

This can be explained by Miedema's rule of reversed stability (Miedema, 1973): the difference in stability of the C14 Laves phases and BCC phase is small so hydrogen transfers readily from one phase to another by changing the temperature or composition. The stability of the hydrides of these phases is therefore similar and results in a single step plateau in PCT measurements of multi-phase alloys.

The microstructure and composition of a $Zr_{0.5}Ti_{0.5}MnV$ alloy (85 wt% C14 Laves and 15 wt% BCC) was examined by SEM/EDX and TEM analysis. From the micrographs, three different

regions were identified: grey (A) and black (C) colonies were found in a matrix phase (B). EDS found that region C contained only Zr, whereas Ti, V and Mn were found in the A particles. The matrix region, B, contained different intensities of all elements. From these results, it was concluded that region A was a BCC solid solution phase, containing Ti, V and Mn. Region B was the C14 Laves phase ($ZrMn_2$ structure) and Region C was a pure Zr phase (Iba & Akiba, 1995).

In 1997 Akiba reported on a Ti-Cr-V BCC-Laves phase solid solution alloys with varying Ti/Cr ratios. PCT measurements on both as-cast and heat treated alloys showed that the as-cast alloy had a sloping plateau, indicating inhomogeneity, whereas the heat treated alloy possessed a much flatter plateau. This highlights the importance of heat treatment, to ensure homogeneity, in BCC solid solution alloys.

Another important finding of the investigation was that variation in the atomic ratio of Ti/Cr had a significant effect on the equilibrium pressure during hydrogen uptake, as shown in Figure 4.12.

Figure 4.12 PCT plot showing the composition dependency of the equilibrium pressure for absorption (●) and desorption (○) in Ti-Cr-V alloys (Akiba & Iba, 1998).

A change in the lattice parameter of 0.025 nm, representing an overall change of 5 at% in the composition of the alloy, resulted in a change in the equilibrium pressure by an order of magnitude. This demonstrates how sensitive the equilibrium pressure is to changes in the lattice parameters in BCC solid solution alloys.

4.3.3 Ti-V-Mn Alloys

Following on from their previous work, later in 1997 Iba & Akiba began investigating the hydrogen storage properties of Ti-V-Mn alloys with modulated structures. The authors proposed that it is the effect of the alloy interface and interaction of each phase that creates a larger capacity than the linear combination of the individual phases.

During this study microstructural analysis showed that crystallised colonies were found in as-cast TiMnV alloys, comprising of 78 wt% BCC solid solution matrix phase and 22 wt% C14 Laves phase colonies.

Figure 4.13 shows a TEM micrograph of the area adjacent to the BCC/C14 Laves interface.

Figure 4.13 TEM micrograph of the area adjacent to the BCC/C14 Laves phase interface in Ti-Mn-V (Akiba, 1999).

From the micrograph, a very fine lamellar structure (10 nm thick) was identified. The diffraction pattern of the matrix phase showed satellites induced by lattice strain in the final structure. It was summarised that these lamella structures adjacent to the BCC/C14 Laves interface were modulated structures formed by spinodal decomposition.

EDS analysis was performed on the phase adjacent to the interface and the composition was found to be $Ti_{1.0}Mn_{0.9}V_{1.1}$. PCT measurements were carried out and it was found that $Ti_{1.0}Mn_{0.9}V_{1.1}$ had a capacity up to two times larger than that of the matrix alloy, with the same composition, and the plateau region was wider. Ti-V alloys cannot usually desorb hydrogen under ambient conditions so this shows a significant improvement over conventional BCC hydrogen absorbing alloys.

In 2000, Nakamura & Akiba investigated the hydrogenation properties and crystal structures of Ti-V-Mn BCC solid solution alloys. Figure 4.14 shows PCT results of $Ti_{1.0}V_{1.1}Mn_{0.9}$, which shows two plateau regions during absorption: the lower plateau pressure was around 0.1 bar and the higher plateau pressure was around 10 bar at 298 K (Nakamura & Akiba, 2000).

Figure 4.14 PCT of as-cast $Ti_{1.0}V_{1.1}Mn_{0.9}$ at 298 K for absorption and 373 K for desorption (Nakamura & Akiba, 2000).

XRD analysis found three types of hydrides were present in the alloy, the hydrogen contents of which are indicated on the PCT measurement in Figure 4.14.

I. Distorted BCC structure, present when hydrogen content is < 0.5 H/M. XRD peaks are broad and asymmetric which suggests the structure is distorted from an original BCC structure.

II. Deformed (pseudo-cubic) FCC structure, present between 0.8 and 1.0 H/M.

III. Full hydride with a FCC structure.

The plateau region at the lower hydrogen pressure (0.1 bar for absorption at 298 K) coexists between hydrides I and II and the second plateau region at the higher hydrogen pressure (1 bar for absorption at 298 K) coexists between hydrides II and III.

An illustration, showing the structure change of the metal sublattice (*a* and *c* lattice parameters) in the Ti-V-Mn alloy during PCT measurement is shown in Figure 4.15.

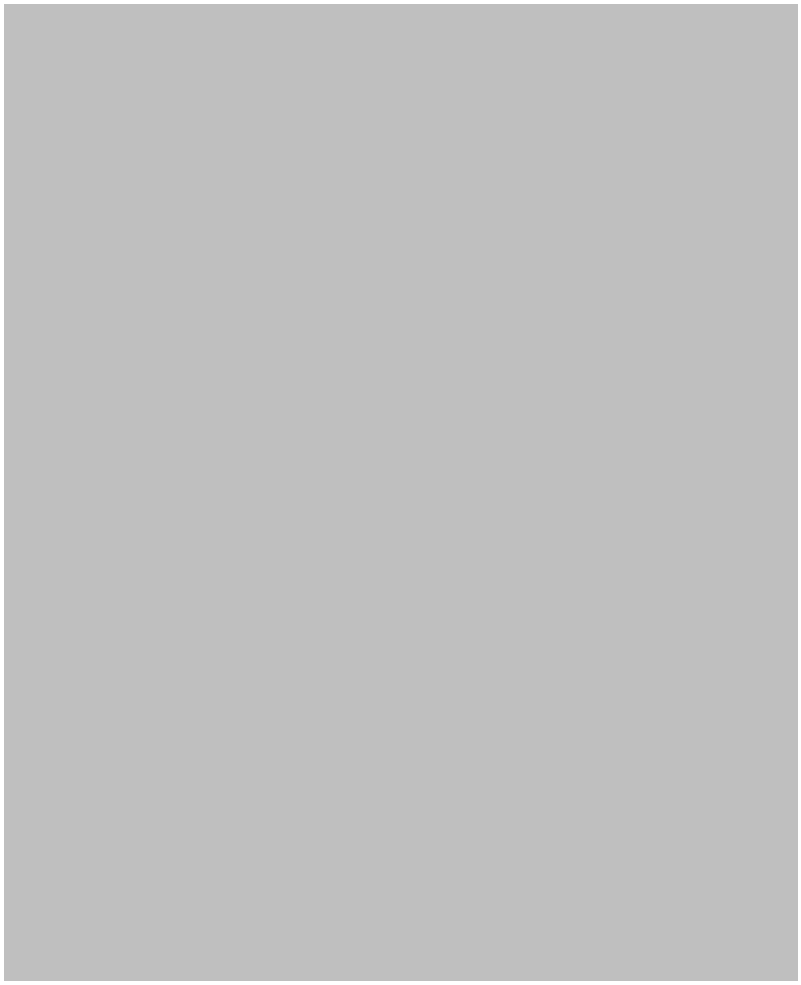

Figure 4.15 Change in the crystal structure of the metal lattice from the BCC alloy to the deformed FCC hydride and full FCC hydride (Nakamura & Akiba, 2000).

Figure 4.15(a) shows the four BCC unit cells, which change to an expanded and distorted structure of hydride I. 4.15(b) shows the FCC structure which formed by contraction of 6 % of the a-axis and expansion of 30 % of the c-axis. Finally, 4.15(c) is formed from an

expansion by 6 % in the a-axis direction and 10 % in the c-axis direction to form hydride III with an FCC structure. The ratio of *c'/a'* changes from 0.71 (BCC) to 0.96 (deformed FCC) and 1.0 (FCC) (Nakamura & Akiba, 2000).

For hydrogen storage applications, it is the lower plateau - caused by the formation of the newly identified deformed FCC hydride phase - which is responsible for an increase in the effective hydrogen storage capacity.

Following on from this investigation, a year later the same authors examined the crystal structure of these hydrides formed in $Ti_{1.0}V_{1.1}Mn_{0.9}$, specifically the occupation sites of the hydrogen atoms in the pseudo-FCC structure (hydride II) by neutron diffraction (Nakamura et al., 2001). It was found that the mono-hydride phase (hydride II) had a pseudo-cubic NaCl structure, which, at the time was different from any hydride formed from BCC solid-solution alloys that had been reported. The di-hydride phase (hydride III) had a CaF2-type structure, which had previously been reported in BCC metals such as V and Nb.

In 2002, Nakamura & Akiba went on to investigate the dependency of alloy composition on the hydriding properties and crystal structure of NaCl-type mono-hydrides. During the investigation it was found that the equilibrium pressure of the two plateau's in the PCT curve was dependent on the unit cell volume of the phases, and subsequent lattice parameters: a large unit cell volume generally resulted in a low plateau pressure. The authors also discovered that the equilibrium pressure of the second plateau, which corresponds to the di-hydride formation, was much more sensitive to changes in the unit cell volume because the first plateau, the mono-hydride, has larger hydrogen occupation sites (Nakamura & Akiba, 2002). This relationship is shown in Figure 4.16.

Figure 4.16 Relationship between unit cell volume *V* and equilibrium (plateau pressure) pressure of the first and the second plateaus for Ti–V–Mn BCC solid solution alloys (Nakamura & Akiba, 2002).

This is in agreement with previous studies investigating the relationship between unit cell volume and equilibrium pressure in AB_5 type alloys, such as $LaNi_5$ (Mendelsohn & Gruen, 1977; Reilly et al., 1999) and AB_2 type alloys (Nakano et al., 1997; Nakano & Wakao, 1995). Additional work is however required to confirm the dependency of the plateau pressure on the unit cell volume in Laves phase related BCC solid solution alloys.

In the same year, Mouri & Iba (2002) investigated the activation properties and reaction rates of Ti-V-Mn Laves phase related BCC solid solution alloys with different Laves phase fractions. It was found that the incubation time - the time to start absorbing hydrogen in the first activation cycle – was reduced by the effect of the Laves phase coexisting with the BCC phase. After activation, the hydrogen absorption rate of Laves phase related BCC solid solution alloys was as high as that of just the single phase C14 Laves alloys.

In addition, the authors concluded that it was the C14 Laves phase which first absorbed hydrogen, leading to the formation of new cracks inside the C14 Laves/BCC phase boundary in the initial stage of activation, shown in Figure 4.17. This is in agreement with previous work reported by Tsukahara et al., (1996).

Figure 4.17 Schematic drawing of crack-formation during activation (Mouri & Iba, 2002).

One of the interesting features of multi-phase Laves alloys, such as $TiMn_2$ and $ZrMn_2$ is the presence of a wide range of homogeneity. Mitrokhin (2005) proposed three different models to explain deviations from stoichiometry in C14 Laves phase alloys:

1. Vacancy Model: formation of vacancies in the lattice.

2. Substitution Model: substitution by superstoichiometric atoms for substoichiometric atom positions within the structure.

3. Interstitial Model: the placement of superstoichiometric atoms in interstitial sites.

Mitrokhin found that in the solid solution region the main thermodynamic and structural parameters of alloys and their hydrides change monotonously with the concentration of the components - supporting the Substitution Model which was put forward.

In simple binary alloys, Vegard's rule can be used to calculate the thermodynamic and structural characteristics because a linear relationship exists between lattice parameters of an alloy and the concentrations of the constituent elements.

4.3.4 $Ti_{0.5}V_{0.5}Mn$ Alloys

Shibuya et al., (2008) investigated the effect of V substitutions on the hydrogen absorption/desorption behaviour and microstructure in Ti-V-Mn alloys, suitable for hybrid hydrogen storage vessels of 350 bar (which will be discussed in the Chapter 5). In the study, three different alloys with varying Ti and V content were produced by arc melting: $Ti_{0.7}V_{0.3}Mn$, $Ti_{0.5}V_{0.5}Mn$ and $Ti_{0.4}V_{0.6}Mn$. Heat treatment was then performed at 1233 K for 6 hours under a vacuum to promote a homogenous microstructure. Figure 4.18 shows the PCT curve of all three alloys at 293 K under 70 bar H_2.

Figure 4.18 PCT curves of the Ti(1-*x*)V*x*Mn (x = 0.3 - 0.6) alloys at 293 K under 70 bar H2 (Shibuya et al., 2008).

From Figure 4.18 it can be seen that the plateau pressure for absorption and desorption increased when the V content increased from $Ti_{0.7}V_{0.3}Mn$ to $Ti_{0.5}V_{0.5}Mn$ and above this, single step absorption occurred in which no plateau was present. Furthermore, the isotherms show that $Ti_{0.5}V_{0.5}Mn$ and $Ti_{0.4}V_{0.6}Mn$ may not have fully saturated up to 70 bar H_2.

PCT measurements were performed on the $Ti_{0.7}V_{0.3}Mn$ and $Ti_{0.5}V_{0.5}Mn$ alloys at 293, 273 and 243 K. At 243 K the maximum hydrogen capacity was found to be 1.7 wt% and 1.8 wt % in $Ti_{0.7}V_{0.3}Mn$ and $Ti_{0.5}V_{0.5}Mn$ respectively. The enthalpy of hydride formation (ΔH) in $Ti_{0.7}V_{0.3}Mn$ was calculated to be - 28.8 kJ/mol H_2 and - 26.8 kJ/mol H_2 for $Ti_{0.5}V_{0.5}Mn$ which both meet the requirements of hybrid hydrogen storage materials (< 20 kJ/mol H_2).

XRD analysis found that all the alloys contained C14 Laves, BCC and FCC minor phases. The FCC phase had a A_3B_3O structure which corresponded to the oxide of the Ti-V-Mn system and was previously reported in the Zr-Ti-Mn-V system by Hout et al., (1995).

Figure 4.19 shows the effect of phase composition in the Ti-V-Mn alloys with different V additions.

Figure 4.19 Effect of composition ratio of C14 Laves (black circles), BCC (white circles) and FCC (white squares) phases in Ti(1-*x*)V*x*Mn alloys and V addition (Shibuya et al., 2008).

From Figure 4.19 it can be seen that the C14 Laves phase decreased and the BCC phase increased with increasing V content. Further, Rietveld refinement found the lattice constants of the BCC phase did not significantly change by increasing V content, however, the lattice constants of the C14 Laves phase decreased with increasing V – the relationship of which is shown in Figure 4.20.

Figure 4.20 Relationship between lattice constant of the C14 Laves phase in Ti(1-*x*)V*x*Mn (x = 0.3 - 0.6) alloys and V addition (Shibuya et al., 2008).

The authors suggest that this is due to the atomic radius of V being smaller than that of Ti; 1.34 Å vs. 1.76 Å. The decrease in unit cell volume of the C14 Laves phase is therefore responsible for the increase in plateau pressure and hysteresis, as shown in Figure 4.18.

SEM analysis on the microstructure of the $Ti_{0.5}V_{0.5}Mn$ alloy showed the presence of a white phase, corresponding to the C14 Laves phase. Within the matrix of the white phase dendrite crystals were found, identified as a Ti-rich FCC phase, along with a third phase. This third phase contained a lamellar texture between the V-rich BCC and C14 phases, indicating a

eutectic reaction between the two phases. The authors summarised that the microstructure of the alloys along with the lattice constant of the C14 Laves phase influence the hydrogen storage properties in Ti-V-Mn alloys.

Following on from this key study, a year later, Shibuya et al., (2009) investigated the hydrogenation properties of the same $Ti_{0.5}V_{0.5}Mn$ alloy up to 350 bar – the working pressure of a hybrid hydrogen storage vessel. Again, the alloy was produced by arc melting and the same heat treatment was also performed.

A PCT measurement of the $Ti_{0.5}V_{0.5}Mn$ at 260 K, up to 350 bar H_2 is shown in Figure 4.21.

Figure 4.21 PCT curve of $Ti_{0.5}V_{0.5}Mn$ at 260 K up to 350 bar H_2 (Shibuya et al., 2009).

The alloy exhibited sloping plateau behaviour, which the authors suggested indicates the presence of a multi-component alloy with chemical heterogeneity. Unlike previous studies, which regarded sloping plateau behaviour as a disadvantage for hydrogen storage applications (Hagström et al., 1998; Park et al., 2002; Yang et al., 2010), Shibuya et al., proposed that this may be suitable for hybrid applications. They suggested that hydrogen absorption/desorption

gradually takes place with an increase or decrease of hydrogen pressure, which prevents vigorous heat of formation.

The alloy was found to possess a maximum capacity of 2.1 wt% and reversible capacity of 1.9 wt% at 260 K under 350 bar H_2. In addition, from Figure 4.21 it can be seen that, again, the alloy may not have fully saturated during the PCT measurement. This therefore requires further investigation at even higher pressures.

Figure 4.22 shows XRD patterns of the $Ti_{0.5}V_{0.5}Mn$ alloy before hydrogenation and after dehydrogenation. The alloy before hydrogenation contained 64.9 wt% C14 Laves phase, 21.9 wt% BCC phase and 13.2 wt% FCC phase. After dehydrogenation, the FCC phase abundance decreased slightly, however, the phase abundance and lattice constants of the C14 Laves and BCC phases did not significantly change during hydrogenation/dehydrogenation. This suggests that the alloy shows good structural stability upon cycling which is a favourable characteristic to possess for hydrogen storage applications.

Figure 4.22 XRD pattern of $Ti_{0.5}V_{0.5}Mn$ (a) before hydrogenation and (b) after dehydrogenation (Shibuya et al., 2009).

SEM analysis was performed on the alloy and yielded similar findings to that of the previous investigation (Shibuya et al., 2008). Figure 4.23 shows a backscattered electron image of the $Ti_{0.5}V_{0.5}Mn$ alloy, featuring dendritic structures. The dendrites, shown in position A, were identified as the Ti-rich FCC phase and had a chemical composition of $Ti_{0.53}V_{0.11}Mn_{0.36}$. These structures were surround by an unknown phase which contained a lamellar like texture composed of the V-rich BCC phase (position B) and C14 Laves phase (position C); the chemical compositions of which were $Ti_{0.06}V_{0.56}Mn_{0.38}$ and $Ti_{0.31}V_{0.17}Mn_{0.52}$, respectively.

Figure 4.23 Backscattered electron image of the $Ti_{0.5}V_{0.5}Mn$ alloy (Shibuya et al., 2009).

This paper provides further evidence that in Ti-V-Mn alloys both the microstructure of the alloy, along with the composition ratio of the XRD phases influences the hydrogen storage capacity, plateau pressure and hysteresis of the PCT curve.

The authors also suggest that the addition of a forth element may increase the hydrogen capacity in Ti-V-Mn alloys and further, that it needs to be investigated.

More recently, the microstructure of Ti-V-Mn BCC-Laves phase alloys before and after hydrogenation was investigated by Matsuda et al., (2011). In their study the authors used

TEM to investigate the introduction of lattice defects during hydrogen absorption/desorption. During the investigation eight alloys with varying Ti, V and Mn content were produced by arc melting. Initial XRD analysis found that the abundance of the BCC phase was dependent on V content. The V-rich compositions contained only the BCC phase, which is in agreement with previous studies (Akiba & Iba, 1998; Shibuya et al., 2009), whereas the V-poor composition contained a C14 Laves phase as well as BCC phases and in some instances a FCC Ti-oxide phase, $ZrTiO_3$ structure (Hout et al., 1995).

Strain contrasts, corresponding to lattice defects along the (101) BCC planes, were observed in the alloys in their as-cast state and after hydrogenation/dehydrogenation. After hydrogen absorption and desorption, twin boundaries and stacking faults occurred along the same (101) BCC planes and the (111) plane of the remaining FCC hydride phase. It was suggested that the effect of lattice strain may improve the hydrogen absorbing/desorbing properties of Ti-V-Mn alloys, however, this would need further investigation. The authors also concluded that it is important to understand the microstructural evolution during hydrogenation in BCC alloys to improve the effective hydrogen capacity and desorbing equilibrium pressure.

4.3.5 Ti-V-TM-Mn based Alloys

It has been shown that an increase in the abundance of the BCC phase can increase the hydrogen storage capacity of AB_2 alloys (Yu et al., 2004). It has also been suggested that the hydrogenation properties, including the plateau and hysteresis pressures may be improved in Ti-V-Mn based alloys by substitution of the transition metals (Shibuya et al., 2008) and the addition of a fourth element may increase the reversible capacity (Shibuya el al., 2009).

One of the focuses of the current work is therefore to investigate the effect of substituting V for other transition metal elements with similar BCC phase stabilising properties. For practical applications it may also be more cost effective than using pure V for the base alloy.

Elements are said to be chemically similar when they possess the same electron configuration in their outer shell. Group V and VI transition metal elements which are chemically similar to V include: Nb, Cr, Mo and Ta.

Phase diagrams are useful tools for identifying what phases are present at a given temperature or pressure. In order to identify which phases are present when V is combined with Nb, Cr, Mo and Ta binary phase diagrams, shown in Figures 4.24 – 4.27 were studied.

Figure 4.24 The Nb-V binary phase diagram (American Society for Metals, 1980).

Figure 4.25 The Cr-V binary phase diagram (American Society for Metals, 1980).

Figure 4.26 The Mo-V binary phase diagram (American Society for Metals, 1980)

Figure 4.27 The Ta-V binary phase diagram (American Society for Metals, 1980)

From the binary phase diagrams it can be seen that the same (A2) BCC phase exists at all compositions between V and Nb, Cr, Mo and Ta between 450 and 2175 K up to the solidus/liquidus line.

The Nb-V phase diagram shows the presence of the single (A2) BCC phase at all compositions between 300 and 2150 K, above which only a liquid is observed. In the Cr-V and Mo-V phase diagrams, again the single (A2) BCC phase occurs at all composition between 1900 and 2175 K in the Cr-V system and between 300 and 2150 K in the Mo-V system. The Ta-V phase diagram shows that several phases are present at different relative concentrations of Ta and V between 400 and 2100 K, including the (A2) BCC, C14 Laves and C15 Laves phases.

4.4 Summary

The AB_2 family of intermetallic alloys, which are largely based on C14 and C15 Laves phase structures, represents a large and versatile group of hydriding materials with PCT properties suitable for ambient temperature applications. Several studies have investigated the correlation between unit cell volume vs. plateau pressure and subsequent enthalpy of formation values in this system of alloys. This enables tuning of the PCT properties to meet the requirements of the given application. However, one of the main drawbacks to this family of alloys is the difficulty in activation.

From a thermodynamic perspective, vanadium hydride is within the desired temperature and pressure range for practical applications, which is subsequently why there is interest in BCC solid solution alloys based on V for hydrogen storage applications. Although V-based solid solution alloys have been shown to possess hydrogen uptake capacities of up to 3.8 wt%, only half of the absorbed hydrogen can be desorbed at room temperature. In addition these alloys are also limited by slow kinetics, difficulties in activation and cost – particularly when pure V is used.

It has been shown that the addition of a second phase can greatly improve the activation of BCC solid solution alloys. The combination of AB_2 type C14 Laves structures to BCC solid solution alloys results in alloys with improved activation and kinetic properties: while the BCC solid solution is responsible for the bulk of hydrogen uptake, it is the C14 Laves phase which first absorbs hydrogen, leading to the stress induced cracking. This results in an increase in the fresh surface area where hydrogen atoms can enter the interstitial sites.

Laves phase related BCC solid solution alloys have since attracted much interest for hydrogen storage and battery electrode applications.

In particular the $Ti_{0.5}V_{0.5}Mn$ alloy shows promising hydrogen storage properties including: good volumetric hydrogen storage capacity at ambient temperatures, fast absorption/desorption kinetics and high stability upon cycling. Previous work on the $Ti_{0.5}V_{0.5}Mn$ system has highlighted that both the microstructure of the alloy, along with the composition of the XRD phases influences PCT properties such as hydrogen storage capacity, plateau pressure and hysteresis during absorption/desorption.

Further, it has been found that it is possible to improve the PCT properties of Ti-V-Mn alloys by substituting V for other transition metals. In a key paper investigating the system, Shibuya et al., (2009) suggested that the addition of a forth element may increase the hydrogen capacity in Ti-V-Mn alloys and subsequently, that it needs to be investigated.

The purpose of the current work is to build on the existing knowledge of the $Ti_{0.5}V_{0.5}Mn$ system and investigate the effect of transition metal substitution. The following chapter describes some of the applications in which metal hydrides, particularly those based on AB_2 and BCC-Laves type solid solution alloys are utilised with a focus on hybrid hydrogen storage and hydrogen compression.

Chapter 5

METAL HYDRIDES: APPLICATIONS

This chapter will provide a review of the different metal hydride technologies, covering their applications with a focus on hybrid hydrogen storage and compression. The aim of this review is to enable understanding of the alloy choices made throughout this project in relation to a total system approach. At the end of the chapter the research aims and objectives will be provided.

5.1 Introduction

The ultimate outcome of research into metal-hydrogen interactions, from either a material or system perspective, is to facilitate the development of commercial products. Metal-hydrogen interactions are utilised in a wide spectrum of applications, which have been broadly categorised into the following areas (Sandrock & Bowman, 2003):

- Hydrogen Storage
    - Stationary & Portable
    - Mobile/Vehicular
- Thermal Compression
    - Hydrogen Compression
    - Closed thermodynamic systems

- Gas Separation
    - Isotope Separation
    - Purification & Gettering
- Electrochemical and Processing
    - Batteries
    - Catalysts
- Other
    - Processing Materials (NdFeB)
    - Switchable Mirrors

Some of the applications have reached commercial maturity, e.g. metal hydride batteries, however, for others, e.g. hydrogen storage, there are still technological barriers that need to be overcome before viable commercial deployment can occur.

This thesis considers metal hydrides specifically in relation to the use in hydrogen storage and compressions applications.

5.2 Hybrid Hydrogen Storage

The concept of a hybrid hydrogen storage vessel combines conventional high pressure gas storage with solid state storage media; in this work a metal hydride is contained within a high-pressure vessel (> 350 bar). A hybrid approach effectively increases the volumetric capacity of the system at the expense of gravimetric capacity, compared to compressed hydrogen. Figure 5.1 shows a summary of the various hydrogen storage techniques along with a hybrid vessel in relation to the DOE system target values for gravimetric and volumetric density.

Figure 5.1 A summary of the various hydrogen storage techniques, including a hybrid vessel , in relation to the 2015 DOE system target values for gravimetric and volumetric densities (Takeichi et al., 2003).

Figure 5.2 shows a schematic model view of a hybrid storage vessel, combining a lightweight high-pressure aluminium–carbon fibre reinforced plastic (Al-CFRP) vessel with a single metal hydride alloy bed. In these types of vessels, the tubes containing the metal hydride material will typically only be filled up to ~50 % to allow for expansion of the metal hydride upon exposure to hydrogen.

Figure 5.2. Schematic model view of a hybrid storage vessel, showing: (1) carbon fibre and epoxy resin, (2) thin aluminium liner, (3) hydrogen storage alloy, (4) valve and (5) hydrogen inlet/outlet. (Takeichi et al., 2003).

Figure 5.3 illustrates the mass and volume of a hybrid Al-CFRP and steel hydrogen storage vessel as a function of the volume fraction of the hydrogen storage alloy, *X*, for 5 kg of H_2 (Takeichi et al., 2003). The volume and weight of a hybrid tank can be adapted by changing the volume fraction of hydrogen storage alloy.

Figure 5.3 Volumetric and gravimetric weight of hybrid hydrogen storage system. Note the system was calculated for an alloy where ρ = 5 g/cm^3 and *h* = 3 wt% Adapted from Takeichi et al., (2003).

5.2.1 Alloy Selection

Alloy selection is a very important consideration when designing hybrid hydrogen storage vessels. When deciding on appropriate hydrogen storage alloys for such systems the key factors to take into account are: reversible hydrogen capacity, plateau pressure, operating temperature and alloy density.

Figure 5.4 shows the volume and weight of a range of hybrid systems, storing 5 kg of hydrogen at 35 MPa (350 bar), containing series of metal hydrides with varying hydrogen storage capacities and densities. This shows that the greatest performance requires the development of dense high capacity metal hydrides.

Figure 5.4 Volume and weight of a hybrid hydrogen storage system required to store 5 kg of hydrogen at 35 MPa and 298 K using various volume fractions of hydrogen storage alloy, X, and a range of hydrogen capacities and densities (Takeichi et al., 2003).

Interstitial hydrides based on Laves phases, which were discussed in Chapter 4, are considered as good hydrogen storage materials for use within hybrid systems due to their favourable PCT properties at ambient temperatures. In particular alloys based on Ti-V-Cr have been shown to possess hydrogen storage capacities of up to 2.4 wt% (Akiba & Iba, 1998).

Mori et al., (2005) built a prototype high pressure tank, equipped with heat exchangers, and loaded it with a $Ti_{1.1}CrMn$ alloy, which had a known reversible capacity of 1.9 wt%. During this investigation a vehicle sized heat management system – including a radiator and fan – was used. A schematic showing the arrangement of the tank can be seen in Figure 5.5.

Figure 5.5 Schematic view of a high-pressure metal hydride tank, adapted from Mori & Hirose (2009).

The performance results of the system developed during the investigation are summarised in Table 5.1 along with a comparison of a low pressure metal hydride tank and a high pressure tank.

Table 5.1 Performance data for hybrid tank in comparison with a low pressure metal hydride tank and high pressure tank. Adapted from Mori et al., (2005) and Mori & Hirose (2009).

Parameter	Low Pressure MH Tank	High Pressure Tank	High Pressure MH Tank (Hybrid Tank)
H_2 storage capacity	5.25 kg tank 180 L	3 kg tank, 180 L	7.3 kg tank, 180L
Tank weight	450 kg	< 100 kg	420 kg
H_2 filling time	0.5 - 1 hr	5 - 10 min	5 min / 80%
Operating Pressure	< 1 MPa	30 MPa	35 MPa

Table 5.1 shows that the high pressure hybrid tank was capable of storing almost 2.5 times more hydrogen, for the same volume, than a conventional high pressure tank; 7.3 kg vs. 3 kg.

For a hybrid tank to achieve the required performance for a practical mobile application, Shibuya et al., (2008) proposed that the metal hydride component should achieve a series targets:

(1) Gravimetric hydrogen capacity > 3 wt.%,

(2) Enthalpy of hydrogenation ΔH < 20 kJ/mol H_2,

(3) Desorption equilibrium pressure > 10 bar at 243K,

(4) Absorption equilibrium pressure < 350 bar at 393 K and

(5) Decrease of storage capacity < 10% over 1000 cycles.

Table 5.2 summarises the metal hydrides currently most suitable for use in hybrid tanks (i.e. operating temperature *ca.* 303 K).

Table 5.2 Summary of metal hydrides currently most suitable for use in hybrid tanks, listed in descending hydrogen storage capacity.

Alloy	Capacity (wt%)	Operating Temp (K)	Dissociation Pressure (bar)	Comments	Reference
$TiCr_{1.1}V_{0.9}$	3.6	298	20	Slow kinetics.	Martínez & Dos Santos (2012)
$TiCr_{1.1}Nb_{0.9}$	2.5	298	20	Improved kinetics with Nb.	Martínez & Dos Santos (2012)
$Ti_{25}Cr_{50}V_{25}$	2.4	298	4	Low dissociation pressure.	Matsunaga et al., (2009)
$Ti_{25}Cr_{50}V_{20}Mo_5$	2.4	298	23	Increased dissociation pressure with Mo.	Matsunaga et al., (2009)
$V_{0.9}Cr_{0.1}$	2.3	293	15.5	High reversible capacity	Mitrokhin et al., (2013)
$Ti_{25}Cr_{50}V_{25}$	1.96	273	10	Expensive.	Towata et al., (2013)
$Ti_{0.5}V_{0.5}Mn$	1.9	260	6	Suitable ΔH (− 26.8 kJ/mol H_2) but low dissociation pressure.	Shibuya et al., (2009)
$Ti_{1.1}CrMn$	1.8	296	110	High dissociation pressure.	Kojima et al., (2006)
$ZrFe_{1.8}Cr_{0.2}$	1.79	298	55	ΔH = 22.3 kJ/mol H_2 Too high for hybrid applications.	Mitrokhin et al., (2013)
$Ti_{1.1}CrMn$	1.5	323	100	Good cold start up ability.	Visaria & Mudawar, (2012)

From Table 5.2 it can be seen that the $Ti_{1.1}CrMn$ alloy, investigated by Visaria & Mudawar, (2012), and Kojima et al., (2006) possesses the most appropriate characteristics for hybrid hydrogen storage material applications – notably high dissociation pressure and subsequent good cold start up ability for vehicles. These results indicate that alloys based on Ti-Cr-Mn are among the most suitable for hybrid hydrogen storage applications of 350 bar.

The $Ti_{0.5}V_{0.5}Mn$ alloy, investigated by Shibuya et al., (2009), showed a promising hydrogen storage capacity at low temperatures and a good enthalpy of hydrogenation but had a desorption plateau pressure in the range of 3 to 6 bar, which is considered too low for practical use. However, the authors suggested that it may be possible to improve the PCT properties, such as the absorption/desorption plateau pressure and subsequent dissociation pressure, of Ti-V-Mn alloy by substituting V for other transition metals.

In order to fully realise the potential of hybrid systems employing high pressure metal hydride storage materials it may be necessary to compensate for the additional mass in hydrogen storage material by the use of higher cost, light weight materials elsewhere in the vehicle (Jorgensen, 2011).

5.3. Metal Hydride Compression

With hydrogen fuel cell vehicles operating at 350 and 700 bar reaching commercial reality, such as the Honda FCX Clarity and BMW Hydrogen 7, there is increasing demand for safe efficient hydrogen compression.

A compressor is a device which is used to increase the pressure inside a given vessel by reducing its volume.

The following equation can be used to explain how gas compression works:

$$\int PdV$$

Where, P is pressure and dV is the change in volume taking place at the corresponding pressure.

The concept of a metal hydride compressor, which takes advantage of the thermodynamic properties of metal hydrides, has been suggested to overcome some of the issues experienced with conventional mechanical compressors. In this process hydrogen is absorbed into an alloy bed at ambient temperatures and is released at elevated pressures when the bed is heated. Compression energy can therefore be supplied by heat (for example hot water, oil or electrical resistance).

Some of the benefits of using metal hydride compressors, as opposed to conventional mechanical compressors, include:

- No moving parts so regular servicing will not be required.
- Silent operation.

- No harmful by-products.
- Results in an ultra-high purity of hydrogen (suitable for PEM fuel cells without the need for membrane separation).

5.3.1 Operating Principle

Figure 5.6 shows the operating principle behind a single stage metal hydride compressor, in relation to the pressure and temperature of the metal hydride.

Figure 5.6 Operating principle behind a single stage metal hydride compressor (Popeneciu et al., 2009).

In Figure 5.6, the left side shows a PCT plot of absorption and desorption and the right side of the figure shows the resulting van't Hoff relationship (as described in Chapter 3). The blue curve represents the lower operating temperature of the compressor and the red curve the upper operating temperature. The blue curve between point D and point A shows the initial

absorption of hydrogen. The temperature is then increased, as shown from point A to B, where the dehydriding of the metal occurs along the red curve at the higher temperature. Point C represents the dehydrided metal hydride which is then cooled back to point D for the process to be repeated.

Heat is the driving force behind metal hydride compression. One way to improve compressor efficiency is therefore to reduce the power consumption required to heat the stages by recovering heat from another process. This was demonstrated by Laurencelle et al., (2006) who developed a metal hydride compressor which linked to an electrolyser. This meant that as well as providing the hydrogen to be compressed in the first place, the compressor operated on waste heat from an electrolyser which it was linked to.

5.3.2 Development of Metal Hydride Compressors

According to Popeneciu et al., (2009), the most important properties of an alloy suitable for hydrogen compression are: good hydrogen absorption-desorption rate, small process enthalpy, fast reaction kinetics and good structural stability during the cycles. Ultimately, metal hydrides with large pressure to temperature gradients are desired.

The first reported use of a metal hydride compressor was in 1973 and involved the development of a prototype compressor based on $LaNi_5$ to compress hydrogen from 4 - 45 bar for a hydrogen refrigerator (Vanmal, 1973). The Joule-Thompson prototype system developed in the study involved the use of three vessels, each containing $LaNi_5$, which after initial pre-cooling to 78 K using liquid nitrogen to cool the hydrogen to below its inversion point, were heated and cooled between 410 K and 290 K in a cyclic operation. Results from the prototype allowed the authors to establish that it was indeed feasible to construct a

hydrogen powered refrigerator with capabilities of 1 W cold production at an operating temperature of 26 K using such a system.

Nomura & Ono (1978) later developed a model engine which used the thermal compression energy from $LaNi_5$ to move a piston, generating an average mechanical power output of 28 W in a cycle that lasted two minutes.

Since these early studies, several research groups have investigated the use of AB_5 type alloys for compressor applications but as well as experiencing difficulties with activation of the alloys, due to their low hydrogen equilibriums and low hydrogen capacities (~ 1.5 wt%) they are only suitable for low pressure applications (< 150 bar).

A study by Dehouche et al., (2005) focused on the use of AB_2 type alloys for hydrogen compression applications. Despite presenting hydrogen capacities and rates 20-50 % higher than those obtained from AB_5 type alloys, previous work found there are still problems associated with their use including thermodynamic instability and unstable reversible hydrogen capacity. During this study the effect of alloy composition in Ti-Zr-V-Mn alloys with different Mn, V and Zr contents, on the hydrogen sorption properties were investigated. It was found that a $Ti_{0.95}Zr_{0.05}V_{0.2}Mn_{1.3}$ alloy exhibited a hydrogen absorption capacity of 1.6 wt%, displayed a high stability during cycling and, most importantly, it possessed a plateau pressure region suitable to that for a thermal compressor.

Currently, vehicle manufacturers are working towards the development of hydrogen fuel cell vehicles which use high pressure storage tanks. From the discussed literature it can be denoted that the pressure capabilities from single stage compressors falls short of the high pressures which may be required in the coming years.

5.3.3 Multi-Stage Compression

The concept of using multiple metal hydride stages has been suggested to improve the range over which hydrogen can be compressed. Essentially, the driving force exerted by the variation in temperature coupled with the differences of enthalpy between the alloys results in the transfer of hydrogen while increasing the exit pressure from one stage to another.

This involves having two or more stages using different metal hydrides with successively higher operating pressures, with the idea being that after heating the first stage, the increase in pressure drives the hydrogen into the second stage, which when heated increases the pressure inside the stage even further. This therefore allows for greater compression energy capabilities in order to achieve a high outlet pressure.

Li et al., (2010) developed a two stage metal hydride compressor with pressure capabilities above 700 bar. The authors selected an AB_5 alloy for the low pressure stage, and an AB_2 alloy for the high pressure stage based on previous findings (Wang et al., 2006). The target hydrogen compression capacity was 2000 L/cycle so in order to improve the compression efficiency of the system, the hydrogen capacity of the first stage was designed to be twice that of the second stage. It was found that by using oil as a heat source to raise the temperature in the first stage to 423K, 745 bar H_2 could be produced with an inlet pressure of 50 bar. A schematic of the compressor developed for the study can be seen in Figure 5.7.

Figure 5.7 Schematic of the two-stage compressor (Li et al., 2010).

More recently, a Chinese group designed a compressor suitable for applications of up to 1000 bar with an input pressure of 40 bar (Guo et al., 2011). The two-stage compressor was designed using two Laves phase metal hydrides based on Ti-Zr-Mn-Cr-V-Fe for the low pressure stage and Ti-Cr-Mn-Fe for the high pressure stage. The alloys were selected based on their high hydrogen capacity and, more importantly, high dehydriding entropy change. The authors found that a $TiCr_{1.55}Mn_{0.2}Fe_{0.2}$ alloy could produce a hydrogen pressure of 1000 bar at 430 K for the high pressure stage but it would require an initial pressure of 100 bar in order to do so. This was achieved through using a $Ti_{0.9}Zr_{0.1}Mn_{1.4}Cr_{0.35}V_{0.2}Fe_{0.05}$ alloy for the low pressure stage; with an input pressure of 40 bar, it had the capability to compress hydrogen to 200 bar.

Currently, there are only a small number of commercially available metal hydride compressors on the market. Ergenics are one of the main manufacturers and distributors of metal hydride compressors and have been supplying them for various applications for over

twenty years. A summary of some of the commercially available metal hydride compressors can be seen in Table 5.3.

Table 5.3 Commercially available metal hydride compressors.

Company	Product/ Project Name	Date	Summary	Reference/ Website
HYSTORSYS	HYMEC-10 (Industry/ Commercial Project)	Current (2013)	Two-stages, output pressure of 160-170 bar with input pressure of 10 bar. Currently being demonstrated in refuelling station in Norway.	(Eriksen, 2013) www.hystorysis.no
Ergenics	Advanced Thermal Hydrogen Compression	2004 (commercially available)	Five stages, output pressure of 200 bar from initial atmospheric pressure.	(Da Costa, 2000) www.ergenics.com
Ergenics	Micro-compressor	2004 (commercially available)	150 bar output pressure from 6.8 bar input. Powered by electrical resistance heating.	www.ergenics.com

From Table 5.3 it can be seen that the compressor developed from Ergenics as part of the Advanced Thermal Hydrogen Compression project has the highest pressure capability. Da Costa (2000) also demonstrated that the compressor had a tolerance for > 1000 ppm of CO in the H_2 inlet for at least 19 cycles without any capacity loss.

Despite the advantages of using metal hydride compression in place of conventional mechanical compressors, to date researchers have not yet been able to optimise the overall energy efficiency of compression systems operating using metal hydrides. In addition, in comparison to diaphragm compressors the capital cost is still too high to be considered commercially viable - largely due to the high cost of hydrogen storage materials. Appropriate metal hydride selection is therefore essential in order to fully realise the potential for metal hydride compressors. Further prototype development and demonstration of hydride compression is important for showing if this technology will be successful in the commercial market.

5.4 Summary

This chapter should have provided an overview of the different applications which will be discussed in the current work. In order for hybrid hydrogen storage and hydrogen compression technologies to reach their full commercial potential, developments in metal hydride research needs to occur. The identification of metal hydrides in which it is possible to tailor the PCT properties - in particular the plateau pressure for absorption and desorption - and which work at ambient temperatures are key for both technologies. As discussed in Chapter 4, Ti-V-Mn based BCC-Laves phase alloys have promising potential in this area so the current work is centered on these types of metal hydrides.

5.5 Research Aims and Objectives

The overall aim of this work is to investigate novel Ti-V-Mn based metal hydrides for hydrogen storage and compression applications. This will involve a range of characterisation techniques, including scanning electron microscopy with energy dispersive spectroscopy, x-ray diffraction as well as pressure composition isothermal measurements to determine the hydrogen sorption properties of the synthesised alloys.

The major objectives of this work are to:

(1) Investigate the ternary Ti-V-Mn system and, specifically, the structural and morphological differences observed due to small deviations in desired stoichiometry and the subsequent influence on the hydrogen storage properties.

(2) Explore the potential for novel Ti-V-TM-Mn metal hydrides, where TM is a Group V or VI transition metal selected based on their thermodynamic properties, as hydrogen storage materials.

(3) Design and develop a metal hydride compressor which is capable of safely and effectively compressing hydrogen from a low inlet pressure (< 10 bar) to one suitable for high pressure applications (> 350 bar).

Chapter 6

PROJECT EXPERIMENTAL

6.1 Introduction

This chapter will detail the experimental procedure used in the project. It can be broadly divided into the following areas: (1) Alloy Synthesis; arc-melting and heat treatment (2) Alloy Characterisation; scanning electron microscopy/energy dispersive x-ray spectroscopy (SEM/EDS) and x-ray diffraction (XRD) and (3) Hydrogen Sorption Measurements; sieverts-type pressure composition isotherms (PCT).

Alloys were stored under argon and handled using latex gloves within designated glove boxes to minimise contamination. The flow chart in Figure 6.1 illustrates the main experimental areas and the characterisation techniques employed in each area.

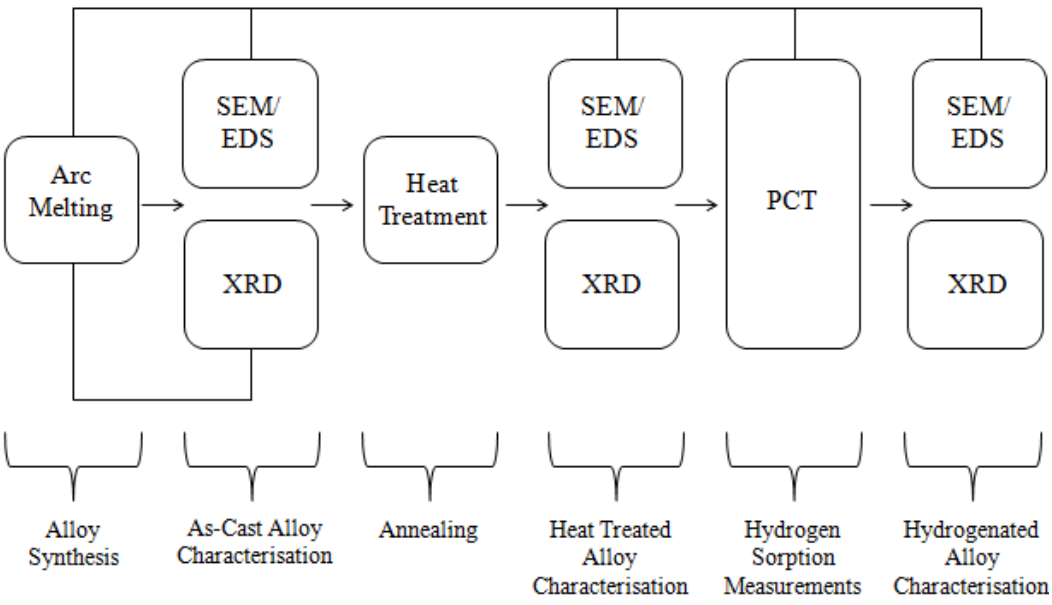

Figure 6.1 Flow chart of experimental procedures and techniques employed.

6.2 Starting Materials

All the elements used in the current work were purchased from Sigma Aldrich, UK. Table 6.1 shows a breakdown of the elemental information for the starting material.

Table 6.1 Elemental information for the starting material.

Element	Form	Purity % (trace metals basis)	Cost (£ per 100g)
Ti	Rods (6.35 mm diameter)	99.7	156.40
V	Turnings (different sizes)	99.7	526
Mn	Chips (< 1.5 mm thickness)	99	7.20
Nb	Wire (1 mm diameter)	99.8	325
Cr	Chips (2 mm thickness)	99.995	128.40
Mo	Foil (0.1 mm thickness)	> 99.99	424.51
Ta	Wire (1 mm diameter)	> 99.99	573.85

6.3 Alloy Synthesis

The experimental procedure for synthesising the alloys was based on an optimised approach used by Shibuya et al., (2008) and Shibuya et al., (2009) during their investigations on Ti-V-Mn alloys.

6.3.1 Arc-Melting

Arc melting was performed to produce the as-cast metal slugs of the required molar ratios. The elements (Sigma Aldrich; ≥ 99.7 % purity) were weighed in the correct molar ratio to produce a 10 g charge. An extra one percent of Mn was added to compensate for potential sublimination losses during arc-melting. The charge was then loaded onto a water-cooled copper hearth within the vacuum arc furnace (< 10^{-6} mbar) (Figure 6.2). In order to remove the air, the system was pumped down via a rotary pump and flushed with argon three times before being filled with 0.8 bar of argon. Before each arc melt, the residual oxygen concentration within the system was reduced by melting a sacrificial titanium oxygen getter, at an arc current of 90 A, for at least 5 minutes. Each sample was then melted and re-melted 3 times, with the sample being turned over in-between each melt, to promote a homogeneous microstructure. Figure 6.2 shows the set-up of the Arc Melter.

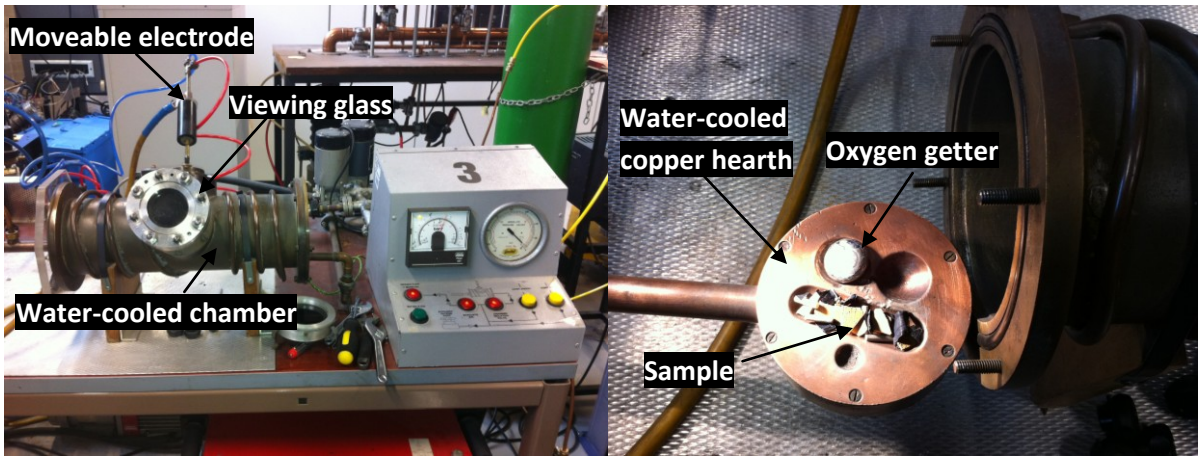

Figure 6.2 View of arc melter along with water cooled copper hearth.

6.3.2 Heat Treatment

Heat treatment was carried out on the as-cast metal slugs to fully homogenise the alloys. This was performed using a vacuum furnace (Edwards), shown in Figure 6.3. Once loaded into the furnace tube, the system was evacuated to an ultra high vacuum (< 10^{-6} mbar) and flushed with argon three times to remove any air from inside the tube. The furnace tube was then heated to 1233 K, using a heating rate of 2 K/min, and held for 6 hours. The temperature control unit on the furnace was then turned off and the furnace tube was left for 3 hours to cool down to room temperature before the alloys were removed.

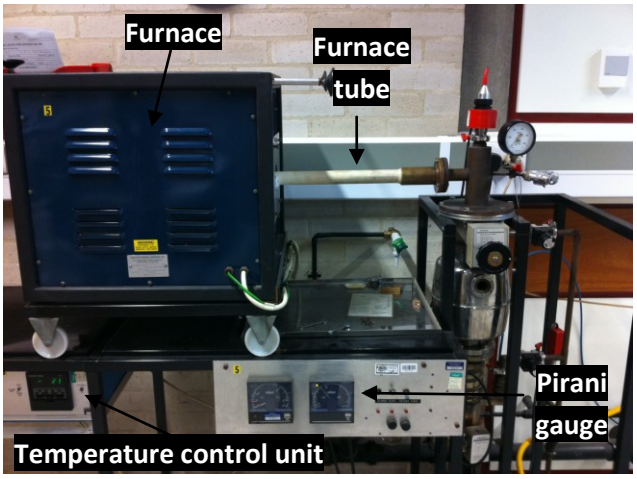

Figure 6.3 Edwards Vacuum Furnace.

6.4 Alloy Characterisation

6.4.1 SEM/EDS

SEM and EDS was undertaken to determine the topography, morphology and composition of the as-cast, heat-treated and hydrogenated material.

During SEM an electron beam is emitted from an electron gun at the top of the microscope and focussed on the sample by a series of magnet lenses (see Figure 6.4). Before reaching the

sample surface, the electron beam passes through scanning coils which deflect the beam across the x and y axes so it scans over a rectangular area of the sample surface.

When the electron beam strikes the surface of a sample either secondary electrons or the backscattered incident electrons are emitted (see Figure 6.4). Secondary electrons (SEI) are produced when an incident electron excites an electron from the sample, and in doing so emits a new electron with a different wavelength. Backscattered electrons (BEI) are produced from primary electrons which are elastically scattered by atoms in the sample (with no loss of energy) when the electron beam strikes the sample.

Energy dispersive x-ray spectroscopy (EDS) is a technique which is commonly used alongside SEM to characterise the composition of a sample. EDS uses x-rays emitted from the sample when the SEM electron beam strikes the surface. These x-rays are produced when electrons are ejected from atoms which make up the sample surface. The resulting electron vacancy is filled by an electron from a higher shell and a photon is emitted as the electron drops to a lower energy state. This photon has a wavelength which is characteristic of the quantified energy gap present in the atom in the x-ray part of the electromagnetic spectrum. The produced spectrum includes peaks corresponding to the energy of the x-rays emitted and it is these peaks that are used to identify the elements which are present. Peak intensity also provides information of the quantity of the detected elements.

For all SEM work a JEOL 6060LV, equipped with an Oxford Instruments detector and INCA EDS software, was used to obtain images in both SEI and BEI mode. To determine elemental composition, spot and area analysis were performed on at least three different areas of the sample. Images were obtained with the microscope operating at 20 kV, a spot size of 60 nm and working distance of 10 mm for EDS analysis. It should be noted that there may be

inconsistencies in atomic concentrations measured by EDS due to the interaction of the electrons with different phases below the surface.

To prepare the alloys for SEM//EDS analysis, cross-sections of the alloys were cut using a diamond cutting wheel before being mounted in conductive Bakelite. The samples were then ground using a series of SiC papers and then polished down to ¼ micron using conventional metallographic techniques.

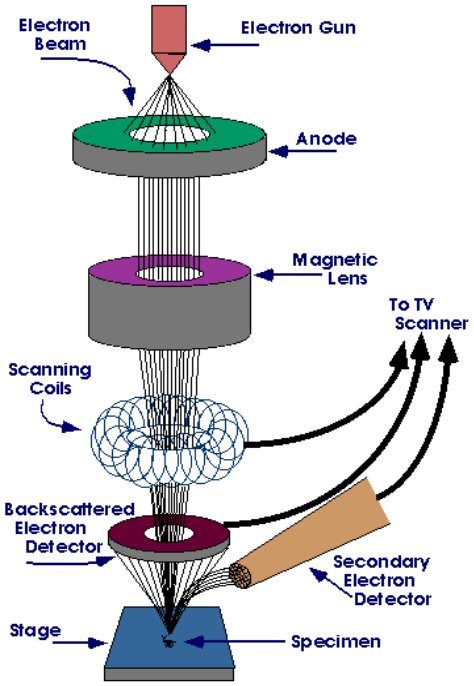

Figure 6.4 Illustration of scanning electron microscopy

6.4.2 XRD

Powder XRD was carried out on the crushed material to determine the composition and crystallography of the alloys.

XRD occurs when parallel monochromatic x-ray beams interact with the surface of an ordered solid material. The x-rays are produced by a beam of electrons, produced by heating a tungsten filament, which strike a Cu target. The beam of electrons cause ionisation and

produce CuK α and β radiation. Removal of unwanted background radiation and CuK_β radiation is achieved by using a Ni filter. X-rays can then be filtered further by use of a crystal monochromator to produce monochromatic $CuK_{\alpha 1}$ x-rays.

The x-rays are focused on the sample at a controlled incident angle (θ). Diffraction originates from the crystallographic planes within the sample. A detector (shown in Figure 6.5) records the diffracted x-rays, at specific angles. The resulting diffraction pattern can then be interpreted to provide structural information about the sample according to Bragg's law, which states:

$$n\lambda = 2d\,sin\theta$$

Where,

n is an integer number (order of reflection)

λ is the x-ray wavelength,

d relates to the plane, and,

θ is the angle between the incident ray and scattering planes at which a diffraction peak is observed (the Bragg angle).

All samples were in powder form so it is assumed that diffraction occurs across all of the available crystallographic planes within the material. Throughout the project a Bruker D8 Advance diffractometer, fitted with a Göbel Mirror and using CuK α radiation (λ = 1.5406 Å), was used. This arrangement is shown in Figure 6.5.

Room temperature x-ray diffraction measurements were performed between 20 - 100° 2θ at a scanning rate of 2°/min using a 7 position multi-changer (also shown in Figure 6.5). A portion was cut from the as-cast and heat treated metal slug and crushed using a pestle and mortar within an argon filled glove box to prevent oxidation from occurring. The powdered

samples were then inertly loaded into an airtight Perspex dome-shaped sample holder for measurements.

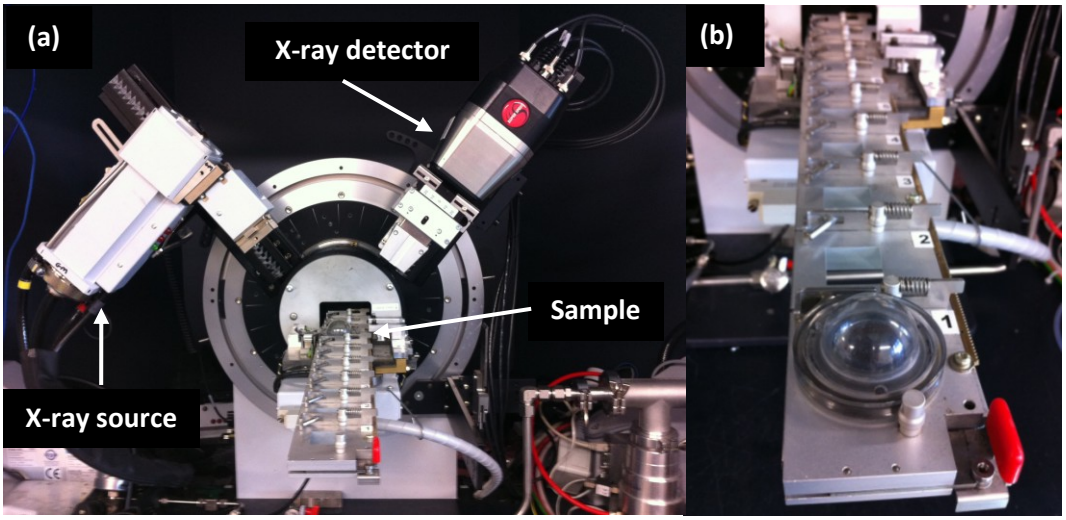

Figure 6.5 Bruker D8 Diffractometer a) Bruker D8 Diffractometer with 7 position multi-changer and b) the airtight Perspex domed-shape sampler holder.

Before each XRD measurement was performed, the detector alignment was calibrated using an Al_2O_3 standard across the whole 2θ range (5 - 140°). Figure 6.6 shows an example of an XRD pattern for Al_2O_3.

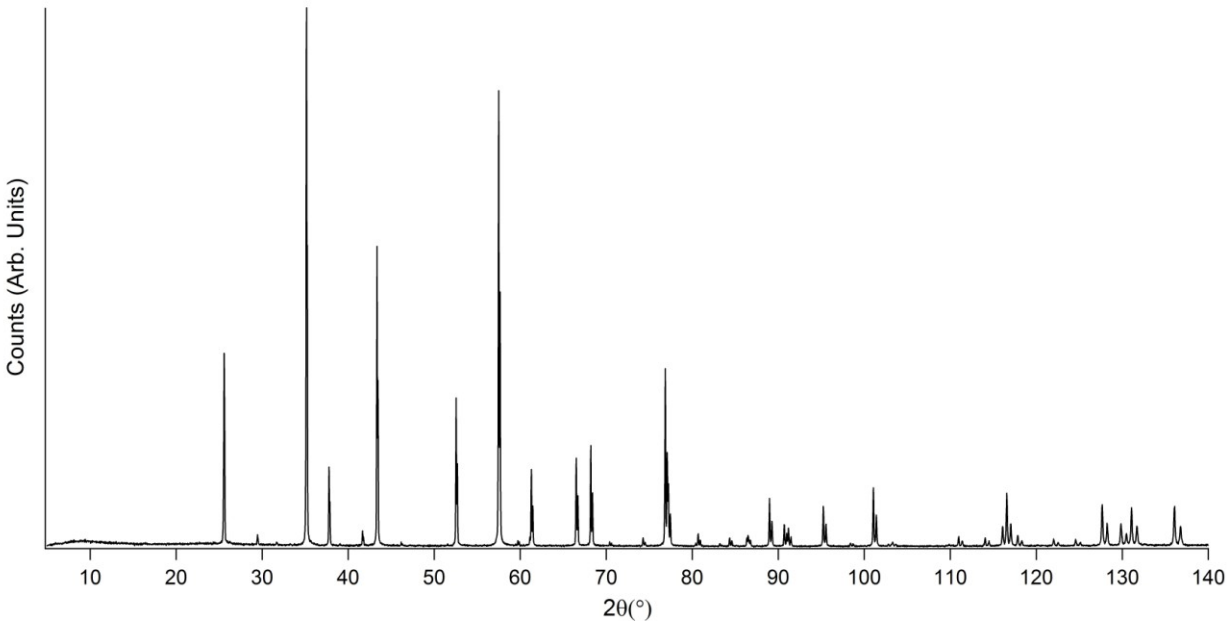

Figure 6.6 XRD pattern of Al_2O_3 standard.

In addition, looking at the intrinsic broadening or sharpening of the XRD peaks allows for comparisons to be made between the as-cast, heat treated and hydrogen cycled alloys.

XRD data was refined via a pseudo-Rietveld method using Topas Academic software (Coelho, 2007) with published crystallographic information files (.cif) obtained from the Inorganic Crystal Systems Database (ICSD) (Fletcher et al., 1996), where only the unit cell parameters, scale factors and peak shape (pseudo-Voigt) were refined. Additional synchrotron x-ray & neutron measurements would be required to fully refine the structure and atomic composition of XRD phases (see Future Work section, Chapter 12).

6.5 Hydrogen Sorption Measurements

Hydrogen sorption measurements were performed to investigate the PCT properties of the metal hydrides. For this the Sieverts method (described in Chapter 3) was employed using a commercially available PCT system. The Sieverts method is a volumetric technique used to determine the amount of hydrogen absorbed or desorbed by a sample by calculating the change in pressure of a fixed volume (Checchetto et al., 2004).

6.5.1 Commercial PCT System (Hiden HTP)

A Hiden Isochema HTPS-2 (shown in Figure 6.7) was used throughout the project to measure the PCT properties of the synthesised metal hydrides. This system measures the pressure change within a sealed volume using a pressure transducer.

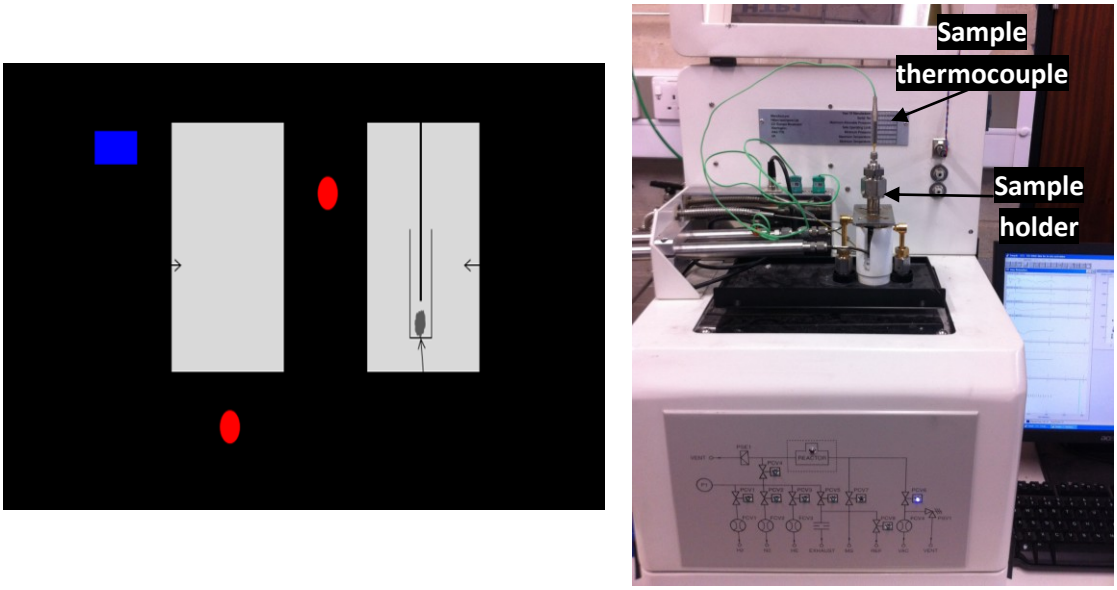

Figure 6.7 Schematic diagram and image of Hiden HTP system.

Before a measurement can be taken the sample volume is determined though helium pycnometry. During this procedure the system is first evacuated to 10^{-6} mbar after which 5 bar of helium is introduced into the dosing chamber and the pressure is measured. Gas is then allowed to flow into the sample chamber and the pressure is left to equilibrate for 2 minutes before another pressure measurement is taken to calculate the pressure drop in the dosing volume. The process is repeated a further four more times and the average drop in pressure is selected to allow for the sample volume to be calculated based on the volume of the empty reactor.

An activation sequence was performed before all hydrogen sorption measurements to ensure that the alloys were readily absorbing hydrogen and that only the reversible hydrogen content was investigated during isothermal measurements. The sequence was performed in situ at 473 K for 6 hours under vacuum and was followed by an absorption isotherm at room temperature between 1 - 120 bar, in 5 bar increments, with a hold time of 1 hour at each

pressure step. Subsequently, all PCT measurements were performed after cycling the alloys once during the activation sequence.

PCT Measurements were performed between 0.5 and 120 bar H_2 in 5 bar increments between 303 and 333 K. Smaller increments (2 bar) were used along the plateau region during absorption and desorption to maximise the reversible capacity. An example of an individual kinetic point during a PCT measurement is shown in Figure 6.8 and the resulting isothermal data point can be seen in Figure 6.9.

In each pressure step the dosing volume is filled to the required pressure (1). The valve between the dosing volume and sample holder is then opened which results in a drop in the pressure (2). The pressure will continue to fall until equilibrium is reached (3), at which point the pressure is measured and any change is monitored (4) and converted into an uptake value (5). This process is repeated and the next pressure step is measured.

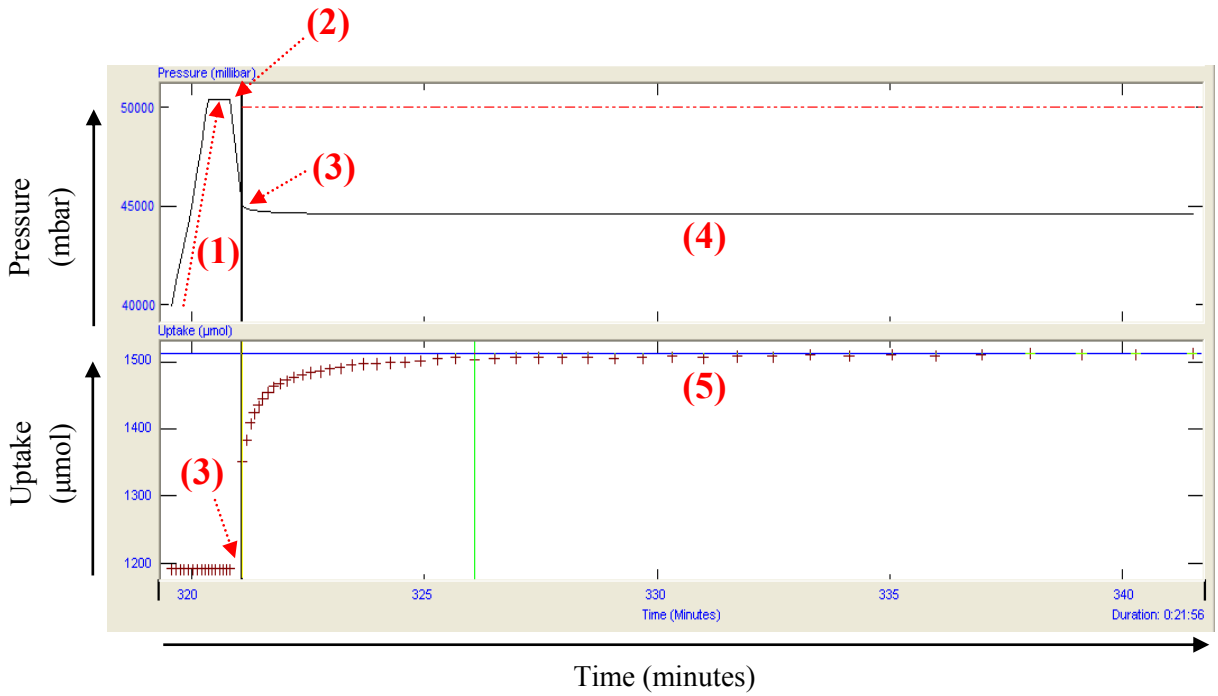

Figure 6.8 Individual kinetic data point for Ti-V-Mn at 303 K during absorption PCT measurement (highlighted in red on isotherm shown in Figure 6.9) showing the pressure and uptake from Hiden Isochema HTP.

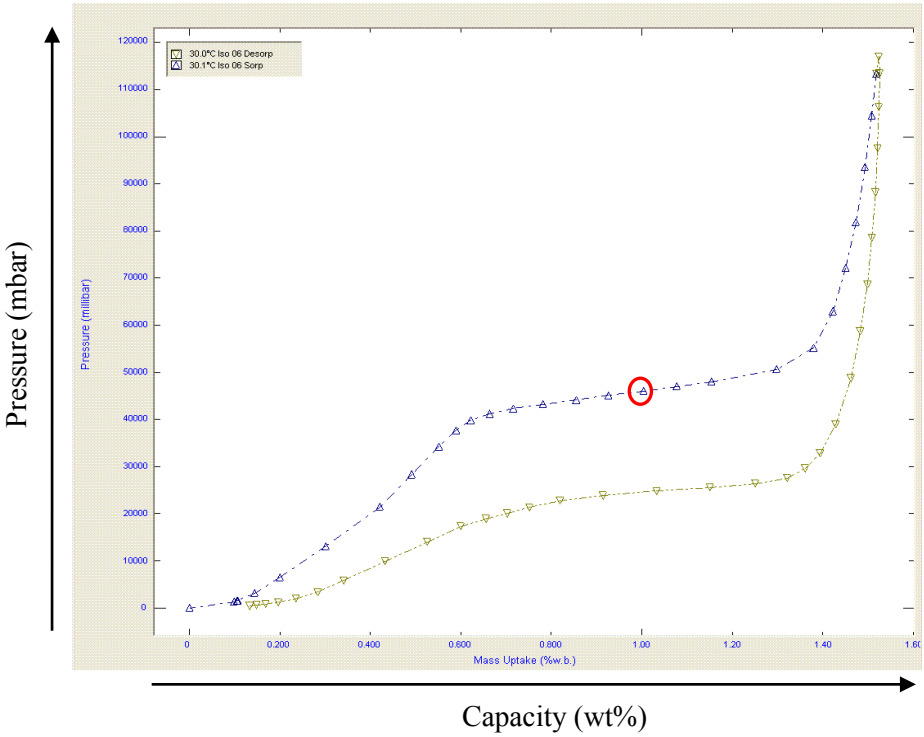

Figure 6.9 PCT measurement for Ti-V-Mn alloy at 303 K 1 - 120 bar H_2 showing uptake from individual kinetic point (shown in Figure 6.8).

The HTP system continuously calculates an asymptote for uptake based on the sorption curve, with minimum and maximum equilibrium times for all measurements. When the sorption curve is plotted within a set tolerance of the calculated asymptote, the system moves on to the next pressure step unless the maximum equilibrium time is reached first. For all PCT measurements the minimum and maximum equilibrium hold times were between 15 and 120 minutes and the tolerance of the fit to the asymptote was set to 99.5 %.

For all the alloys, the mid-point of the plateau during absorption/desorption isotherms were determined by calculating the equilibrium pressure using linear interpolation between the two nearest data points at approximately the plateau mid-point. Standard errors for the mid-point plateau pressure value may be introduced due to this approximation, however, it is assumed that these were negated for by using the same method for determining the plateau mid-point for all the isotherms.

6.5.2 Accuracy in Gas Sorption Measurements

It is important to ensure accuracy in gas sorption measurement techniques and to have a thorough understanding of the potential sources of error that may occur during these measurements to achieve reproducibility. This comes largely in response to controversial results reported for carbon nanostructures in the 1990's when their hydrogen capacity was hugely over estimated (Dillon et al., 1997).

For volumetric measurements, a general rule is that the error in the accuracy of the pressure measuring device should be small enough to make it negligible in comparison to the expected drop in pressure as a result of hydrogen absorption, or increase in pressure for hydrogen desorption.

In order to ensure accurate results during hydrogen sorption measurements, there are several important considerations (Broom, 2007):

1. Instrument and equipment calibration: This must be performed before each measurement.

2. Ability to accurately monitor and control temperature: In general, this is more difficult as temperatures are further away from ambient due to thermal gradients throughout the apparatus. One advantage of the sieverts technique is that there is a sensor in contact with the sample within the sample holder which allows for accurate monitoring of temperature during a measurement.

3. Sample size and sensitivity issues: Appropriate sample size is dependent upon the sensitivity of the equipment being used. In addition, care must be taken to ensure the

storage of the samples is the same to prevent any potential sources of contamination/oxidation which may affect uptake.

4. Accumulative errors during volumetric uptake: These are errors that may be introduced from the determination of the quantity of gas from a number of sources (e.g. points 1, 2, 3 and 5 in this discussion).

5. Gas leaks: This is important to prevent because small gas leaks could be mistaken as sorption by the material. These should be apparent from initial leak tests or the shape of the resultant isotherm.

6. Hydrogen compressibility: This becomes more significant as the pressure during a measurement increases. The compressibility factor must be accurately described when calculating the uptake of hydrogen using the appropriate equation of state (as described in Chapter 3) to prevent accumulative errors from occurring.

During uptake measurements these factors were considered by following strict operating procedures. In addition, prior to testing the alloys synthesised for this work, measurements were performed using metal hydride standards (in this case Pd). This was performed to check the equipment calibration and ensure results were repeatable (see Appendix A).

Chapter 7

THE Ti-V-Mn SYSTEM

7.1 Introduction

Ti-V-Mn BCC-Laves phase alloys have been shown to possess a good volumetric hydrogen storage capacity with fast absorption/desorption kinetics at ambient temperatures. In particular, a $Ti_{0.5}V_{0.5}Mn$ alloy has shown promising hydrogen storage properties with a reversible capacity of 1.9 wt% under H_2 pressure up to 350 bar at 260 K (Shibuya et al., 2009). Such properties make these alloys suitable for a range of applications; from hybrid hydrogen storage materials to metal hydride compressors.

Despite the promising storage properties these alloys possess, a wide range of inhomogeneity exists within Laves phase alloys, resulting in deviations from desired stoichiometry. This phenomena has been explored in several Laves phase compounds, including $TiV_{0.75}Mn_{1.12}$ (Mayer et al., 1982), $Ti_{1.2}Mn_{1.8}$ (Fruchart et al., 1984), and more recently on the Ti(Zr)-Mn-V system (Mitrokhin, 2005). However, the effect of deviations from stoichiometry on this particular $Ti_{0.5}V_{0.5}Mn$ system has not been fully investigated.

This chapter presents and discusses the structural and morphological difference observed due to small deviations in desired stoichiometry in $Ti_{0.5}V_{0.5}Mn$ alloys and the subsequent influence on their hydrogen storage properties.

Elemental Ti, V and Mn (Sigma Aldrich: ≥ 99.7% purity, see Chapter 6) was weighed out into three batches of mole ratio $Ti_{0.5}V_{0.5}Mn$. The following table represents the calculations involved in producing the 10g alloys. An extra one percent of Mn was added to compensate for Mn losses during arc-melting.

Table 7.1 Calculations used to make up a 10g $Ti_{0.5}V_{0.5}Mn$ samples from elemental Ti, V and Mn.

at%			Molecular Weight	wt%			Weight (g)		
Ti	V	Mn		Ti	V	Mn	Ti	V	Mn
0.25	0.25	0.5	52.171	22.94	24.41	52.65	2.29	2.44	5.32

Note, Table 7.1 shows the target composition for the $Ti_{0.5}V_{0.5}Mn$ alloys but the three alloys synthesised vary in composition (as shown by the EDS Results).

7.2 Characterisation of As-Cast Alloys

Characterisation of the three as-cast alloys was carried out using a combination of SEM/EDS and XRD to investigate microstructure and composition after arc-melting. The arc melting process itself has several limitations associated with it, including the introduction of defects (shrinkage/porosity/segregation) due to uncontrolled solidification, so characterising the as-cast material was important to determine initial composition.

7.2.1 SEM/EDS on As-Cast Alloys

Figures 7.1 - 7.6 show BEI images of cross-sections of as-cast alloys 1, 2 and 3 at low (x 500) and high (x 1000) magnification. The high magnification images also contain annotations which show the key features of the micrographs.

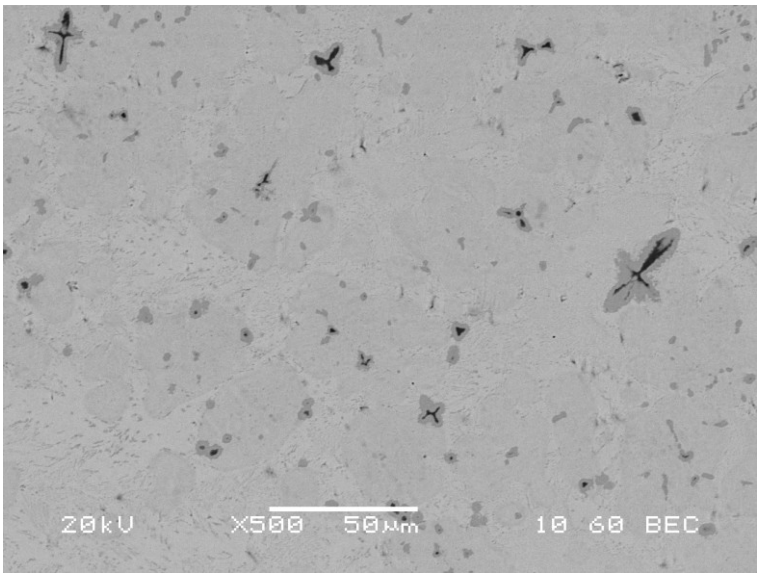

Figure 7.1 SEM BEI image of as-cast 1 (x 500)

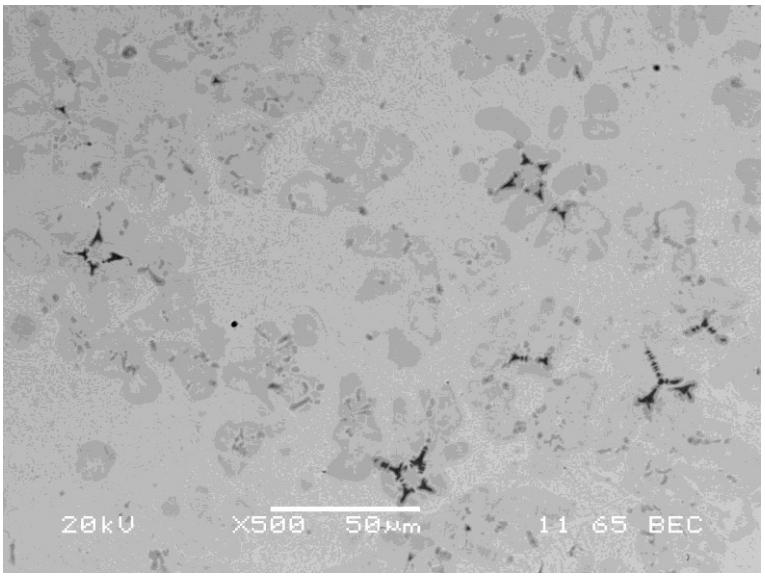

Figure 7.2 SEM BEI image of as-cast 2 (x 500)

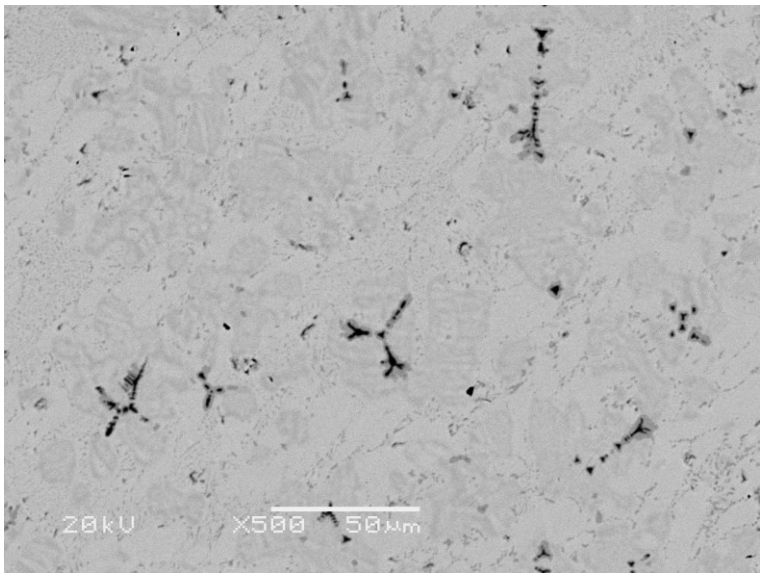

Figure 7.3 SEM BEI image of as-cast 3 (x 500)

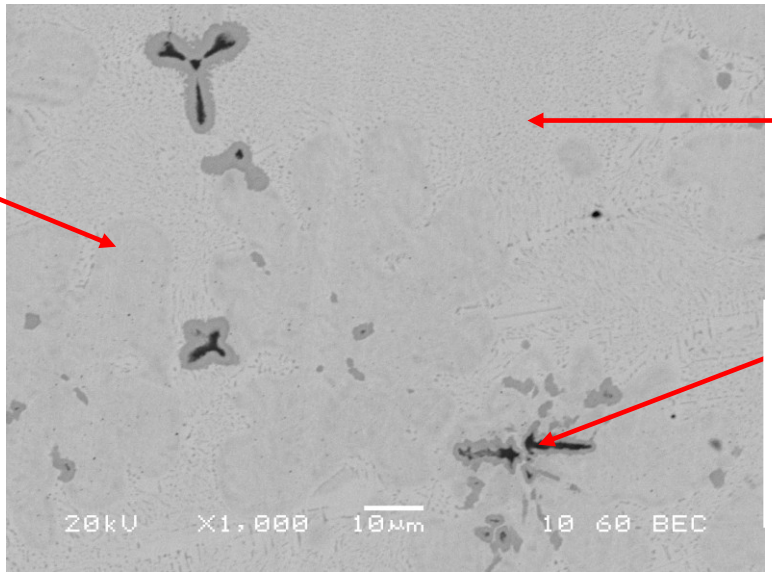

Figure 7.4 SEM BEI image of As-cast 1 (x 1000)

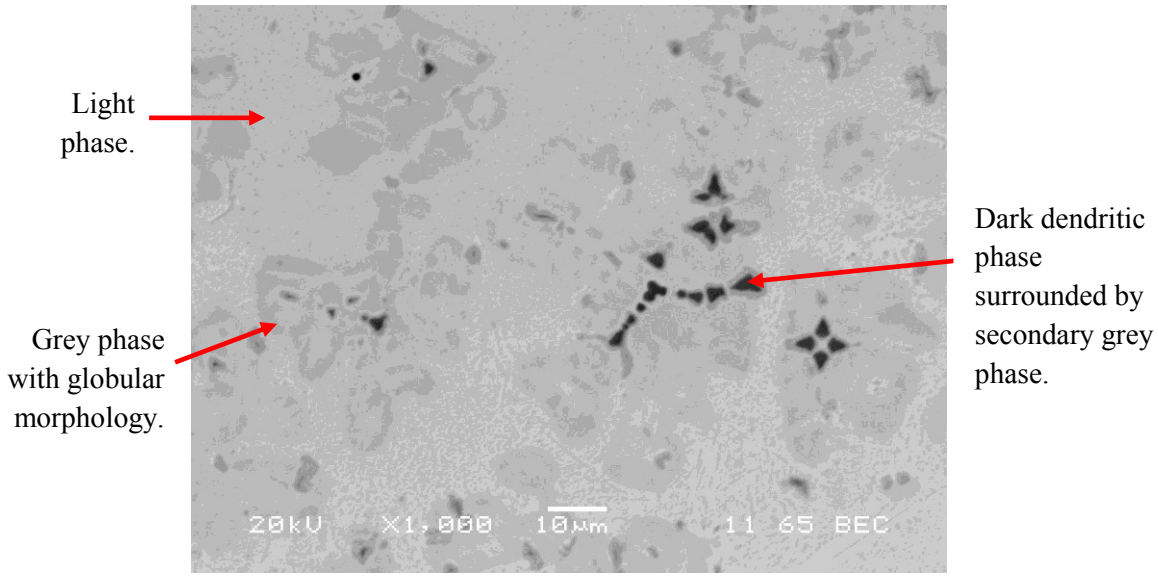

Figure 7.5 SEM BEI image of As-cast 2 (x 1000)

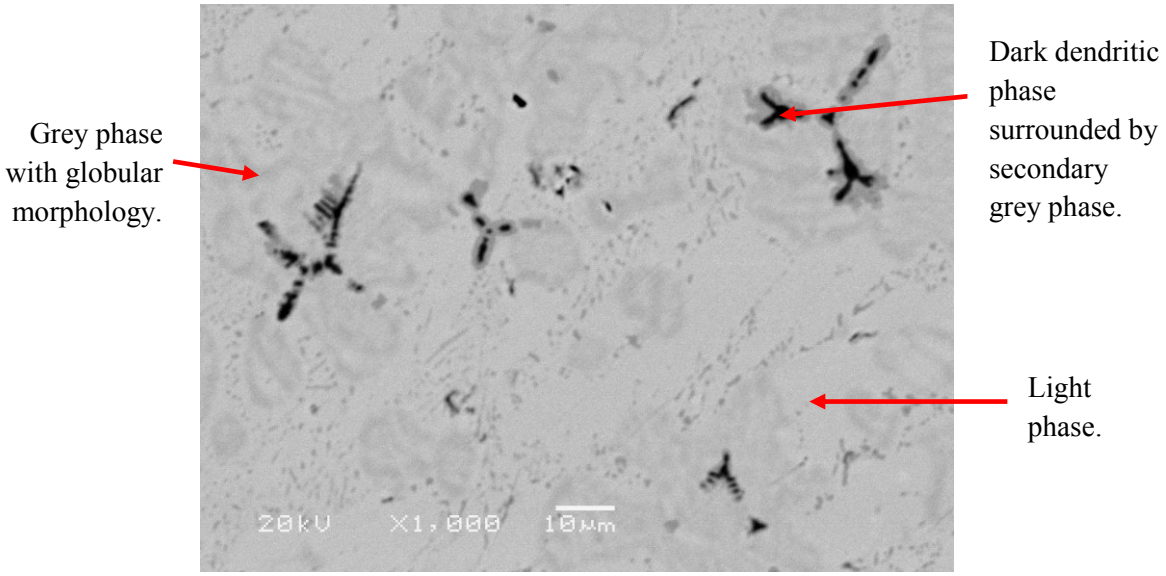

Figure 7.6 SEM BEI image of as-cast 3 (x 1000)

From the micrographs of the as-cast alloys, three different phases can be identified: a light phase, grey phase with globular morphology and dark dendritic phase surrounded by a secondary grey phase. At high magnification coring is observed in all three alloys, as shown by differences in contrast in the phases. This indicates that solidification may have occurred at different rates within the alloys and results in compositional variation.

EDS analysis was performed on the as-cast alloys to identify the composition of these phases, with the results shown in Table 7.2. Analysis was carried out by taking an average of three different areas/points within BEI images of as-cast alloy 1, 2 and 3. It should be noted that all the results shown are in atomic percent (at %).

Table 7.2 Average EDS analysis (at%) on as-cast alloy 1, 2 and 3 with standard deviation associated with mean values. Note analysis was carried out by taking an average of three different areas/points within BEI images of the alloys.

Alloy	Phase Location	Ti	σ	V	σ	Mn	σ	Average Composition Ratio (Ti/V/Mn)
As-cast alloy 1	Area	24.24	7.6	25.01	6.2	50.74	8.7	0.48/0.49/1
	Light	27.71	6.5	21.57	6.9	50.76	7.5	0.55/0.42/1
	Grey	18.24	7.4	33.46	8.3	45.53	9.2	0.40/0.73/1
	Dark	81.45	6.9	5.62	7.2	12.93	8.1	6.29/0.43/1
As-cast alloy 2	Area	24.03	6.8	24.25	8.6	51.72	9.4	0.47/0.47/1
	Light	27.19	7.3	18.21	7.9	54.6	8.3	0.50/0.33/1
	Grey	17.56	8.1	33.32	6.5	49.12	7.9	0.36/0.68/1
	Dark	90.38	6.3	4.07	6.8	5.55	7.1	16.28/0.73/1
As-cast alloy 3	Area	24.41	8.6	24.49	9.1	51.1	9.6	0.48/0.48/1
	Light	28.47	6.7	15.54	8.6	56	7.5	0.51/0.28/1
	Grey	17.52	7.9	34.99	8.3	47.49	9.1	0.37/0.74/1
	Dark	42.07	6.4	12.47	7.6	45.47	8.3	0.93/0.27/1

The area analysis shows that the average composition for as-cast 1 is $Ti_{0.48}V_{0.49}Mn_1$, 2 is $Ti_{0.47}V_{0.47}Mn_1$ and 3 is $Ti_{0.48}V_{0.48}Mn_1$.

The difference in atomic mass of the elements results in different interactions with electrons when using SEM: heavier elements produce more backscattered electrons so therefore appear brighter. The brightness/contrast of the different phases can therefore be attributed to the differences in atomic mass of the elements: Ti is 47.87, V is 50.94 and Mn is 54.94 amu.

In as-cast alloy 1, in comparison to the average area composition the light phase appears to be slightly richer in Ti (24.24 vs. 27.71 at%), grey phase is richer in V (25.01 vs. 33.46 at%) and the dark phase is also richer in Ti (24.24 vs. 81.45 at%).

In as-cast alloy 2, the light phase appears to be slightly richer in Ti (24.03 vs. 27.19 at%) and Mn (51.72 vs. 54.6 at%), grey phase is richer in V (24.25 vs. 33.32 at%) and dark phase is richer in Ti (24.03 vs. 90.38 at%).

In as-cast alloy 3, the light phase is slightly richer in Ti (24.41 vs. 28.47 at%) and Mn (51.1 vs. 56 at%), grey phase is richer in V (24.49 vs. 34.99 at%) and dark phase is richer in Ti (24.41 vs. 42.07 at%).

7.2.2 XRD on As-Cast Alloys

Figure 7.7 shows XRD patterns of as-cast alloy 1 (top, black), 2 (middle, red) and 3 (blue, bottom) with the peaks indexed. Appendix B shows individual XRD patterns of the as-cast alloys showing the observed pattern and calculated fit after pseudo-Rietveld refinement.

From XRD analysis, three phases were identified in the as-cast alloys:

- C14 Laves phase (hexagonal MgZn2 structure with space group *P63/mmc*).
- BCC phase (space group *Im-3m).*
- FCC (A_3B_3O) oxide phase (space group *Fd-3m).*

Refinement of the structures are based on those proposed for the C14 Laves phase by Mitrokhin et al., (2003) and the BCC and FCC oxide by Hout et al., (1995). Table 7.3 shows crystal structure refinement results for as-cast 1, 2 and 3.

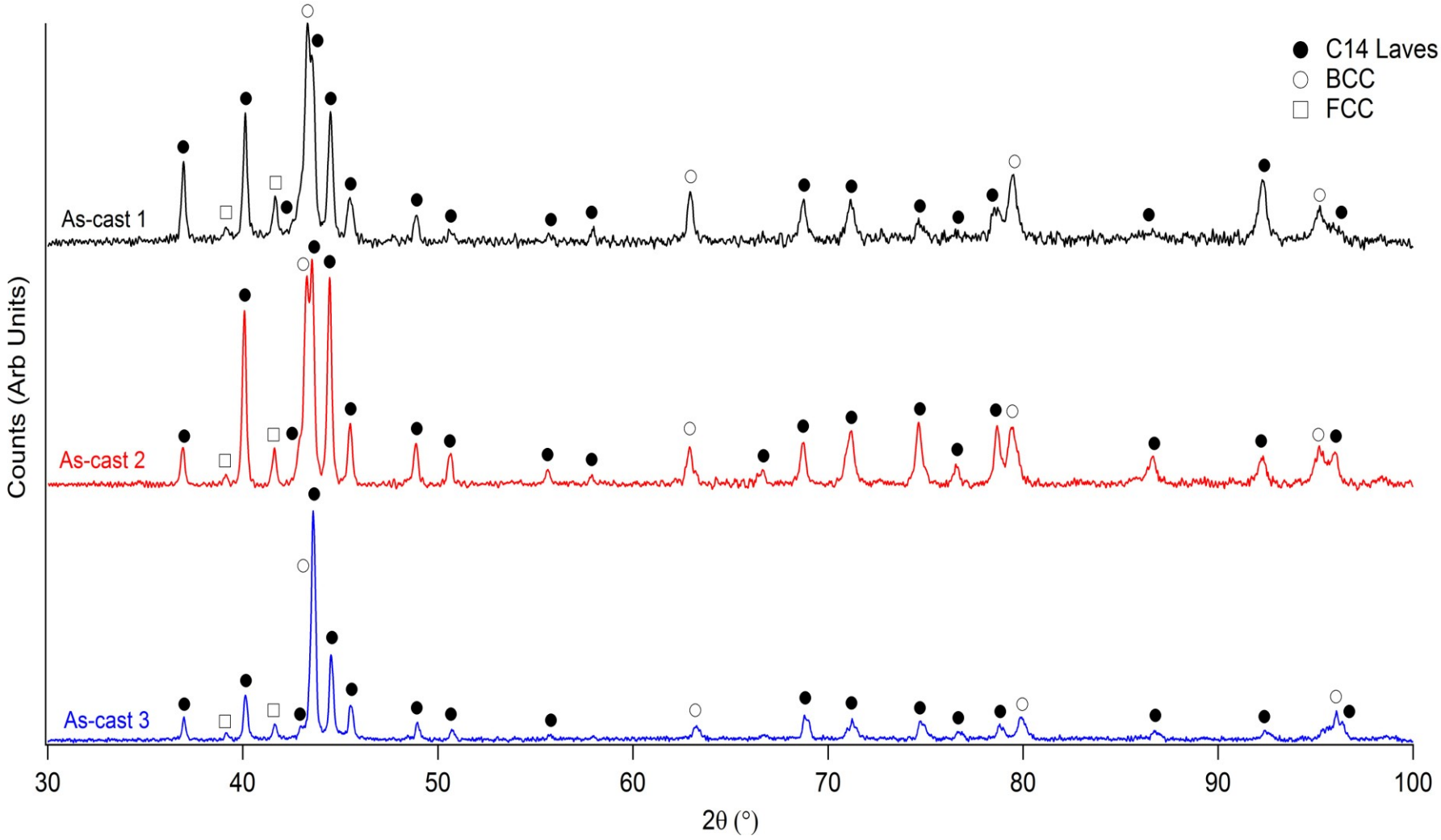

Figure 7.7 XRD patterns of as-cast 1 (top, black), 2 (middle, red) and 3 (bottom, blue) with peaks indexed.

Table 7.3 Crystal structure refinement results for as-cast alloys showing lattice parameters and phase abundance. Note the values in parentheses are three standard deviations and refer to the last digit.

Alloy	As-Cast			
	Phase	Lattice Parameters		Abundance (wt%)
1	C14	*a*	4.857(9)	53(6)
		c	7.963(16)	
	BCC	*a* + *c*	2.951(5)	38(2)
	FCC	*a* + *c*	11.271(12)	8(3)
2	C14	*a*	4.859(3)	63(5)
		c	7.970(5)	
	BCC	*a* + *c*	2.952(1)	27(4)
	FCC	*a* + *c*	11.252(7)	9(4)
3	C14	*a*	4.856(2)	58(5)
		c	7.961(3)	
	BCC	*a* + *c*	2.935(1)	32(5)
	FCC	*a* + *c*	11.260(5)	9(2)

The C14 Laves phase appears to be the dominant phase in all three alloys occupying; 53 wt% in as-cast 1, 63 wt% in as-cast 2 and 58 wt% in as-cast 3.

The FCC phase corresponds to an oxide and has presented itself in a number of studies looking at the Ti-V-Mn system, including Shibuya et al., (2008) and Shibuya et al., (2009).

The C14 Laves unit cell volumes for the as-cast alloys are 162.72(7) $Å^3$, 162.99(3) $Å^3$ and 162.68(9) $Å^3$ in alloys 1, 2 and 3, respectively. The small difference in unit cell volumes for the C14 Laves phase are due to the small variation in the composition.

A similar difference is also observed in the BCC phase; 25.72(6) $Å^3$ in alloy 1, 25.74(5) $Å^3$ in alloy 2 and 25.67(3) $Å^3$ in alloy 3. This indicates that both the C14 Laves phase and BCC phase are affected with higher V content, resulting in a smaller unit cell.

Variations in the relative intensities of the C14 Laves reflections between the three alloys can be best seen in Figure 7 at approximately 37^o (110), 40.16^o (013), 44.54^o (021) and 74.74^o (025) 2θ. These variations are shown in Table 7.4 and are indicative of site occupancy effects of the B-site (Mn, V) on the *2a* and *6h* sites and position *z* for the A atom (Ti) on the *4f* site within the C14 Laves lattice.

Table 7.4 Relative intensities of C14 Laves phase reflections for as-cast 1, 2 and 3.

2θ	hkl	Relative Intensities		
		As-cast 1	As-cast 2	As-cast 3
37	110	60.3	17.4	25.5
40.16	013	95.6	82.1	51.1
44.54	021	100	100	100
74.74	025	16.4	26.1	21.3

Based on the XRD analysis and phases identified during SEM analysis, these results indicate that the light area, which appears to be the dominant phase in the micrographs, corresponds to the C14 Laves phase, the grey phase corresponds to the BCC phase and the minor FCC phase appears as the dark dendritic phase.

7.3 Characterisation of Heat Treated Alloys

Characterisation of the three heat treated alloys was carried out to investigate the effect of heat treatment and to ensure the alloys were fully homogenous. For all the alloys heat treatment was performed for 6 hours in a vacuum furnace (< 10^{-6} mbar) at 1233 K, as described in the Project Experimental (Chapter 6).

7.3.1 SEM/EDS on Heat Treated Alloys

Figures 7.8-7.13 show BEI images of heat treated alloys 1, 2 and 3 at low (x 500) and high (x 1000) magnification.

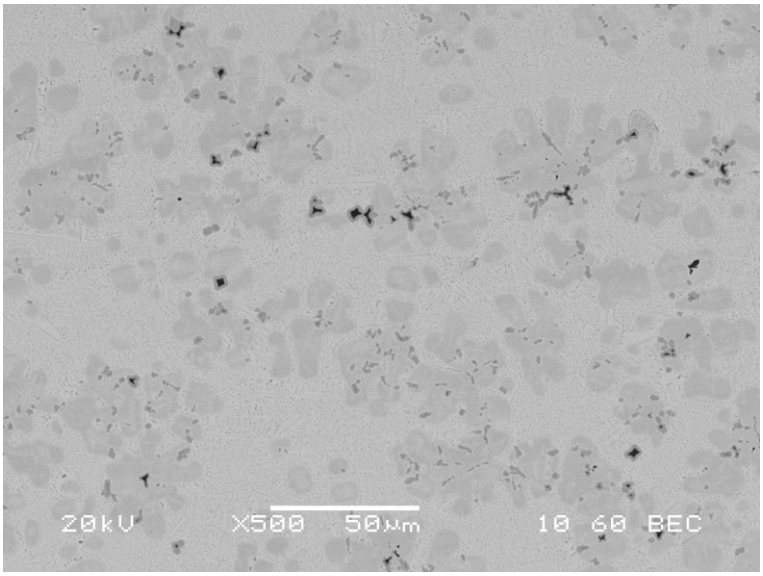

Figure 7.8 SEM BEI image of heat treated 1 (x 500)

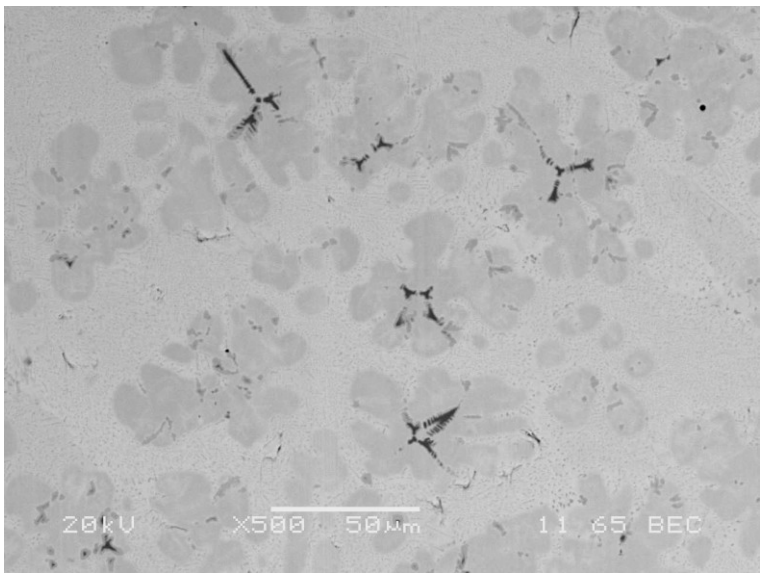

Figure 7.9 SEM BEI image of heat treated 2 (x 500)

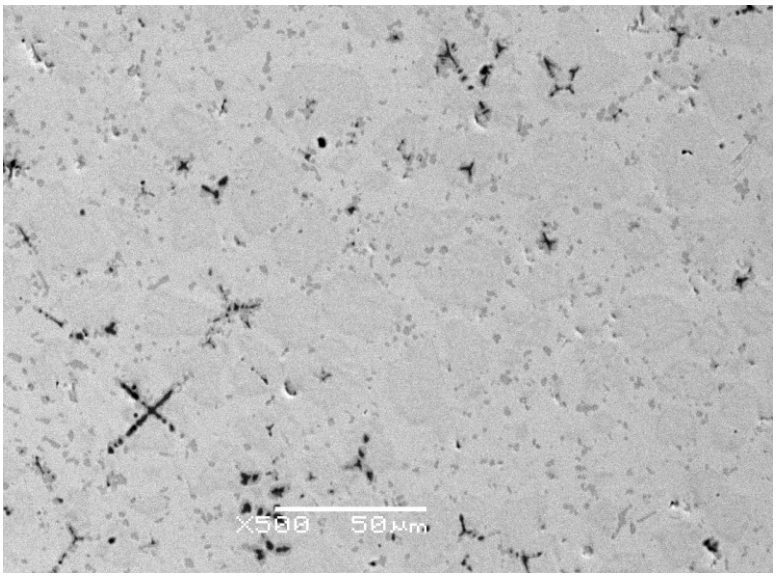

Figure 7.10 SEM BEI image of heat treated 3 (x 500)

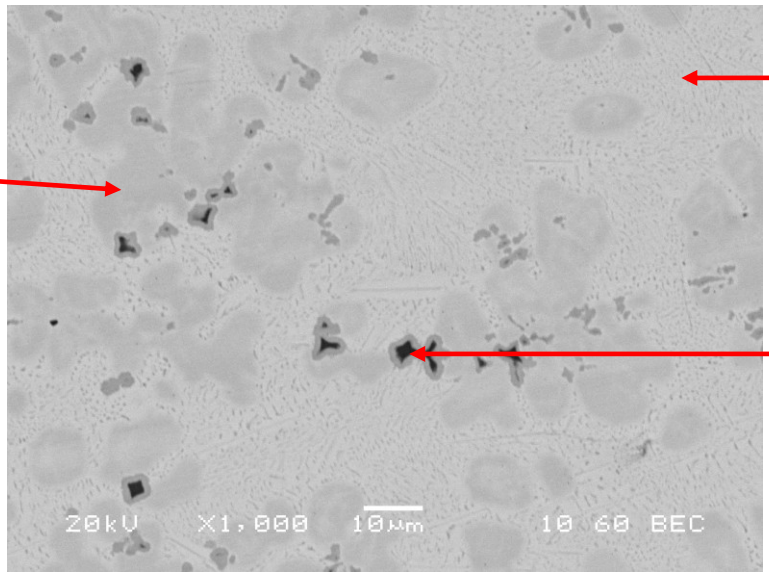

Figure 7.11 SEM BEI image of heat treated 1 (x 1000)

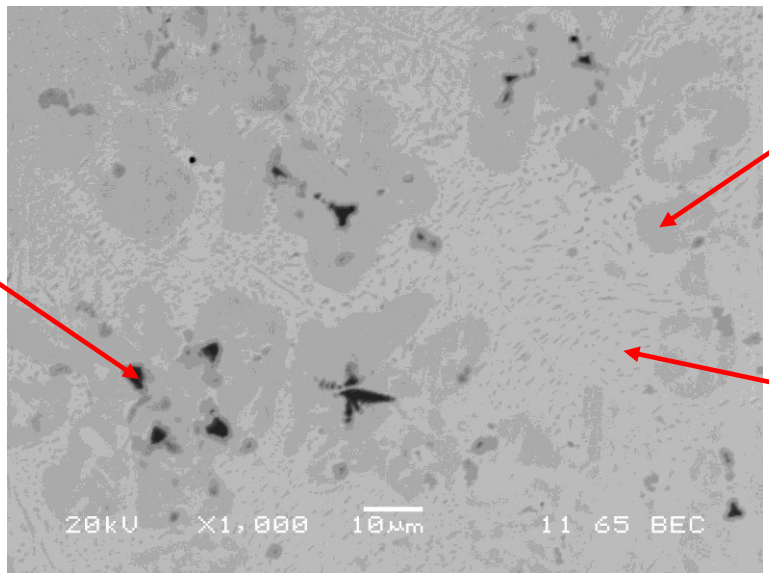

Figure 7.12 SEM BEI image of heat treated 2 (x 1000)

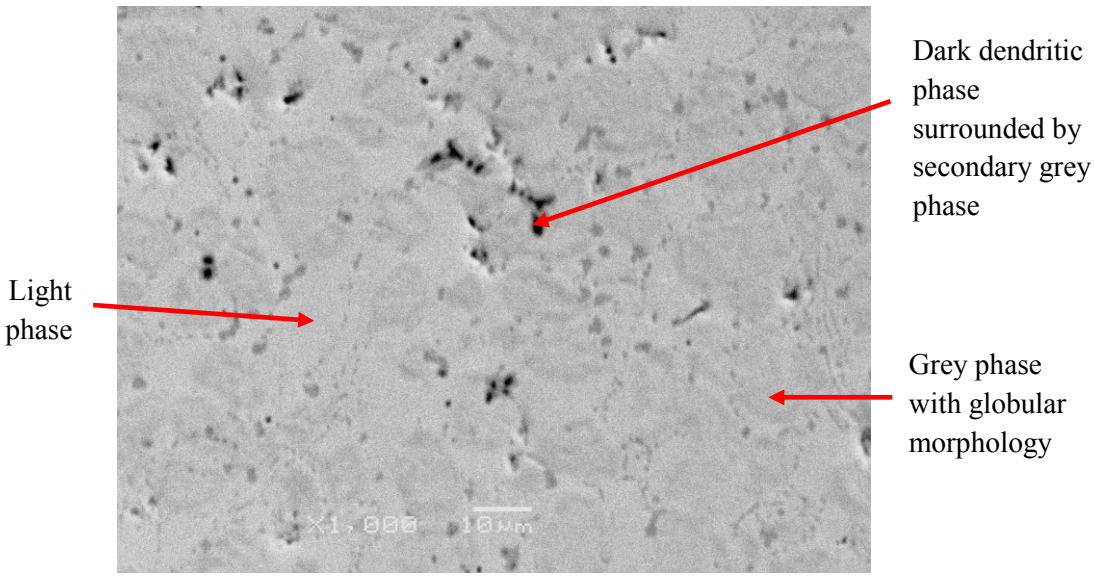

Figure 7.13 SEM BEI image of heat treated 3 (x 1000)

Heat treatment was performed on the arc-melted ingots to minimise any compositional heterogeneities associated with segregation of the elements. While it appears as though heat treatment has homogenised alloy 3, there still appears to be coring present in the high magnification images of alloy 1 and 2. This suggests that longer heat treatment times may be required in order to fully homogenise the alloys.

In Figures 7.8 – 7.13, similar microstructures are observed to the as-cast alloys with light, grey and dark dendritic phases present. EDS analysis was performed on the heat treated alloys to identify the composition of these phases, with the results shown in Table 7.5. It should be noted that the results shown are in atomic percent (at %).

Table 7.5 Average EDS analysis on heat treated 1, 2 and 3 with standard deviation associated with mean values. Note analysis was carried out by taking an average of three different areas/points within BEI images of the alloys.

Alloy	Phase Location	Ti	σ	V	σ	Mn	σ	Average Composition Ratio (Ti/V/Mn)
Heat treated 1	Area	24.37	7.4	23.73	8.1	51.91	6.7	0.47/0.46/1
	Light	28.20	6.9	17.80	7.2	54.04	7.8	0.52/0.33/1
	Grey	17.85	6.5	33.49	6.9	48.67	7.1	0.37/0.69/1
	Dark	56.57	7.9	14.39	7.2	29.03	6.8	1.95/0.50/1
Heat treated 2	Area	24.40	6.8	23.79	8.1	51.82	7.3	0.47/0.46/1
	Light	28.08	7.2	16.95	7.9	54.98	8.2	0.51/0.31/1
	Grey	19.96	6.9	30.49	6.5	50.55	7.1	0.39/0.60/1
	Dark	63.74	8.3	10.27	7.6	25.99	8.7	2.45/0.40/1
Heat treated 3	Area	25.02	9.1	25.32	8.6	49.66	7.9	0.50/0.51/1
	Light	27.64	8.4	16.12	8.9	56.25	9.2	0.49/0.29/1
	Grey	16.30	6.2	35.14	6.5	48.55	7.1	0.34/0.72/1
	Dark	42.48	7.7	12.35	7.5	45.17	8.3	0.94/0.27/1

The area analysis shows that the average composition for heat treated 1 is $Ti_{0.47}V_{0.46}Mn_1$, 2 is $Ti_{0.47}V_{0.46}Mn_1$ and 3 is $Ti_{0.50}V_{0.51}Mn_1$.

Heat treatment has resulted in there being similar phase compositions amongst the alloys. In all three alloys, the light phase is now richer in Ti and Mn, grey phase is richer in V and dark phase is rich in Ti.

7.3.2 XRD on Heat Treated Alloys

Figure 7.14 shows XRD patterns of heat treated 1 (top, black), 2 (middle, red) and 3 (blue, bottom) after Rietveld refinement with the peak indexed. Appendix B shows individual XRD traces of the heat treated alloys showing the observed pattern and calculated fit after pseudo-Rietveld refinement.

The same three phases are identified in all the heat treated alloys. Table 7.6 shows crystal structure refinement results for heat treated alloy 1, 2 and 3 in comparison to the as-cast alloys.

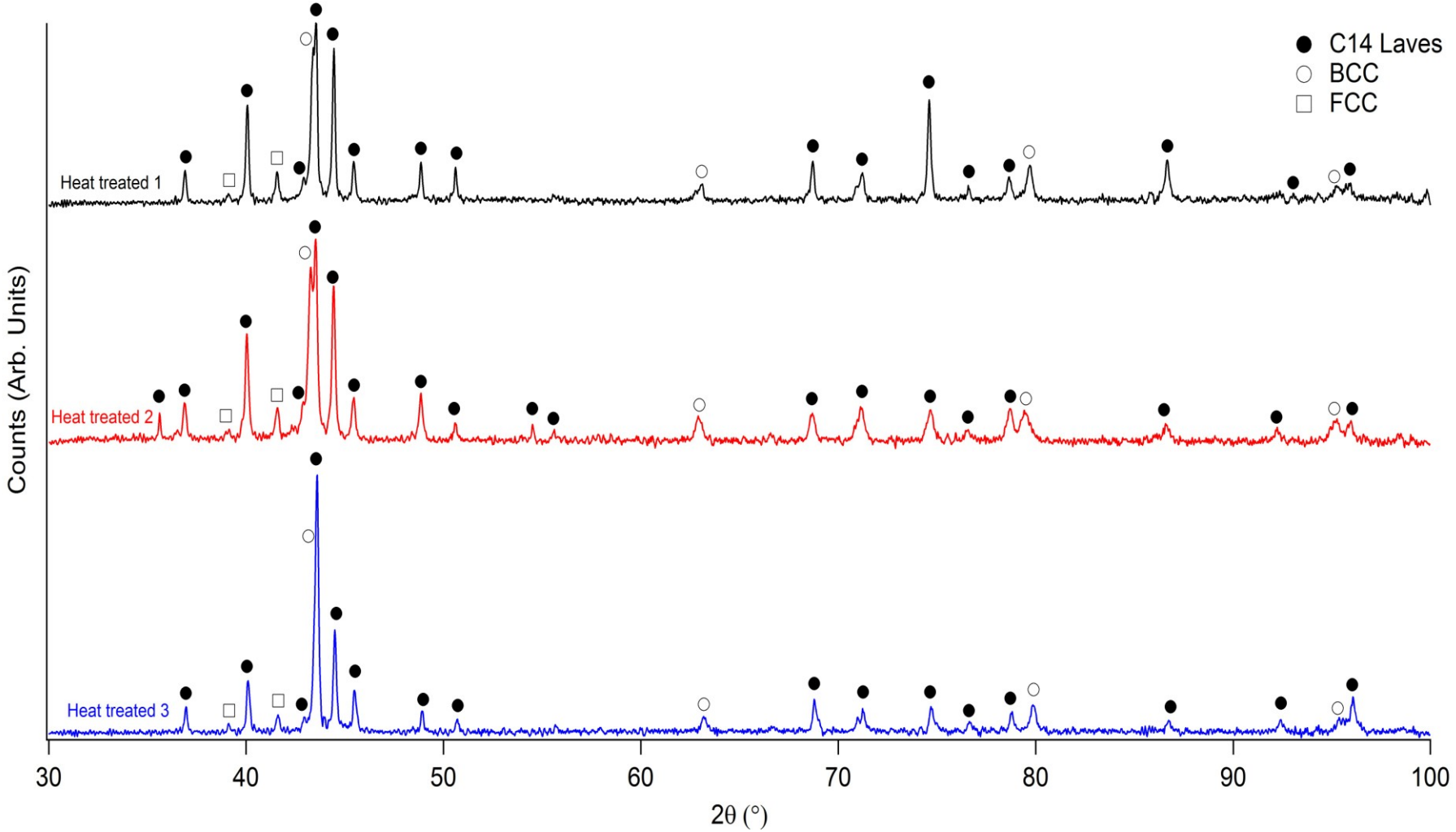

Figure 7.14 XRD patterns of heat treated 1 (top, black), 2 (middle, red) and 3 (bottom, blue) with peaks indexed.

In comparison to the XRD patterns of the as-cast alloys the XRD peaks appear sharper in the heat treated alloys which indicates a less strained microstructure after annealing, leading to higher crystallinity.

Table 7.6 Crystal structure refinement results for heat treated alloys (values on right) in comparison to as-cast alloys. Note the values in parentheses are three standard deviations and refer to the last digit.

Alloy	As-Cast				Heat Treated			
	Phase	Lattice Parameters		Abundance	Phase	Lattice Parameters		Abundance
1	C14	a	4.857(9)	53(6)	C14	a	4.865(3)	70(6)
		c	7.963(16)			c	7.975(6)	
	BCC	a + c	2.951(5)	38(2)	BCC	a + c	2.948(3)	22(3)
	FCC	a+ c	11.271(12)	8(3)	FCC	a+ c	11.273(9)	8(3)
2	C14	a	4.859(3)	63(5)	C14	a	4.863(6)	69(2)
		c	7.970(5)			c	7.970(11)	
	BCC	a + c	2.952(1)	27(4)	BCC	a + c	2.952(4)	24(6)
	FCC	a+ c	11.252(7)	9(4)	FCC	a+ c	11.276(8)	7(4)
3	C14	a	4.856(2)	58(5)	C14	a	4.860(6)	58(6)
		c	7.961(3)			c	7.968(9)	
	BCC	a + c	2.935(1)	32(5)	BCC	a + c	2.938(3)	34(3)
	FCC	a+ c	11.260(5)	9(2)	FCC	a+ c	11.270(12)	8(3)

Again, the C14 Laves phase appears to be the dominant phase in all three heat treated alloys occupying; 70 wt% in alloy 1, 69 wt% in alloy 2 and 58 wt% in alloy 3.

Alloys 1 and 2 appear to have homogenised during heat treatment because they both have similar phase abundances. Heat treatment has not significantly affected alloy 3 which shows very similar phase abundances to the as-cast state.

The *a* and *c* lattice parameters for the C14 Laves, BCC and FCC phases does not appear to have significantly changed after heat treatment, indicating high bonding strength between the atoms in all three alloys.

Variations in the relative intensities of the C14 Laves reflections between the three alloys at 37^{o} (110), 40.16^{o} (013), 44.54^{o} (021) and 74.74^{o} 2θ are shown in Table 7.7 and are, again, indicative of site occupancy and/or ordering effects within the C14 Laves phase lattice.

Table 7.7 The composition relative intensities of the C14 phase for Heat treated 1, 2 and 3.

2θ	hkl	Relative Intensities		
		1	2	3
37	110	19.3	24.1	27.8
40.16	013	63.3	67.7	72.2
44.54	021	100	100	100
74.74	025	67.9	18.75	19.4

The unit cell volumes of the C14 Laves phase in the heat treated alloys are 163.45(9) $Å^3$, 163.22(7) $Å^3$ and 163.00(11) $Å^3$ in alloys 1, 2 and 3 respectively. This shows an expansion of between 0.23 and 0.73 $Å^3$ in comparison to the as-cast alloys.

There is also a change in the unit cell volume of the BCC phase in the heat treated alloys: alloy 1 is 25.54(8) $Å^3$, alloy 2 is 25.75(11) $Å^3$ and alloy 3 is 25.35(7) $Å^3$. This show a difference of between 0.01 and 0.32 $Å^3$ in comparison to alloy before heat treatment.

Such differences are the result of different metallic radii of the elements in the Ti-V-Mn system: Ti is 1.47 Å, V is 1.35 Å and Mn is 1.27 Å.

Looking at the difference in composition (at%) of the light C14 Laves phase and grey BCC phase between the as-cast and heat treated alloys from the EDS data it is possible to calculate which elements have increased or decreased. This gives an indication to which substitutions have taken place within the respective unit cell after heat treatment (see Appendix B).

In alloy 1 the increase in the unit cell volume of the C14 Laves phase can be attributed to the substitution of 4 V atoms for 4 Mn atoms during the heat treatment process. This is because V has a larger metallic radius than Mn which causes an expansion of the lattice. In alloys 2 and 3 there is also an increase in the unit cell volume of the C14 Laves phase as a result of substitution of 1 Ti atom for 1 V atom in both alloys.

In alloy 1 the decrease in the unit cell volume of the BCC phase can be attributed to the substitution of 2 Mn atoms for 1 Ti atom and 1 V atom: Mn has a smaller metallic radius than Ti and V which therefore leads to a contraction of the lattice. In alloy 2 there is an increase in the unit cell volume of the BCC phase as a result of substitution of 2 Ti atoms and 1 Mn atom for 3 V atoms. Finally, in alloy 3 there is a decrease in the unit cell volume of the BCC phase as 1 Mn atom is substituted for 1 Ti atom. These results indicate that both the C14 Laves phase and BCC phase are effected by elemental substitution.

This supports previous work by Shibuya et al., (2008) who showed that the BCC phase abundance increases and C14 Laves phase abundance decreases with V content in Ti-V-Mn alloys: alloy 3 has the largest V content (0.05 at% more than alloy 1 and 2) and has the largest BCC phase abundance and smallest C14 Laves phase abundance of the three alloys.

7.4 Characterisation of Hydrogen Sorption Properties

7.4.1 PCT Measurements

HTP measurements were performed at 303 K, 313 K and 323 K up to 120 bar H_2, for alloys 1, 2 and 3 (Figures 7.15, 7.16 and 7.17). For the measurements, 778 mg of alloy 1, 889 mg of alloy 2 and 624 mg of alloy 3 was loaded. Note, lines are included between data points on isotherms for ease of understanding. Prior to measurements, an activation sequence was performed on all the heat treated alloys (see Project Experimental in Chapter 6). The isotherms shown are therefore the 2nd, 3rd and 4th cycle at 303 K, 313 K and 323 K, respectively.

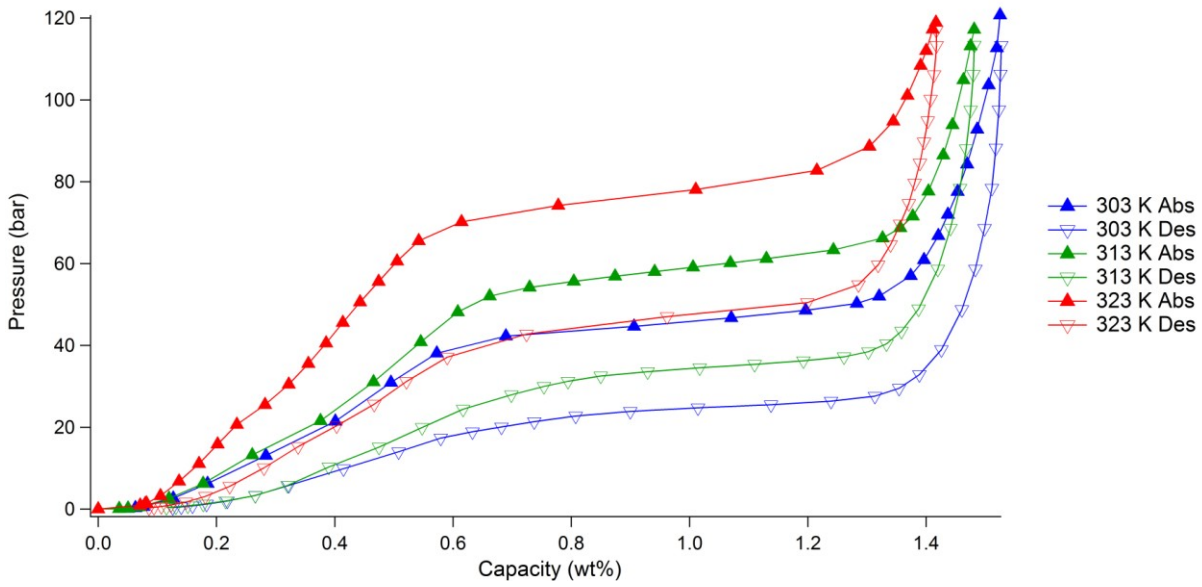

Figure 7.15 PCT measurement of alloy 1 at 303 K (blue), 313 K (green) and 323 K (red) showing absorption (upwards triangles) and desorption (downwards triangles) from 0.5 to 120 bar H_2.

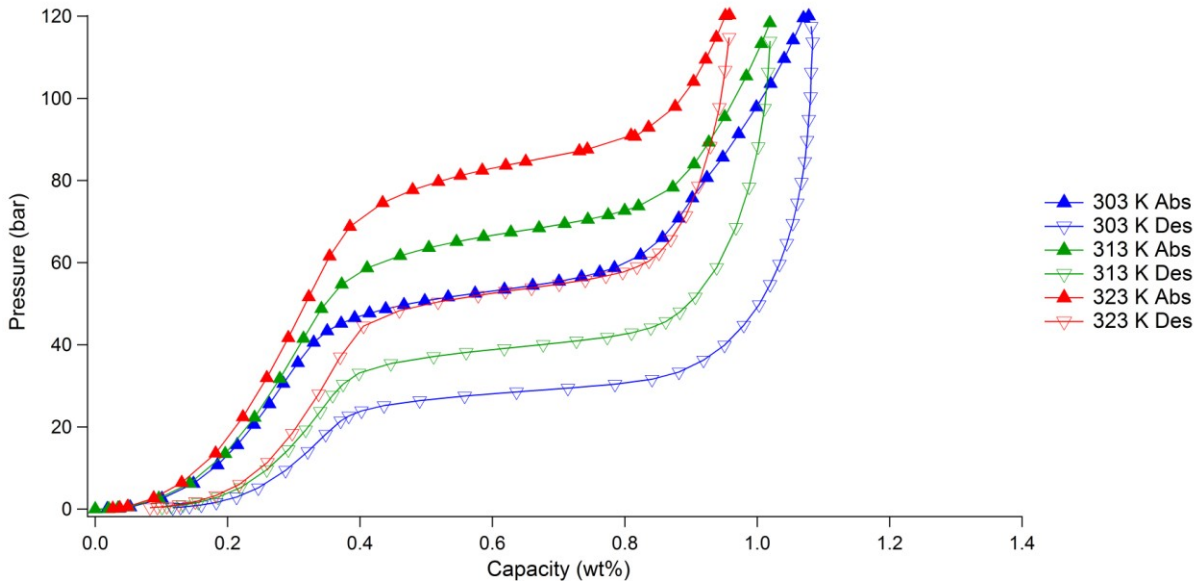

Figure 7.16 PCT measurement of alloy 2 at 303 K (blue), 313 K (green) and 323 K (red) showing absorption (upwards triangles) and desorption (downwards triangles) from 0.5 to 120 bar H_2.

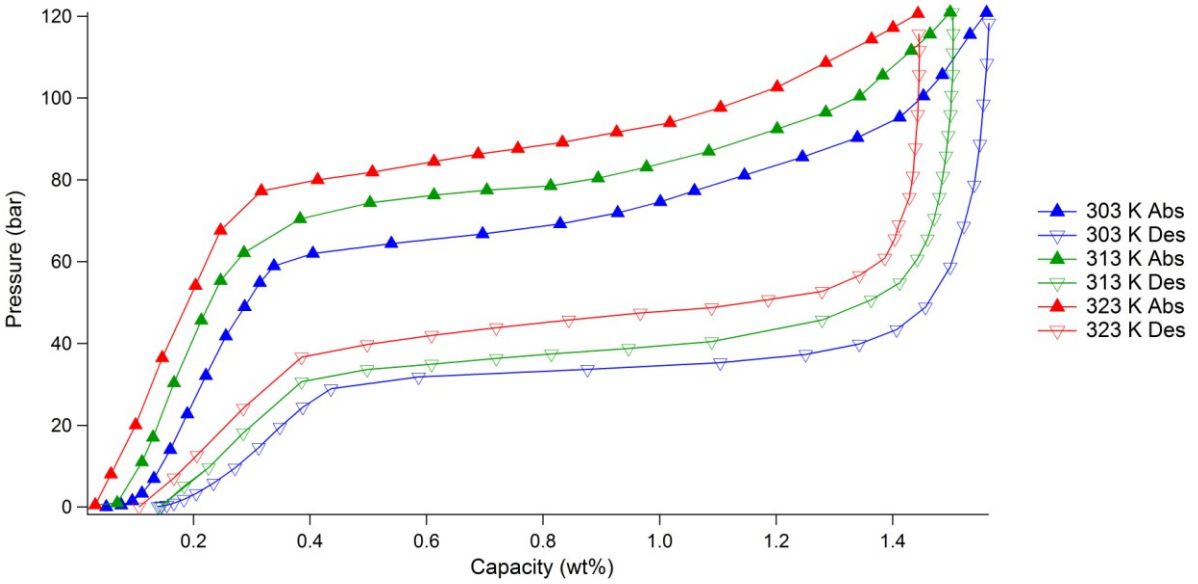

Figure 7.17 PCT measurement of alloy 3 at 303 K (blue), 313 K (green) and 323 K (red) showing absorption (upwards triangles) and desorption (downwards triangles) from 0.5 to 120 bar H_2.

Comparing Figures 7.15, 7.16 and 7.17, the three alloys exhibit different hydrogen sorption behaviour as a result of their compositional differences. All the alloys show two step uptake where two plateaus are present for absorption and desorption.

Alloy 3 shows the greatest uptake but may not have fully saturated at 120 bar due to a sloped absorption plateau. Alloy 1 appears to fully saturate up to 120 bar, exhibiting smaller hysteresis between absorption and desorption and possesses much flatter absorption and desorption plateaus. Sloping behaviour in metal hydrides indicates inhomogeneity (Akiba & Iba, 1998) which may suggest that alloy 1 may be more homogenous than the other two alloys. The significant difference in capacity in alloy 2 suggests saturation was not achieved up to 120 bar H_2, with a continual increase in uptake above the main plateau. It did, however, exhibit a smaller hysteresis than alloy 3. A metal hydride exhibiting relatively small hysteresis may be useful in applications where hydrogen is absorbed and desorbed over hundreds or thousands of cycles, as energy efficiency will be improved (Sandrock, 1999).

Figure 7.18 shows a comparison of isotherms for all three heat treated alloys at 303 K up to 120 bar H_2. PCT properties, including capacity, plateau pressure and hysteresis, of all four alloys at 303 K are provided in Table 7.8.

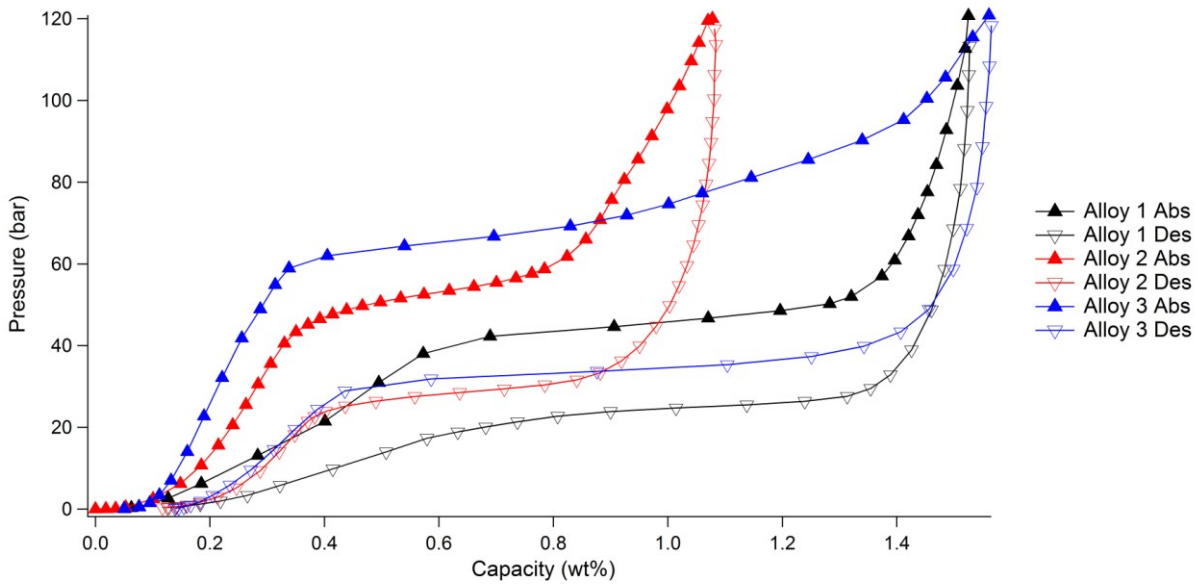

Figure 7.18 PCT measurement of alloy 1 (black), 2 (red) and 3 (blue) showing absorption (upwards triangles) and desorption (downwards triangles) at 303 K from 0.5 to 120 bar H_2.

Table 7.8 Summary of capacity, plateau pressure and hysteresis for alloys 1, 2 and 3 based on PCT isotherms at 303 K. Hysteresis factor: 0 = no hysteresis, 1 = large hysteresis. Note measured errors for capacity are estimated to be 0.05 wt% based on 3 PCT measurements using a Pd standard (see Appendix A).

Alloy	Maximum Capacity (wt%)	Reversible Capacity (wt%)	Abs Plateau P (bar)	Des Plateau P (bar)	Hysteresis Factor $Log(P_{Abs}/P_{Des})$
1	1.58	1.53	42 - 52	25 - 15	0.371
2	1.11	1.08	50 - 60	35 - 25	0.263
3	1.63	1.56	60 - 70	40 - 30	0.269

The reversible capacities shown here are lower than those previously reported for the $Ti_{0.5}V_{0.5}Mn$ system; 1.9 wt% at 260 K under 350 bar H_2 (Shibuya et al., 2009). This is likely to be due to differences in temperature and pressure during measurement.

To ensure all the alloys reached equilibrium along the plateau, the kinetic data from the HTP system was studied. Figures 7.19 – 7.21 show examples of the kinetic data taken from the mid-point plateau for absorption at 303 K in alloy 1, 2 and 3 respectively.

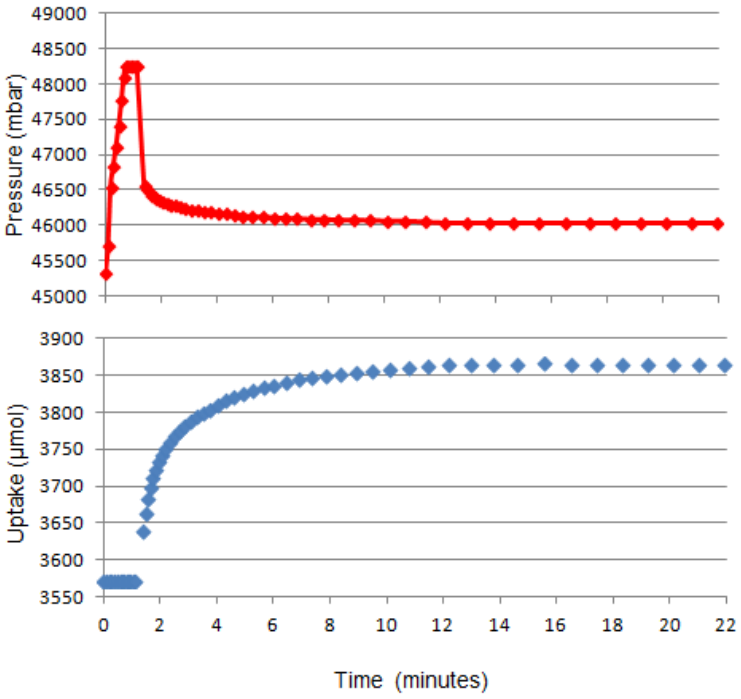

Figure 7.19 Kinetic data for alloy 1 showing pressure (red) and uptake (blue) at the mid-point plateau for absorption at 303 K.

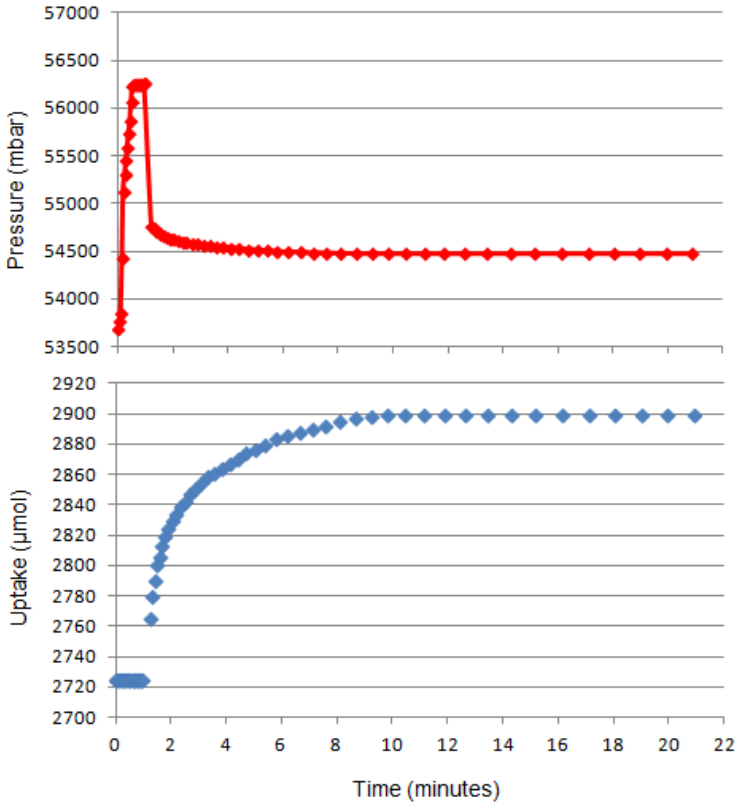

Figure 7.20 Kinetic data for alloy 2 showing pressure (red) and uptake (blue) at the mid-point plateau for absorption at 303 K.

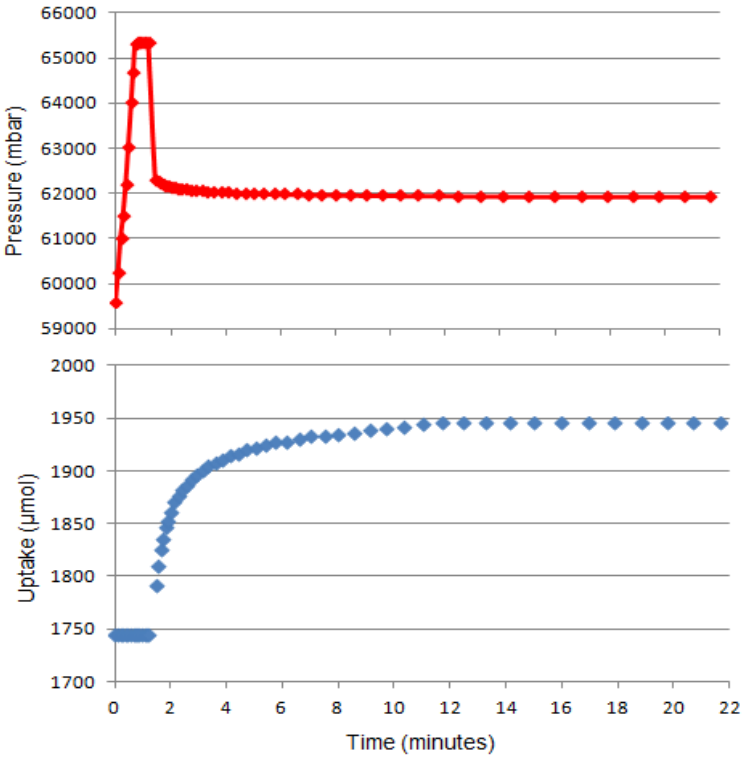

Figure 7.21 Kinetic data for alloy 3 showing pressure (red) and uptake (blue) at the mid-point plateau for absorption at 303 K.

Looking at the kinetic data for the alloys it appears as though all three alloys reach equilibrium between 0 and 22 minutes during absorption.

Van't hoff plots, calculated in Appendix B, showing hydrogen absorption and desorption are shown in Figure 7.22 with the derived enthalpies and entropies in Table 7.9.

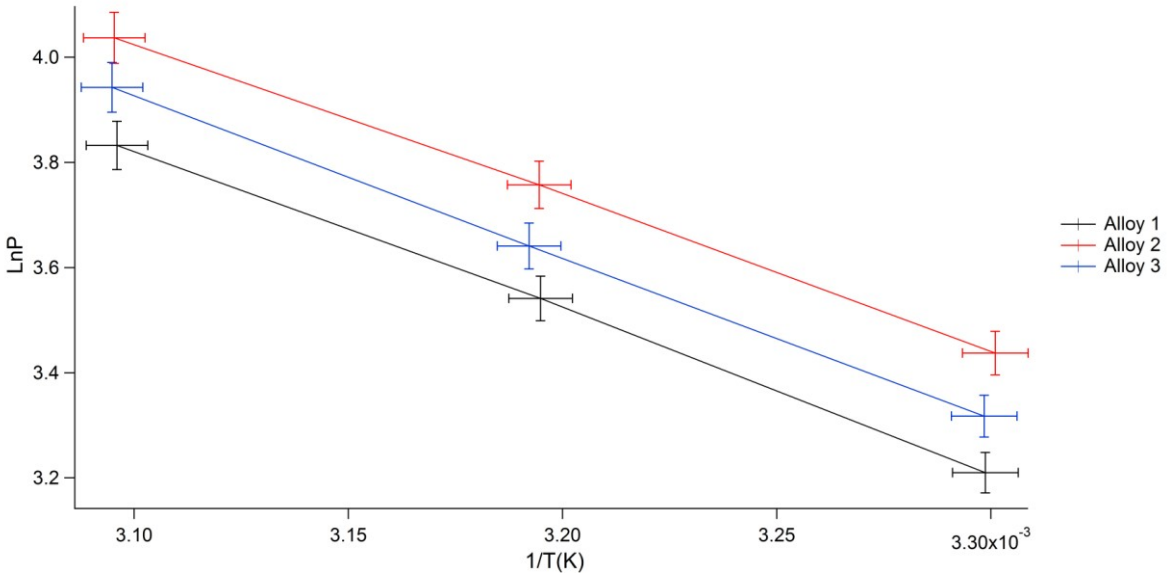

Figure 7.22 Van't hoff plot of alloy 1, 2 and 3 showing desorption (with associated errors).

Table 7.9 Enthalpy and Entropy data for desorption in Alloy 1, 2 and 3.

Alloy	ΔH (kJ/mol H_2)	ΔS (J/mol H_2)
1	-25.40	110.94
2	-25.94	108.65
3	-26.63	111.77

The calculated desorption ΔH are within the target value for interfacing stores to PEM fuel cell applications; higher than -30 kJ/mol H_2 (Shibuya et al., 2008). This work therefore supports previous work showing that $Ti_{0.5}V_{0.5}Mn$ alloys are suitable alloys for use in a hybrid system.

It has previously been shown that the maximum hydrogen storage capacity of Ti-V based BCC phase alloys decreases with the increase of Laves phase formation (Dou et al., 2008), as can be seen here: with alloy 3 having the lowest phase abundance of the C14 Laves phase. In addition, Shibuya et al., (2008) found that an increase in the BCC phase abundance resulted in

an increase in plateau pressure and hysteresis in Ti-V-Mn alloys which has also been confirmed in this investigation.

7.5 Characterisation of Hydrogen Cycled Alloys

7.5.1 SEM/EDS on Hydrogen Cycled Alloys

SEM images and EDS analysis was performed on the hydrogen decrepitated powders of alloys 1, 2 and 3, after hydrogen sorption measurements. All the alloys were dehydrogenated under vacuum before being exposed to air in a controlled manner. SEM BEI images (x 500 magnification) of the hydrogen cycled alloys are shown in Figures 7.23 – 7.25. Note, all the alloys were cycled with hydrogen under the same conditions (see Chapter 6).

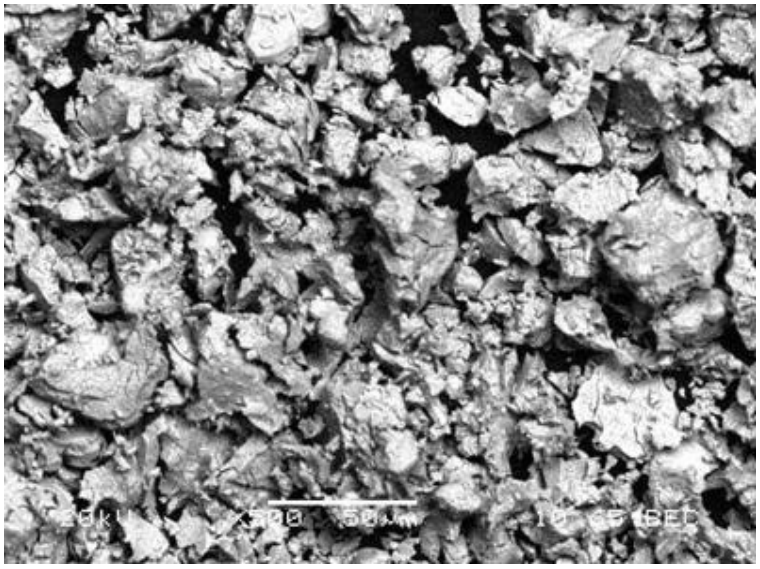

Figure 7.23 SEM BEI image of the hydrogen cycled 1 (x 500).

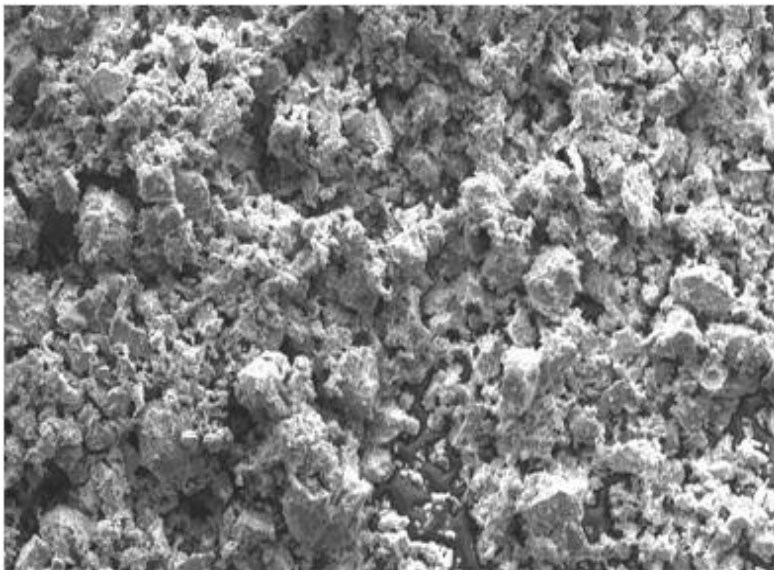

Figure 7.24 SEM BEI image of the hydrogen cycled 2 (x 500)

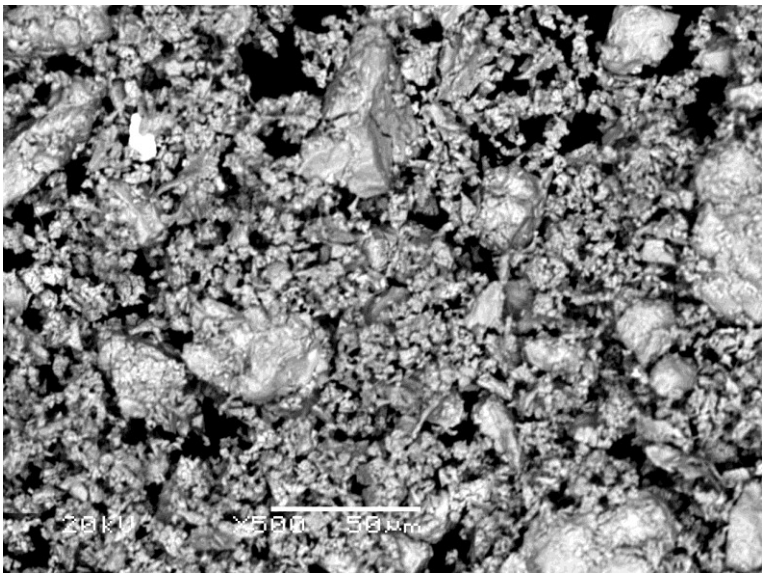

Figure 7.25 SEM BEI image of the hydrogen cycled 3 (x 500)

SEM micrographs of the hydrogen cycled powders show significant differences. This suggests that different fracture mechanisms may have occurred within the alloys.

Alloy 1 forms large particles with smooth edges and cracks within the particles, which would be expected from a ductile fracture. In alloy 2, small (8μm) rough-edged particles can be seen which appear to agglomerate together. The rough edges are consistent with what would be expected from a brittle intergranular fracture observed during hydrogen decrepitation. Alloy 3 appears to be similar to alloy 1 but features smaller particles, indicating that the alloy has decrepitated more than alloy 1. This may explain why alloy 3 exhibited a higher maximum and reversible capacity.

EDS analysis was carried out on different areas/spots in the powdered alloys. The average composition of the hydrogen cycled 1 is $Ti_{0.57}V_{0.48}Mn_1$, 2 is $Ti_{0.53}V_{0.44}Mn_1$, and 3 is $Ti_{0.65}V_{0.55}Mn_1$.

7.5.2 XRD on Hydrogen Cycled Alloys

XRD patterns of hydrogen decrepitated powders of alloys 1, 2 and 3 after hydrogen sorption measurements are shown in Figure 7.26. Table 7.10 shows crystal structure refinement results for the hydrogen cycled alloys. Appendix B shows individual XRD traces of the hydrogen cycled alloys showing the observed pattern and calculated fit after pseudo-Rietveld refinement.

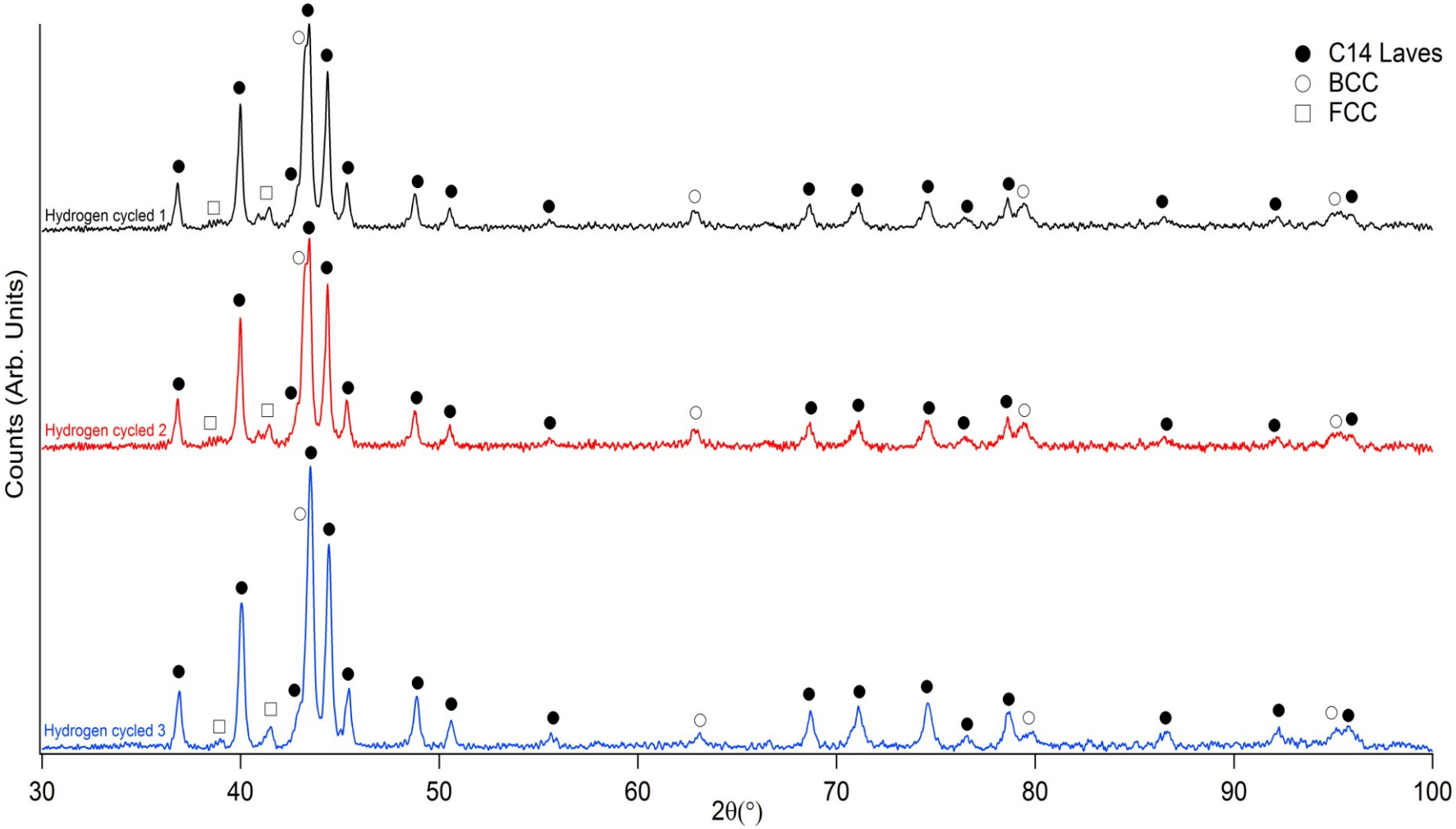

Figure 7.26 XRD patterns of hydrogen cycled 1 (top, black), 2 (middle, red) and 3 (bottom, blue) with peaks indexed.

The XRD peaks of the hydrogen cycled alloys appear broader than the heat treated alloys. This may be due to a particle size effect which has occurred upon hydrogenation, resulting in smaller crystallite size.

Table 7.10 Crystal structure refinement results for hydrogen cycled alloys (values on right), in comparison to heat treated alloys.

Alloy	Heat Treated				Hydrogen Cycled			
	Phase	Lattice Parameters		Abundance	Phase	Lattice Parameters		Abundance
1	C14	a	4.865(3)	70(6)	C14	a	4.869(9)	78(3)
		c	7.975(6)			c	7.984(15)	
	BCC	a + c	2.948(3)	22(3)	BCC	a + c	2.950(6)	16(3)
	FCC	a+ c	11.273(9)	8(3)	FCC	a+ c	11.303(21)	6(3)
2	C14	a	4.863(6)	69(2)	C14	a	4.864(16)	73(5)
		c	7.970(11)			c	7.979(20)	
	BCC	a + c	2.952(4)	24(6)	BCC	a + c	2.950(10)	22(9)
	FCC	a+ c	11.276(8)	7(4)	FCC	a+ c	11.303(9)	5(2)
3	C14	a	4.860(6)	58(6)	C14	a	4.865(6)	79(3)
		c	7.968(9)			c	7.978(9)	
	BCC	a + c	2.938(3)	34(3)	BCC	a + c	2.947(3)	14(3)
	FCC	a+ c	11.270(12)	8(3)	FCC	a+ c	11.309(15)	7(3)

The C14 Laves phase is still the dominant phase in all three hydrogen cycled alloys, occupying 78 wt% in alloy 1, 73 wt% in alloy 2 and 79 wt% in alloy 3. There is an increase in the relative phase abundance of the C14 Laves phase in all three alloys in comparison to the heat treated alloys. Subsequently there is a decrease in the relative phase abundance of the BCC and FCC phases in all three alloys.

Hydrogenation has had the effect of homogenising the C14 Laves, BCC and FCC phase abundances with all three samples having similar phase proportions.

The subtle variations in the relative intensities of the (110), (013), (021) and (025) reflections are shown in Table 11 and can be attributed to an underlining variation in the C14 Laves phase.

Table 7.11 The composition relative intensities of the C14 Laves phase for Hydrogen cycled 1, 2 and 3.

2θ	hkl	Relative Intensities		
		1	2	3
37	110	24.1	29.2	26.7
40.16	13	69	79.2	70.7
44.54	21	100	100	100
74.74	25	13.8	14.6	20

The unit cell volume of the C14 Laves phase shows an expansion of 0.5 $Å^3$ compared to the heat treated alloys. This may be explained by remnant hydrogen trapped within the C14 Laves phase as seen by the reduction in the hydrogen uptake after the first cycle (maximum capacity). There also appears to be homogenisation of the BCC phase, with unit cell volumes of 25.67(4) $Å^3$, 25.68(3) $Å^3$ and 25.58(3) $Å^3$ found for hydrogen cycled alloys 1, 2 and 3 respectively. The small change in the unit cell volume of alloy 1 indicates that it is unlikely that any hydrogen would be trapped within this phase.

It is known that an increase in unit cell volume leads to a decrease in dissociation pressure for both AB_5 type alloys, such as $LaNi_5$ (Mendelsohn & Gruen, 1977; Reilly et al., 1999) and AB_2 C14 Laves type alloys (Nakano et al., 1997; Nakano & Wakao, 1995).

Figure 7.27 shows the relationship between C14 Laves phase unit cell volume vs. desorption plateau pressure and Figure 7.28 shows the relationship between the BCC phase unit cell volume vs. desorption plateau pressure for alloy 1, 2 and 3.

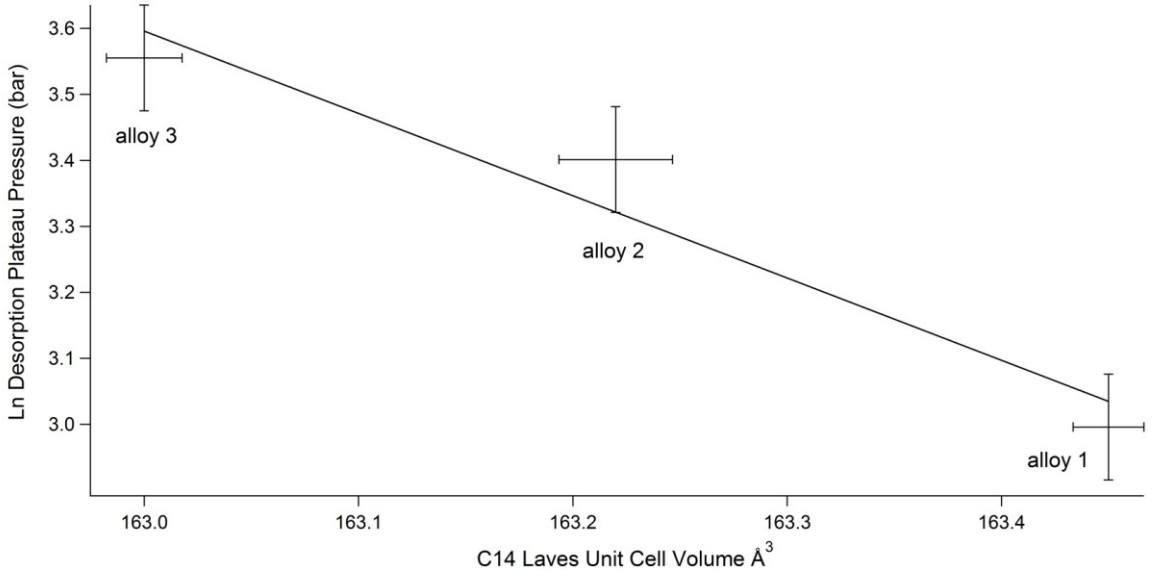

Figure 7.27 Correlation between C14 Laves unit cell volume (Å^3) vs. Ln Desorption plateau pressure (bar) for alloy 1, 2 and 3 with corresponding error bars. Note, line added between data points on for ease of understanding.

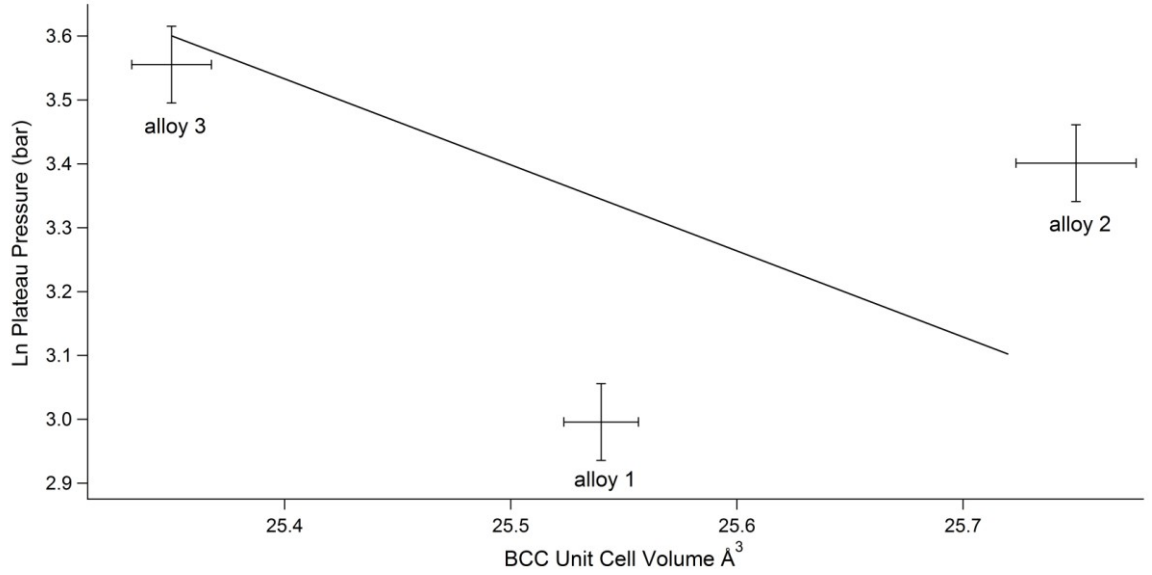

Figure 7.28 Correlation between BCC phase unit cell volume (Å^3) vs. Ln Desorption plateau pressure (bar) for alloy 1, 2 and 3 with corresponding error bars. Note, line added between data points on for ease of understanding.

The correlation shown in Figure 7.27 is in agreement with previous studies showing a decrease in desorption plateau pressure with increasing C14 Laves phase unit cell volume. This is due to there being larger interstitial sites for hydrogen atoms to enter.

Figure 7.28 shows a weak relationship between desorption plateau pressure and BCC phase unit cell volume, however, further data points would be required to confirm the correlation. This indicates that the BCC unit cell volume is not as sensitive to changes in composition as the C14 Laves phase.

7.6 Summary

This aim of this chapter was to present and discuss the structural and morphological differences observed due to small deviations in the desired stoichiometry of three alloys with the target composition $Ti_{0.5}V_{0.5}Mn$ and discuss the influence of these changes on their hydrogen storage properties.

SEM analysis found that three microstructural phases were present in the alloys: a light Mn-rich phase, a grey V-rich phase and dark dendritic Ti-rich phase. In addition, coring was present in both the as-cast and heat treated alloys. This indicates that longer heat treatment times are required to fully homogenise the alloys.

Analysis of the XRD traces found that in all three alloys C14 Laves, BCC and FCC phases were present. The C14 Laves phase was the dominant phase both before and after heat treatment, occupying 70 wt%, 69 wt% and 58 wt% in the heat treated alloys 1, 2, and 3.

The small difference in composition led to variations in the relative intensities of the C14 Laves reflections between the three alloys. These variations are indicative of site occupancy

effects of the B-site (Mn, V) on the *2a* and *6h* sites and position *z* for the A atom (Ti) on the *4f* site within the C14 lattice.

Compositional differences also resulted in different unit cell volumes of the C14 Laves and BCC phases in the three alloys. Elemental Ti, V and Mn have different metallic radii so the variation in unit cell volume was due to different elemental substitutions taking place in the Ti-V-Mn system. This was confirmed by looking at the difference in atomic composition of the light C14 Laves phase and grey BCC phase from EDS results on the as-cast and heat treated alloys: unit cell volumes increased as a result of substitution of elements with larger metallic radii and decreased through substitution of elements with smaller metallic radii.

PCT measurements showed that the alloys possessed different hydrogen storage sorption behaviours: alloys 1, 2 and 3 demonstrated reversible hydrogen sorption capacities of 1.53, 1.08 and 1.56 +/- 0.05 wt% respectively, up to 120 bar H_2 at 303 K. In addition, there was a significant difference in plateau pressure and enthalpy of hydride decomposition values between the alloys: a variation in composition by 0.05 at% resulted in a shift in plateau pressure by 20 bar. This is in agreement with previous studies investigating the relationship between unit cell volume vs. plateau pressure and enthalpy of hydride decomposition.

Small changes in composition in the $Ti_{0.5}V_{0.5}Mn$ system, may allow the plateau pressure to be 'tuned' to meet the requirements of certain solid-state hydrogen storage applications, such as the different stages of a metal hydride compressor (Pickering et al., 2013).

As explained in the Research Aims & Objectives in Chapter 5, the next stage of the current work was to investigate the effect of small additions of a fourth element to the $Ti_{0.5}V_{0.5}Mn$ system, in relation to microstructure, crystallography and subsequent hydrogen sorption properties.

Chapter 8

THE Ti-V-TM-Mn SYSTEM

8.1 Introduction

It has been suggested that the hydrogenation properties, including the plateau and hysteresis pressures may be improved in alloys based on Ti-V-Mn by substitution of the transition metals (Shibuya et al., 2008) and the addition of a fourth element may increase the reversible capacity (Shibuya el al., 2009).

In this chapter the effect of substituting V for other transition metal elements with similar BCC phase stabilising properties, namely, Nb, Cr, Mo and Ta, is investigated. For practical applications these alloys may also be more cost effective than using pure V for the base alloy (see Chapter 6).

The key finding from the previous chapter, investigating the Ti-V-Mn system, was that small (0.05 at%) changes in composition resulted in different unit cell volumes of C14 Laves and BCC phases. It was therefore decided to use only small amounts of elemental substitution in experimental trials. Alloys with following compositions were synthesised:

- $Ti_{0.5}V_{0.4}Nb_{0.1}Mn$ (Nb = 0.1)

- $Ti_{0.5}V_{0.4}Cr_{0.1}Mn$ (Cr = 0.1)

- $Ti_{0.5}V_{0.4}Mo_{0.1}Mn$ (Mo = 0.1)

- $Ti_{0.5}V_{0.4}Ta_{0.1}Mn$ (Ta = 0.1)

Elemental Ti, V, Nb, Cr, Mo and Ta and Mn (Sigma Aldrich: ≥ 99.7% purity, see Chapter 6) was weighed out into the mole ratios shown below. The following table represents the calculations involved in producing 10g samples. An extra one percent of Mn was added to compensate for Mn losses during arc-melting.

Table 8.1 Calculations used to make up 10g $Ti_{0.5}V_{0.4}TM_{0.1}Mn$ samples. Note: TM = transition metal (Nb, Cr, Mo and Ta).

Mole Ratio	at%				Molecular Weight	wt%				Weight (g)			
	Ti	V	TM	Mn		Ti	V	TM	Mn	Ti	V	TM	Mn
Nb = 0.1	0.25	0.2	0.05	0.5	54.27	22.06	18.77	8.56	50.62	2.21	1.88	0.86	5.06
Cr = 0.1	0.25	0.2	0.05	0.5	52.23	22.92	19.51	4.98	52.59	2.29	1.95	0.50	5.31
Mo = 0.1	0.25	0.2	0.05	0.5	54.43	21.99	18.72	8.82	50.47	2.2	1.87	0.88	5.1
Ta = 0.1	0.25	0.2	0.05	0.5	58.68	20.40	17.37	15.42	46.81	2.04	1.74	1.54	4.73

Note, Table 8.1 shows the target composition for the $Ti_{0.5}V_{0.4}TM_{0.1}Mn$ alloys but the alloys synthesised vary in composition (as shown by the EDS Results).

8.2 Characterisation of As-Cast Alloys

The as-cast alloys were characterised by SEM/EDS and XRD to investigate microstructure and composition after arc-melting.

8.2.1 SEM/EDS on As-Cast Alloys

Figures 8.1- 8.12 show BEI images of cross-sections of as-cast Nb = 0.1, Cr = 0.1, Mo = 0.1 and Ta = 0.1 at low (x 500) and high (x 1000) magnifications.

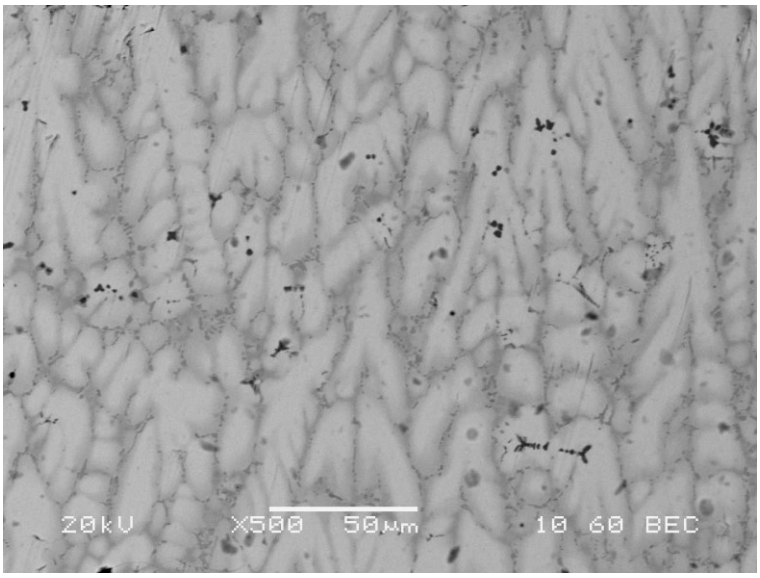

Figure 8.1 SEM BEI image of as-cast Nb = 0.1 (x 500).

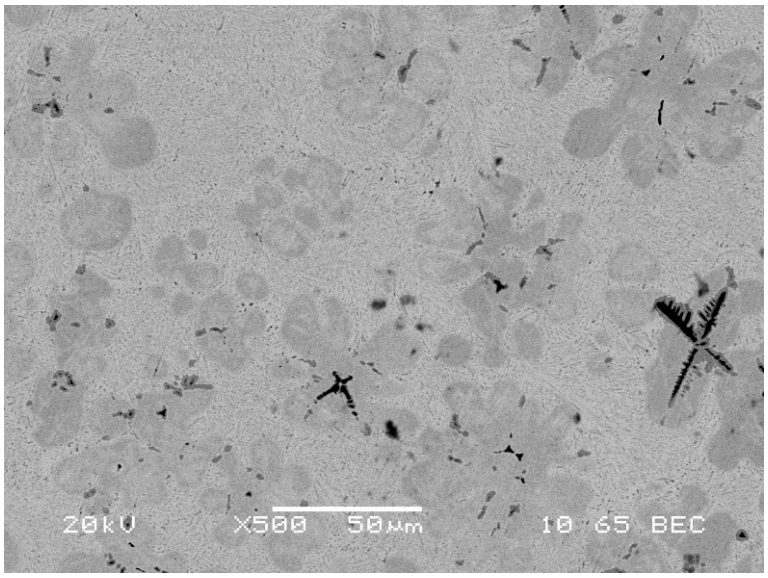

Figure 8.2 SEM BEI image of as-cast Cr = 0.1 (x 500).

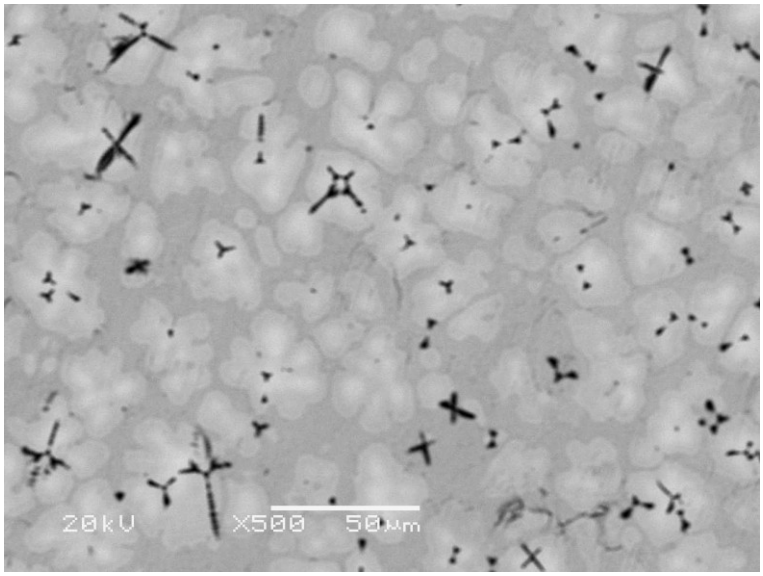

Figure 8.3 SEM BEI image of as-cast Mo = 0.1 (x 500).

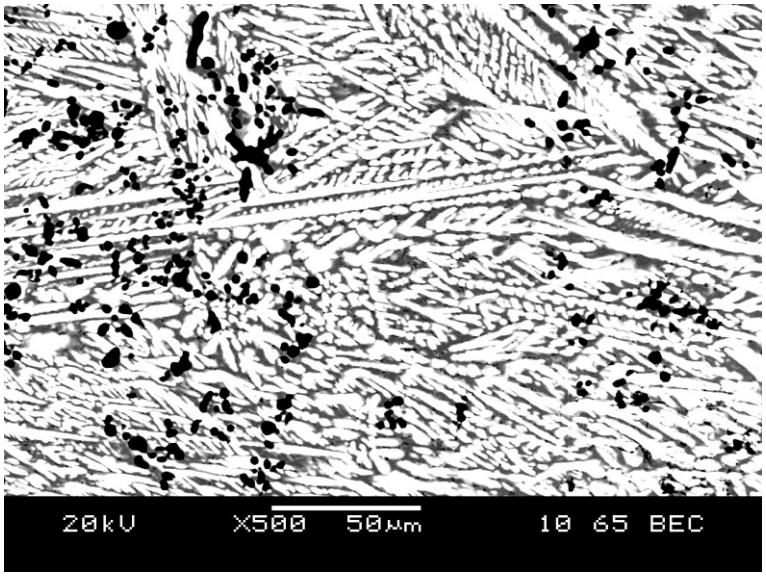

Figure 8.4 SEM BEI image of as-cast Ta = 0.1 (x 500).

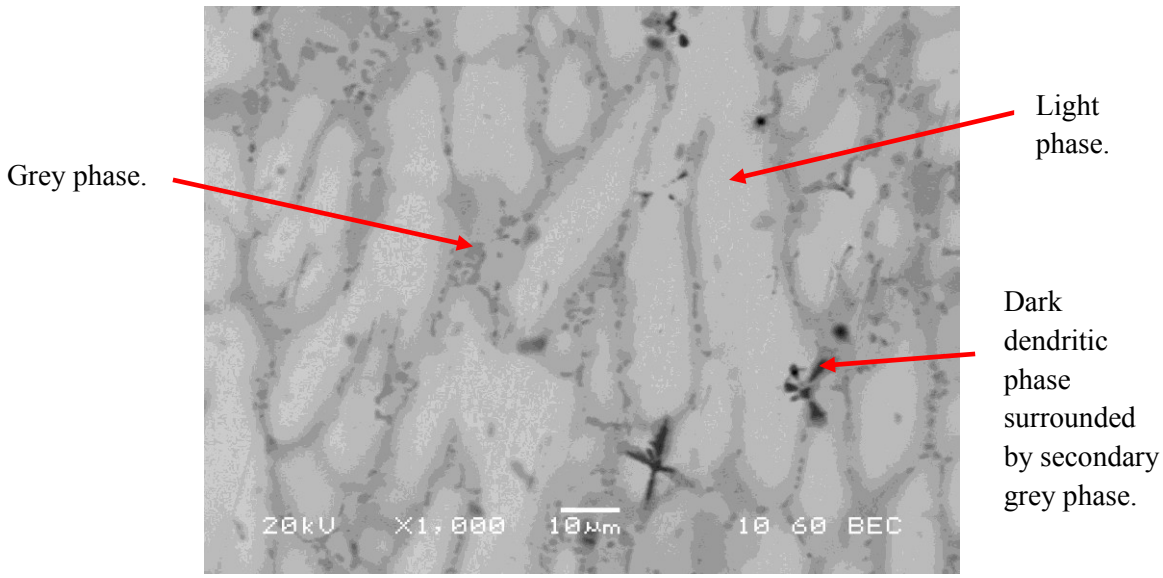

Figure 8.5 SEM BEI image of as-cast Nb = 0.1 (x 1000).

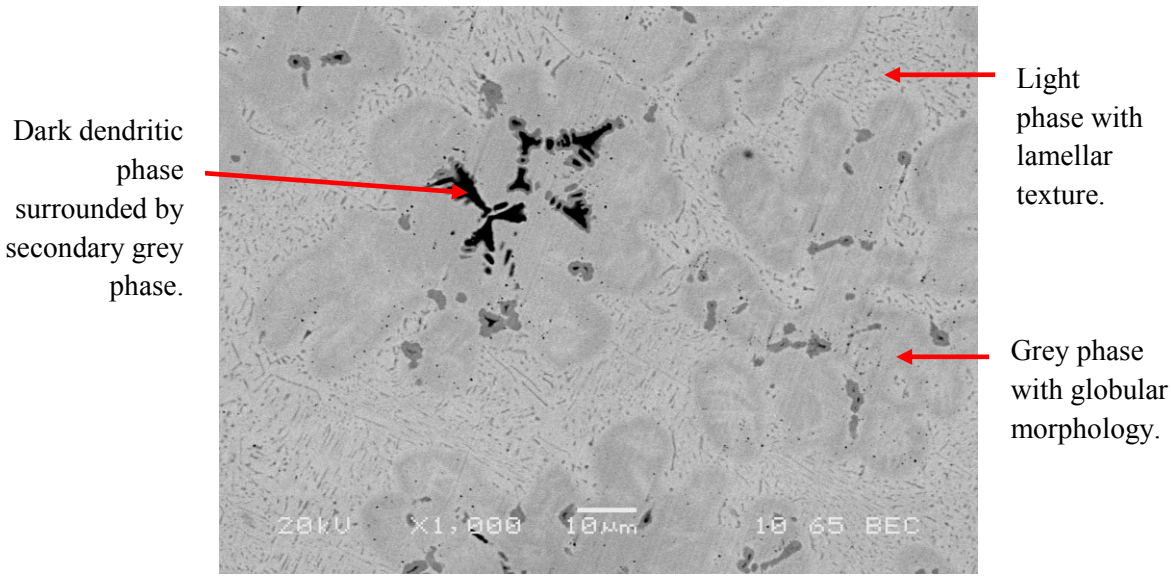

Figure 8.6 SEM BEI image of as-cast Cr = 0.1 (x 1000).

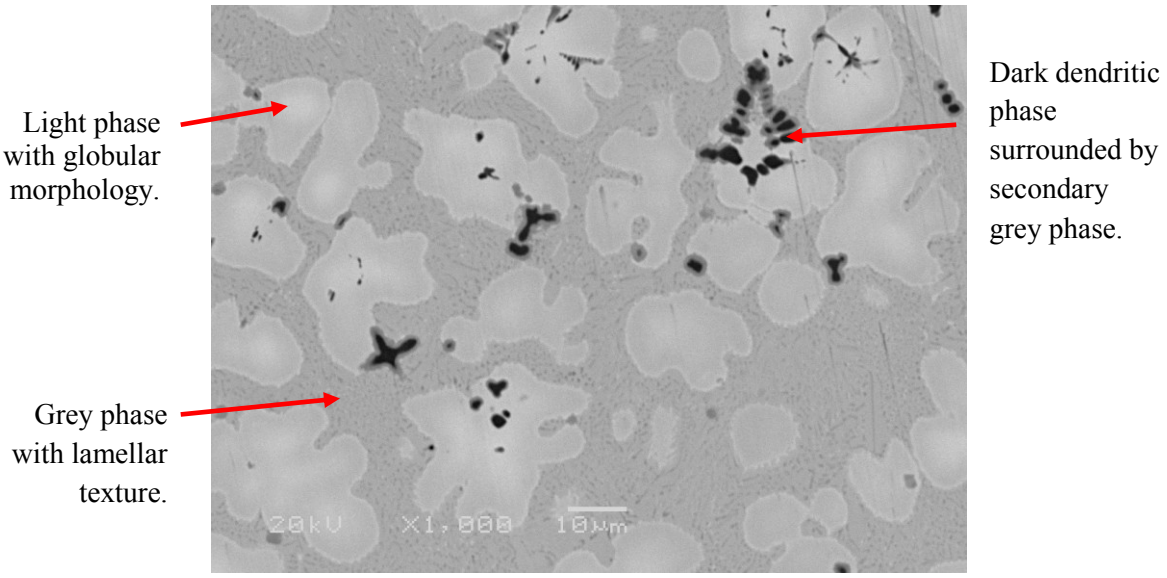

Figure 8.7 SEM BEI image of as-cast Mo = 0.1 (x 1000).

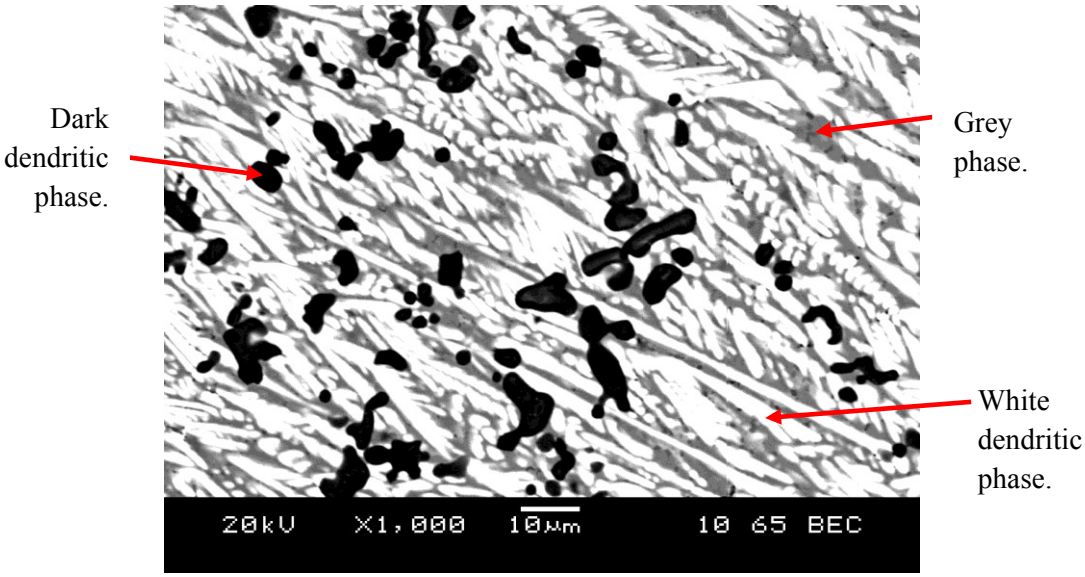

Figure 8.8 SEM BEI image of as-cast Ta = 0.1 (x 1000).

Different microstructures can be seen in the micrographs shown in Figures 8.1 – 8.8. In comparing Nb = 0.1, Cr = 0.1, Mo = 0.1 and Ta = 0.1 substitutions for V, three microstructural phases can be identified in varying amounts: a light/white phase, grey phase and dark dendritic phase. Furthermore, in all four alloys coring is observed which suggests that solidification may have occurred at different rates within the alloys.

In Nb = 0.1 the micrograph shows the light phase is the most dominant phase in the alloy. The grey phase is present around the outside of the grains, inside which the dark dendritic and secondary grey phase occurs. The shape of the grains shows the direction of the cooling which appears to be consistent in both the low and high magnification images.

In Cr = 0.1 the grey phase has a globular morphology, inside which the dark dendritic phase and secondary grey phase is present. From the high magnification image you can see where nucleation has started to occur by the small dark phase regions.

In Mo = 0.1 it is the light phase which has a globular morphology and the dark dendritic phase and secondary grey phase occur inside both the light and grey phase. In addition, the grains have a consistent size and seem to be equally distributed in the micrograph.

At high magnification, a lamellar texture is observed in the micrographs of Cr = 0.1 and Mo = 0.1. This indicates a eutectic reaction may have occurred in which the metal transforms into two different solid phases during cooling.

In Ta = 0.1 the white phase is dendritic and presents itself much more prominently, along with what appears to be a secondary dark dendritic phase and grey phase. The dark spots could be where the dendrites are starting to grow or they may be defects from the arc-melting process: Ti is the lightest element within the alloy (which results in a dark appearance) so this may be small amounts of un-reacted Ti. At high magnification, the white phase appears to be going in one direction whereas the low magnification image shows this phase in different directions. This indicates that the solidification upon cooling has occurred in different directions.

These differences in microstructure are due to the different atomic mass of the transition metal substitutions: Nb is 92.91, Cr is 52, Mo is 95.94 and Ta is 180.95 and amu's. Ta is a

much heavier element which results in different interactions with electrons when using SEM, and why the micrographs appear significantly brighter in contrast.

The composition of the as-cast alloys was confirmed by EDS analysis, the results of which are displayed in Table 8.2. It should be noted that the results shown are in atomic percent (at %).

Table 8.2 Average EDS analysis on as-cast Nb = 0.1, Cr = 0.1, Mo = 0.1 and Ta = 0.1 with standard deviation associated with mean values. Note analysis was carried out by taking an average of three different areas/points within BEI images of the alloys.

Alloy	Phase Location	Ti	σ	V	σ	TM	σ	Mn	σ	Average Composition Ratio (Ti/V/TM/Mn)
As-cast Nb = 0.1	Area	26.58	6.1	20.63	6.3	4.12	6.3	48.67	6.5	0.55/0.42/0.08/1
	Light	24.35	6.8	18.87	7.3	5.26	7.4	51.52	7.5	0.47/0.37/0.1/1
	Grey	21.87	7.6	35.24	7.2	0.98	7.7	41.91	6.9	0.52/0.84/0.02/1
	Dark	65.38	6.3	8.59	6.6	1.84	6.5	24.19	6.2	2.70/0.36/0.08/1
As-cast Cr = 0.1	Area	25.98	6.6	20.79	6.2	5.14	6.9	48.09	7.1	0.54/0.43/0.11/1
	Light	30.03	6.9	13.42	7.3	4.87	7.5	51.68	7.8	0.58/0.26/0.09/1
	Grey	17.41	7.6	30.67	7.1	6.3	6.8	45.62	6.3	0.38/0.67/0.14/1
	Dark	87.23	7.2	4.07	6.8	0.77	6.9	7.93	7.1	11/0.51/0.1/1
As-cast Mo = 0.1	Area	27.80	7.4	21.35	6.3	3.97	7.6	46.88	7.4	0.59/0.46/0.08/1
	Light	21.89	6.8	29.16	6.4	7.54	6.1	41.41	7.2	0.53/0.70/0.18/1
	Grey	31.87	7.6	14.22	6.9	1.21	7.5	52.4	7.1	0.61/0.27/0.02/1
	Dark	85.2	6.8	4.45	6.9	0.37	6.4	9.98	6.1	8.54/0.45/0.04/1
As-cast Ta = 0.1	Area	30.21	7.5	20.79	7.1	4.15	6.8	44.85	6.3	0.67/0.46/0.09/1
	Light	17.67	7.1	20.52	7.9	11.85	7.3	49.96	7.5	0.35/0.41/0.24/1
	Grey	22.71	6.8	30.81	7.1	0.48	7.3	46	7.3	0.49/0.67/0.01/1
	Dark	91.47	7.6	3.68	7.2	0.49	6.8	4.36	7.6	20.98/0.84/0.11/1

The area analysis shows that the average composition for as-cast Nb = 0.1 is $Ti_{0.55}V_{0.42}Nb_{0.08}Mn_1$, Cr = 0.1 is $Ti_{0.54}V_{0.43}Cr_{0.11}Mn_1$, Mo = 0.1 is $Ti_{0.59}V_{0.46}Mo_{0.08}Mn_1$ and Ta = 0.1 is $Ti_{0.67}V_{0.46}Ta_{0.09}Mn_1$. This shows that all the alloys are close to the target compositions.

In Nb = 0.1, when comparing the composition taken from the area average, the light phase appears to be richer in Mn (48.67 vs. 51.52 at%), the grey phase richer in V (20.63 vs. 35.24 at%) and the dark phase rich in Ti (26.58 vs. 65.38 at%). Mn is a heavy element (54.94 amu) and Ti is a relatively light element (47.87 amu) which is why these elements are present in greater amounts in the light and dark phase.

In the Cr = 0.1 alloy, when comparing the composition from the average area the light phase appears to be richer in Ti (25.98 vs. 30.03 at%), the grey phase richer in V (20.79 vs. 87.23 at%) and the dark phase rich in Ti (25.98 vs. 87.23 at%).

In the Mo = 0.1 alloy, when comparing the composition from the average area the light phase appears to be richer is V (21.35 vs. 29.16 at%), the grey phase richer in Mn (46.88 vs. 52.4 at%) and the dark phase rich in Ti (27.80 vs. 91.47 at%).

In the Ta = 0.1 alloy, when comparing the composition from the average area the light phase appears to be richer in Ta (4.15 vs. 11.85 at%), the grey phase richer in V (20.79 vs. 30.81 at%) and the dark phase rich in Ti (30.21 vs. 91.47 at%). As previously discussed Ta is the heaviest element which is why the light/white phase appears significantly brighter in the micrographs.

8.2.2 XRD on As-Cast Alloys

Figure 8.9 shows XRD patterns of as-cast Nb = 0.1 (top, black), Cr = 0.1 (middle, red), Mo = 0.1 (middle, green) and Ta = 0.1 (blue, bottom) with the peaks indexed. Appendix C shows individual XRD traces of the as-cast alloys, showing the observed pattern and calculated fit after pseudo-Rietveld refinement.

The XRD analysis performed on as-cast alloys shows the presence of three phases in all samples that were identified as:

- C14 Laves phase (hexagonal $MgZn_2$ structure with space group *P63/mmc*).
- BCC phase (space group *Im-3m).*
- FCC oxide phase (space group *Fd-3m).*

Refinement of the structures are based on those proposed for the C14 Laves phase by Mitrokhin et al., (2003) and the BCC and FCC oxide by Hout et al., (1995). Table 8.3 shows crystal structure refinement results for as-cast Nb = 0.1, Cr = 0.1, Mo = 0.1 and Ta = 0.1.

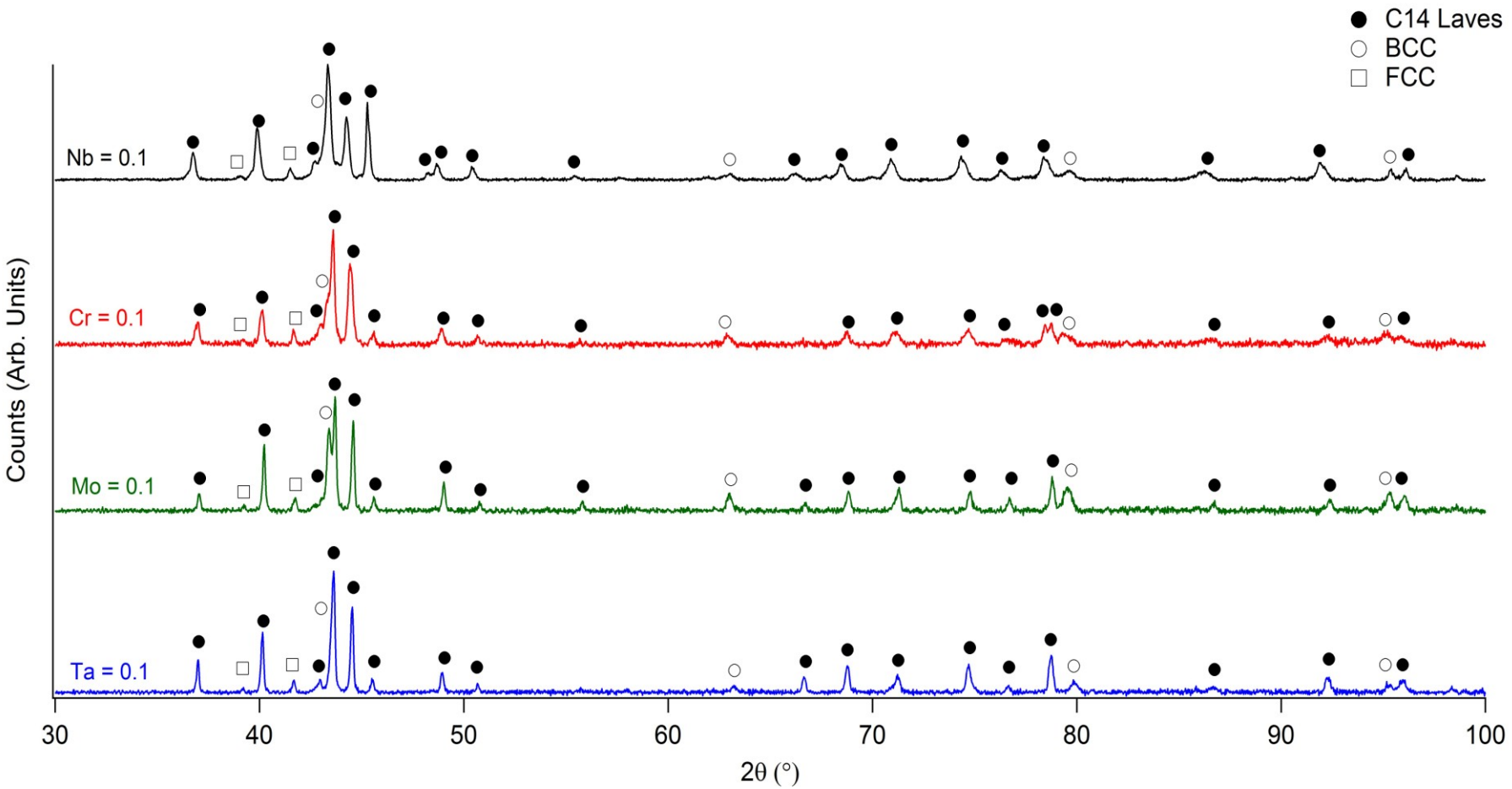

Figure 8.9 XRD patterns of as-cast Nb = 0.1 (top, black), Cr = 0.1 (middle, red), Mo = 0.1 (middle, green) and Ta = 0.1 (bottom, blue) with peaks indexed.

Table 8.3 Crystal structure refinement results for as-cast Nb = 0.1, Cr = 0.1, Mo = 0.1 and Ta = 0.1, showing lattice parameters and phase abundance. Note the values in parentheses are three standard deviations and refer to the last digit.

Alloy	As-cast			
	Phase	Lattice Parameters		Abundance
Nb = 0.1	C14	*a*	4.876(4)	74(2)
		c	7.992(7)	
	BCC	*a* + *c*	2.952(2)	19(9)
	FCC	*a* + *c*	11.283(6)	7(6)
Cr = 0.1	C14	*a*	4.868(3)	65(5)
		c	7.971(5)	
	BCC	*a* + *c*	2.954(2)	30(5)
	FCC	*a* + *c*	11.261(5)	5(3)
Mo = 0.1	C14	*a*	4.861(3)	62(3)
		c	7.964(2)	
	BCC	*a* + *c*	2.952(5)	31(4)
	FCC	*a* + *c*	11.262(2)	7(3)
Ta = 0.1	C14	*a*	4.859(2)	76(5)
		c	7.967(5)	
	BCC	*a* + *c*	2.939(2)	18(4)
	FCC	*a* + *c*	11.258(2)	6(3)

The C14 Laves phase appears to be the dominant phase in all three as-cast alloys occupying; 74 wt% in Nb = 0.1, 65 wt% in Cr = 0.1, 62 wt% in Mo = 0.1 and 76 wt% in Ta = 0.1.

The difference in phase abundance of the as-cast alloys is related to the different outer shell electron configurations and subsequent atomic number. The atomic number of Nb is 41, Cr is 24, Mo is 42 and Ta is 73. This difference may result in different atomic scattering factors.

The C14 Laves unit cell volumes for the as-cast alloys are: Nb = 0.1 is 164.54(6) $Å^3$, Cr = 0.1 is 165.53(7) $Å^3$, Mo = 0.1 is 163.02(6) $Å^3$ and Ta = 0.1 is 162.93(2) $Å^3$.

The differences observed in the unit cell volumes for the C14 Laves phase are due to the difference in atomic radii of the transition metal elements. The atomic radius of Nb is 1.46 Å, Cr is 1.28 Å, Mo is 1.39 Å and Ta is 1.46 Å.

Similar unit cell volumes can be seen for the BCC phase in the as-cast alloys: Nb = 0.1 is 25.73(8) $Å^3$, Cr = 0.1 is 25.77(5) $Å^3$, Mo = 0.1 is 25.71(2) $Å^3$ and Ta = 0.1 is 25.4(6) $Å^3$. It would therefore appear that the BCC phase is not as sensitive to changes in composition as the C14 Laves phase.

Based on the XRD analysis and the phases identified during SEM analysis, these results indicate that in Nb = 0.1 and Cr = 0.1 the light area, which appears to be the dominant phase in the micrographs, corresponds to the C14 Laves phase, the grey phase corresponds to the BCC phase and the minor FCC phase appears as the dark dendritic phase. In Mo = 0.1 the grey phase is the dominant phase which suggests that this is the C14 Laves phase, the light phase corresponds to the BCC phase and the dark dendritic phase is the FCC phase. In Ta = 0.1 the light dendritic phase is the dominant phase so that is most likely to correspond to the C14 Laves phase, the BCC corresponds to the grey phase and the dark phase the FCC phase.

8.3 Characterisation of Heat Treated Alloys

The alloys were characterised after heat treatment to confirm composition and to ensure the alloys were fully homogenous.

8.3.1 SEM/EDS on Heat Treated Alloys

Figures 8.10 – 8.17 show BEI images of heat treated Nb = 0.1, Cr = 0.1, Mo = 0.1 and Ta = 0.1 at low (x 500) and high (x 1000) magnification.

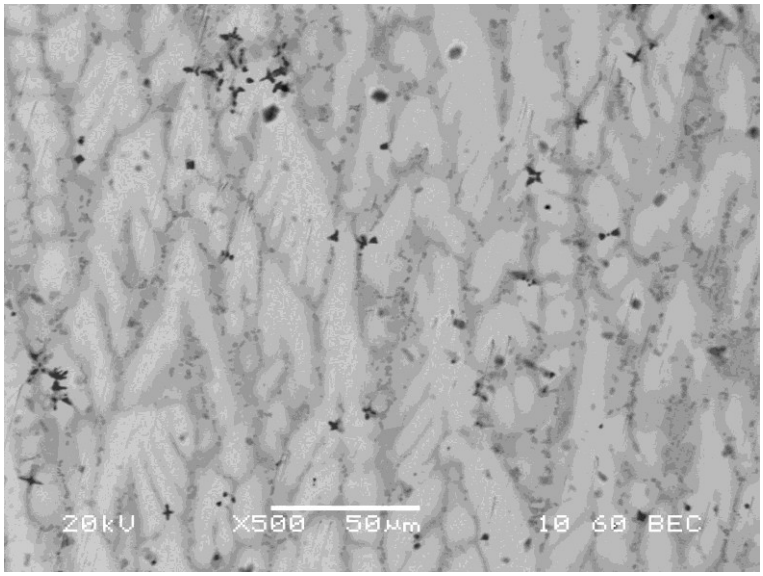

Figure 8.10 SEM BEI image of heat treated Nb = 0.1 (x 500).

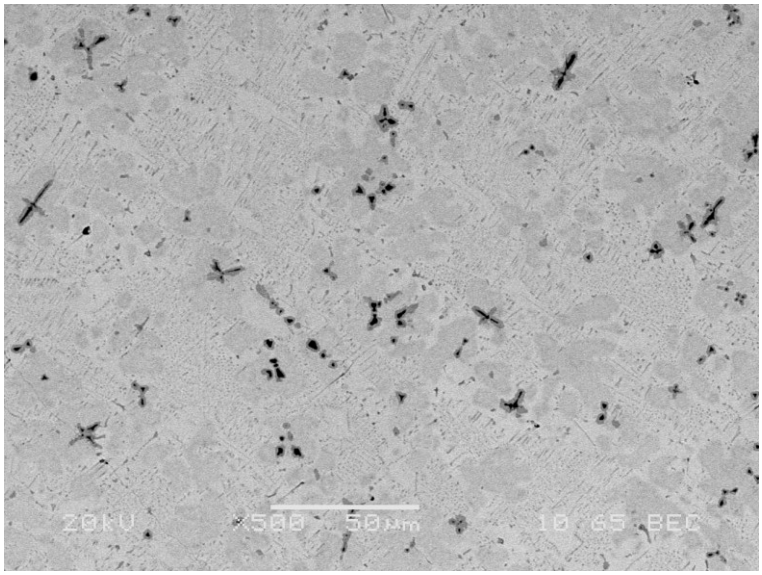

Figure 8.11 SEM BEI image of heat treated Cr = 0.1 (x 500).

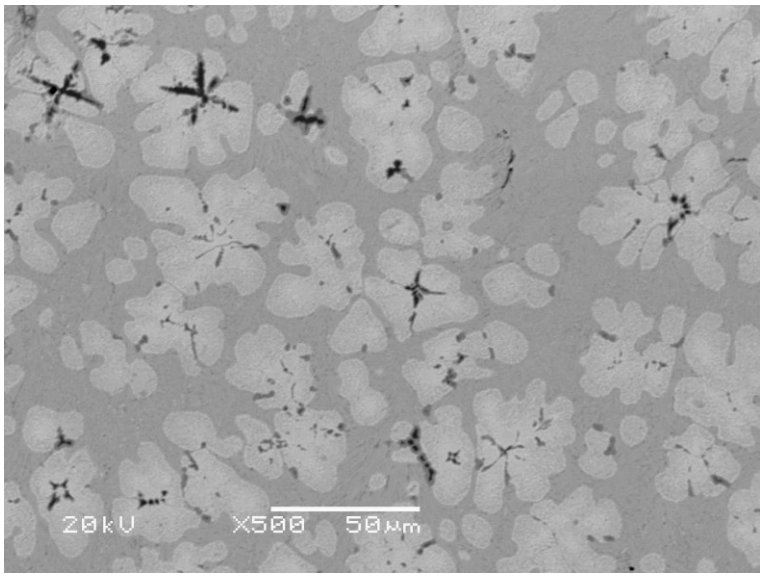

Figure 8.12 SEM BEI image of heat treated Mo = 0.1 (x 500).

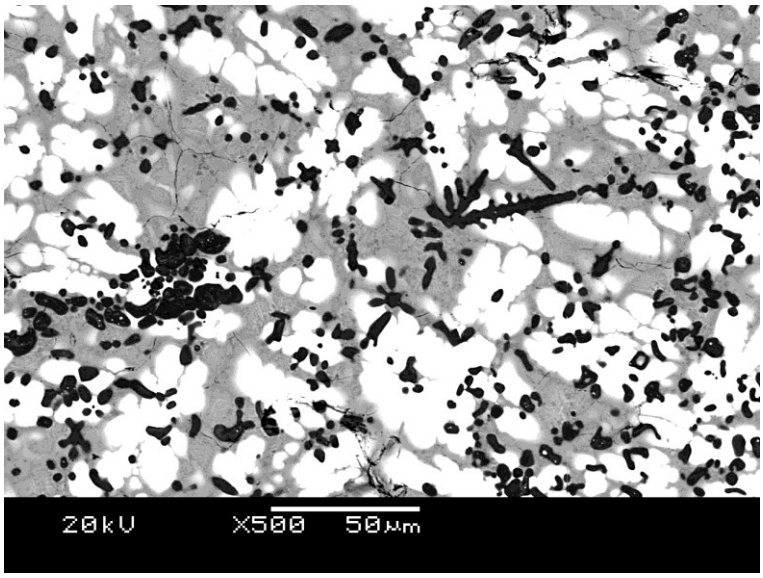

Figure 8.13 SEM BEI image of heat treated Ta = 0.1 (x 500).

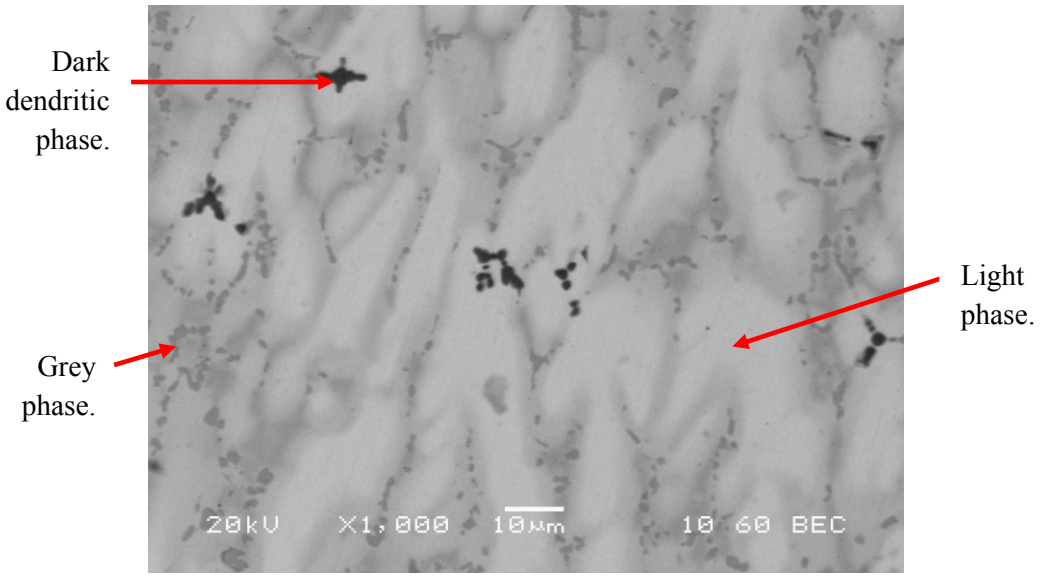

Figure 8.14 SEM BEI image of heat treated Nb = 0.1 (x 1000).

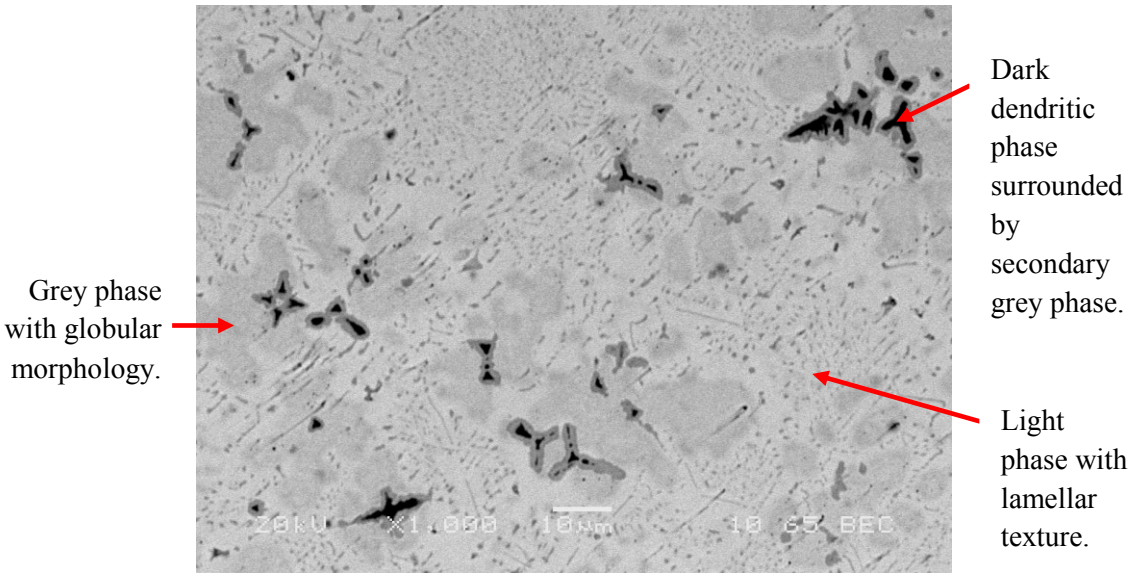

Figure 8.15 SEM BEI image of heat treated Cr = 0.1 (x 1000).

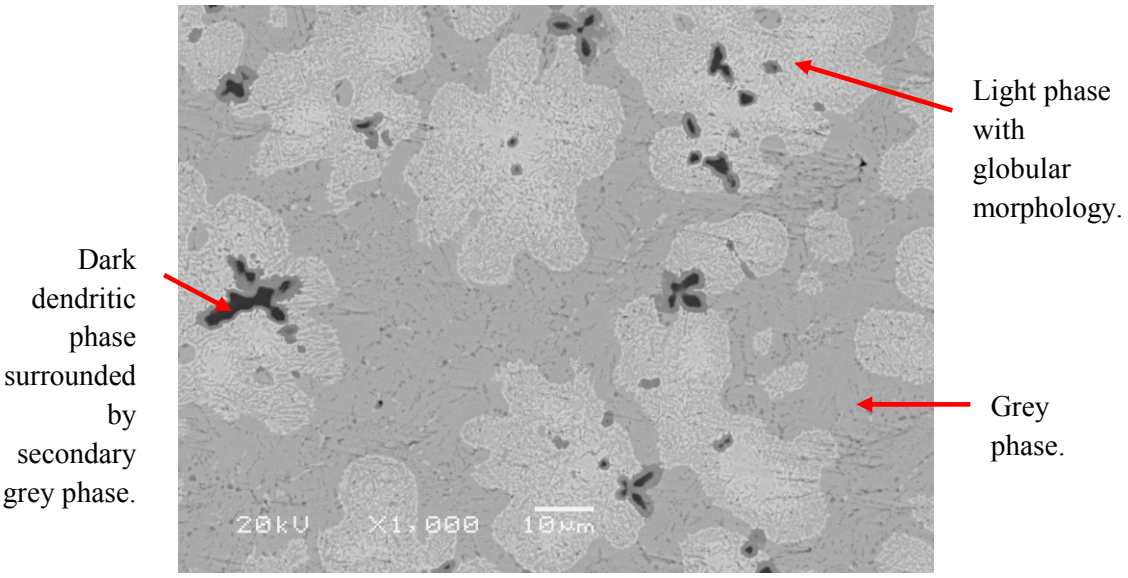

Figure 8.16 SEM BEI image of heat treated Mo = 0.1 (x 1000).

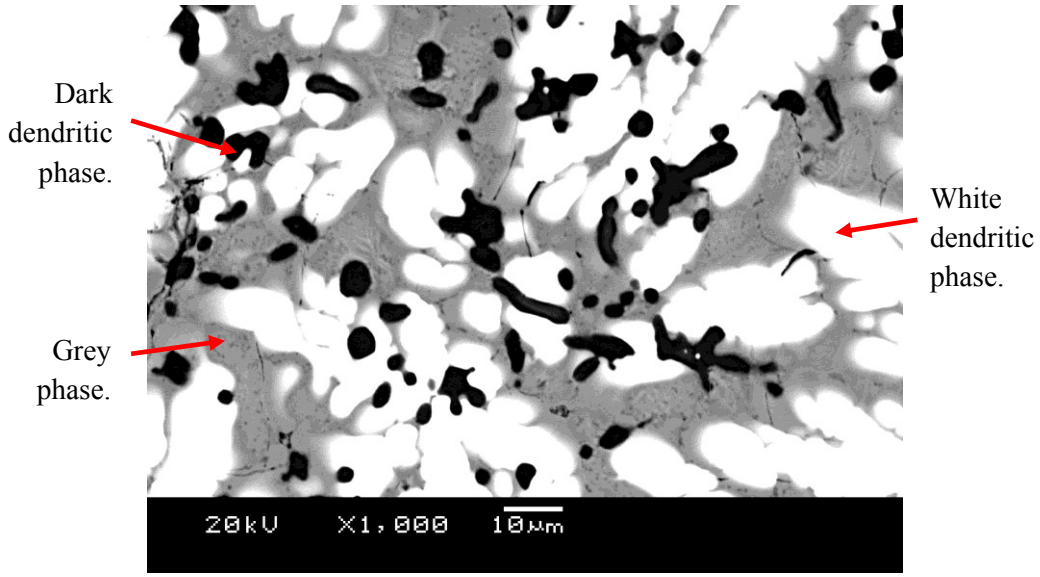

Figure 8.17 SEM BEI image of heat treated Ta = 0.1 (x 1000).

In Figures 8.10 – 8.17 similar microstructures are observed to the as-cast alloys, with light, grey and dark dendritic phases present in all four alloys. There does still appear to be coring present in the high magnification images of Nb = 0.1, Cr = 0.1 and Mo = 0.1 which suggests that longer heat treatment times are required in order to fully homogenise the alloys.

EDS analysis was performed on the heat treated alloys, with the results shown in Table 8.4. It should be noted that the results shown are in atomic percent (at %).

Table 8.4 Average EDS analysis on heat treated Nb = 0.1, Cr = 0.1, Mo = 0.1 and Ta = 0.1 with standard deviation associated with mean values. Note analysis was carried out by taking an average of three different areas/points within BEI images of heat treated alloys.

Alloy	Phase Location	Ti	σ	V	σ	TM	σ	Mn	σ	Average Composition Ratio (Ti/V/TM/Mn)
Heat treated Nb = 0.1	Area	27.08	6.8	20.33	7.2	4.38	7.3	48.21	6.5	0.56/0.42/0.09/1
	Light	23.8	7.1	18.3	6.7	7.67	6.3	50.27	6.5	0.47/0.36/0.15/1
	Grey	20.14	6.5	35.81	7.4	1.01	7.8	43.04	7.1	0.47/0.83/0.02/1
	Dark	61.57	6.2	10.37	6.7	2.71	6.1	25.35	6.9	2.43/0.41/0.11/1
Heat treated Cr = 0.1	Area	26.49	7.2	20.29	6.3	5.13	6.8	48.09	6.3	0.55/0.42/0.11/1
	Light	29.57	6.5	13.86	6.8	4.61	7.2	51.98	7.5	0.57/0.27/0.09/1
	Grey	17.85	6.8	30.33	7.1	6.29	7.3	45.53	6.9	0.38/0.67/0.14/1
	Dark	89.81	6	3.25	6.3	0.51	6.8	6.43	7.1	13.97/0.51/0.08/1
Heat treated Mo = 0.1	Area	27.21	7.6	21.67	7.2	4.18	6.8	46.94	6.9	0.58/0.46/0.09/1
	Light	21.5	6.5	29.95	6.3	8.37	7.1	40.18	6.8	0.54/0.75/0.21/1
	Grey	31.57	6.3	14.45	7.2	1.56	7.5	52.42	7.6	0.6/0.28/0.03/1
	Dark	87.74	6.8	4.37	6.2	0.22	6.4	7.67	7.3	11.4/0.57/0.03/1
Heat treated Ta = 0.1	Area	29.08	7.6	21.95	7.1	4.44	7.5	44.53	7.6	0.65/0.49/0.1/1
	Light	16.72	6.5	21.27	6.7	13.05	7.8	48.96	6.6	0.34/0.43/0.27/1
	Grey	23.48	7.2	29.49	7.7	0.59	7.6	46.44	6.9	0.51/0.64/0.01/1
	Dark	95.16	6.5	3.01	6.8	0.87	6.9	0.96	7.1	99.19/3.15/0.91/1

The area analysis shows that the average composition for heat treated Nb = 0.1 is $Ti_{0.56}V_{0.42}Nb_{0.09}Mn_1$, Cr = 0.1 is $Ti_{0.55}V_{0.42}Cr_{0.11}Mn_1$, Mo = 0.1 is $Ti_{0.58}V_{0.46}Mo_{0.09}Mn_1$ and Ta = 0.1 is $Ti_{0.65}V_{0.49}Ta_{0.1}Mn_1$.

In Nb = 0.1, the light phase is slightly richer in Nb (4.38 vs. 7.67 at%), grey phase richer in V (20.33 vs. 35.81 at%) and dark dendritic phase is rich in Ti (27.08 vs. 61.57 at%).

In Cr = 0.1, the light phase is slightly richer in Ti (26.49 vs. 29.57 at%), grey phase is richer in V (20.29 vs. 30.33 at%) and dark dendritic phase is richer in Ti (26.49 vs. 89.81 at%).

In Mo = 0.1, the light phase is richer in V (21.67 vs. 29.95 at%) and Mo (4.18 vs. 8.37 at%), grey phase is richer in Mn (46.94 vs. 52.42 at%) and the dark dendritic phase is richer in Ti (27.21 vs. 87.74 at%).

Finally, in Ta = 0.1, the light phase is richer in Ta (4.44 vs. 13.05 at%), grey phase is richer in V (21.95 vs. 29.49 at%) and the dark phase is richer in Ti (29.08 vs. 95.16 at%).

8.3.2 XRD on Heat Treated Alloys

Figure 8.18 shows XRD patterns of heat treated Nb = 0.1 (top, black), Cr = 0.1 (middle, red), Mo = 0.1 (middle, green) and Ta = 0.1 (bottom, blue) after pseudo-Rietveld refinement with the peaks indexed. The same three phases are identified in all the heat treated alloys. Appendix C shows individual XRD traces of the heat treated alloys, showing the observed pattern and calculated fit after pseudo-Rietveld refinement.

Table 8.5 shows crystal structure refinement results for the heat treated alloys.

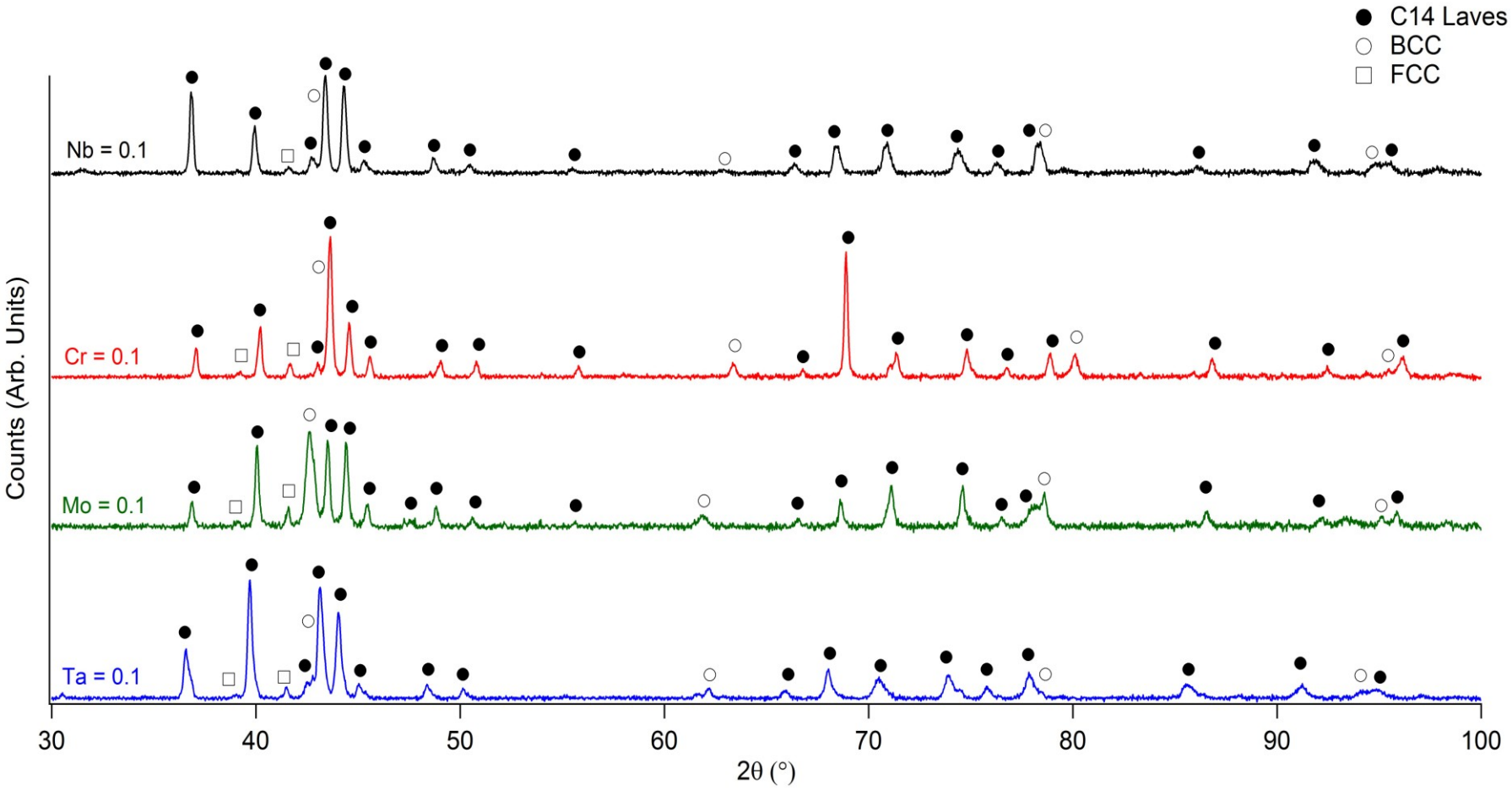

Figure 8.18 XRD patterns of heat treated Nb = 0.1 (top, black), Cr = 0.1 (middle, red), Mo = 0.1 (middle, green) and Ta = 0.1 (bottom, blue) with peaks indexed.

Table 8.5 Crystal structure refinement results for heat treated alloys (values on right) in comparison to as-cast alloys. Note the values in parentheses are three standard deviations and refer to the last digit.

Alloy	As-Cast				Heat Treated			
	Phase	Lattice Parameters		Abundance	Phase	Lattice Parameters		Abundance
Nb = 0.1	C14	a	4.876(4)	74(2)	C14	a	4.883(2)	81(8)
		c	7.992(7)			c	8.004(4)	
	BCC	a + c	2.952(2)	19(9)	BCC	a + c	2.963(2)	13(6)
	FCC	a+ c	11.283(6)	7(6)	FCC	a+ c	11.268(6)	6(4)
Cr = 0.1	C14	a	4.868(3)	65(5)	C14	a	4.850(3)	67(9)
		c	7.971(5)			c	7.951(6)	
	BCC	a + c	2.954(2)	30(5)	BCC	a + c	2.933(2)	24(4)
	FCC	a+ c	11.261(5)	5(3)	FCC	a+ c	11.248(9)	9(7)
Mo = 0.1	C14	a	4.861(3)	62(3)	C14	a	4.864(7)	62(3)
		c	7.964(2)			c	7.969(3)	
	BCC	a + c	2.952(5)	31(4)	BCC	a + c	2.993(5)	31(2)
	FCC	a+ c	11.262(2	7(3)	FCC	a+ c	11.264(4)	7(2)
Ta = 0.1	C14	a	4.859(2)	76(5)	C14	a	4.899(4)	90(11)
		c	7.967(5)			c	8.030(7)	
	BCC	a + c	2.939(2)	18(4)	BCC	a + c	2.945(3)	6(4)
	FCC	a+ c	11.258(2)	6(3)	FCC	a+ c	11.280(9)	4(5)

Again, the C14 Laves phase appears to be the dominant phase in all five heat treated alloys occupying; 81 wt% in Nb = 0.1, 67 wt% in Cr = 0.1, 62 wt% in Mo = 0.1 and 90 wt% in Ta = 0.1.

The unit cell volumes of the C14 Laves phase in the heat treated alloys are 165.40(9) $Å^3$ in Nb = 0.1, 162.01(4) $Å^3$ in Cr = 0.1, 163.27(9) $Å^3$ in Mo = 0.1 and 166.89(8) $Å^3$ in Ta = 0.1.

In relation to the as-cast alloys, this shows an increase in unit cell volume of between 0.25 and 3.96 $Å^3$ for Nb = 0.1, Mo = 0.1 and Ta = 0.1 and a decrease of 3.52 $Å^3$ in Cr = 0.1.

There is also a small change in the unit cell volume of the BCC phase in the heat treated alloys: Nb = 0.1 increases slightly to 25.87(4) $Å^3$, Cr = 0.1 decreases to 25.23(5) $Å^3$, Mo = 0.1 increases to 26.82(4) $Å^3$ and Ta = 0.1 increases slightly to 25.54(3) $Å^3$.

The difference in metallic radii of the transition metal elements indicates that different substitutions of the B-site V, TM and Mn elements have taken place. Figure 8.19 shows the metallic radii of the different elements which could potentially be found within the B-site of the C14 Laves and BCC phase unit cell in the Ti-V-TM-Mn system.

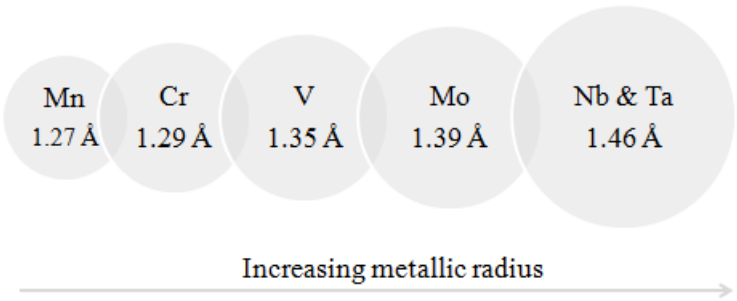

Figure 8.19 Metallic Radii of elements in B-site of C14 Laves phase unit cell in Ti-V-TM-Mn system.

Looking at the difference in composition (at%) of the C14 Laves phase and BCC phase between the as-cast and heat treated alloys from the EDS data it is possible to calculate which elements have increased or decreased. This gives an indication to which substitutions have taken place within in the respective unit cell after heat treatment. This information can then be used along with the metallic radii information to see which elemental substitutions have taken place. The calculations used to show which elemental substitutions have taken place are shown in Appendix C.

In Nb = 0.1 there is an increase in the C14 Laves unit cell volume as a result of substitution of 3 Nb atoms for 2 Mn atoms and 1 V atom. This can be attributed to Nb have a larger metallic radius than Mn and V. The increase in C14 Laves phase unit cell volume in Mo = 0.1 can be attributed to substitution of 1 V atom and 1 Mo atom for 2 Mn atoms. In Ta = 0.1 there is an increase in the C14 unit cell volume as a result of substitution of 1 V atom and 1 Ta atom for 2 Mn atoms.

In Cr = 0.1 there does not appear to be any significant differences in the composition of the light C14 Laves phase between the as-cast and heat treated alloy. This indicates that the reduction in C14 Laves unit cell volume may not be due to substitution but in fact an ordering effect on the B-site (Mn, V) *6h* site upon annealing. In addition, the XRD pattern shows an increase in the intensity of the peak occurring along the (123) plane at 68.5 2θ which results in an increase in *c* and *a* lattice parameters.

There is no significant change in the composition of the grey BCC phase between the as-cast and heat treated alloys. This means that elemental substitution has not taken place within the BCC phase and the difference in unit cell volumes after heat treatment is also a result of ordering effects of the B-site upon annealing.

8.4 Characterisation of Hydrogen Sorption Properties

8.4.1 PCT Measurements

HTP measurements were performed at 303 K, 313 K and 323 K up to 120 bar H_2 for Nb = 0.1, Cr = 0.1, Mo = 0.1 and Ta = 0.1 (Figures 8.20, 8.21, 8.22 and 8.23 respectively). For the measurements, 610 mg of Nb = 0.1, 660 mg of Cr = 0.1, 713 mg of Mo = 0.1 and

705 mg of Ta = 0.1 was loaded. Prior to measurements, an activation sequence was performed on all the heat treated alloys (see Project Experimental in Chapter 6). The isotherms shown are therefore the 2nd, 3rd, 4th and 5th cycle at 303 K, 313 K, 323 K and 333 K, respectively.

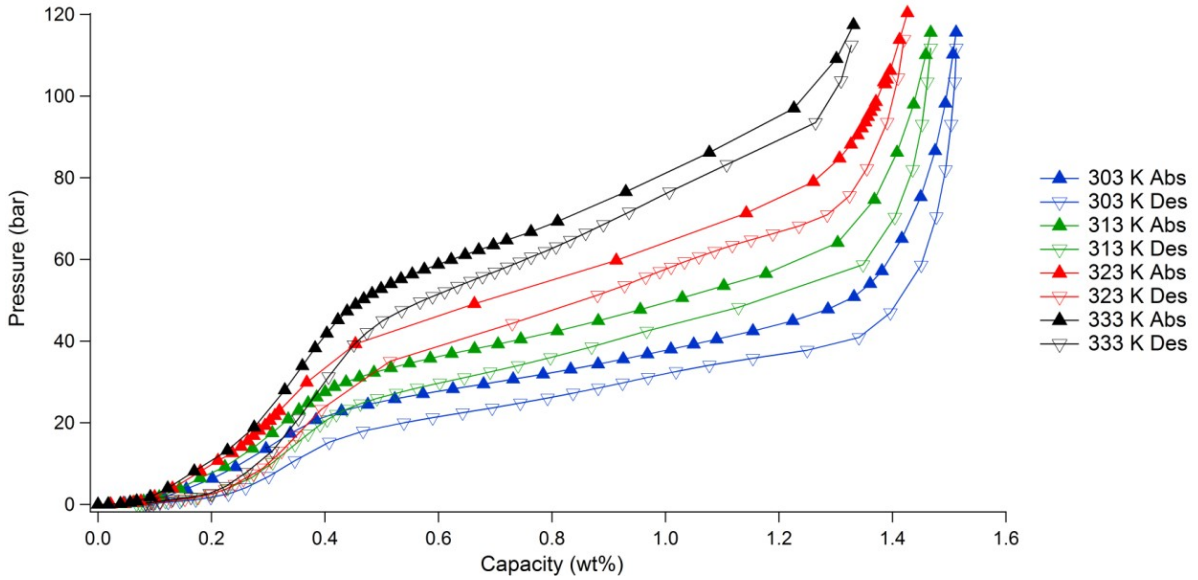

Figure 8.20 PCT measurement of Nb = 0.1 at 303 K (blue), 313 K (green), 323 K (red) and 333 K (black) showing absorption (upwards triangles) and desorption (downwards triangles) from 0.5 to 120 bar H_2.

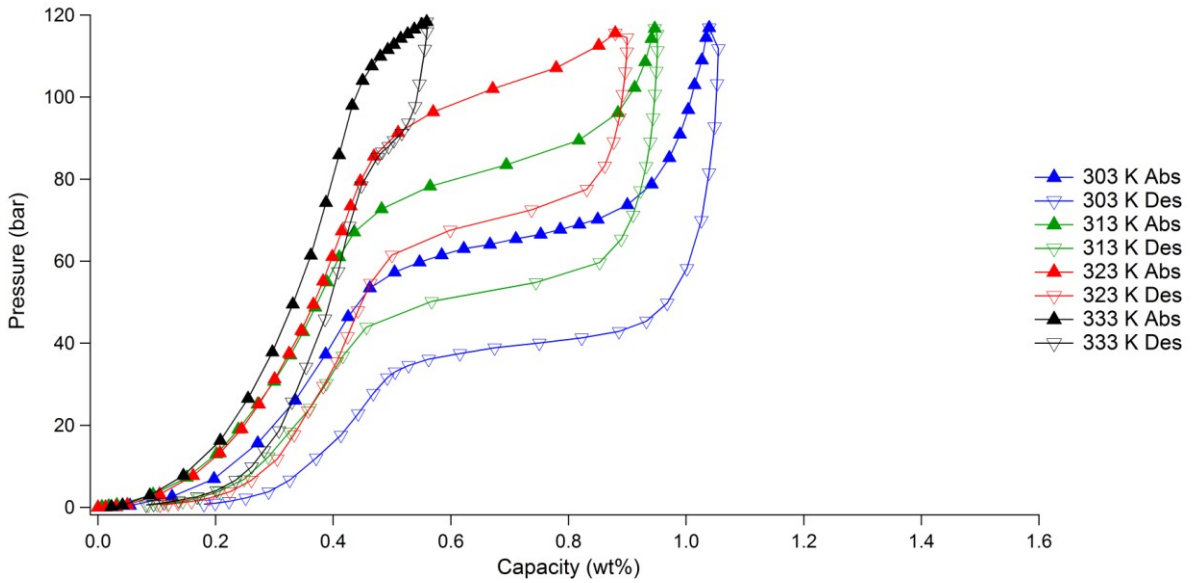

Figure 8.21 PCT measurement of Cr = 0.1 at 303 K (blue), 313 K (green), 323 K (red) and 333 K (black) showing absorption (upwards triangles) and desorption (downwards triangles) from 0.5 to 120 bar H_2.

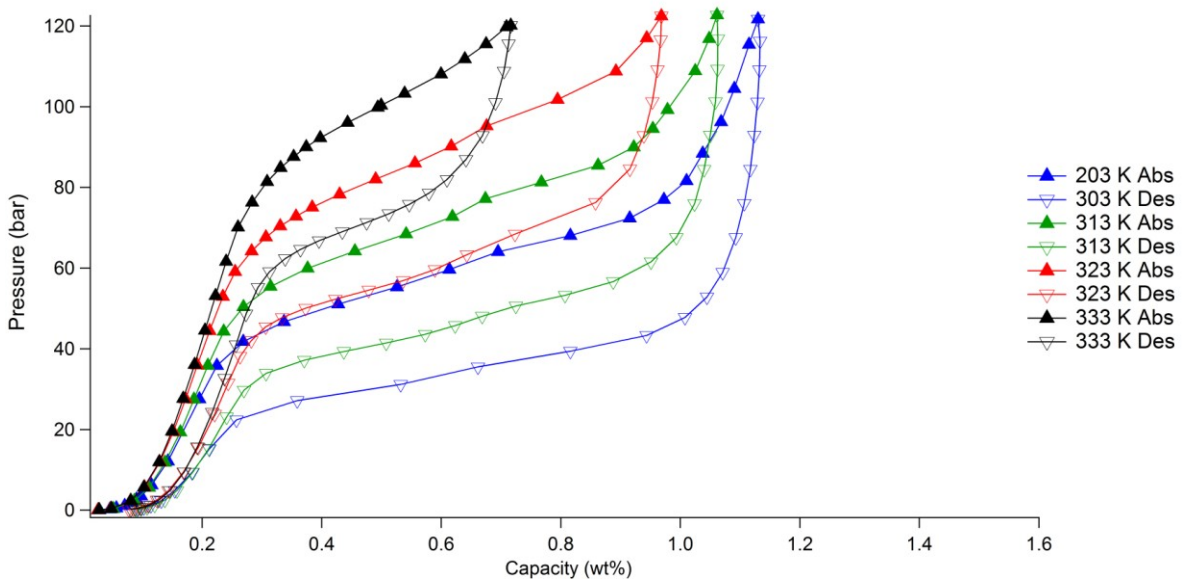

Figure 8.22 PCT measurement of Mo = 0.1 at 303 K (blue), 313 K (green), 323 K (red) and 333 K (black) showing absorption (upwards triangles) and desorption (downwards triangles) from 0.5 to 120 bar H_2.

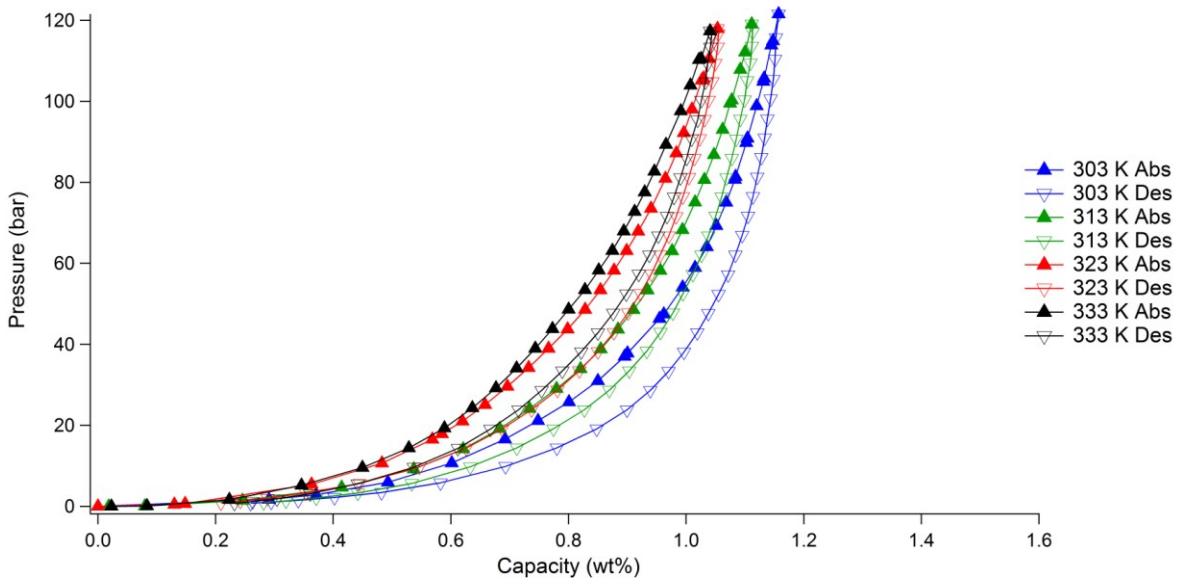

Figure 8.23 PCT measurement of Ta = 0.1 at 303 K (blue), 313 K (green), 323 K (red) and 333 K (black) showing absorption (upwards triangles) and desorption (downwards triangles) from 0.5 to 120 bar H_2.

Comparing Figures 8.20, 8.21, 8.22 and 8.23, the four alloys clearly exhibit different hydrogen storage properties as a result of their compositional differences.

In Nb = 0.1 the second plateau during absorption and desorption is long and becomes more sloped with increasing temperature due to the increase in plateau pressures. In addition, small hysteresis is observed between absorption and desorption.

In Cr = 0.1 two plateaus are observed between 303 and 323 K, showing large hysteresis between absorption and desorption. At 333 K the alloy appears to be reaching critical temperature because the second absorption and desorption plateau becomes smaller, indicating that there is only a small $\alpha + \beta$ two phase region.

Mo = 0.1 shows similar uptake and discharge behaviour to Cr = 0.1 with large hysteresis and the isotherm at 333 K showing a much shorter plateau as it approaches critical temperature.

Ta = 0.1 show significantly different isotherms to the other alloys, in which only single step uptake is observed. In this alloy higher uptake can be seen at the start of the isotherm, up to 30 bar, after which there is a lower uptake up to 120 bar. No plateau is present in the isotherm which may indicate that the first step at 0.5 bar during PCT measurement is higher than the plateau pressure. Plateau pressure is very sensitive to unit cell volumes so this can be explained by the large unit cell volume of the C14 Laves phase, 166.89 $Å^3$, which results in larger interstitial sites for the hydrogen to enter.

The sloping plateaus present in Nb = 0.1, Cr = 0.1 and Mo = 0.1 suggests that the alloys are not fully homogenous (Akiba & Iba, 1998). This confirms that longer heat treatment times are required to fully homogenise the alloys.

A comparison of the PCT measurements at 303 K up to 120 bar H_2 is shown in Figure 8.24 for all four heat treated alloys.

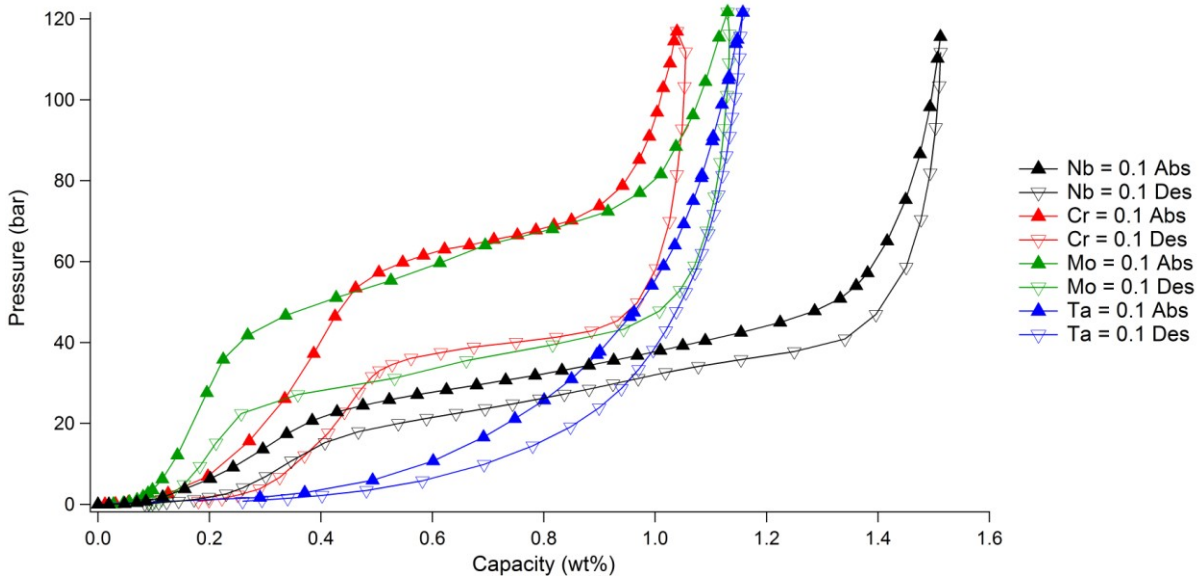

Figure 8.24 PCT measurement of Nb = 0.1 (black), Cr = 0.1 (red), Mo = 0.1 (green) and Ta = 0.1 (blue) showing absorption (upwards triangles) and desorption (downwards triangles) at 303 K from 0.5 to 120 bar H_2.

In Nb = 0.1, Cr = 0.1 and Mo = 0.1 alloys, at 303 K the first plateau in the absorption and desorption isotherms is present between 0 and 5 bar.

Table 8.6 shows a summary of the PCT properties, including capacity, plateau pressure and hysteresis for all the Ti-V-TM-Mn alloys at 303 K. Note measured errors for capacity are estimated to be 0.05 wt% based on 3 PCT measurements using a Pd standard (Appendix A).

Table 8.6 Summary of capacity, plateau pressure and hysteresis data for Nb = 0.1, Cr = 0.1, Mo = 0.1 and Ta = 0.1 based on PCT isotherms up to 120 bar H_2 at 303 K. Hysteresis factor: 0 = no hysteresis, 1 = large hysteresis.

Alloy	Maximum Capacity (wt%)	Reversible Capacity (wt%)	Abs Plateau P (bar)	Des Plateau P (bar)	Hysteresis Factor $Log(P_{Abs}/P_{Des})$
Nb = 0.1	1.53	1.51	25 - 50	40 - 15	0.135
Cr = 0.1	1.10	1.06	58 - 73	47 – 32	0.172
Mo = 0.1	1.16	1.13	45 - 70	50 - 25	0.186
Ta = 0.1	1.18	1.16	-	-	-

From Table 8.6 it can be seen that Nb = 0.1 showed the greatest uptake with a reversible capacity of 1.51 (+/- 0.05) wt% up to 120 bar H_2 at 303 K. In addition, Nb = 0.1 also showed the smallest hysteresis during absorption and desorption of all the alloys. This may be advantageous for applications in which hydrogen is absorbed-desorbed over hundreds of cycles as energy efficiency will be improved (Sandrock, 1999).

Figures 8.25 – 8.28 show kinetic data taken from the mid-point plateau for absorption at 303 K for Nb = 0.1, Cr = 0.1, Mo = 0.1 and Ta = 0.1 respectively. This data was examined to ensure all the alloys reached equilibrium along the plateau.

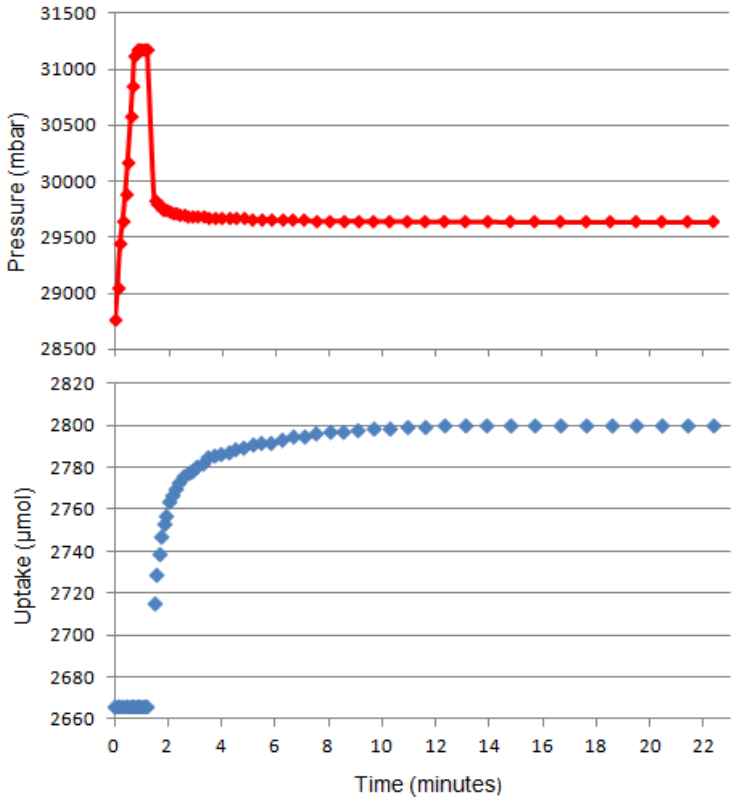

Figure 8.25 Kinetic data for Nb = 0.1 showing pressure (red) and uptake (blue) at the mid-point plateau for absorption at 303 K.

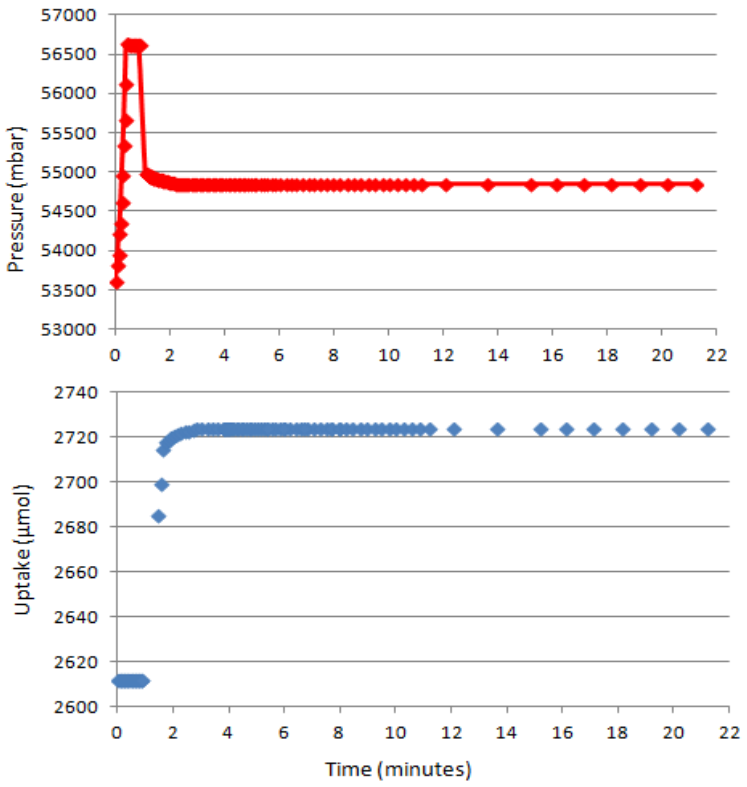

Figure 8.26 Kinetic data for Cr = 0.1 showing pressure (red) and uptake (blue) at the mid-point plateau for absorption at 303 K.

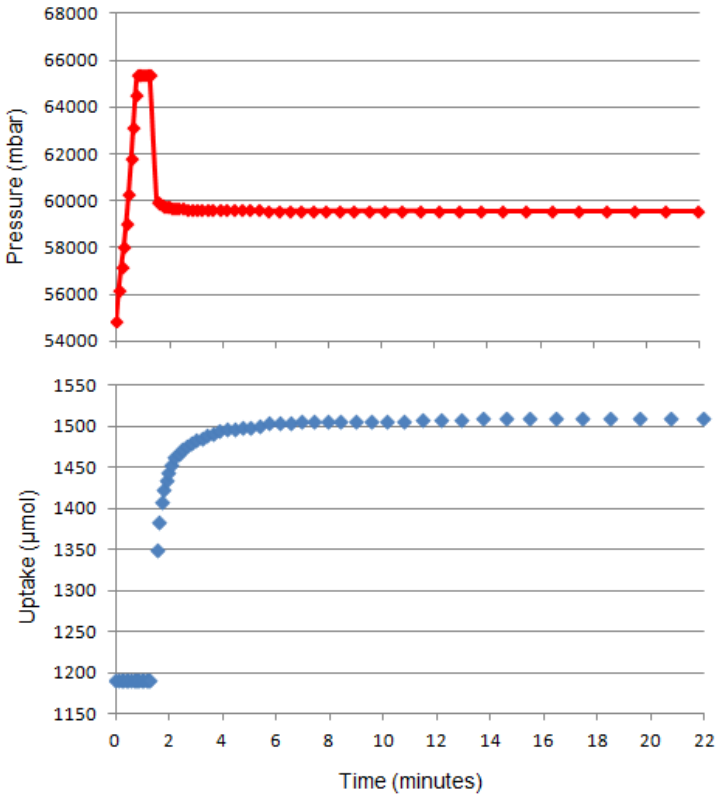

Figure 8.27 Kinetic data for Mo = 0.1 showing pressure (red) and uptake (blue) at the mid-point plateau for absorption at 303 K.

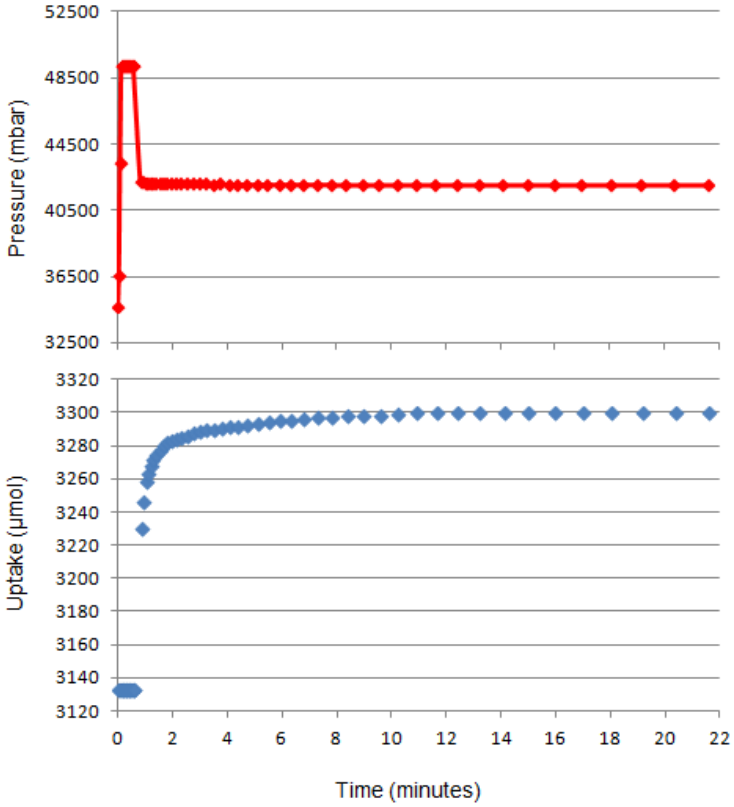

Figure 8.28 Kinetic data for Ta = 0.1 showing pressure (red) and uptake (blue) at the mid-point plateau for absorption at 303 K.

The kinetic data for the alloys shows that all four alloys reach equilibrium between 0 and 22 minutes.

Van't hoff plots, calculated in Appendix C, showing hydrogen absorption and desorption for Nb = 0.1, Cr = 0.1 and Mo = 0.1 are shown in Figure 8.29 with the derived enthalpies and entropies in Table 8.7. Note Ta = 0.1 was not included because no clear plateau was visible for absorption and desorption.

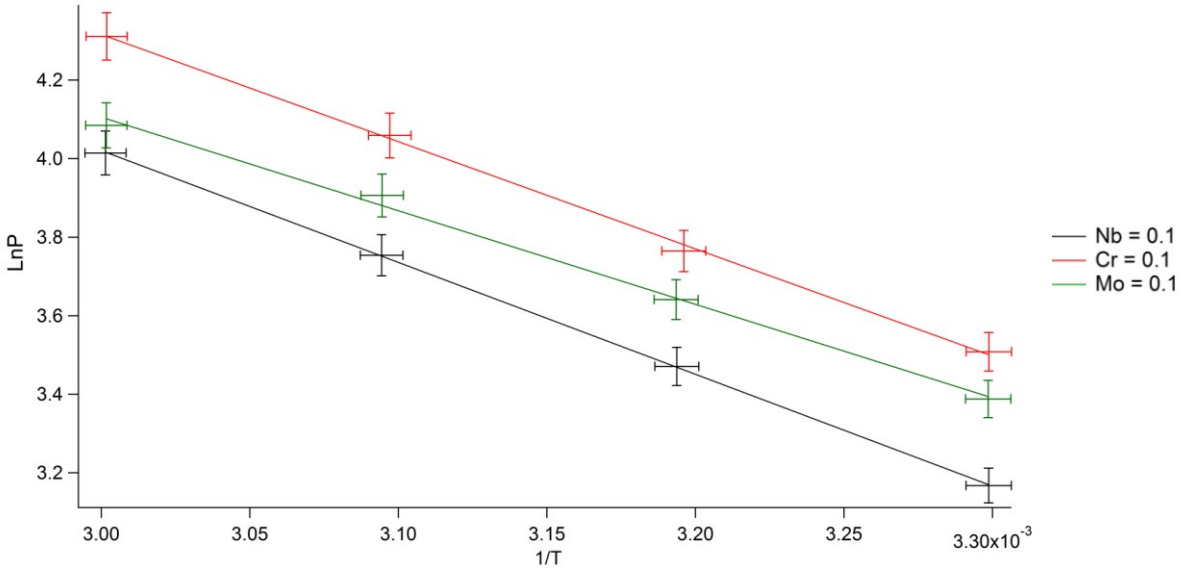

Figure 8.29 Van't hoff plots showing hydrogen desorption for Nb = 0.1 (black) , Cr = 0.1 (red) and Mo = 0.1 (green).

Table 8.7 Enthalpy and Entropy data for desorption in Nb = 0.1, Cr = 0.1 and Mo = 0.1.

Alloy	ΔH (kJ/mol H_2)	ΔS (J/mol H_2)
Nb = 0.1	-23.68	104.48
Cr = 0.1	-27.73	103.97
Mo = 0.1	-19.81	93.58

Mo = 0.1 shows the highest ΔH value at -19.81 kJ/mol H_2 which means it requires the least amount of energy for hydrogen to dissociate from the lattice during desorption.

The calculated desorption ΔH for Nb = 0.1, Cr = 0.1 and Mo = 0.1 are all higher than -30 kJ/mol H_2, making them suitable for use in interfacing stores for PEM fuel cell applications (Shibuya et al., 2008).

8.5 Characterisation of Hydrogen Cycled Alloys

8.5.1 SEM/EDS on Hydrogen Cycled Alloys

SEM images and EDS analysis was performed on the hydrogen decrepitated powders for Nb = 0.1, Cr = 0.1, Mo = 0.1 and Ta = 0.1 after hydrogen sorption measurements. SEM SEI images (x 500 magnification) are shown in Figures 8.30 – 8.33. Note, all the alloys were cycled with hydrogen under the same conditions (see Chapter 6).

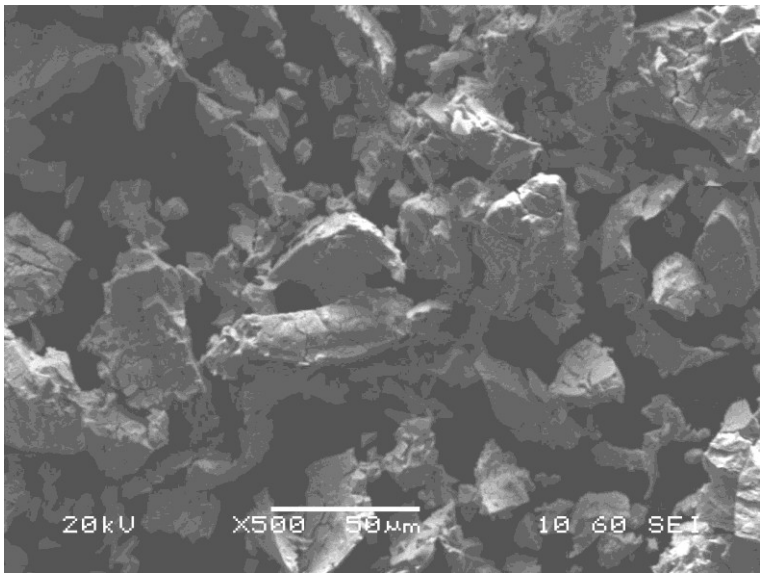

Figure 8.30 SEM SEI image of hydrogen cycled Nb = 0.1 (x 500).

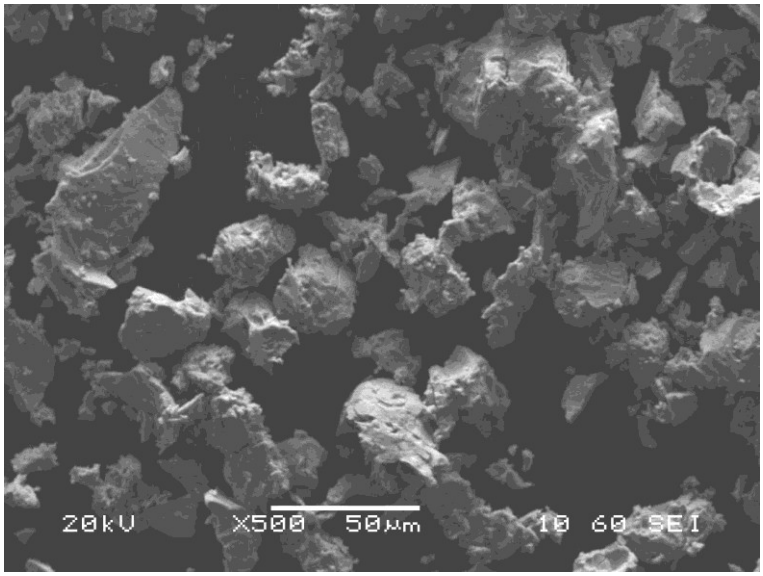

Figure 8.31 SEM SEI image of hydrogen cycled Cr = 0.1 (x 500).

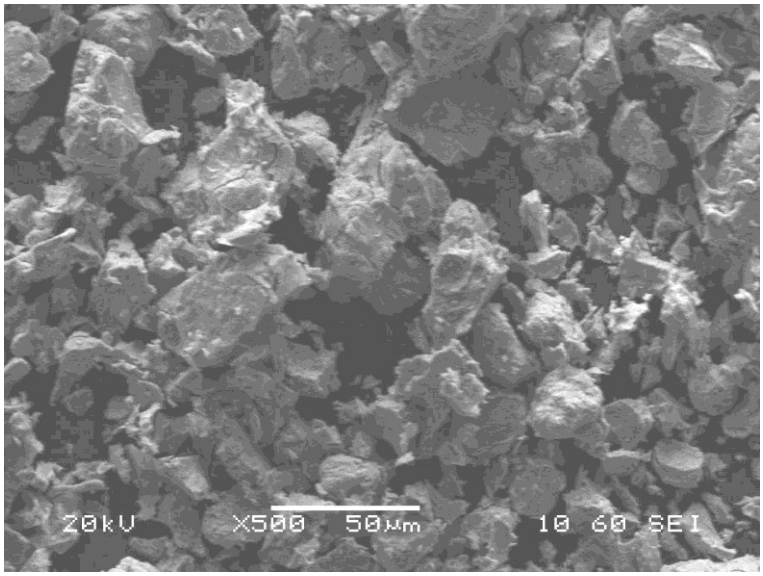

Figure 8.32 SEM SEI image of hydrogen cycled Mo = 0.1 (x 500).

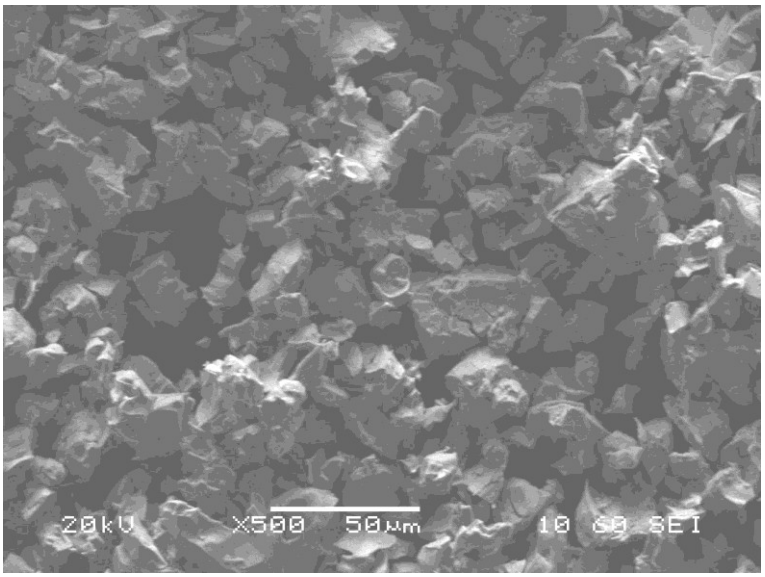

Figure 8.33 SEM SEI image of hydrogen cycled Ta = 0.1 (x 500).

SEM micrographs of the hydrogen cycled powders show different powder morphologies. This may have arisen due to different hydrogen interactions with the alloys, producing different levels of internal stress within powder particles and possibly different mechanical strength properties from the different alloy compositions.

Micrographs of hydrogen cycled Nb = 0.1, Cr = 0.1 and Mo = 0.1 shows large particles with smooth edges and cracks within the particles which suggest a ductile fracture has occurred during hydrogen decrepitation.

Hydrogen cycled Ta = 0.1 shows fairly uniform particles with rough edges which would be expected from a brittle intergranular fracture.

EDS analysis was carried out on different areas/spots in the powdered alloys. The average composition of hydrogen cycled Nb = 0.1 is $Ti_{0.58}V_{0.43}Nb_{0.07}Mn_1$, Cr = 0.1 is $Ti_{0.57}V_{0.48}Cr_{0.06}Mn_1$, Mo = 0.1 is $Ti_{0.61}V_{0.40}Mo_{0.06}Mn_1$ and Ta = 0.1 is $Ti_{0.61}V_{0.43}Ta_{0.06}Mn_1$.

8.5.2 XRD on Hydrogen Cycled Alloys

XRD patterns of hydrogen decrepitated powders of Nb = 0.1, Cr = 0.1, Mo = 0.1 and Ta = 0.1 after hydrogen sorption measurements are shown in Figure 8.34. Appendix C shows individual XRD traces of the hydrogen cycled alloys, showing the observed pattern and calculated fit after pseudo-Rietveld refinement.

Table 8.8 shows crystal structure refinement results for the hydrogen cycled alloys.

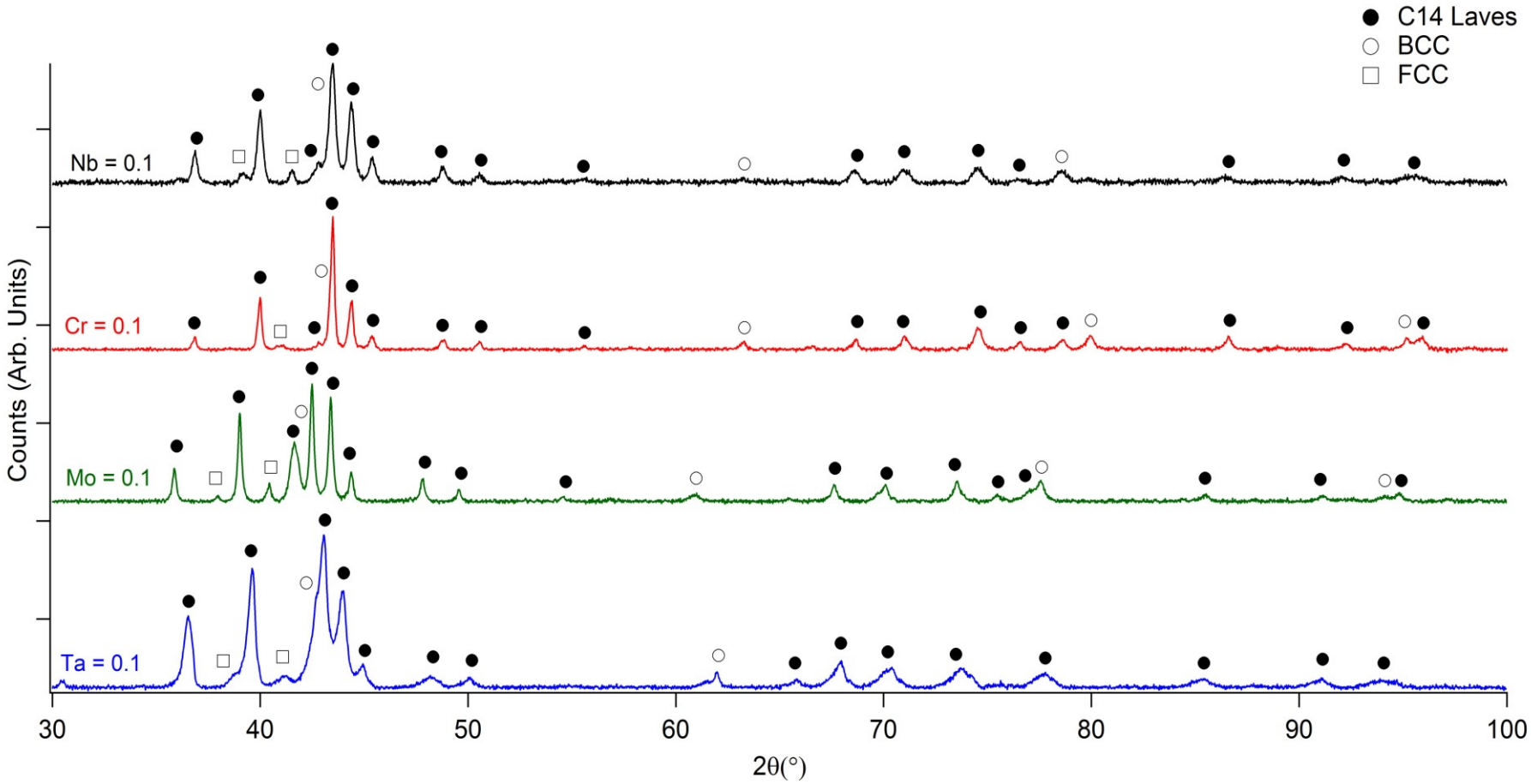

Figure 8.34 XRD patterns of hydrogen cycled Nb = 0.1 (top, black), Cr = 0.1 (middle, red), Mo = 0.1 (middle, green) and Ta = 0.1 (bottom, blue) with peaks indexed.

Table 8.8 Crystal structure refinement results for hydrogen cycled alloys (values on right) in comparison to heat treated alloys. Note the values in parentheses are three standard deviations and refer to the last digit.

Alloy	Heat Treated				Hydrogen Cycled			
	Phase	Lattice Parameters		Abundance	Phase	Lattice Parameters		Abundance
Nb = 0.1	C14	a	4.883(2)	81(8)	C14	a	4.871(10)	80(4)
		c	8.004(4)			c	7.987(4)	
	BCC	a + c	2.963(2)	13(6)	BCC	a + c	2.978(7)	13(4)
	FCC	a+ c	11.268(6)	6(4)	FCC	a+ c	11.251(6)	7(2)
Cr = 0.1	C14	a	4.850(3)	67(9)	C14	a	4.862(4)	70(4)
		c	7.951(6)			c	7.973(3)	
	BCC	a + c	2.933(2)	24(4)	BCC	a + c	2.954(4)	22(3)
	FCC	a+ c	11.248(9)	9(7)	FCC	a+ c	11.268(5)	8(3)
Mo = 0.1	C14	a	4.864(7)	62(3)	C14	a	4.869(6)	74(9)
		c	7.969(3)			c	7.981(6)	
	BCC	a + c	2.993(5)	31(2)	BCC	a + c	2.996(4)	19(6)
	FCC	a+ c	11.264(4)	7(2)	FCC	a+ c	11.313(5)	7(4)
Ta = 0.1	C14	a	4.899(4)	90(11)	C14	a	4.917(8)	94(5)
		c	8.030(7)			c	8.065(6)	
	BCC	a + c	2.945(3)	6(4)	BCC	a + c	2.988(5)	6(5)
	FCC	a+ c	11.280(9)	4(5)	FCC	a+ c	-	-

Comparing the crystal structure refinement data for the heat treated and hydrogen cycled alloys, several differences can be seen. The C14 Laves phase is still the dominant phase in the hydrogen cycled alloys - occupying 80 wt% in Nb = 0.1, 70 wt% in Cr = 0.1, 74 wt% in Mo = 0.1 and 94 wt% in Ta = 0.1 – but there is a decrease in the phase abundance in Nb = 0.1 and Cr = 0.1 and increase in Mo = 0.1 and Ta = 0.1.

After cycling with hydrogen, the unit cell volume of the C14 Laves phase in the alloys was found to be 165.86(3) $Å^3$, 163(7) $Å^3$, 163.91(5) $Å^3$ and 169.27(4) $Å^3$ in Nb = 0.1, Cr = 0.1, Mo = 0.1 and Ta = 0.1 respectively. This shows an increase of between 0.46 and 2.38 $Å^3$ in Nb = 0.1, Cr = 0.1, Mo = 0.1 and Ta = 0.1.

The unit cell volumes of the BCC phase in the alloys after cycled are: 25.97(4) $Å^3$ in Nb = 0.1, 25.75(2) $Å^3$ in Cr = 0.1, 26.90(2) $Å^3$ in Mo = 0.1 and 26.8(9) $Å^3$ in Ta = 0.1. Again, this shows an increase of between 0.08 and 1.26 $Å^3$ in the hydrogen cycled alloys.

The expansion in the volume may be the result of remnant hydrogen trapped within the C14 Laves and BCC phase as seen by the reduction in the hydrogen uptake after the first cycle (maximum capacity).

The lattice parameters for Nb = 0.1, Cr = 0.1, Mo = 0.1 and Ta = 0.1 did not significantly change in the hydrogen cycled alloys which indicates good structural stability upon cycling.

Figure 8.35 shows the relationship between C14 Laves phase unit cell volume vs. desorption plateau pressure and Figure 8.36 shows the relationship between the BCC phase unit cell volume and desorption plateau pressure for alloy Nb = 0.1, Cr = 0.1 and Mo = 0.1.

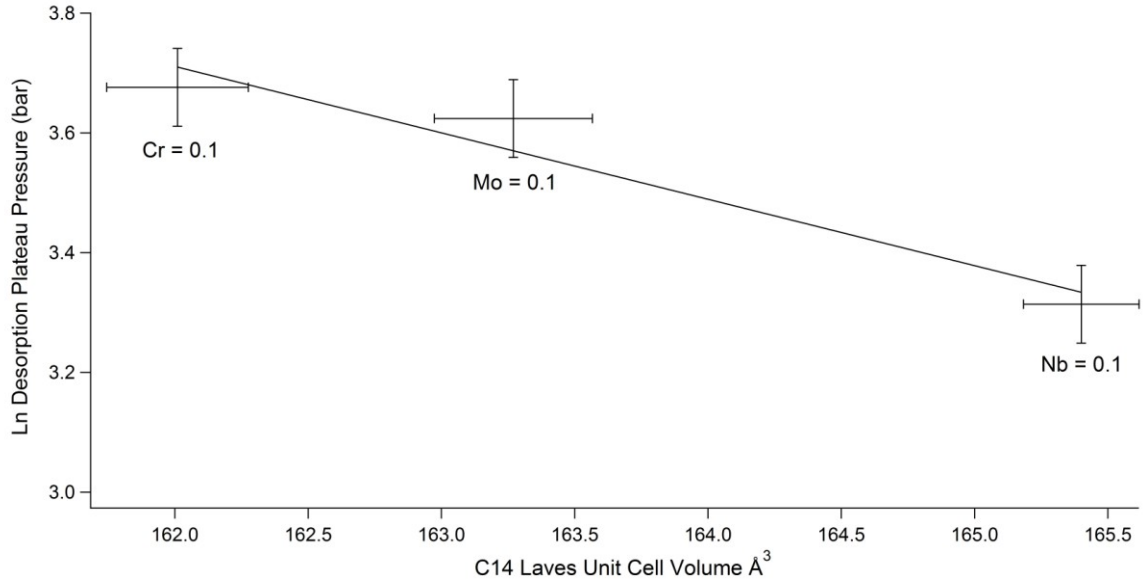

Figure 8.35 Correlation between C14 Laves unit cell volume (Å^3) vs. Ln Desorption plateau pressure (bar) for Nb = 0.1, 0.1, Cr = 0.1 and Mo = 0.1. Note, line added between data points on for ease of understanding.

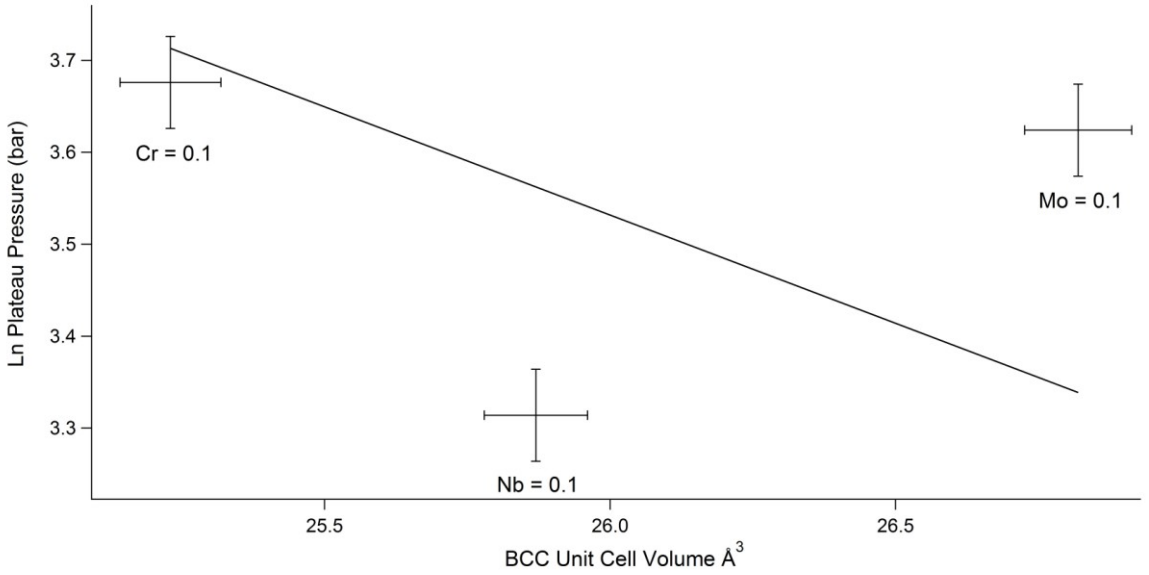

Figure 8.36 Correlation between BCC phase unit cell volume (Å^3) vs. Ln Desorption plateau pressure (bar) for Nb = 0.1, 0.1, Cr = 0.1 and Mo = 0.1. Note, line added between data points on for ease of understanding.

The correlation between unit cell volume and desorption plateau pressure shown in Figure 8.35 is in agreement with previous studies on AB_5 type alloys (Mendelsohn & Gruen, 1977; Reilly et al., 1999) and AB_2 C14 Laves type alloys (Nakano et al., 1997; Nakano & Wakao, 1995).

Figure 8.36 shows a weak relationship between desorption plateau pressure and unit cell volume for the BCC phase, however, further data points would be required to confirm the correlation.

8.6 Summary

Following on from work reported by Shibuya et al., (2008) it was decided to investigate the effect of transition metal substitution in the Ti-V-Mn system as a way of improving the PCT properties. The previous chapter described how small changes in composition (~ 0.05 at%) resulted in different unit cell volumes of the C14 Laves phase which influenced the plateau pressure, and subsequent enthalpy of hydride decomposition.

Transition metals were selected based on their phase diagrams which showed that all the alloys formed BCC phases within the transition metal V-binary phase diagram. $Ti_{0.5}V_{0.4}Nb_{0.1}Mn$ (Nb = 0.1), $Ti_{0.5}V_{0.4}Cr_{0.1}Mn$ (Cr = 0.1), $Ti_{0.5}V_{0.4}Mo_{0.1}Mn$ (Mo = 0.1) and $Ti_{0.5}V_{0.4}Ta_{0.1}Mn$ (Ta = 0.1) were selected for study.

SEM micrographs of the alloys showed significant differences in microstructure: Nb = 0.1, Cr = 0.1 and Mo = 0.1 featuring light, grey and dark dendritic phases whereas Ta = 0.1 appeared to have a light dendritic phase, secondary dark dendritic phase and a grey phase. The composition of these phases was different between the alloys, for example the light phase

was richer in Mn in Nb = 0.1, Ti in Cr = 0.1, V in Mo = 0.1 and Ta in Ta = 0.1. This can be attributed to the different atomic masses of the transition metal substitutions: Nb is 92.91 amu, Cr is 52 amu, Mo is 95.94 amu and Ta is 180.95 amu. Coring could be seen in the micrographs of as-cast and heat treated Nb = 0.1, Cr = 0.1 and Mo = 0.1, which indicates that longer heat treatment times are required to fully homogenise these alloys.

The same three XRD phases were identified in all the Ti-V-TM-Mn alloys as the $Ti_{0.5}V_{0.5}Mn$ system: C14 Laves, BCC and FCC oxide phases. XRD analysis showed a variation in the phase abundance of the alloys, due to different outer shell electron configurations between the alloys. The C14 Laves phase appeared to be the dominant phase in the as-cast, heat treated and hydrogen cycled alloys.

Differences in the unit cell volumes of the C14 Laves and BCC phases were also present between the alloys and occurred as a result the difference in atomic radii of the transition metal elements.

The heat treated alloys showed variations in the unit cell volumes of the phases in comparison to the as-cast alloys. The difference in metallic radii of the transition metal elements resulted in different substitutions of the B-site V, TM and Mn elements take place. Analysis of the EDS compositions of the C14 Laves (light phase) and BCC (grey phase) in the as-cast and heat treated alloys showed that different elemental substitution took place in the C14 Laves unit cell. There was no significant difference in the composition of the BCC phase after heat treatment which indicates that no elemental substitution took place and may be the result of an ordering effect upon annealing.

All the alloys showed different behaviour with hydrogen during PCT measurements. Nb = 0.1 showed the greatest uptake with a reversible capacity of 1.51 (+/- 0.05) wt% up to

120 bar H_2 at 303 K. In addition, Nb = 0.1 also showed the smallest hysteresis during absorption and desorption of all the alloys which is advantageous for applications involving heat.

The sloping plateaus present in isotherms of Nb = 0.1, Cr = 0.1 and Mo = 0.1 indicates that the alloys are no fully homogenous. This confirms with the SEM analysis that longer heat treatment times are required.

The isotherm for Ta = 0.1 did not exhibit a clear plateau during absorption and desorption. The shape of the isotherm of Ta = 0.1 indicates that the first step at 0.5 bar during PCT measurement may be higher than the plateau pressure. Plateau pressure is very sensitive to unit cell volume so this could be explained by the large unit cell volume of the C14 Laves phase in the alloy, which increased from 166.89 $Å^3$ to 169.27 $Å^3$ after exposure to hydrogen.

As with the $Ti_{0.5}V_{0.5}Mn$ system, there was a correlation between C14 Laves and BCC phase unit cell volume and desorption plateau pressure in Nb = 0.1, Cr = 0.1 and Mo = 0.1. This is in agreement with previous studies looking at this relationship.

Overall, the Nb = 0.1 alloy showed the most promising hydrogen storage properties. The next stage of the work focuses on investigating Ti-V-Mn alloys, with substitution of Nb for V over a range of different compositions.

Chapter 9

THE Ti-V-Nb-Mn SYSTEM

9.1 Introduction

The investigation on the effect of transition metal substitutions (Nb, Cr, Mo and Ta - see Chapter 8), which contain BCC phases, to the B-site of the $Ti_{0.5}V_{0.5}Mn$ showed that the addition of 0.1 at% Nb to the system resulted in a reduction in hysteresis between absorption and desorption and resulted in an increase in plateau pressures. In addition, of all the novel compositions it showed the highest reversible capacity at 1.51 (+/- 0.05) wt%.

Following on from the results of the Ti-V-TM-Mn system, it was decided to examine the Ti-V-Nb-Mn system as Nb was substituted for V in the B site, in more detail. For this, three different alloys with varying Nb additions were produced to be investigated along with the Nb = 0.1 alloy from the previous chapter, so the system could be fully understood.

Alloys with the following compositions were therefore synthesised:

- $Ti_{0.5}V_{0.45}Nb_{0.05}Mn$ (Nb = 0.05)

- $Ti_{0.5}V_{0.4}Nb_{0.1}Mn$ (Nb = 0.1)

- $Ti_{0.5}V_{0.3}Nb_{0.2}Mn$ (Nb = 0.2)

- $Ti_{0.5}Nb_{0.5}Mn$ (Nb = 0.5)

* Note the Nb = 0.1 system was investigated during the previous chapter but will be explained again during the following chapter.

For ease of understanding, alloys will be referred to by their specific Nb content.

Elemental Ti, V, Nb and Mn (Sigma Aldrich: ≥ 99.7% purity, see Chapter 6) was weighed out into the mole ratios shown above. The following table represents the calculations involved in producing 10g samples. As with the other alloy systems, an extra one percent of Mn was added to compensate for Mn losses during arc-melting.

Table 9.1 Calculations used to make up 10g $Ti_{0.5}V_{0.5-x}Nb_xMn$, where x = 0.05, 0.1, 0.2 and 0.5 alloys.

Mole Ratio	at%				Molecular Weight	wt%				Weight (g)			
	Ti	V	Nb	Mn		Ti	V	Nb	Mn	Ti	V	Nb	Mn
Nb = 0.05	0.25	0.225	0.025	0.5	53.220	22.49	21.54	4.36	51.61	2.25	2.15	0.44	5.16
Nb = 0.1	0.25	0.2	0.05	0.5	54.274	22.06	18.77	8.56	50.62	2.21	1.88	0.86	5.06
Nb = 0.2	0.25	0.15	0.1	0.5	56.368	21.24	13.56	16.48	48.73	2.12	1.36	1.65	4.87
Nb = 0.5	0.25	0	0.25	0.5	62.668	19.10	0	37.07	43.84	1.91	0	3.71	4.38

Note, Table 9.1 shows the target composition for the $Ti_{0.5}V_{0.5-x}Nb_xMn$ alloys but the alloys synthesised vary in composition (as shown by the EDS Results).

9.2 Characterisation of As-Cast Alloys

The as-cast alloys were characterised by SEM/EDS and XRD to investigate microstructure and composition after arc-melting.

9.2.1 SEM/EDS on As-Cast Alloys

Figures 9.1 - 9.8 show BEI images of cross-sections of as-cast Nb = 0.05, Nb = 0.1, Nb = 0.2 and Nb = 0.5 at low (x 500) and high (x 1000) magnification.

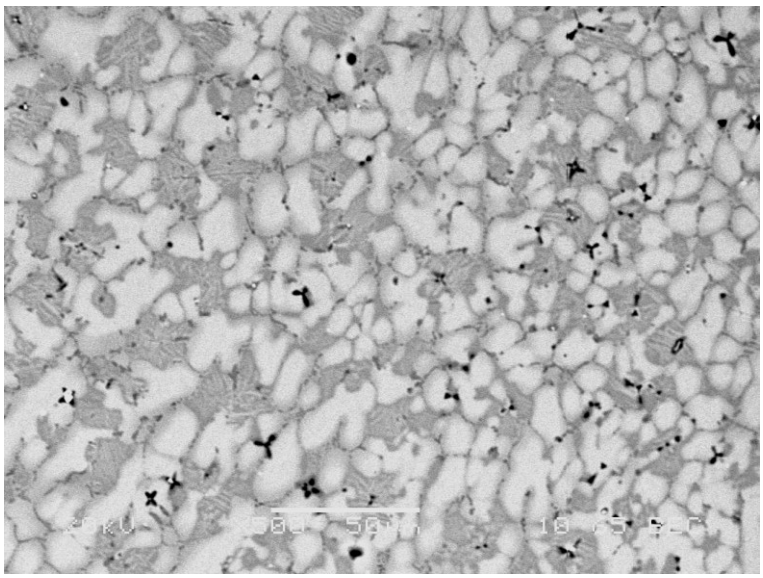

Figure 9.1 SEM BEI image of as-cast Nb = 0.05 (x 500).

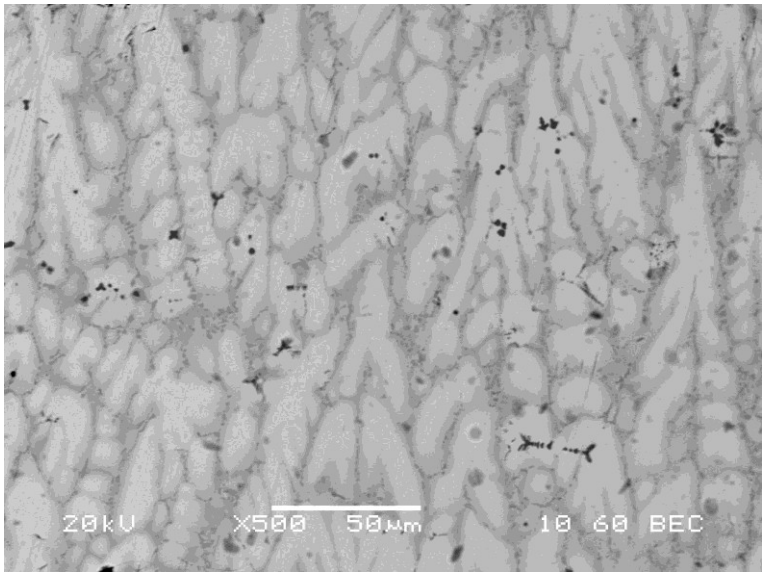

Figure 9.2 SEM BEI image of as-cast Nb = 0.1 (x 500).

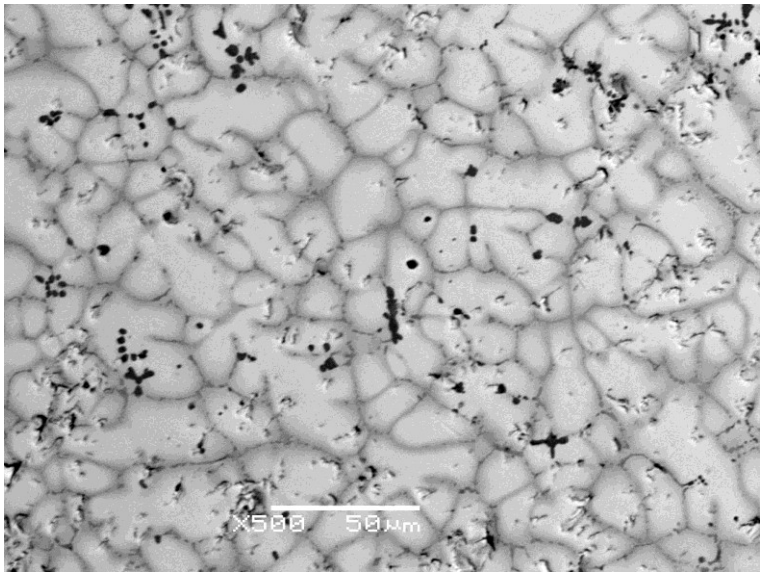

Figure 9.3 SEM BEI image of as-cast Nb = 0.2 (x 500).

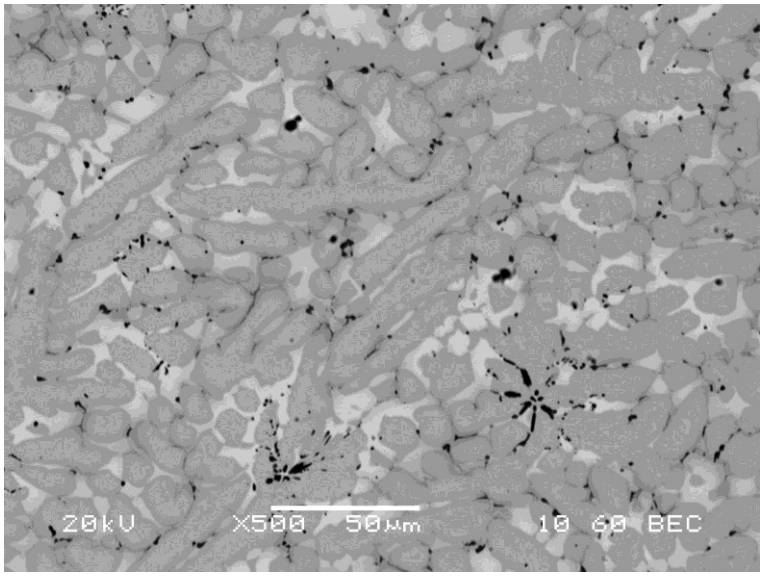

Figure 9.4 SEM BEI image of as-cast Nb = 0.5 (x 500).

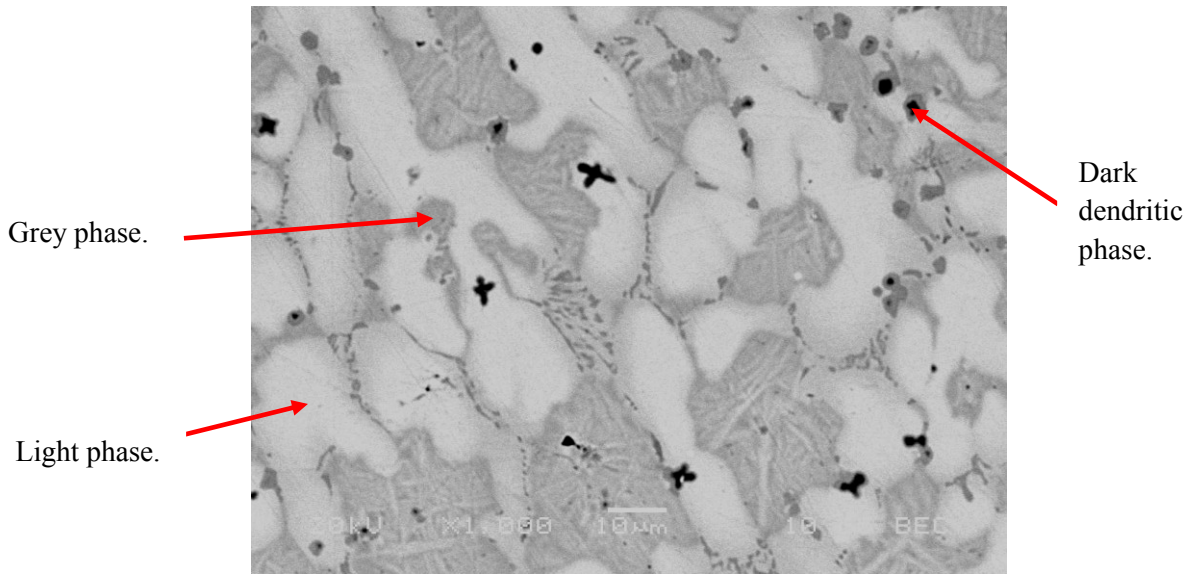

Figure 9.5 SEM BEI image of as-cast Nb = 0.05 (x 1000).

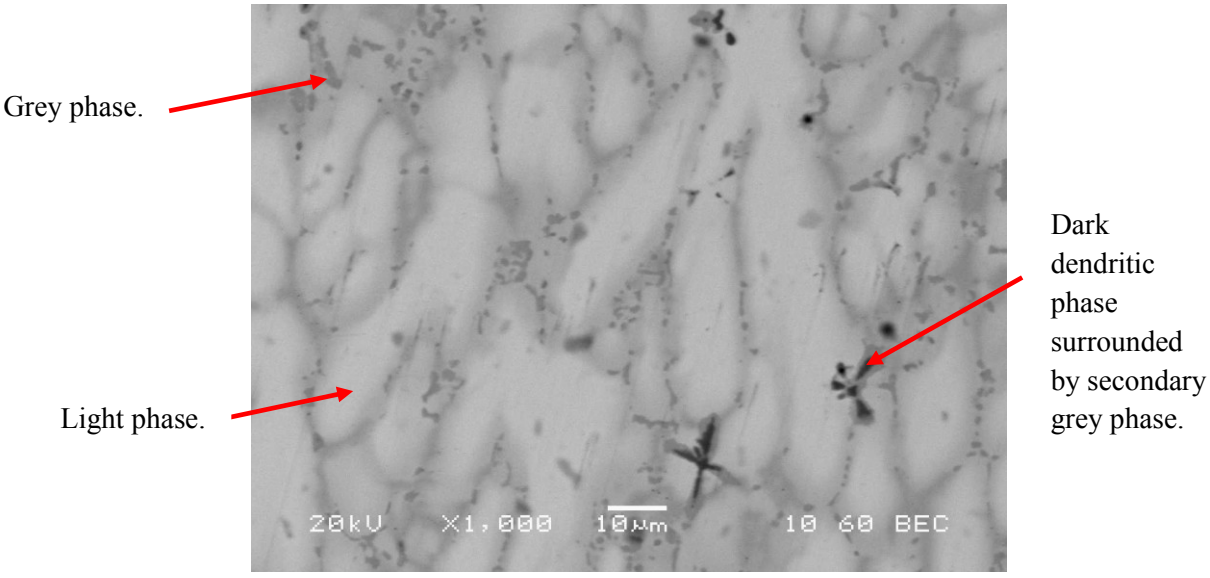

Figure 9.6 SEM BEI image of as-cast Nb = 0.1 (x 1000).

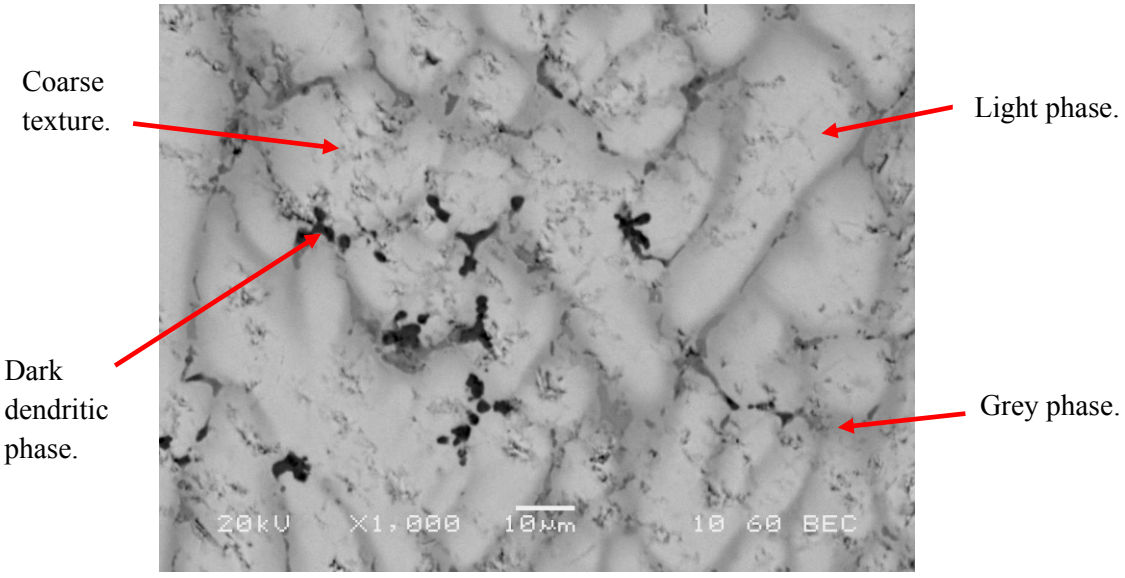

Figure 9.7 SEM BEI image of as-cast Nb = 0.2 (x 1000).

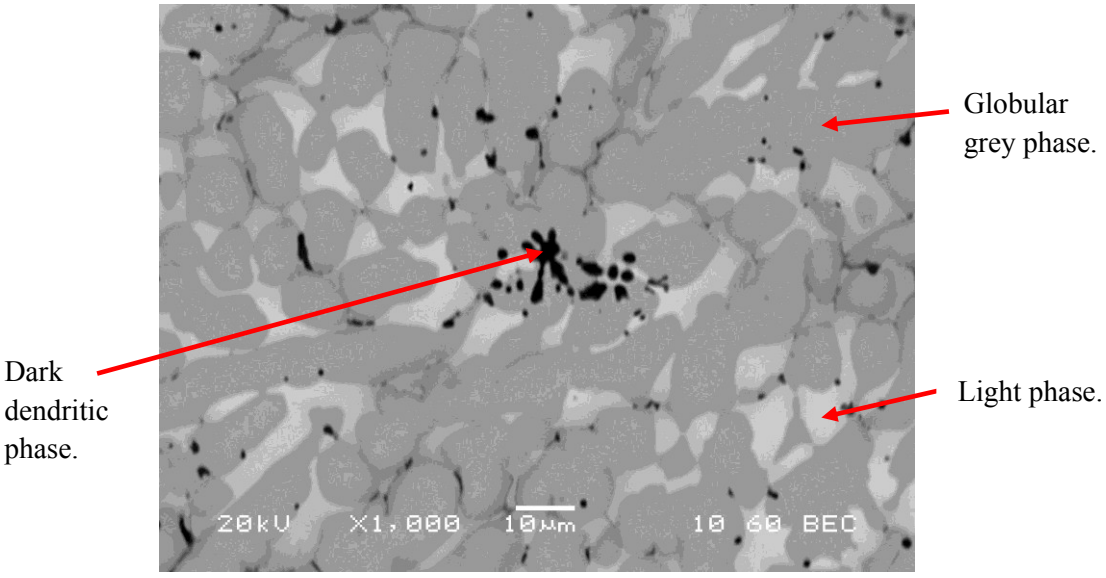

Figure 9.8 SEM BEI image of as-cast Nb = 0.5 (x 1000).

Images of the as-cast alloys show significant variations in microstructure as a result of their compositional differences. This indicates that different grain growth has occurred during the solidification process.

In all four alloys, three microstructural phases can be identified in varying amounts: a light phase, grey phase and dark dendritic phase. The dendrites appear similar in size in all four alloys which suggests the alloys solidified under similar cooling conditions. Coring can be seen in the high magnification images of Nb = 0.1 and Nb = 0.2 which indicates the alloys are not fully homogenous.

The micrographs of Nb = 0.05 show that the light phase is the dominant phase in the alloy and the grey phase appears to be growing within the grain boundaries. The majority of the dark dendritic phase can be seen within the grey phase at the grain boundaries, however, there are dark spots within the grains. These dark spots could be where the dendrites are starting to grow or they may defects from the arc-melting process: Ti is the lightest element within the alloy (which results in a dark appearance) so this may be small amounts of un-reacted Ti.

Micrographs of Nb = 0.1 also show the light phase is the most abundant within the alloy. The grey phase occurs at the grain boundaries, within which the dark dendritic phase is positioned. The shape of the grains shows the direction of the cooling which appears to be consistent in both the low and high magnification images.

The light phase is also the dominant phase within Nb = 0.2. The grey phase can be very clearly seen at the grain boundaries in the low magnification image. The surface of the alloy shows a coarse texture with large grain size which suggests that cooling may have occurred at different rates within that section of the alloy.

In Nb = 0.5 it is the grey phase with a globular morphology which is the dominant phase in the micrographs, with the light phase only present in small amounts in between the grains. The dark dendritic phase appears to be precipitated at the grain boundaries and grows where the grains meet. The micrographs show equiaxed grains which may indicate recrystallisation

has occurred during the arc-melting. Black spots are also present in the micrographs, similar to the ones shown in the Nb = 0.05. These may either be where the dendrites are starting to grow or they may defects from the arc-melting process.

The composition of the alloys was confirmed by EDS analysis, the results of which are displayed in Table 9.2. Note that the results shown are in atomic percent (at %).

Table 9.2 Average EDS analysis of as-cast Nb = 0.05, Nb = 0.1, Nb = 0.2 and Nb = 0.5 with standard deviation associated with mean values. Note analysis was carried out by taking an average of three different areas/points within BEI images of as-cast alloys.

Alloy	Phase Location	Ti	σ	V	σ	Nb	σ	Mn	σ	Average Composition Ratio (Ti/V/Nb/Mn)
As-cast Nb = 0.05	Area	25.72	6.8	22.36	7.1	2.48	7.3	49.26	6.5	0.52/0.45/0.05/1
	Light	25.31	6.1	17.85	6.4	4.76	6.7	52.87	6.2	0.48/0.34/0.09/1
	Grey	20.03	7.3	33.84	6.9	0.86	7.4	45.33	7.5	0.44/0.75/0.02/1
	Dark	62.46	6.7	8.75	7.1	1.37	6.8	27.42	7.3	2.28/0.32/0.05/1
As-cast Nb = 0.1	Area	26.58	6.1	20.63	6.3	4.12	6.3	48.67	6.5	0.55/0.42/0.08/1
	Light	24.35	6.8	18.87	7.3	5.26	7.4	51.52	7.5	0.47/0.37/0.1/1
	Grey	21.87	7.6	35.24	7.2	0.98	7.7	41.91	6.9	0.52/0.84/0.02/1
	Dark	65.38	6.3	8.59	6.6	1.84	6.5	24.19	6.2	2.70/0.36/0.08/1
As-cast Nb = 0.2	Area	25.47	6.4	15.61	6.7	9.75	7.2	49.21	7.6	0.52/0.32/0.20/1
	Light	21.34	6.8	15.7	6.5	12.25	6.1	50.87	6.7	0.42/0.30/0.24/1
	Grey	31.93	7.3	17.54	7.5	3.64	7.6	46.89	7.2	0.68/0.37/0.08/1
	Dark	78.06	6.8	2.57	6.3	2.45	6.4	16.92	6.1	4.61/0.15/0.14/1
As-cast Nb = 0.5	Area	25.69	6.2	0	-	25.02	6.7	49.67	7.3	0.52/0.51/1
	Light	36.27	6.6	0	-	36.91	7.1	26.14	7.5	1.38/1.41/1
	Grey	17.64	7.6	0	-	22.77	7.2	59.51	6.9	0.30/0.38/1
	Dark	78.21	6.8	0	-	9.03	6.5	12.76	6.1	6.13/0.71/1

The area analysis shows that the average composition for as-cast Nb = 0.05 is $Ti_{0.52}V_{0.45}Nb_{0.05}Mn_1$, Nb = 0.1 is $Ti_{0.55}V_{0.42}Nb_{0.08}Mn_1$, Nb = 0.2 is $Ti_{0.52}V_{0.32}Mo_{0.2}Mn_1$ and Nb = 0.5 is $Ti_{0.52}Nb_{0.51}Mn_1$. This confirms that the alloys are close to the target compositions.

In Nb = 0.05, when comparing the composition taken from the average area analysis, the light phase is richer in Mn (49.26 vs. 52.08 at%) and Nb (2.48 vs. 4.76 at%) because they are heavier elements. The grey phase richer in V (22.36 vs. 33.84 at%) and the dark phase rich in Ti (25.72 vs. 62.46 at%) because it is the lightest element.

There is a similar result in Nb = 0.1 with the light phase being richer in Mn (48.67 vs. 50.87 at%) and Nb (4.12 vs. 5.26 at%), grey phase richer in V and dark phase richer in Ti.

In Nb = 0.2, the light phase is also richer in Mn (49.21 vs. 51.52 at%) and Nb (9.75 vs. 12.83 at%) but the both the grey and dark phases are now richer in Ti: 25.47 vs. 36.27 at% and 25.47 vs. 78.06 at% respectively.

When V is completely substituted for Nb in Nb = 0.5, the light phase becomes richer in Ti (25.69 vs. 51.52 at%) and Nb (25.02 vs. 67.59 at%), the grey phase richer in Mn (49.67 vs. 58.99 at%) and the dark phase richer in Ti (25.69 vs. 78.21 at%). This may be explained by different interaction of the elements leading to different surface morphologies.

9.2.2 XRD on As-Cast Alloys

Figure 9.9 shows XRD patterns of as-cast Nb = 0.05 (top, black), Nb = 0.1 (middle, red), Nb = 0.2 (middle, green) and Nb = 0.5 (blue, bottom) with the peaks indexed. Appendix D shows individual XRD patterns of the as-cast alloys, showing the observed pattern and calculated fit after pseudo-Rietveld refinement.

From XRD analysis, the same three phases were identified in the as-cast alloys:

- C14 Laves phase (hexagonal MgZn2 structure with space group *P63/mmc*).
- BCC phase (space group *Im-3m).*
- FCC oxide phase (space group *Fd-3m).*

Refinement of the structures are based on those proposed for the C14 Laves phase by Mitrokhin et al., (2003) and the BCC and FCC oxide by Hout et al., (1995). Table 9.3 shows crystal structure refinement results for as-cast Nb = 0.05, Nb = 0.1, Nb = 0.2 and Nb = 0.5.

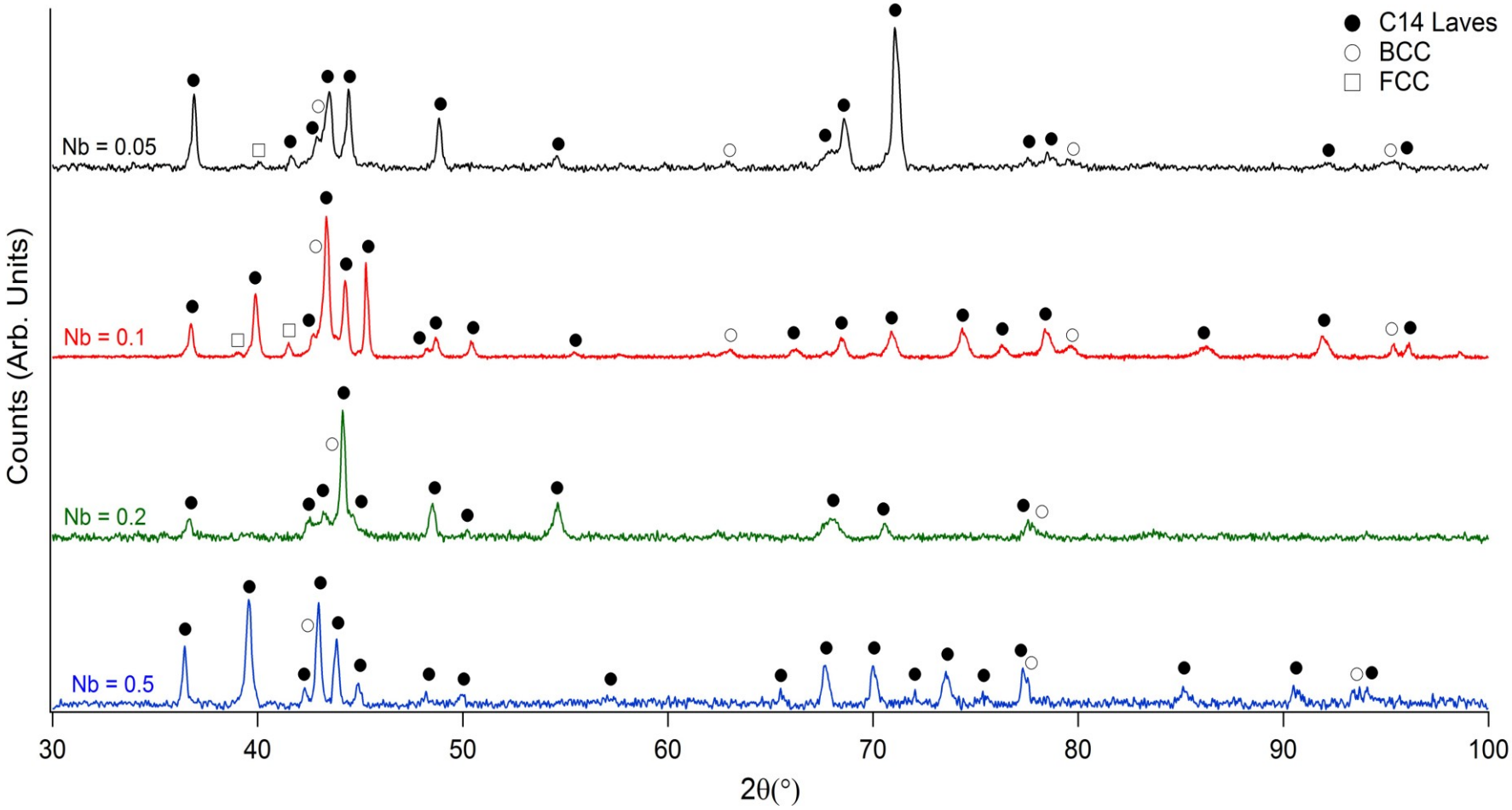

Figure 9.9 XRD patterns of as-cast Nb = 0.05 (top, black), Nb = 0.1 (middle, red), Nb = 0.2 (middle, green) and Nb = 0.5 (bottom, blue) with peaks indexed.

Table 9.3 Crystal structure refinement results for as-cast Nb = 0.05, Nb = 0.1, Nb = 0.2 and Nb = 0.5, showing lattice parameters and phase abundance. Note the values in parentheses are three standard deviations and refer to the last digit.

Alloy	As-Cast			
	Phase	Lattice Parameters		Abundance
Nb = 0.05	C14	*a*	4.869(3)	72(9)
		c	7.981(2)	
	BCC	*a* + *c*	2.973(7)	21(2)
	FCC	*a* + *c*	11.241(3)	6(4)
Nb = 0.1	C14	*a*	4.876(4)	74(2)
		c	7.992(7)	
	BCC	*a* + *c*	2.952(3)	19(9)
	FCC	*a* + *c*	11.283(6)	7(6)
Nb = 0.2	C14	*a*	4.882(5)	82(7)
		c	7.806(4)	
	BCC	*a* + *c*	2.964(7)	13(5)
	FCC	*a* + *c*	11.298	5(3)
Nb = 0.5	C14	*a*	4.932(3)	91(9)
		c	8.077(5)	
	BCC	*a* + *c*	2.966(2)	4(4)
	FCC	*a* + *c*	-	5(3)

From Figure 9.9, significant differences can be seen in the XRD traces of the alloys including variation in peak height. This indicates that site occupancy or ordering effects have occurred as a result of the compositional variation.

Although the same three phases are present in all four alloys, apart from Nb = 0.5 in which no FCC phase was identified, there are differences in the phase abundances. This is a result of the alloys having different outer shell electron configurations.

The C14 Laves phase appears to be the dominant phase in all three as-cast alloys occupying 72 wt% in Nb = 0.05, 72 wt% in Nb = 0.1, 82 wt% in Nb = 0.2 and 91 wt% in Nb = 0.5. This shows that there an increase in the abundance of the C14 Laves phase with increasing Nb content.

The unit cell volume of the C14 Laves phase is also effect by Nb content: Nb = 0.05 is 163.90(9) $Å^3$, Nb = 0.1 is 164.54(6) $Å^3$, Nb = 0.2 is 165.84(8) $Å^3$ and Nb = 0.5 is 169.95(11) $Å^3$. The relationship between Nb content (at%) and C14 Laves unit cell volume from the EDS and XRD values in shown in Figure 9.10.

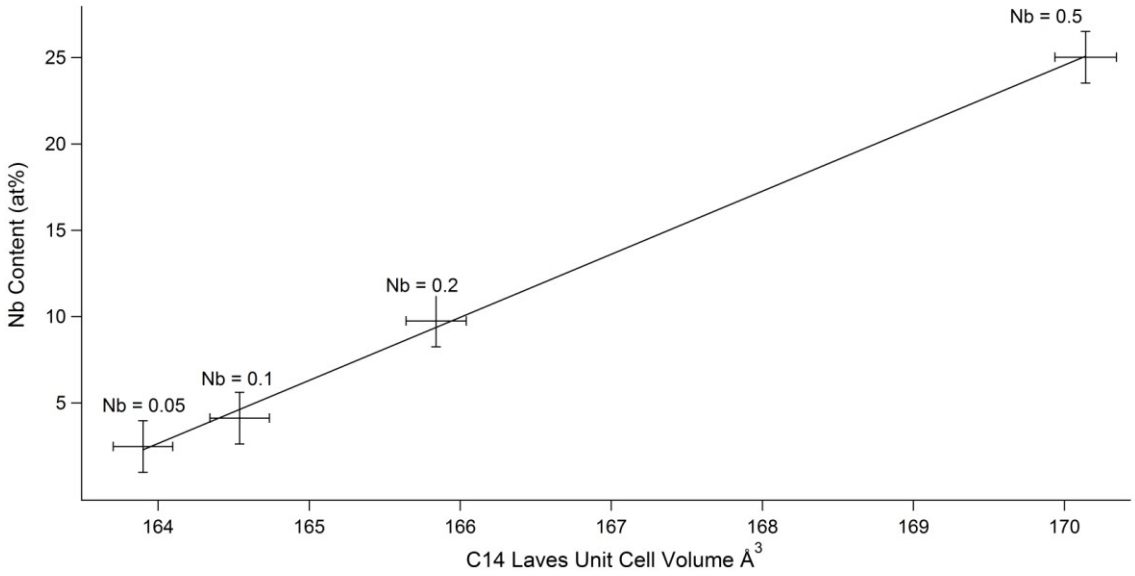

Figure 9.10 Correlation between C14 Laves unit cell volume vs. Nb-content (area at%) in $Ti_{0.5}V_{0.5-x}Nb_xMn$, where x = 0.05, 0.1, 0.2 and 0.5.

From Figure 9.10 is can be seen that an increase in Nb content results in an increase in the C14 Laves unit cell volume. This is due to Nb having a larger metallic radius than

V: 1.46 vs. 1.35 Å. This subsequently explains the increase in lattice parameter with increasing Nb content.

The unit cell volume of the BCC phase in Nb = 0.05 is 26.27(11) $Å^3$, Nb = 0.1 is 25.73(8) $Å^3$, Nb = 0.2 is 25.26(5) $Å^3$ and Nb = 0.5 is 26.09(6) $Å^3$. This indicates that the BCC is not as sensitive to changes in Nb content as the C14 Laves phase.

Based on the XRD analysis and the phases identified during SEM analysis, these results indicate that in Nb = 0.05, Nb = 0.1 and Nb = 0.2 the light area, which appears to be the dominant phase in the micrographs, corresponds to the C14 Laves phase, the grey phase corresponds to the BCC phase and the minor FCC phase appears as the dark dendritic phase. In Nb = 0.5 the grey phase is dominant phase which suggests that this is the C14 Laves phase, the light phase corresponds to the BCC phase and the dark dendritic phase is the FCC phase.

9.3 Characterisation of Heat Treated Alloys

The alloys were characterised after heat treatment to confirm composition and to ensure the alloys were fully homogenous.

9.3.1 SEM/EDS on Heat Treated Alloys

Figures 9.11 - 9.18 show BEI images of heat treated alloys 1, 2 and 3 at low (x 500) and high (x 1000) magnification.

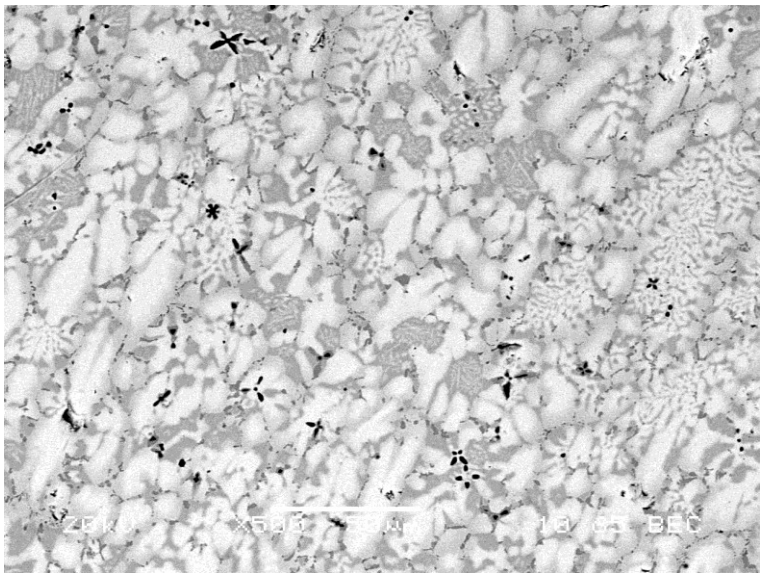

Figure 9.11 SEM BEI image of heat treated Nb = 0.05 (x 500).

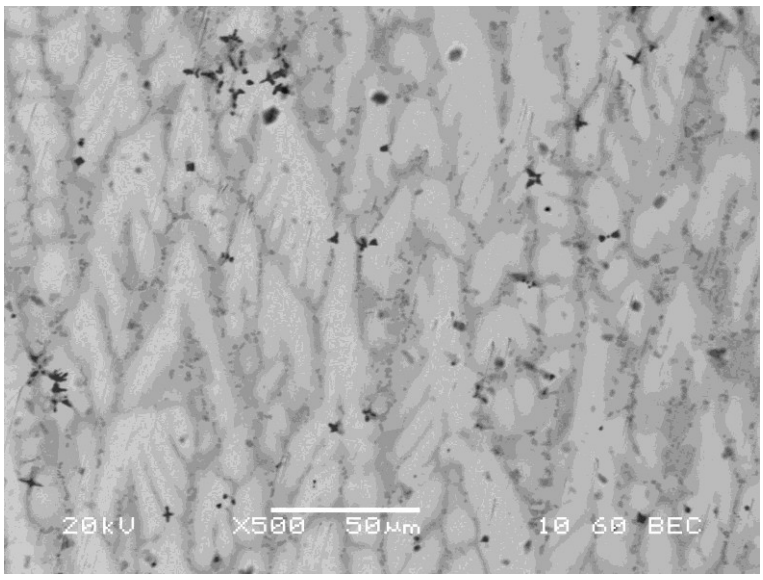

Figure 9.12 SEM BEI image of heat treated Nb = 0.1 (x 500).

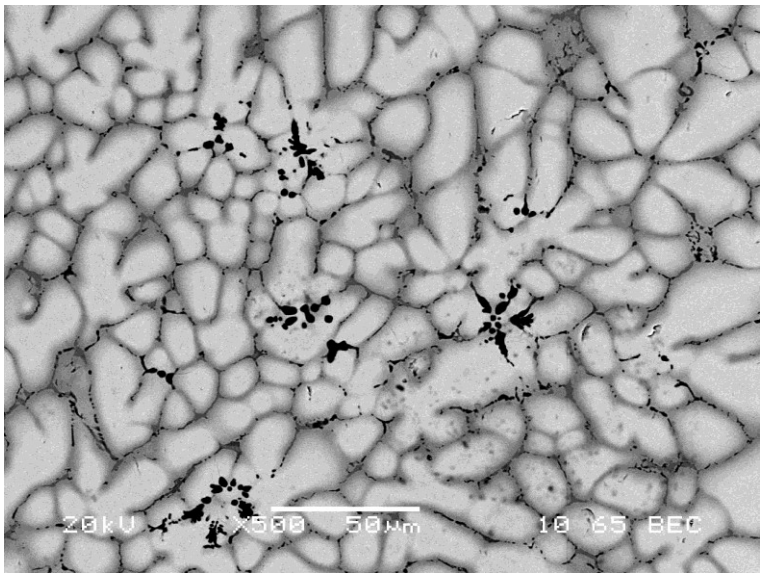

Figure 9.13 SEM BEI image of heat treated Nb = 0.2 (x 500).

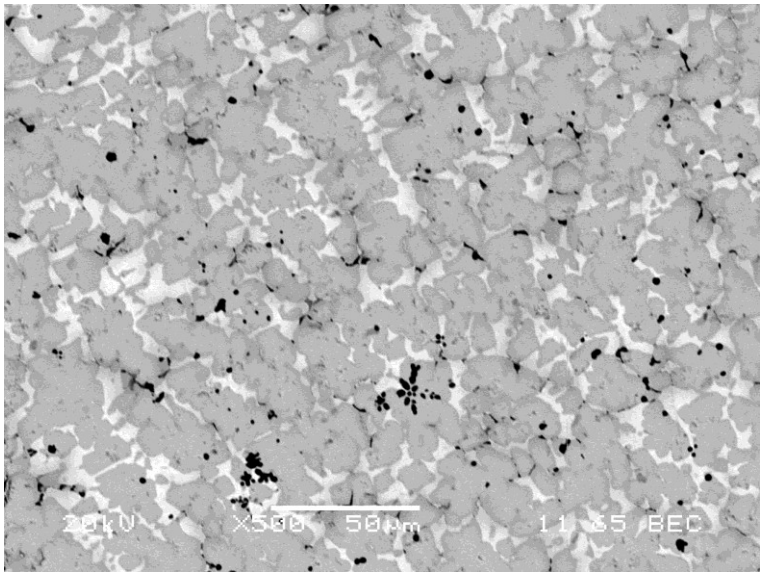

Figure 9.14 SEM BEI image of heat treated Nb = 0.5 (x 500).

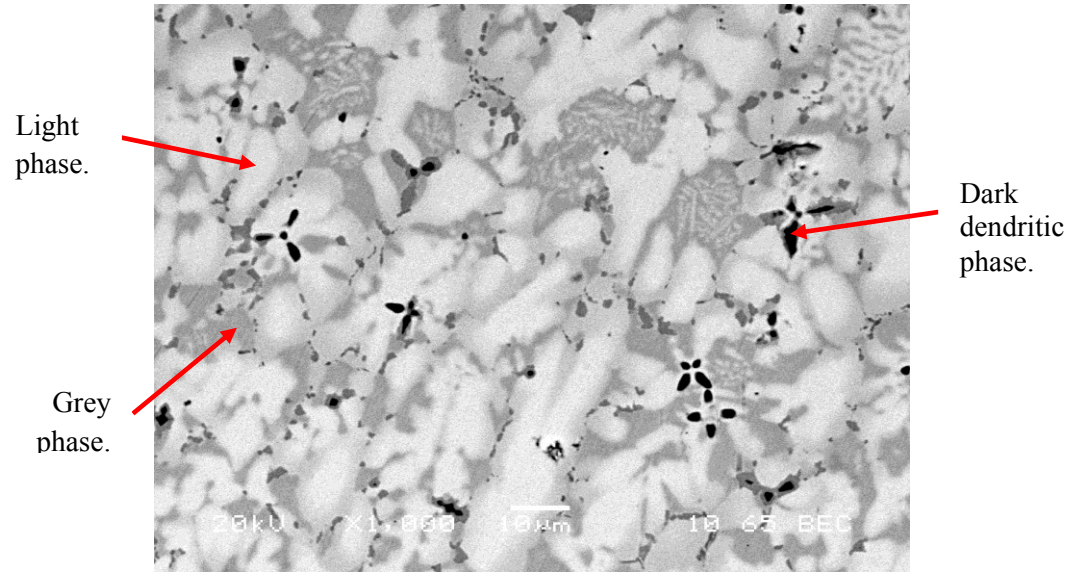

Figure 9.15 SEM BEI image of heat treated Nb = 0.05 (x 1000).

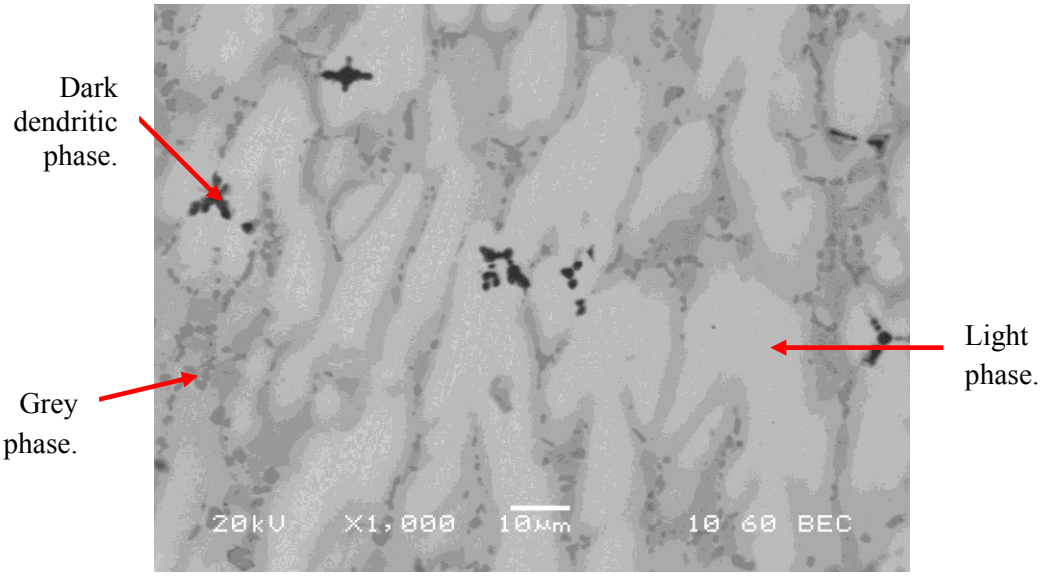

Figure 9.16 SEM BEI image of heat treated Nb = 0.1 (x 1000).

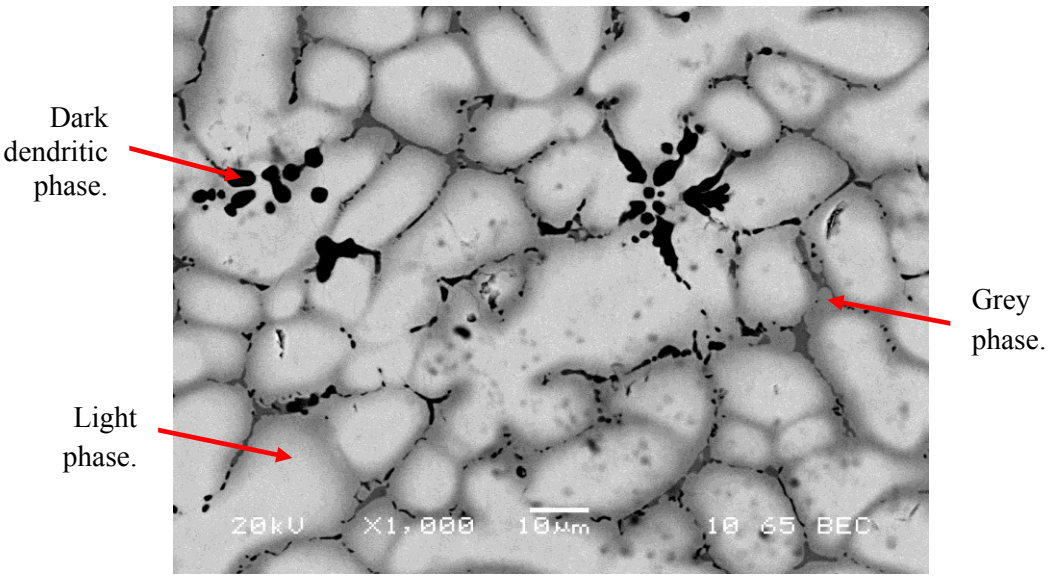

Figure 9.17 SEM BEI image of heat treated Nb = 0.2 (x 1000).

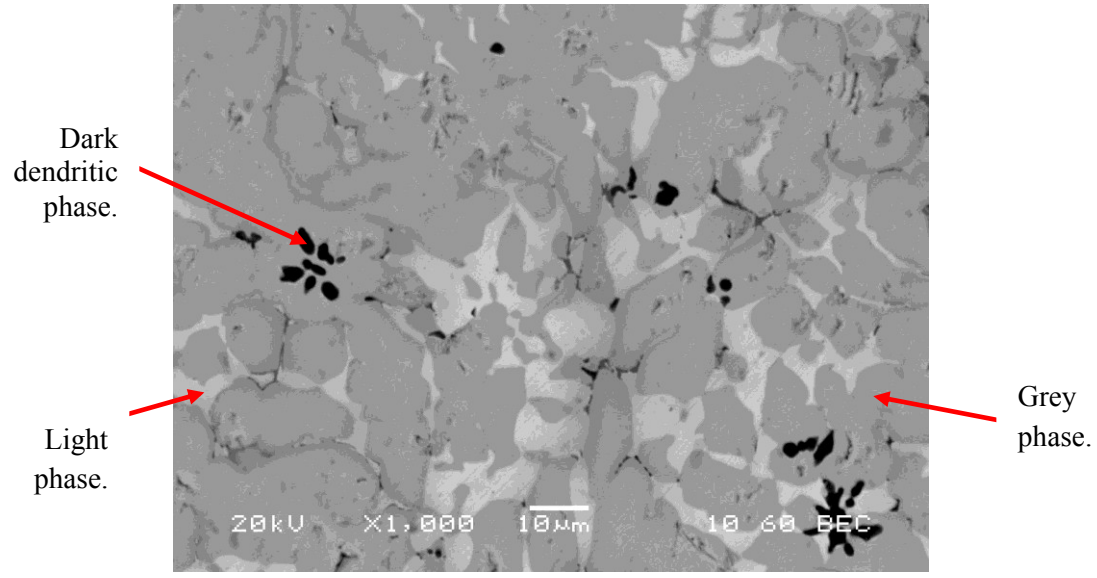

Figure 9.18 SEM BEI image of heat treated Nb = 0.5 (x 1000).

Heat treatment was performed on the arc-melted ingots to minimise any compositional heterogeneities associated with segregation of the elements. During the process the alloys are exposed to high temperatures for over 6 hours which may result in significant grain growth.

In Figures 9.11 - 9.18 the same three phases can be identified as the as-cast alloys but the grains generally appear bigger in size in all four alloys. This can be explained by the slow cooling rate at the end of the heat treatment process.

Coring can still be seen in the heat treated micrographs of Nb = 0.1 and Nb = 0.2. This indicates that longer heat treatment times are required to ensure the alloys are fully homogenous.

EDS analysis was performed on the heat treated alloys to identify the composition of these phases, with the results shown in Table 9.4. It should be noted that the results shown are in atomic percent (at %).

Table 9.4 Average EDS analysis on heat treated Nb = 0.05, Nb = 0.1, Nb = 0.2 and Nb = 0.5. Note analysis was carried out by taking an average of three different areas/points within BEI images of heat treated alloys.

Alloy	Phase Location	Ti	σ	V	σ	Nb	σ	Mn	σ	Average Composition Ratio (Ti/V/Nb/Mn)
Heat-treated Nb = 0.05	Area	26.38	6.3	22.29	7.2	2.33	7.1	49	6.8	0.54/0.45/0.05/1
	Light	26.18	6.6	18.36	6.2	4.59	6.8	51.03	7.3	0.51/0.36/0.08/1
	Grey	19.24	7.5	34.63	6.8	0.8	6.9	44.87	7.1	0.43/0.77/0.02/1
	Dark	64.78	6.3	9.89	6.4	1	7.2	24.33	7.5	2.66/0.41/0.04/1
Heat-treated Nb = 0.1	Area	27.08	6.8	20.33	7.2	4.38	7.3	48.21	6.5	0.56/0.42/0.09/1
	Light	23.8	7.1	18.3	6.7	7.67	6.3	50.27	6.5	0.47/0.36/0.15/1
	Grey	20.14	6.5	35.81	7.4	1.01	7.8	43.04	7.1	0.47/0.83/0.02/1
	Dark	61.57	6.2	10.37	6.7	2.71	6.1	25.35	6.9	2.43/0.41/0.11/1
Heat-treated Nb = 0.2	Area	27.07	6.8	15.84	6.3	8.91	6.7	48.18	6.1	0.56/0.33/0.19/1
	Light	20.59	7.5	14.96	6.4	12.83	7.3	51.46	6.7	0.40/0.29/0.25/1
	Grey	31.04	7.6	16.78	7.1	4.48	6.9	47.7	6.3	0.65/0.35/0.09/1
	Dark	89.03	6.5	3.27	6.2	1.9	7.7	5.8	7.6	15.35/0.56/0.33/1
Heat-treated Nb = 0.5	Area	26.43	7.9	0	-	22.34	6.8	50.24	6.5	0.51/0/0.44/1
	Light	38.36	6.2	0	-	37.17	6.5	24.82	7.2	1.55/0/1.50/1
	Grey	18.09	6.8	0	-	23.86	7.1	58.76	6.5	0.31/0/0.41/1
	Dark	80.11	7.1	0	-	8.65	6.8	11.24	7.1	7.13/0/0.77/1

The area analysis shows that the average composition for heat treated Nb = 0.05 is $Ti_{0.54}V_{0.45}Nb_{0.05}Mn_1$, Nb = 0.1 is $Ti_{0.56}V_{0.42}Nb_{0.09}Mn_1$, Nb = 0.2 is $Ti_{0.56}V_{0.33}Nb_{0.19}Mn_1$ and Nb = 0.5 is $Ti_{0.51}Nb_{0.44}Mn_1$.

In the heat treated alloys, similar to the as-cast alloys, in Nb = 0.05 and Nb = 0.1 the light phase is richer in Nb and Mn, grey phase is richer in V and dark phase is richer in Ti as a result of the different atomic masses of the elements.

In Nb = 0.2 the light phase is richer in Nb (8.91 vs. 12.25 at%) and Mn (48.18 vs. 51.46 at%), grey phase richer in Ti (27.07 vs. 31.04 at%) and dark phase rich in Ti (27.07 vs. 89.03 at%).

Finally, in Nb = 0.5 the light phase is richer in Ti (26.43 vs. 38.36 at%) and Nb (22.34 vs. 36.83 at%), grey phase is richer in Mn (50.24 vs. 59.15 at%) and dark phase is also richer in Ti (26.43 vs. 80.11 at%).

9.3.2 XRD on Heat Treated Alloys

Figure 9.19 shows XRD patterns of heat treated Nb = 0.05 (top, black), Nb = 0.1 (middle, red), Nb = 0.2 (middle, green) and Nb = 0.5 (blue, bottom) with the peaks indexed. Appendix D shows individual XRD patterns of the heat treated alloys, showing the observed pattern and calculated fit after pseudo-Rietveld refinement. The same three phases are identified in all the heat treated alloys.

Table 9.5 shows crystal structure refinement results for the heat treated alloys.

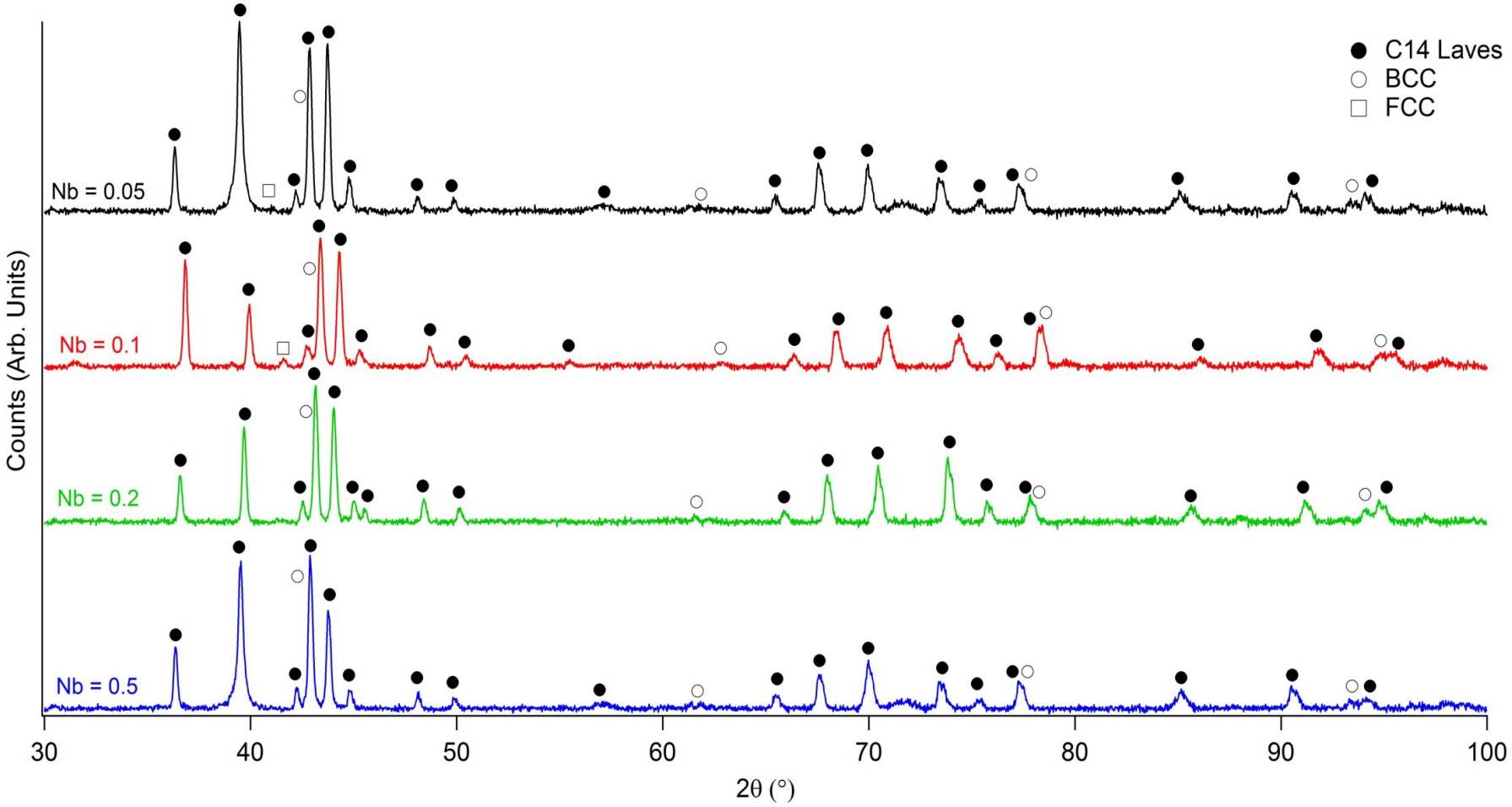

Figure 9.19 XRD patterns of heat treated Nb = 0.05 (top, black), Nb = 0.1 (middle, red), Nb = 0.2 (middle, green) and Nb = 0.5 (bottom, blue) with peaks indexed.

Table 9.5 Crystal structure refinement results for heat treated alloys (values on right) in comparison to as-cast alloys. Note the values in parentheses are three standard deviations and refer to the last digit.

Alloy	As-cast				Heat Treated			
	Phase	Lattice Parameters		Abundance	Phase	Lattice Parameters		Abundance
Nb = 0.05	C14	a	4.869(3)	72(9)	C14	a	4.928(2)	73(11)
		c	7.981(2)			c	8.068(3)	
	BCC	a + c	2.973(7)	21(2)	BCC	a + c	2.822(9)	19(6)
	FCC	a+ c	11.241(3)	6(4)	FCC	a+ c	11.811(6)	8(5)
Nb = 0.1	C14	a	4.876(4)	74(2)	C14	a	4.883(2)	81(8)
		c	7.992(7)			c	8.004(4)	
	BCC	a + c	2.952(3)	19(9)	BCC	a + c	2.963(2)	13(6)
	FCC	a+ c	11.283(6)	7(6)	FCC	a+ c	11.268(6)	6(4)
Nb = 0.2	C14	a	4.882(5)	82(7)	C14	a	4.904(2)	88(9)
		c	7.806(4)			c	8.043(3)	
	BCC	a + c	2.964(7)	13(5)	BCC	a + c	2.813(5)	7(6)
	FCC	a+ c	11.298	5(3)	FCC	a+ c	11.336(2)	5(3)
Nb = 0.5	C14	a	4.931(3)	91(9)	C14	a	4.936(2)	92(5)
		c	8.077(5)			c	8.081(3)	
	BCC	a + c	2.966(2)	4(4)	BCC	a + c	2.962(6)	3(2)
	FCC	a+ c	11.286(4)	5(3)	FCC	a+ c	11.304(2)	5(6)

Again, the C14 Laves phase appears to be the dominant phase in all three heat treated alloys occupying; 73 wt% in Nb = 0.05, 81 wt% in Nb = 0.1, 88 wt% in Nb = 0.2 and 92 wt% in Nb = 0.5. This shows an increase in C14 Laves phase abundance in comparison to the as-cast alloys and subsequently results in a decrease in the BCC phase abundance after heat treatment.

The unit cell volumes of the C14 Laves phase are 163.97(6) $Å^3$, 165.40(9) $Å^3$, 167.54(11) $Å^3$ and 170.14(7) $Å^3$ in heat treated Nb = 0.05, Nb = 0.1, Nb = 0.2 and Nb = 0.5, respectively. In comparison with the as-cast alloys this is shows an increase of between 0.07 and 1.7 $Å^3$ in the alloys after heat treatment.

There is also an increase in the unit cell volume of the BCC phase in the heat treated alloys: Nb = 0.05 increases to 26.86(11) $Å^3$, Nb = 0.1 increases to 25.87(4) $Å^3$, Nb = 0.2 increases to 25.47(3) $Å^3$ and Nb = 0.5 increases to 26.73(3) $Å^3$. This shows an increase of between 0.14 and 0.64 $Å^3$ in the BCC phase unit cell volume of the heat treated alloys.

Differences in metallic radii of the transition metal elements means that different substitutions of the B-site V, Nb and Mn elements take place. In V the metallic radii is 1.35 Å, Nb is 1.46 Å and Mn is 1.27 Å.

Looking at the difference in composition (at%) of the C14 Laves phase and BCC phase between the as-cast and heat treated alloys from the EDS data it is possible to calculate which elements have increased or decreased. This gives an indication to which substitutions have taken place within in the respective unit cell after heat treatment (see Appendix D).

The increase in the C14 Laves phase unit cell volume in Nb = 0.05 can be attributed to the substitution of 1 V atom for 1 Mn atom during the heat treatment process. This is because V has a larger metallic radius than Mn. In Nb = 0.1 the increase in the C14 Laves phase unit cell volume is a result of substitution of Nb atoms for 2 Mn atoms. Substitution of 1 Nb atom for 1 V atom in Nb = 0.5 has also resulted in an increase in the C14 Laves phase unit cell volume.

In Nb = 0.05 the increase in the unit cell volume of the BCC phase can be attributed to substitution of 1 V atom for 1 Mn atom. In Nb = 0.2 there is an increase in the unit cell

volume of the BCC phase as a result of substitution of 1 Nb atom for 1 V atom. The increase in BCC phase unit cell volume in Nb = 0.5 is a result of substitution of 1 Nb atom for 1 Mn atom.

In Nb = 0.1 there does not appear to be any significant differences in the composition of the grey BCC phase between the as-cast and heat treated alloy. This indicates that the reduction in the BCC phase unit cell volume may not be due to substitution but in fact an ordering effect on the B-site (Mn, V) *4f* or *2a* site upon annealing.

9.4 Characterisation of Hydrogen Sorption Properties

9.4.1 PCT Measurements

HTP measurements were performed at 303 K, 313 K, 323 K and 333 K up to 120 bar H_2 for Nb = 0.05, Nb = 0.1, Nb = 0.2 and Nb = 0.5 (Figures 9.20, 9.21, 9.22 and 9.23 respectively). For the measurements, 726 mg of Nb = 0.05, 610 mg of Nb = 0.1, 653 mg of Nb = 0.2 and 670 mg of Nb = 0.5 was loaded. Prior to measurements, an activation sequence was performed on all the heat treated alloys (see Project Experimental in Chapter 6). The isotherms shown are therefore the 2^{nd}, 3^{rd}, 4^{th} and 5^{th} cycle at 303 K, 313 K, 323 K and 333 K, respectively.

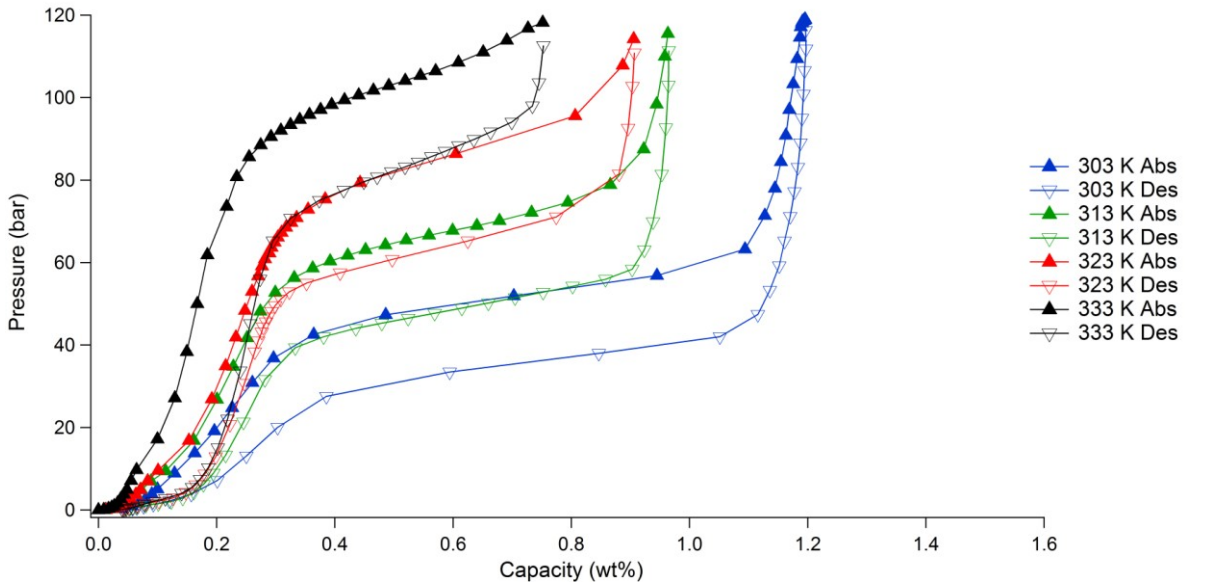

Figure 9.20 PCT measurement of Nb = 0.05 at 303 K (blue), 313 K (green), 323 K (red) and 333 K (black) showing absorption (upwards triangles) and desorption (downwards triangles) from 0.5 to 120 bar H_2.

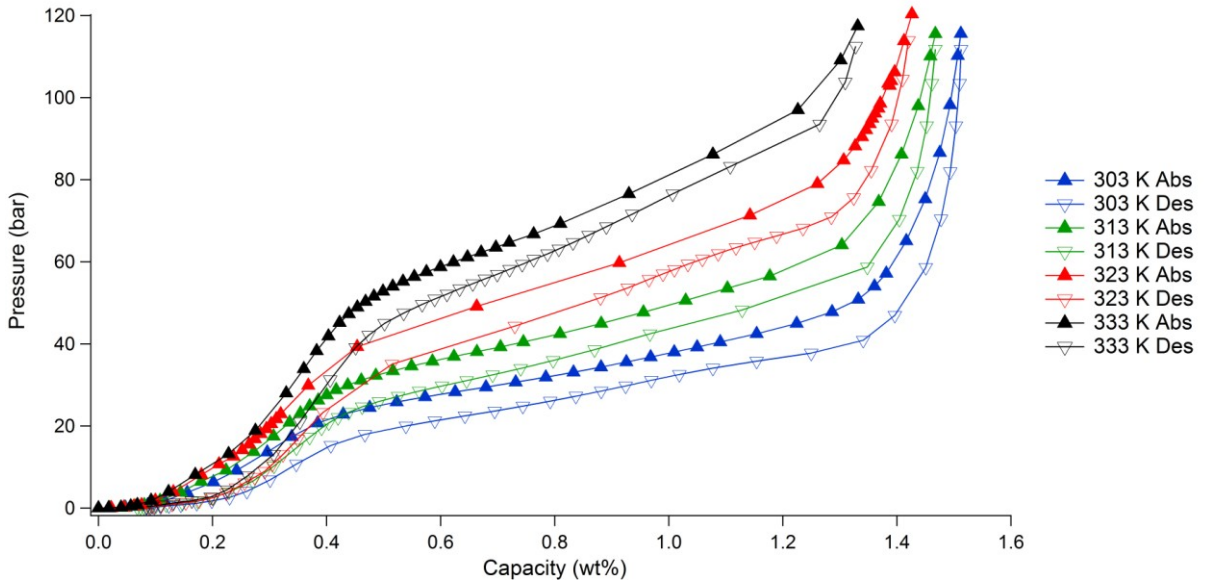

Figure 9.21 PCT measurement of Nb = 0.1 at 303 K (blue), 313 K (green), 323 K (red) and 333 K (black) showing absorption (upwards triangles) and desorption (downwards triangles) from 0.5 to 120 bar H_2.

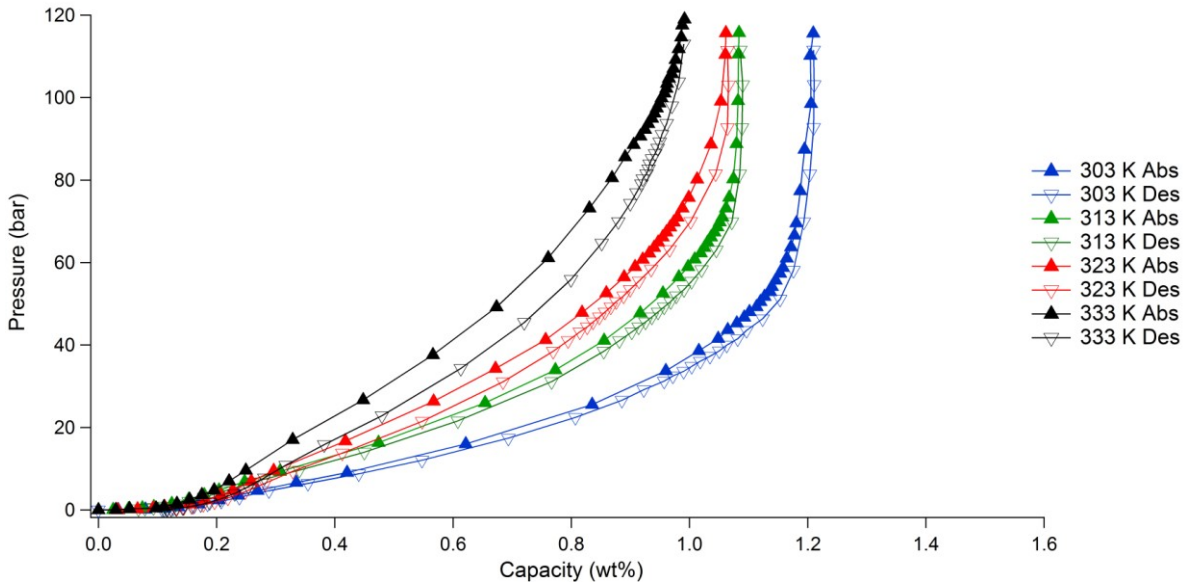

Figure 9.22 PCT measurement of Nb = 0.2 at 303 K (blue), 313 K (green), 323 K (red) and 333 K (black) showing absorption (upwards triangles) and desorption (downwards triangles) from 0.5 to 120 bar H_2.

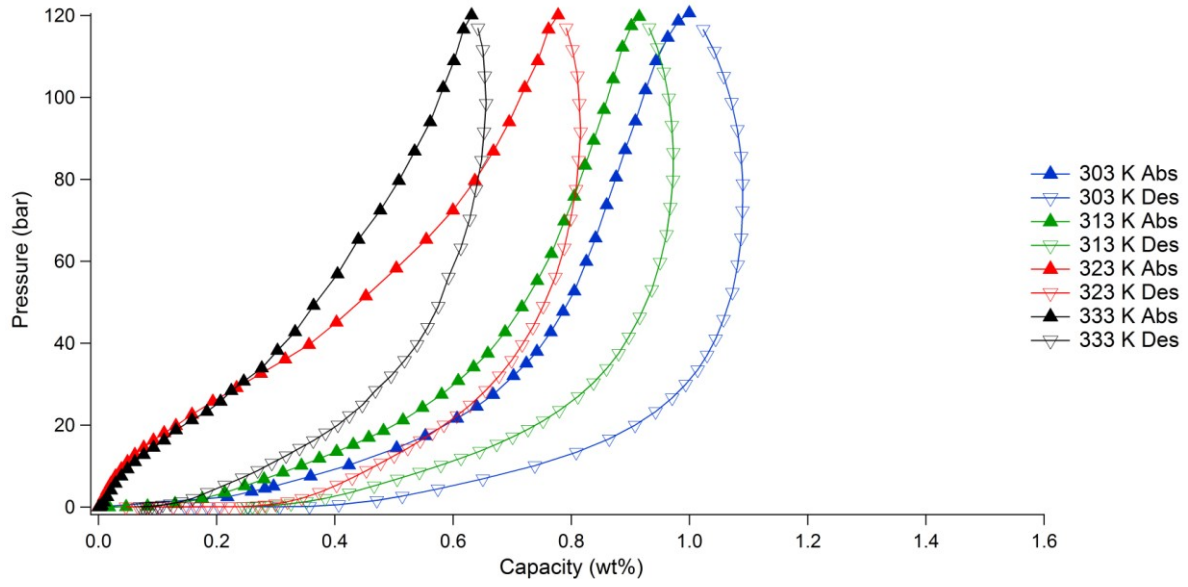

Figure 9.23 PCT measurement of Nb = 0.5 at 303 K (blue), 313 K (green), 323 K (red) and 333 K (black) showing absorption (upwards triangles) and desorption (downwards triangles) from 0.5 to 120 bar H_2.

Comparing Figures 9.20, 9.21, 9.22 and 9.23 the four alloys exhibit different hydrogen storage properties as a result of their different Nb contents: in the alloys where Nb ≥ 0.2 at% significant differences in uptake are observed.

In Nb = 0.05 the second plateau for absorption and desorption, which is responsible for the bulk of the uptake, is relatively flat in comparison to the other alloys. There is also a reasonable amount of hysteresis between the plateaus. At 333 K the alloy appears to be reaching critical temperature because the second absorption and desorption plateau becomes smaller, indicating that there is only a small $\alpha + \beta$ two phase region.

In Nb = 0.1 the second plateau during absorption and desorption is long and becomes more sloped with increasing temperature due to the increase in plateau pressures. In this alloy only a small amount of hysteresis is observed between absorption and desorption.

In Nb = 0.2 only one plateau is observed during absorption/desorption and uptake is observed until saturation is reached at around 60 bar. This behaviour is not typically observed for interstitial metal hydrides, where a discrete solid solution and thermodynamic plateau are observed. There is little hysteresis upon desorption indicating that the hydrogen is weakly bound within the structure and requires an overpressure to remain within the material. This would suggest a sorption mechanism not typical of a metal hydride, showing similarities to what has been observed with porous materials whereby the coverage is dependent upon the pressure. This behaviour may be explained by the large unit cell volume, and subsequent large interstitial volume resulting in weak binding energies of the hydrogen on these sites. Subsequent investigations into the bonding strength using techniques such as inelastic neutron scattering should be considered and will be discussed in the Future Work section of Chapter 12.

The sloping plateaus present in both Nb = 0.1 and Nb = 0.2 indicates inhomogeneity (Akiba & Iba, 1998). This confirms along with the SEM analysis that longer heat treatment times are required to fully homogenise these alloys.

Finally Nb = 0.5 shows only a very small plateau for absorption and desorption but still shows uptake up to 120 bar. At 323 and 333 K, the shape of the isotherms is significantly different from the lower temperatures up to around 30 bar. This indicates that between 0.5 and 30 bar the isotherms are not temperature dependent above 313 K. This suggests that uptake may be limited by kinetics, such as the hydrogen dissociation energy, rather than temperature. Large hysteresis occurs between absorption and desorption which indicates that initially more pressure is required for hydrogen to go into the interstitial sites. During desorption, the hydrogen becomes locked into interstitial sites at higher pressure so can only be released at low pressures. In addition, the shape of the isotherms suggest that saturation has not been reached up to 120 bar H_2.

Figure 9.24 shows a comparison of isotherms for all three heat treated alloys at 303 K up to 120 bar H_2. PCT properties, including capacity, plateau pressure and hysteresis, of all four alloys at 303 K are provided in Table 9.6.

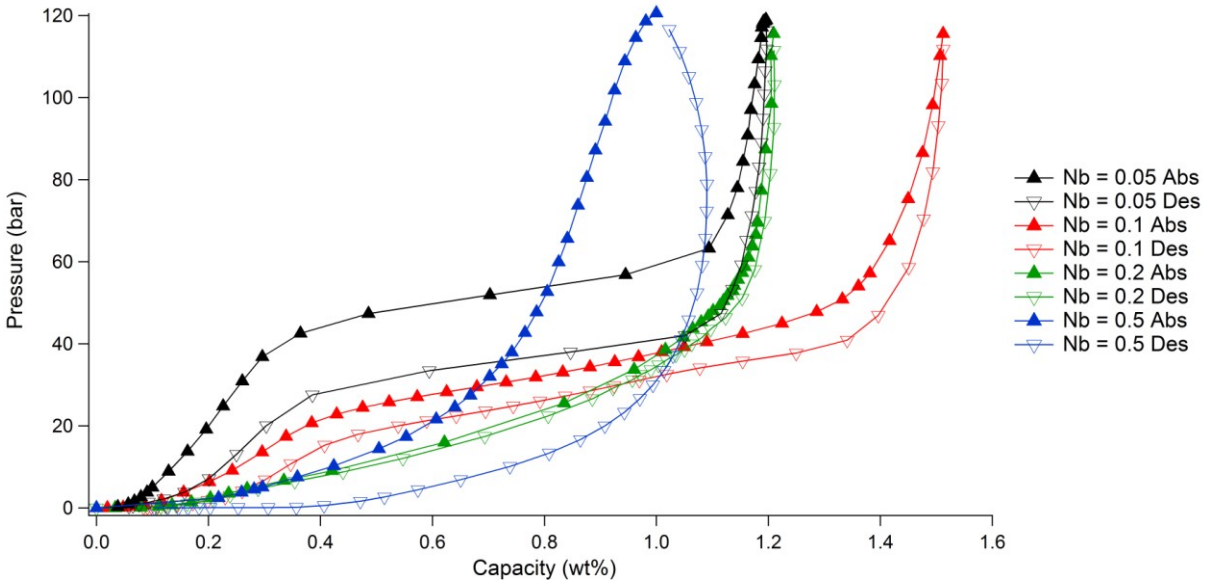

Figure 9.24 PCT measurement of Nb = 0.05 (black), Nb = 0.1 (red), Nb = 0.2 (green) and Nb = 0.5 (blue) showing absorption (upwards triangles) and desorption (downwards triangles) at 303 K from 0.5 to 120 bar H_2.

Table 9.6 Summary of capacity, plateau pressure and hysteresis data for Nb = 0.05, Nb = 0.1, Nb = 0.2, and Nb = 0.5 based on PCT isotherms at 303 K. Hysteresis factor: 0 = no hysteresis, 1 = large hysteresis. Note measured errors for capacity are estimated to be 0.05 wt% based on 3 PCT measurements using a Pd standard (see Appendix A).

Alloy	Maximum Capacity (wt%)	Reversible Capacity (wt%)	Abs Plateau P (bar)	Des Plateau P (bar)	Hysteresis Factor $Log(P_{Abs}/P_{Des})$
Nb = 0.05	1.26	1.21	42 - 62	42 - 28	0.172
Nb = 0.1	1.55	1.51	25 - 50	40 - 15	0.135
Nb = 0.2	1.25	1.21	1 - 45	45 - 1	0
Nb = 0.5	1.16	1.09	1 - 30	30 - 1	0

There is a significant difference in the shape of the isotherms and the plateau pressures for absorption and desorption in the alloys at 303 K.

In Nb = 0.05 and Nb = 0.1 at 303 K the first plateau in the absorption isotherm is present between 0 and 5 bar. In Nb = 0.2 and Nb = 0.5 there only appears to be one plateau during absorption and desorption.

Kinetic data taken from the mid-point plateau for absorption in Nb = 0.05, Nb = 0.1, Nb = 0.2 and Nb = 0.5 at 303 K is shown in Figures 9.25 – 9.28 respectively.

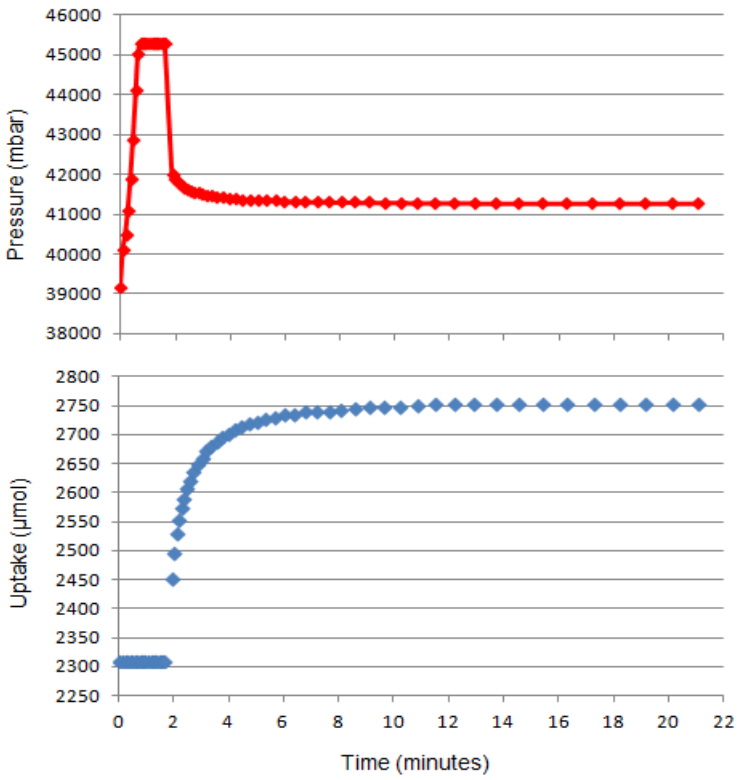

Figure 9.25 Kinetic data for Nb = 0.05 showing pressure (red) and uptake (blue) at the mid-point plateau for absorption at 303 K.

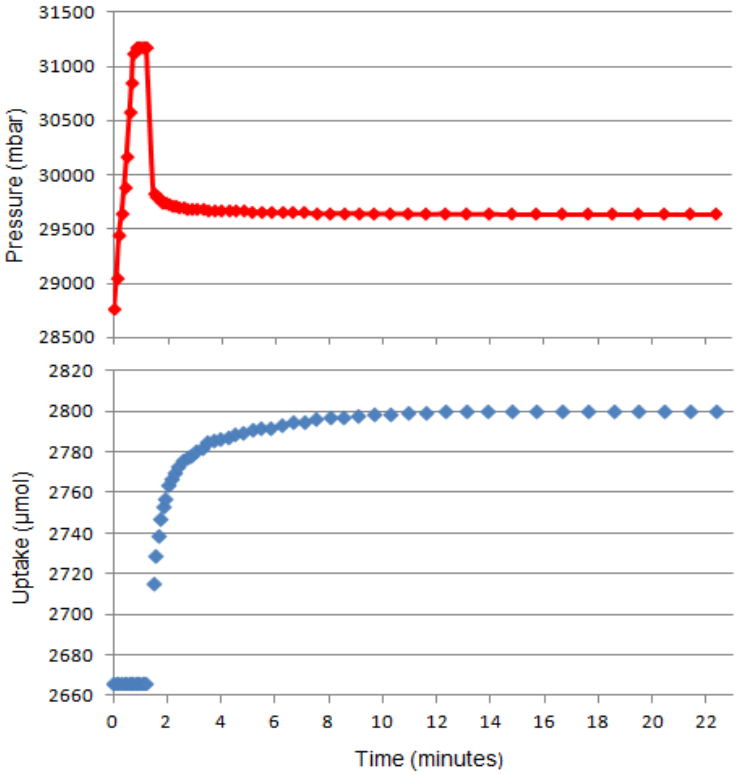

Figure 9.26 Kinetic data for Nb = 0.1 showing pressure (red) and uptake (blue) at the mid-point plateau for absorption at 303 K.

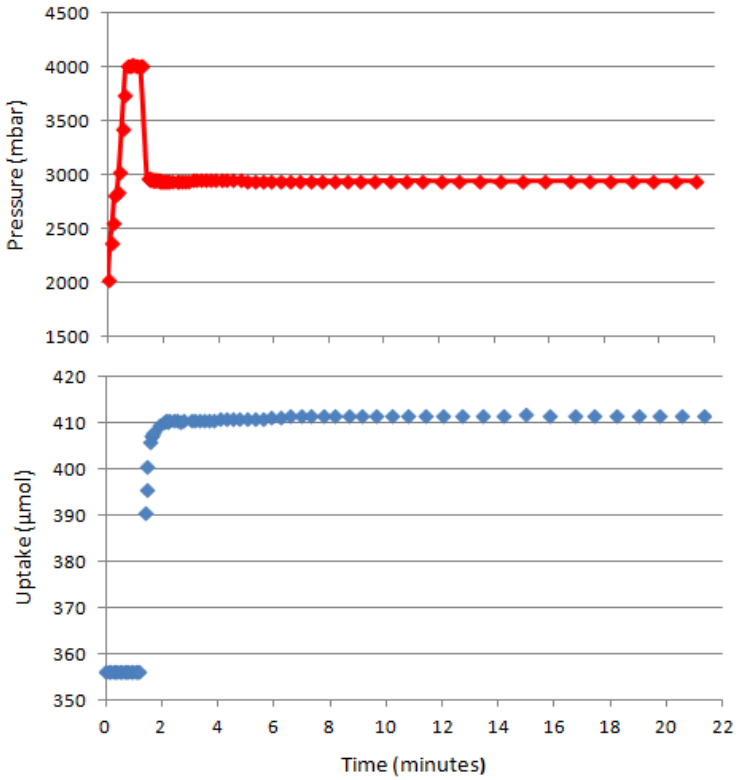

Figure 9.27 Kinetic data for Nb = 0.2 showing pressure (red) and uptake (blue) at the mid-point plateau for absorption at 303 K.

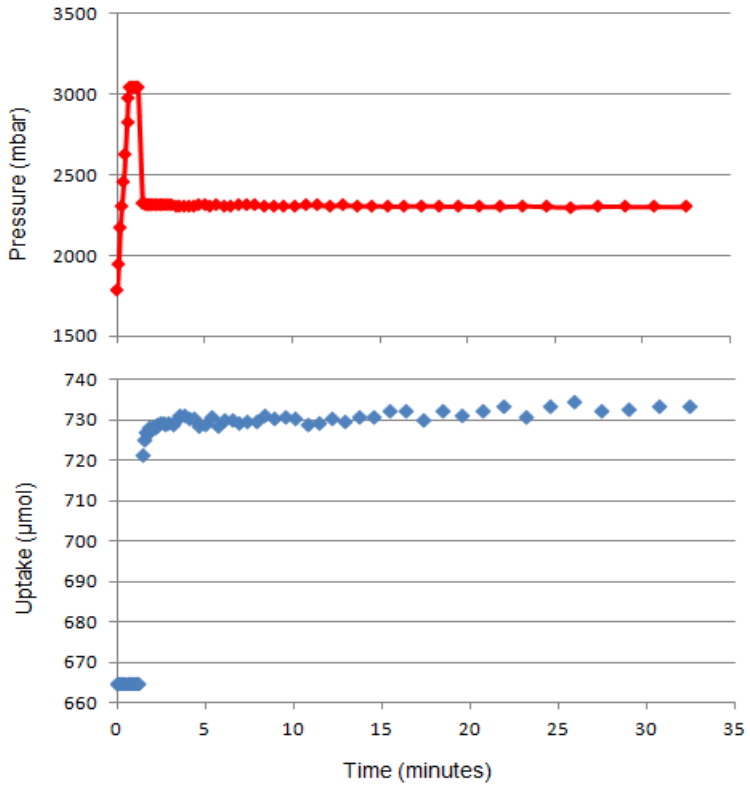

Figure 9.28 Kinetic data for Nb = 0.5 showing pressure (red) and uptake (blue) at the mid-point plateau for absorption at 303 K.

The kinetic data for the alloys shows that Nb = 0.05, Nb = 0.1 and Nb = 0.2 reach equilibrium between 0 and 22 minutes during absorption. However, from the kinetic data of Nb = 0.5 it is evident that equilibrium is not reached up to 35 minutes – as shown by the non-linear appearance of the uptake graph. This may explain the unusual shape of the isotherm for the Nb = 0.5 alloy and suggests that either longer equilibrium hold times are required or the tolerance of the fit to the asymptote needs to be increased for the alloy.

Van't hoff plots, calculated using data from Appendix D, showing hydrogen desorption for the alloys are shown in Figure 9.29 with the derived enthalpies and entropies in Table 9.7.

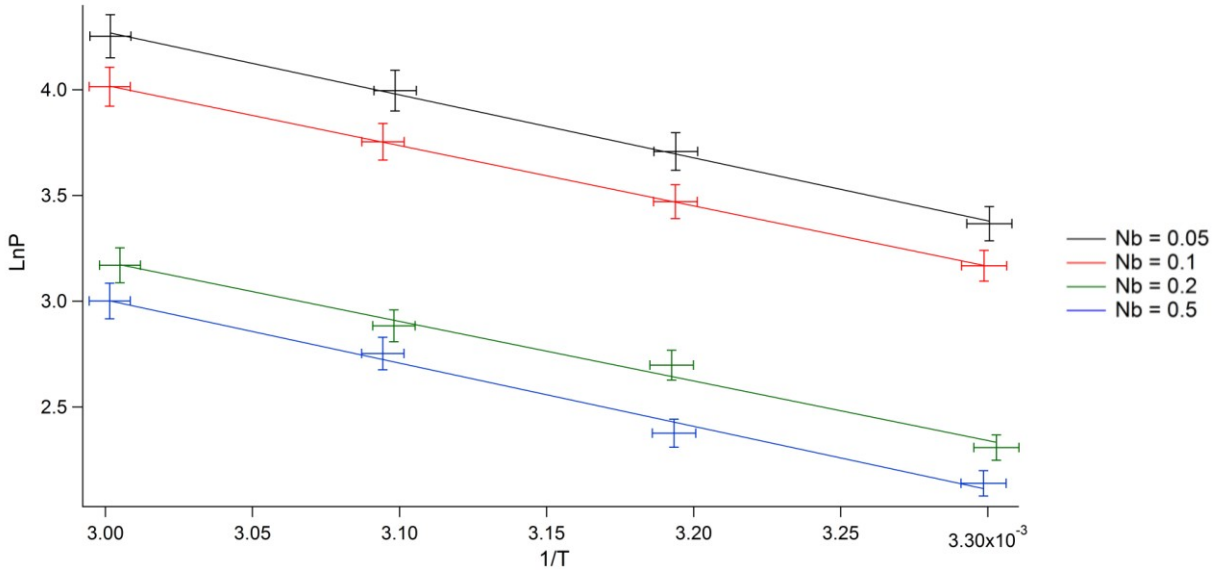

Figure 9.29 Van't hoff plot of Nb = 0.05, Nb = 0.1, Nb = 0.2 and Nb = 0.5 showing desorption (with associated errors).

Table 9.7 Enthalpy and Entropy data for desorption in Nb = 0.05 and Nb = 0.1

Alloy	ΔH (kJ/mol H_2)	ΔS (J/mol H_2)
Nb = 0.05	-25.71	109.73
Nb = 0.1	-23.68	104.48
Nb = 0.2	-23.41	96.72
Nb = 0.5	-23.19	99.52

The calculated desorption ΔH of all the alloys are within the target value for interfacing stores to PEM fuel cell applications; higher than -30 kJ/mol H_2 (Shibuya et al., 2008).

9.5 Characterisation of Hydrogen Cycled Alloys

9.5.1 SEM/EDS on Hydrogen Cycled Alloys

SEM images and EDS analysis was performed on the hydrogen decrepitated powders of Nb = 0.05, Nb = 0.1, Nb = 0.2 and Nb = 0.5 after hydrogen sorption measurements. SEM SEI images (x 500 magnification) are shown in Figures 9.30 - 9.33. Note, all the alloys were cycled with hydrogen under the same conditions (see Chapter 6).

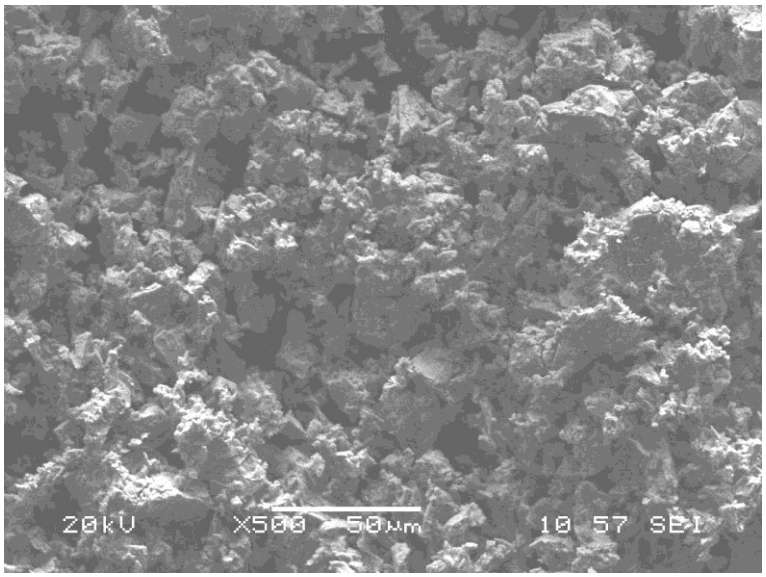

Figure 9.30 SEM SEI image of hydrogen cycled Nb = 0.05 (x 500).

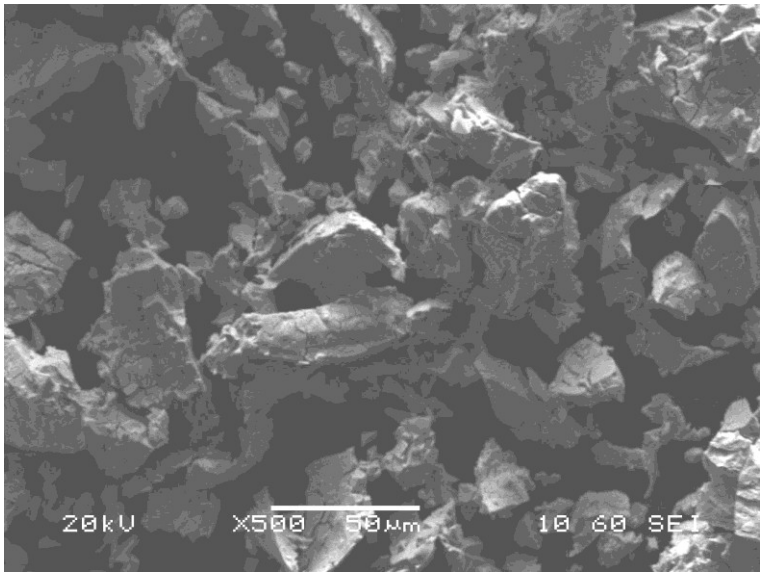

Figure 9.31 SEM SEI image of hydrogen cycled Nb = 0.1 (x 500).

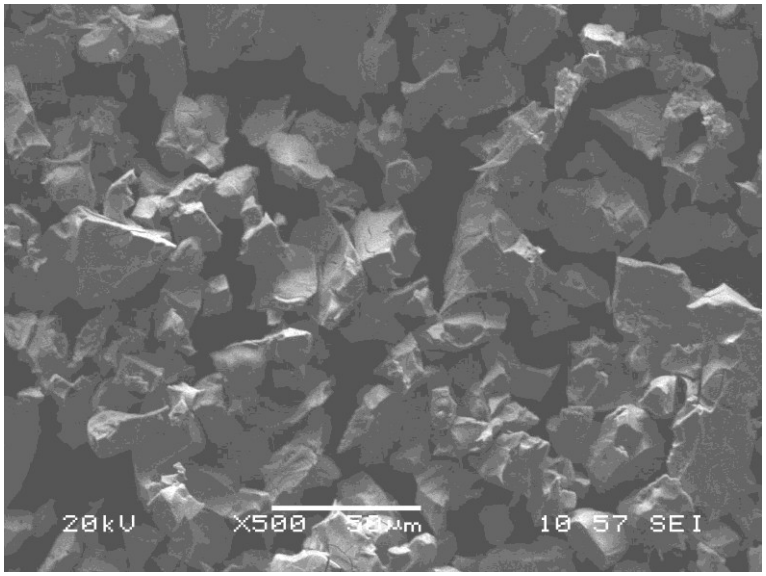

Figure 9.32 SEM SEI image of hydrogen cycled Nb = 0.2 (x 500).

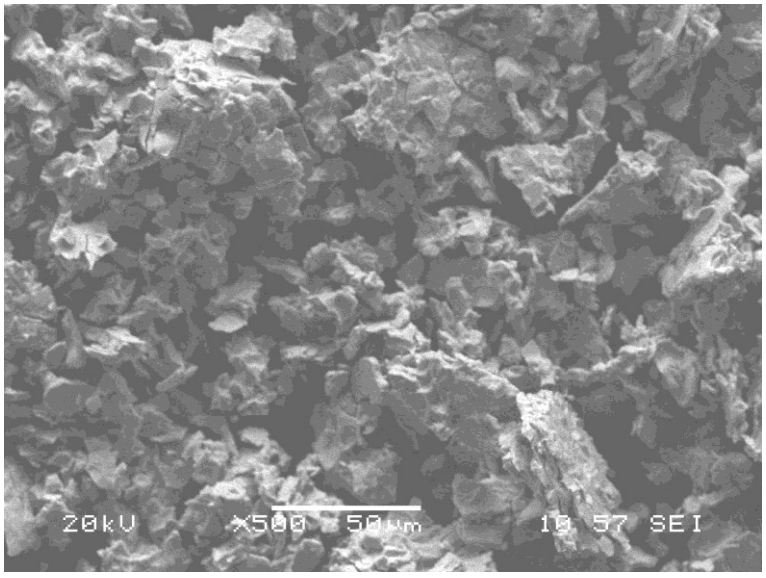

Figure 9.33 SEM SEI image of hydrogen cycled Nb = 0.5 (x 500).

SEM micrographs of the hydrogen cycled powders show significant differences, indicating that different fracture mechanisms may have occurred upon exposure to hydrogen.

In Nb = 0.05 small rough-edged particles which appear to agglomerate together, characteristic of a brittle intergranular fracture, can be seen. The micrograph of hydrogen cycled Nb = 0.1 shows large particles with smooth edges and cracks within the particles which suggest a ductile fracture has occurred. Nb = 0.2 shows fairly uniform particles with rough edges which would be expected from a brittle fracture. Finally, in Nb = 0.5 the micrograph appears to be similar to Nb = 0.05 but shows larger rough-edged particles which are consistent with a brittle intergranular fracture. The larger particles seen in Nb = 0.5 may explain why the capacity was low in comparison to the other alloys: there would have been less surface area for the hydrogen atoms to enter the interstitial sites.

EDS analysis was carried out on different areas/spots in the powdered alloys. The average composition of hydrogen cycled Nb = 0.05 is $Ti_{0.57}V_{0.44}Nb_{0.05}Mn_1$, Nb = 0.1 is $Ti_{0.58}V_{0.43}Nb_{0.07}Mn_1$, Nb = 0.2 is $Ti_{0.64}V_{0.36}Nb_{0.16}Mn_1$ and Nb = 0.5 is $Ti_{0.52}Nb_{0.37}Mn_1$.

9.5.2 XRD on Hydrogen Cycled Alloys

XRD patterns of hydrogen decrepitated powders of Nb = 0.05, Nb = 0.1, Nb = 0.2 and Nb = 0.5 after hydrogen sorption measurements are shown in Figure 9.34. Appendix D shows individual XRD patterns of the hydrogen cycled alloys, showing the observed pattern and calculated fit after pseudo-Rietveld refinement.

Table 9.8 shows crystal structure refinement results for the hydrogen cycled alloys.

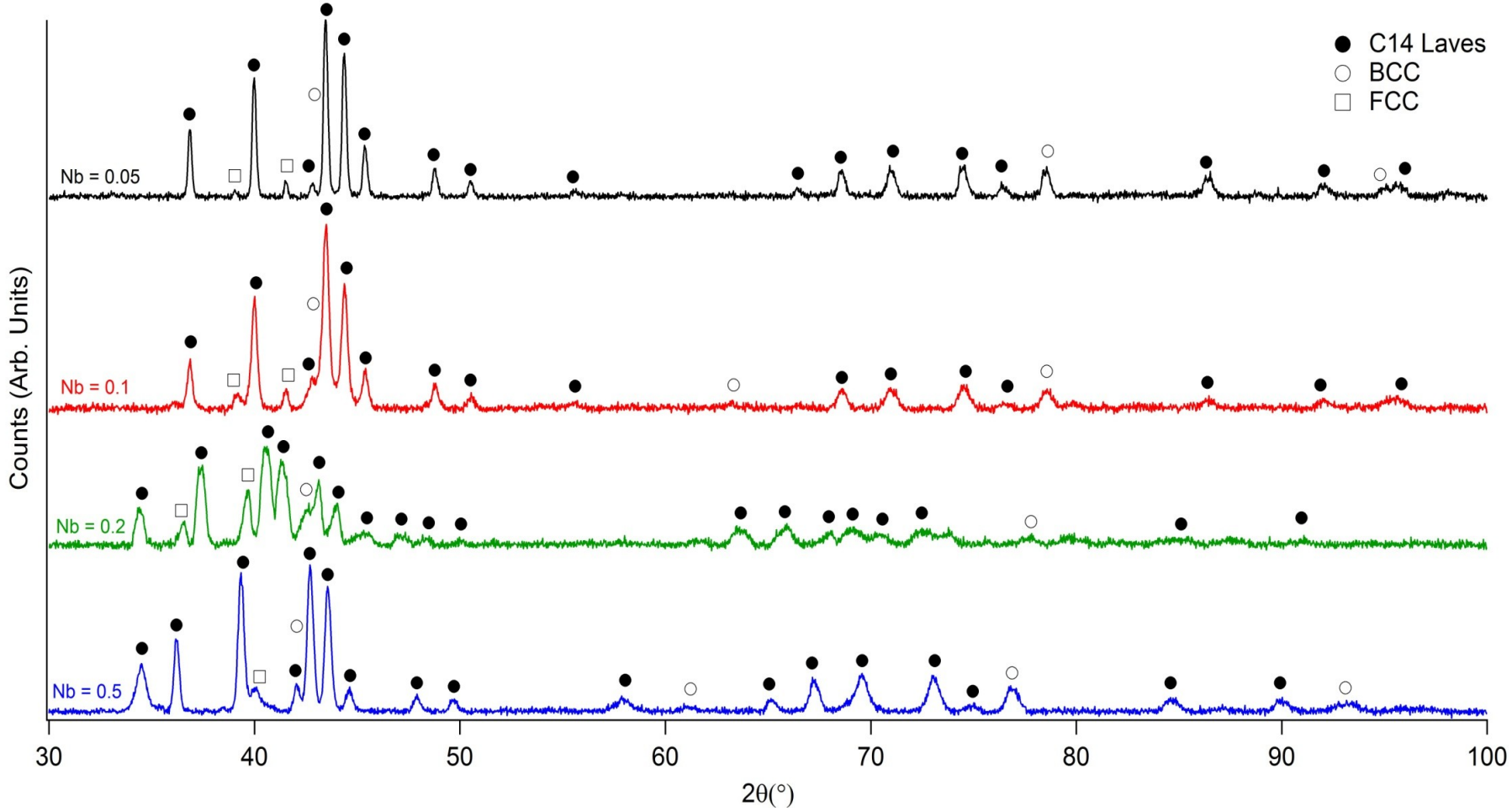

Figure 9.34 XRD patterns of hydrogen cycled Nb = 0.05 (top, black), Nb = 0.1 (middle, red), Nb = 0.2 (middle, green) and Nb = 0.5 (bottom, blue) with peaks indexed.

Table 9.8 Crystal structure refinement results for hydrogen cycled alloys (values on right) in comparison to heat treated alloys. Note the values in parentheses are three standard deviations and refer to the last digit.

Alloy	Heat Treated				Hydrogen Cycled			
	Phase	Lattice Parameters		Abundance	Phase	Lattice Parameters		Abundance
Nb = 0.05	C14	a	4.928(2)	73(11)	C14	a	4.936(4)	77(5)
		c	8.068(3)			c	80.075(6)	
	BCC	a + c	2.822(9)	19(6)	BCC	a + c	2.835(7)	16(9)
	FCC	a+ c	11.811(6)	8(5)	FCC	a+ c	11.805(3)	7(5)
Nb = 0.1	C14	a	4.883(2)	81(8)	C14	a	4.869(10)	80(4)
		c	8.004(4)			c	7.985(4)	
	BCC	a + c	2.963(2)	13(6)	BCC	a + c	2.973(7)	13(4)
	FCC	a+ c	11.268(6)	6(4)	FCC	a+ c	11.241(6)	7(2)
Nb = 0.2	C14	a	4.904(2)	88(9)	C14	a	7.911(2)	92(7)
		c	8.043(3)			c	8.052(7)	
	BCC	a + c	2.813(5)	7(6)	BCC	a + c	2.801(5)	3(3)
	FCC	a+ c	11.336(2)	5(3)	FCC	a+ c	11.317(8)	5(4)
Nb = 0.5	C14	a	4.936(2)	92(5)	C14	a	4.963(6)	97(7)
		c	8.081(3)			c	8.113(9)	
	BCC	a + c	2.962(6)	3(2)	BCC	a + c	2.924(4)	3(4)
	FCC	a+ c	11.304(2)	5(6)	FCC	a+ c	-	

XRD patterns similar to those of the heat treated alloys are observed in Nb = 0.05 and Nb = 0.1, however, significant differences can be seen in the patterns for hydrogen cycled Nb = 0.2 and Nb = 0.5. In particular, In Nb = 0.2, it appears as though the effect of exposure to hydrogen and heat during the activation sequence prior to PCT measurement may have broken down the lattice which may explain the unusual uptake behaviour.

In all four alloys, the C14 Laves phase remains the dominant phase occupying 77 wt%, 80 wt%, 92 wt% and 97 wt% for hydrogen cycled Nb = 0.05, Nb = 0.1, Nb = 0.2 and Nb = 0.5, respectively. This shows a small increase in the abundance of the C14 Laves phase upon cycling.

There is only a small change in the lattice parameters in the hydrogen cycled alloys which shows that the alloys possess good structural stability upon cycling with hydrogen.

The unit cell volume of the C14 Laves phase after cycling with hydrogen was found to increase in all four alloys: Nb = 0.05 is 164.01(7) $Å^3$, Nb = 0.1 is 165.86(3) $Å^3$, Nb = 0.2 is 168.23(9) $Å^3$ and Nb = 0.5 is 173.22(5) $Å^3$. This shows an increase of between 0.04 and 3.08 $Å^3$.

Similarly, the unit cell volume of the BCC phase also increased after cycling with hydrogen: Nb = 0.05 is 27.35(8) $Å^3$, Nb = 0.1 is 25.97(4) $Å^3$, Nb = 0.2 is 26.06(11) $Å^3$ and Nb = 0.5 is 28.04(5) $Å^3$. This shows an increase of between 0.1 and 2.31 $Å^3$.

Figure 9.35 shows the relationship between C14 Laves phase unit cell volume vs. desorption plateau pressure and Figure 9.36 for shows the relationship between BCC phase unit cell volume vs. desorption plateau pressure Nb = 0.05, Nb = 0.1, Nb = 0.2 and Nb = 0.5.

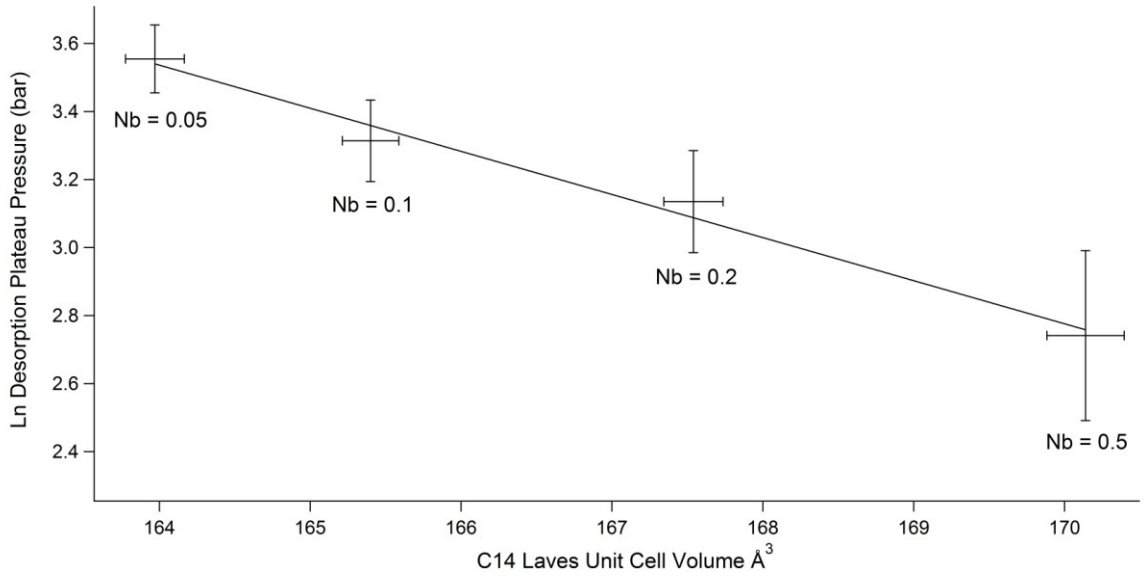

Figure 9.35 Correlation between C14 Laves unit cell volume (Å^3) vs. Desorption plateau pressure (bar) for Nb = 0.05, Nb = 0.1, Nb = 0.2 and Nb = 0.5. Note, line added between data points on for ease of understanding.

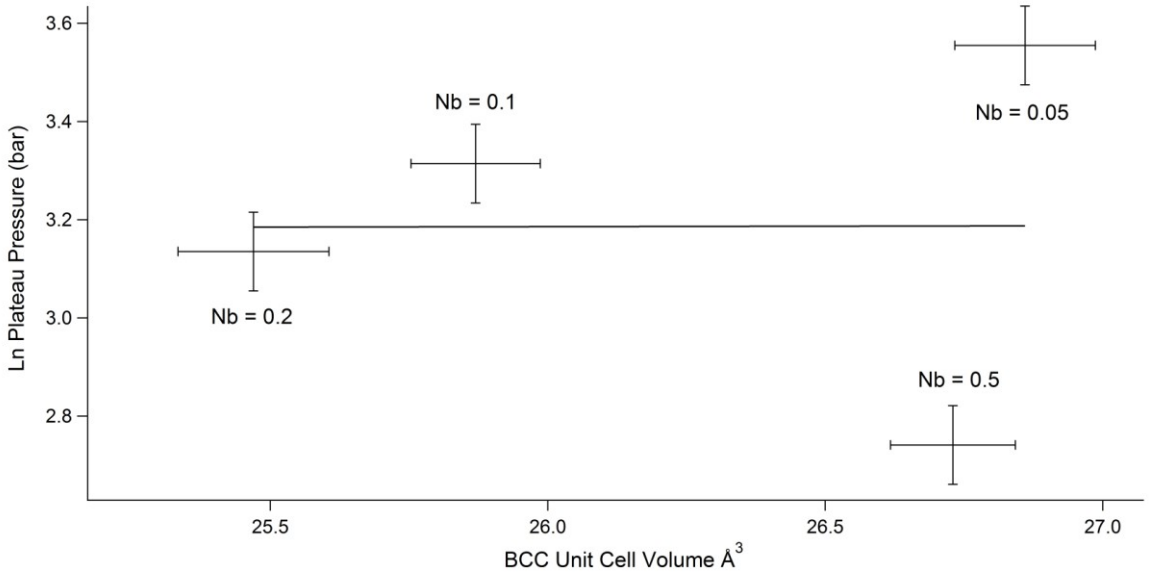

Figure 9.36 Correlation between BCC phase unit cell volume (Å^3) vs. Desorption plateau pressure (bar) for Nb = 0.05, Nb = 0.1, Nb = 0.2 and Nb = 0.5. Note, line added between data points on for ease of understanding.

The relationship between the C14 Laves phase unit cell volume and desorption plateau pressure is in agreement with previous studies on AB_5 type alloys (Mendelsohn & Gruen, 1977; Reilly et al., 1999), AB_2 C14 Laves type alloys (Nakano et al., 1997; Nakano & Wakao, 1995) and the Ti-V-TM-Mn system results chapter. On the other hand, the relationship between the BCC phase unit cell volume and desorption pressure does not show a correlation. This indicates that the BCC unit cell volume is not as sensitive to changes in composition as the C14 Laves phase.

9.6 Summary

During the investigation four $Ti_{0.5}V_{0.5-x}Nb_xMn$, where x = 0.05, 0.1, 0.2 and 0.5, alloys were synthesised and characterised around their microstructure, crystallography and hydrogen sorption properties.

Similar to the Ti-V-Mn system, SEM/EDS found the presence of three microstructural phases in the as-cast and heat treated alloys: a light, grey and dark dendritic phase in varying amounts. In addition coring was observed in Nb = 0.1 and Nb = 0.2 in both the as-cast state and after heat treatment. This indicates that longer heat treatment times are required to fully homogenise the alloys.

XRD analysis found that C14 Laves, BCC and FCC phases were present in all the alloys, with the C14 Laves phase being the dominant phase. In addition, there was found to be a linear relationship between Nb content and C14 Laves unit cell volume. This can be attributed to Nb having a larger atomic radii than V: 1.46 vs. 1.34 Å.

The heat treated alloys showed variations in the unit cell volumes of the C14 Laves and BCC phases in comparison to the as-cast alloys. The difference in metallic radii of the transition

metal elements resulted in different substitutions of the B-site V, Nb and Mn elements take place. There was no significant difference in the composition of the BCC phase in the Nb = 0.1 alloy after heat treatment. This indicates that no elemental substitution took place and so variation of the unit cell of the BCC phase may be the result of an ordering effect upon annealing.

PCT measurement found that all four alloys displayed different hydrogen sorption properties as a result of the elemental substitutions: in the alloys where Nb ≥ 0.2 at% significant differences in uptake were observed.

Nb = 0.1 showed the greatest reversible uptake of 1.51 (+/- 0.05) wt% at 303 K under 120 bar H_2. The lowest capacity was found in Nb = 0.5 which showed single step absorption and desorption with large hysteresis. XRD analysis found that this alloy contained 92 wt% C14 Laves phase, with only 3 wt% BCC phase so the low capacity may be a result of only a small amount of BCC phase (Yu, 2004).

Isotherms of Nb = 0.2 and Nb = 0.5 showed single step uptake with only a very small plateau between absorption and desorption which is not typical for interstitial hydrides. This suggests that different mechanisms of uptake have occurred within these alloys and further work would be required to examine this behaviour.

The kinetic data for Nb = 0.5 shows that equilibrium is not reached up to 35 minutes, which may explain the unusual shape of the isotherm. This indicates that either longer equilibrium hold times are required or the tolerance of the fit to the asymptote needs to be increased for this alloy.

The highest plateau pressures for absorption and desorption was found in the Nb = 0.05 alloy: between 37 - 47 bar for absorption and 34 – 24 for desorption. This alloy also showed a reversible capacity of 1.21 (+/- 0.05) wt%, with small hysteresis which is of interest for practical applications.

A summary of the different alloy systems: $Ti_{0.5}V_{0.5}Mn$, $Ti_{0.5}V_{0.4}TM_{0.1}Mn$ (where, TM is Nb, Cr, Mo, Ta and W) and $Ti_{0.5}V_{0.5-x}Nb_xMn$ (where x = 0.05, 0.1, 0.2 and 0.5), is provided in the following chapter. This will review the results in terms of the literature on Ti-V-Mn Laves phase related BCC solid solution alloys and go on to explain the rationale for the alloy selected to be used within the two stage metal hydride compressor.

Chapter 10

DISCUSSION OF Ti-V-Mn BASED ALLOY SYSTEMS

10.1 Introduction

This chapter will bring together all the results obtained in this thesis, investigating the relationships present within Laves phase related BCC solid solution alloys formed by alloying Ti-V-Mn with other transition metals. Particular attention will be paid to the relationship between the crystallography and the hydrogen sorption properties of the alloys.

10.2 Summary of Results

In total ten alloys, based on Ti-V-Mn Laves phase related BCC solid solution alloys were synthesised for the project based upon the nominal $Ti0.5V_{0.5}$-xTMxMn. For clarity the samples investigated in this work are:

- $Ti_{0.47}V_{0.46}Mn_1$ (Alloy 1)
- $Ti_{0.47}V_{0.46}Mn_1$ (Alloy 2)
- $Ti_{0.50}V_{0.51}Mn_1$ (Alloy 3)

} The Ti-V-Mn System (Chapter 7)

- $Ti_{0.56}V_{0.42}Nb_{0.09}Mn_1$ (Nb = 0.1)
- $Ti_{0.55}V_{0.42}Cr_{0.11}Mn_1$ (Cr = 0.1)
- $Ti_{0.58}V_{0.46}Mo_{0.09}Mn_1$ (Mo = 0.1)
- $Ti_{0.65}V_{0.49}Ta_{0.1}Mn_1$ (Ta= 0.1)

} The Ti-V-TM-Mn System (Chapter 8)

- $Ti_{0.54}V_{0.45}Nb_{0.05}Mn_1$ (Nb = 0.05)
- $Ti_{0.56}V_{0.33}Nb_{0.19}Mn_1$ (Nb = 0.2)
- $Ti_{0.51}Nb_{0.44}Mn_1$ (Nb = 0.5)

} The Ti-V-Nb-Mn System (Chapter 9)

Whilst the control alloys 1, 2 and 3, have previously been investigated (Shibuya et al., 2008; Shibuya et al., 2009), it was still necessary to understand a purely Ti-V-Mn system before investigations into the effects of novel transition metal additions to the alloy took place. For commercial applications, cost reduction is required and therefore this work aims to substitute the expensive element vanadium for less expensive elements (Nb, Cr, Mo and Ta) with the desire of maintaining or improving hydrogen storage and/or compression properties (Chapter 6).

For mobile hybrid hydrogen storage applications the key parameters are to maximise the gravimetric capacity (wt%) and achieve an enthalpy greater than - 30 kJ/mol H_2 to allow operation at room temperature and a dissociation pressure above 10 bar. For efficient metal hydride compression the important requirements are small hysteresis, large volumetric capacity and the ability to tune plateau pressures.

In these alloys the density is similar and, therefore, the hydrogen to metal ratio can be considered the volumetric density. Table 10.1 provides a summary of the PCT properties for all ten alloys at 303 K.

Table 10.1 Summary of capacity, plateau pressure and hysteresis data for all 10 alloys under 120 bar H_2 at 303 K. Note for hysteresis factor 0 = no hysteresis and 1 = large hysteresis.

Alloy	Reversible Capacity (wt%)	Hydrogen to Metal Ratio (H/M)	Abs Plateau P (bar)	Des Plateau P (bar)	Hysteresis Factor $Log(P_{Abs}/ P_{Des})$	ΔH ($KJ/molH_2$)	ΔS ($J/molH_2$)
1	1.53	0.791	42 - 52	25 - 15	0.371	-25.40	110.94
2	1.08	0.533	50 - 60	35 - 25	0.263	-25.94	108.65
3	1.56	0.810	60 - 70	40 - 30	0.269	-26.63	111.77
Nb = 0.1	1.51	0.811	25 - 50	40 - 15	0.135	-23.68	104.48
Cr = 0.1	1.06	0.327	58 - 73	47 – 32	0.172	-27.73	103.97
Mo = 0.1	1.13	0.604	45 - 70	50 - 25	0.186	-19.81	93.58
Ta = 0.1	1.16	0.665	-	-	-	-	-
Nb = 0.05	1.21	0.770	42 - 62	42 - 28	0.172	-25.71	109.73
Nb = 0.2	1.21	0.591	1 - 45	45 - 1	0	-23.41	96.72
Nb = 0.5	1.09	0.630	1 - 30	30 - 1	0	-23.19	99.52

For mobile hybrid hydrogen storage applications, based on the above criteria, alloys 3, 1 and Nb = 0.1 show the most potential. These alloys demonstrate the largest gravimetric capacities at 303 K (1.56, 1.53 and 1.51 +/- 0.05 wt%), possess enthalpy values above -30 kJ/mol H_2 (-26.63, -25.40 and -23.68 kJ/mol H_2) and show dissociation pressures above 10 bar (40 - 30 bar, 25 - 15 bar and 40 - 15 bar). However, in order for their potential as hybrid hydrogen storage alloys to be fully realised further improvements in gravimetric capacity would be required.

For compression applications, in terms of the system requirements, Nb = 0.1, Nb = 0.05 and Mo = 0.1 are the most suitable from the alloys developed in this investigation. These alloys show the smallest hysteresis factor values (0.135, 0.172 and 0.186) and promising H/M ratios

(0.811, 0.770 and 0.604 H/M). In addition, it is possible to influence the plateau pressures in these alloys (this will be discussed later in this Chapter).

As previously discussed (Chapter 8) the Ta = 0.1 alloy did not exhibit a clear plateau in either absorption and desorption therefore preventing a reliable and accurate enthalpy and entropy to be determined. Sorption pressures have been shown to be influenced by unit cell volume (and therefore interstitial volume) (Mendelsohn & Gruen, 1977). This may be explained by the large unit cell volume of the C14 Laves phase in Ta = 0.1 which increased from 166.89 $Å^3$ to 169.27 $Å^3$ after exposure to hydrogen, resulting in larger interstitial sites for the hydrogen to enter.

10.2.1 Relationship Between Phases Present and Uptake

Previous work has suggested that there is an increases in capacity with a greater proportion of BCC phase present (Tsukahara et al., 1996). In these studies the authors have considered gravimetric capacity, however, for a true comparison this work consider the hydrogen to metal (H/M) ratio. By considering the H/M ratio, variations in mass of the added transition metal elements are negated, giving a true reflection of the amount of hydrogen uptake. The relationship between H/M ratio and the relative phase abundance of the C14 Laves phase is shown in Figure 10.1.

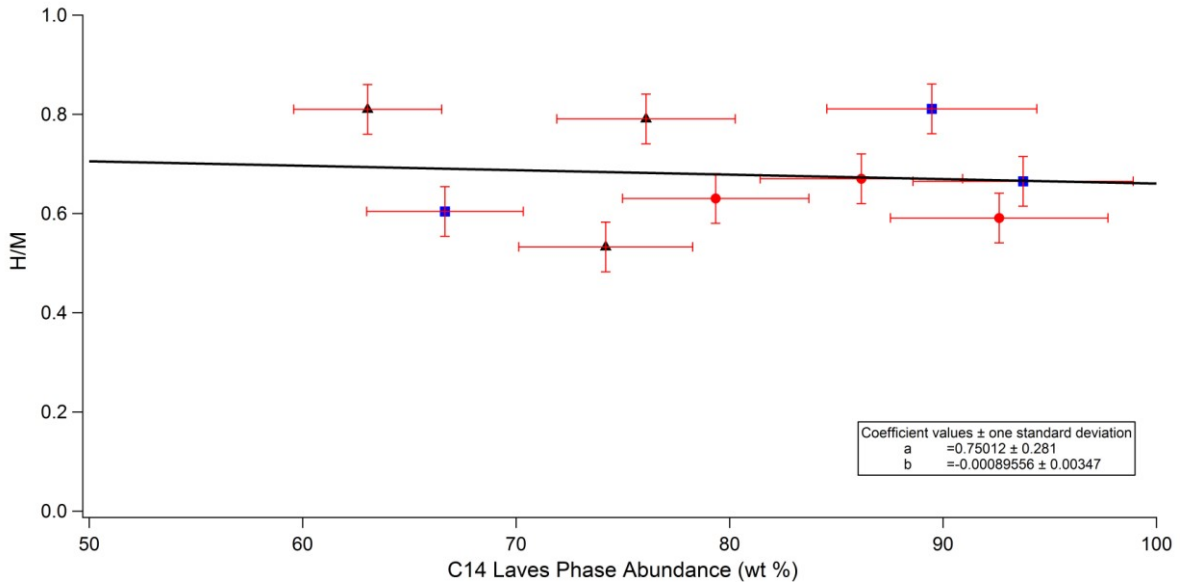

Figure 10.1 Relationship between C14 Laves phase abundance and H/M ratio in all the developed alloys.

This shows that there is no correlation between the H/M ratio and C14 Laves phase (and subsequently the BCC phase) abundance. This indicates that capacity is not determined by the percentage of C14 Laves phase present within the alloys over this composition range, contrary to previous investigations.

A greater understanding of the active interstitial sites within the different compounds is needed to ascertain the limiting factors in uptake, such as diffusivity limitation within the hydride solution and energy barriers between interstitial sites. Further studies are discussed later in the Future Work section of Chapter 12.

10.2.2 Relationship Between Unit Cell Volume and Enthalpy of Hydride Decomposition

Whilst there is no relationship between the capacity and phase proportion of these alloys, hydrogen atoms as still believed to be absorbed within interstitial sites. It is therefore feasible

to assume a relationship between the enthalpy of decomposition and interstitial volumes. The dimensions of the interstitial volumes have not been determined in this work, however, there is a strong correlation between the interstitial volume and unit cell (Lundin et al., 1977) allowing the comparison between unit cell volume and enthalpy.

Figure 10.2 shows the relationship between the C14 Laves phase unit cell volume and the enthalpy of hydride decomposition for all the alloys developed in the current work. The Ti-V-Mn system data points are shown as black triangles, the Ti-V-TM-Mn system data points are shown as blue squares and the Ti-V-Nb-Mn system data points are shown in red circles.

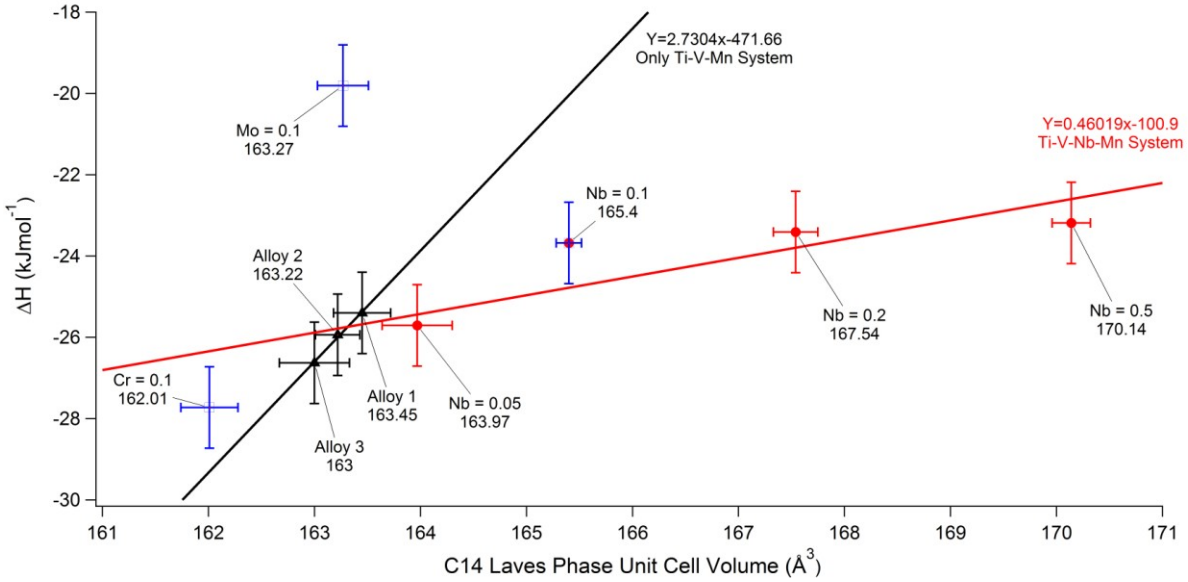

Figure 10.2 Relationship between C14 laves phase unit cell volume and enthalpy of hydride decomposition for Ti-V-Mn system alloys (black triangles), Ti-V-TM-Mn system alloys (blue squares) and Ti-V-Nb-Mn system alloys (red circles). Note, lines added between data points for ease of understanding.

First it is worth considering the Ti-V-Mn system, where any changes in enthalpy can be attributed exclusively to volume changes. The expected linear relationship indicates that in a

purely Ti-V-Mn system, subtle changes in unit cell volume result in significant changes in desorption enthalpy and pressure.

The substitution of 0.1 at.% transition metal for vanadium does not appear to show any correlation between C14 unit cell volume and enthalpy of decomposition. The causes of this will be discussed later in the chapter.

The substitution of niobium for vanadium shows a correlation between the C14 Laves unit cell volume and the enthalpy of decomposition. This suggests that the C14 Laves phase is the dominant phase in terms of hydrogen sorption in these alloys.

The linear relationship between the C14 Laves phase unit cell volume and enthalpy differs from that of a purely Ti-V-Mn alloy, indicative that the enthalpy of decomposition in the Ti-V-Nb-Mn alloys, is influenced by more factors than simply the interstitial volume. Small changes to alloy composition are likely to result in different diffusion mechanisms within the system (Kehr, 1978).

Niobium additions appear to stabilise the C14 Laves hydride phase, compared to the Ti-V-Mn alloy. This stabilisation is coupled with a reduction in hysteresis between absorption and desorption and indicates that the hydrogen has a higher binding energy with the alloys with Nb additions. This may indicate that the diffusivity in the alloys is decreased with Nb additions, although further work would be required to confirm this.

To better understand the effect of niobium on the C14 Laves phase Figure 10.3 shows the relationship between total Nb content for the system and C14 Laves phase unit cell volume, Nb content in the C14 Laves phase (EDS) and enthalpy of hydrogen decomposition.

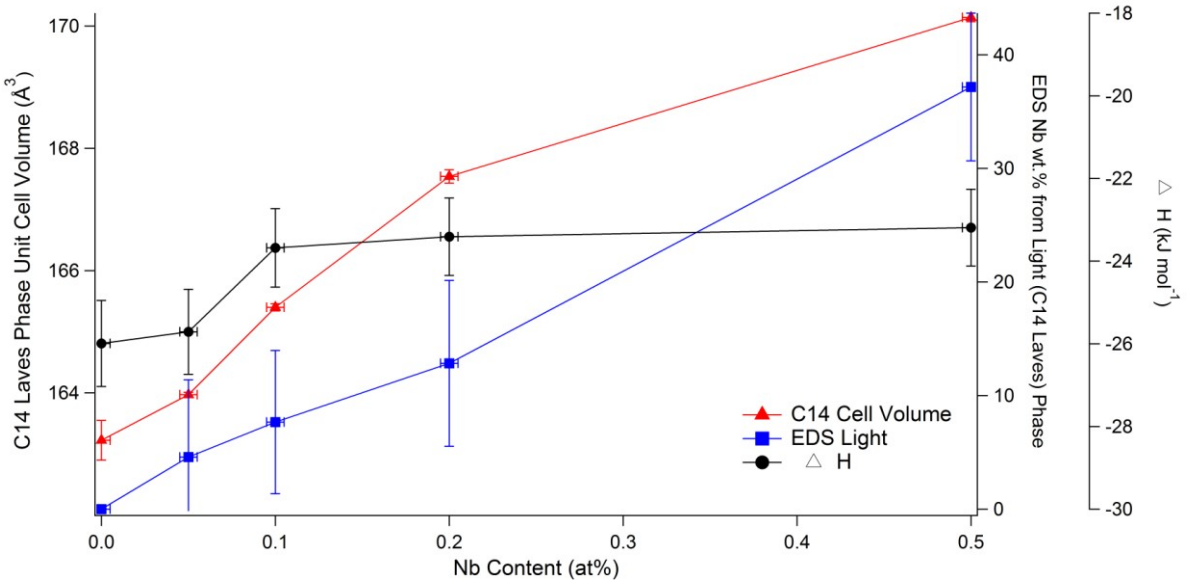

Figure 10.3 Relationship between Nb content, C14 Laves phase unit cell volume, average EDS composition of light (C14 Laves) phase and enthalpy of hydride decomposition.

Whilst there is a linear relationship between the enthalpy of desorption and unit cell volume, these parameters do not exhibit a similar relationship with Nb content. A linear increase in Nb content in the C14 Laves phase seems to be shown in the EDS results. However, considering the C14 Laves unit cell volume, there is not the expected Vegard's relationship between total Nb content and cell volume. This would suggest that Nb is preferentially substituted into the C14 Laves phase over the BCC phase, explaining why the C14 Laves phase plays a large part in the hydrogen sorption these alloys.

Between Nb = 0.05 and Nb = 0.1 at% there appears to be a jump in the enthalpy values. This indicates that there may be some influence from the BCC phase at Nb = 0.1, resulting in a destabilisation of the hydride phase. However, above 0.1 at% Nb, the Nb content does not influence the enthalpy which indicates that above this point it becomes a unit cell affect.

The relationship between the BCC phase unit cell volume and the enthalpy of hydride decomposition for all the alloys is shown in Figure 10.4.

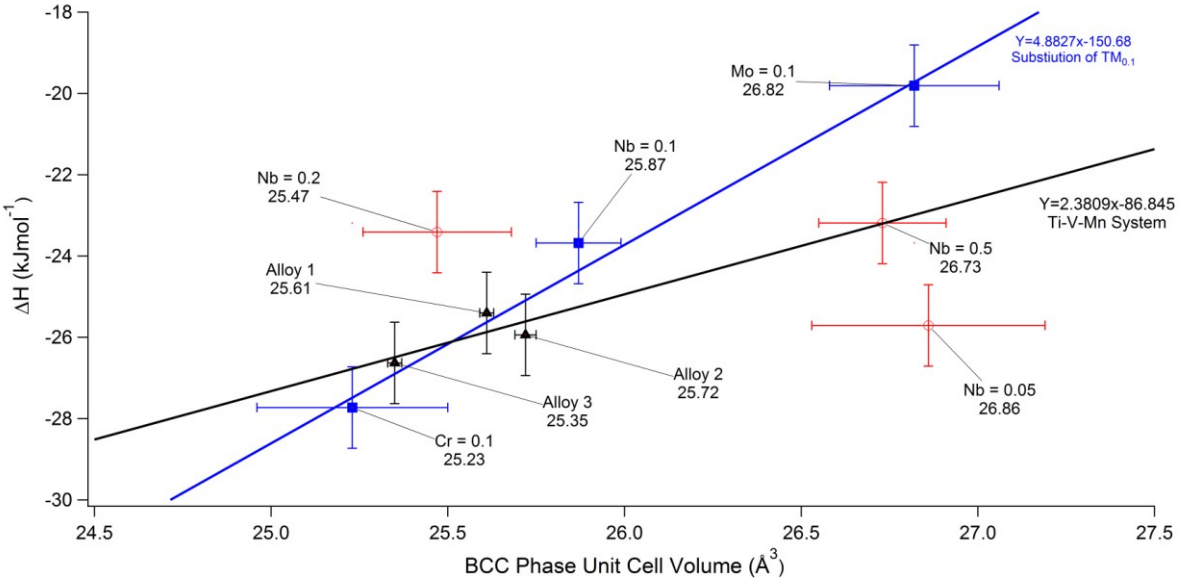

Figure 10.4 Relationship between BCC phase unit cell volume and enthalpy of hydride decomposition for Ti-V-Mn system alloys (black triangles), Ti-V-TM-Mn system alloys (blue squares) and Ti-V-Nb-Mn system alloys (red circles). Note, lines added between data points for ease of understanding.

Considering the Ti-V-Mn system, it is shown that changes in enthalpy occur as a result of changes to the BCC phase unit cell volume: a increase in enthalpy, and subsequently an increase in plateau pressure, can be attributed to an increase in unit cell volume.

The substitution of 0.05, 0.2 and 0.5 at% Nb for V does not appear to show any correlation between the BCC phase unit cell volume and enthalpy of desorption, which confirms that the C14 Laves phase is dominant in this alloy systems.

In contrast, the substitution of 0.1 at% TM (including Nb), shows a correlation between the BCC phase unit cell and enthalpy of desorption.

In comparison to the Ti-V-Mn system, TM substitutions appear to destabilise the BCC phase: as seen as a shift of the graph to the left. In Mo = 0.1, this results in an increase in plateau pressure (increase in enthalpy) in relation to the Ti-V-Mn system. In addition, the destabilisation of the BCC phase and is coupled with a reduction in hysteresis between absorption and desorption.

Nb = 0.1 appears to be following the same correlation as Cr = 0.1 and Mo = 0.1 which confirms that it does have a small effect on the BCC phase, as speculated from Figure 10.2.

Another interesting finding from this graph is that when V is completely substituted for Nb in the Nb = 0.5 alloy system, it follows the same correlation as the Ti-V-Mn system. This suggests that similar binding energies may be present in these alloys, however, further work would be required to confirm this.

10.3 Summary

This work has involved the synthesis of 10 Laves phase related BCC solid solution alloys and provides evidence for the effect of elemental substitution on the B-site of the Ti-V-Mn system. As well as offering advantages in terms of plateau pressure and enthalpy values, the use of alternative transition metals in the B-site of Ti-V-Mn alloys may also offer advantages in terms of cost.

For practical applications such as hydrogen storage and hydrogen compression, several of the developed alloys possess properties which meet the requirements of these systems.

For hybrid hydrogen storage applications, where gravimetric capacity, enthalpy and dissociation pressure are key, alloys 3, 1 and Nb = 0.1 of the developed alloys show the most potential, however further improvements in gravimetric capacity would be required.

For compression applications, where small hysteresis, large H/M and tuneable plateau pressures are necessary, Nb = 0.1, Nb = 0.05 and Mo = 0.1 are the most appropriate for use. In particular, Nb = 0.05 demonstrated small hysteresis between absorption and desorption, suitably high H/M ratio and a high desorption pressure making it a promising candidate for use within a metal hydride compressor.

By examining the relationships between unit cell volumes and enthalpy of hydride decomposition several correlations were observed. Firstly niobium substitutions appear to stabilise the C14 Laves phase hydride, thereby allowing the hydride to occur at lower pressures. Further, this stabilisation is coupled with a reduction in hysteresis. Secondly, transition metal substitutions (0.1 at%) destabilise the BCC phase. As a result of this, the plateau pressure increases when 0.1 at% V is substituted for Mo.

These findings indicate that the enthalpy of decomposition in Ti-V-TM-Mn and Ti-V-Nb-Mn alloys is influenced by more factors than unit cell and interstitial volume. This provides evidence for similar relationships existing in other Laves phase related BCC solid solution alloys.

In summary, these findings confirm that it is possible to tailor the plateau pressure and enthalpy of a metal hydride system formed by alloying Ti-V-Mn and another transition metal.

The following chapter presents findings on the design and development of a two-stage metal hydride compressor which utilises the Nb = 0.05 alloy in the high pressure stage.

Chapter 11

DESIGN AND DEVELOPMENT OF A TWO-STAGE METAL HYDRIDE COMPRESSOR

11.1 Introduction

Utilising one of the alloys developed during the project, a two-stage metal hydride compressor was developed with the aim being to design a safe and efficient system for the compression of hydrogen from a low inlet pressure (< 10 bar) to one suitable for high pressure applications (> 500 bar). For the development of the compressor factors such as thermal management, cycle time and cost had to be considered. It should be note the key objective of the compressor was performance as opposed to energy efficiency.

11.2 Design

The compressor was designed with a hydride bed based on $LaNi_5$ for the low pressure stage and $Ti_{0.5}V_{0.45}Nb_{0.05}Mn$ (Nb = 0.05), discussed in Chapter 9, for the high pressure second stage. These alloys were carefully selected based on their plateau pressures and thermodynamic properties (see Figures 11.1 and 11.2).

The $LaNi_5$ was provided by LCM (Less Common Metals) and the Nb = 0.05 was prepared in house by arc-melting. Both alloys were activated according to the sequence described in the Project Experimental in Chapter 6.

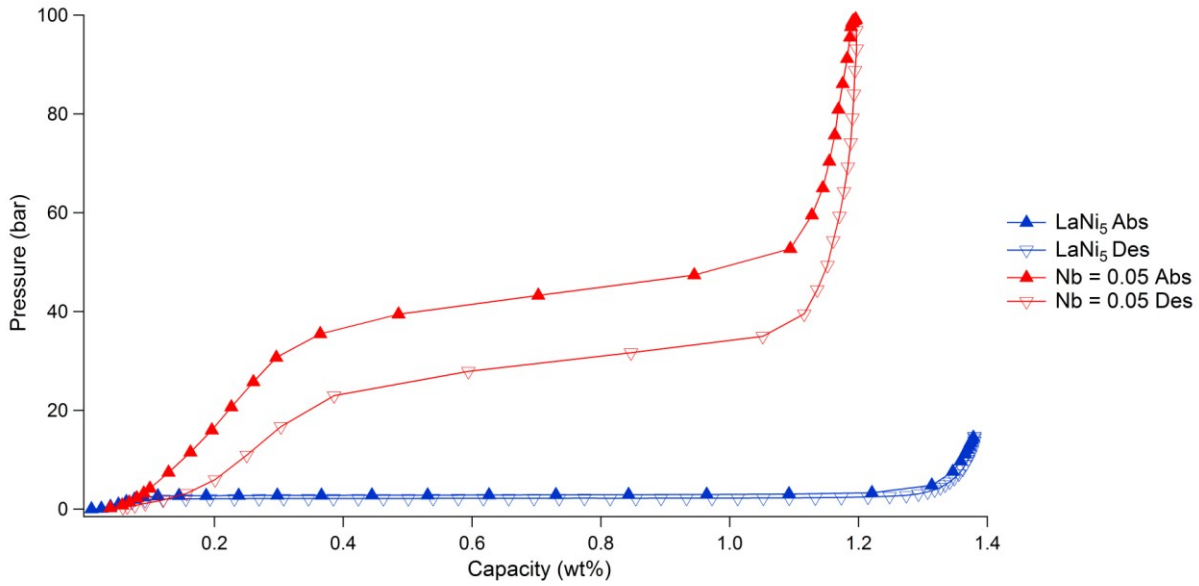

Figure 11.1 PCT data for $LaNi_5$ (blue) and Nb = 0.05 (red) at 303 K under 15 and 100 bar H_2 showing absorption (upwards triangles) and desorption (downwards triangles).

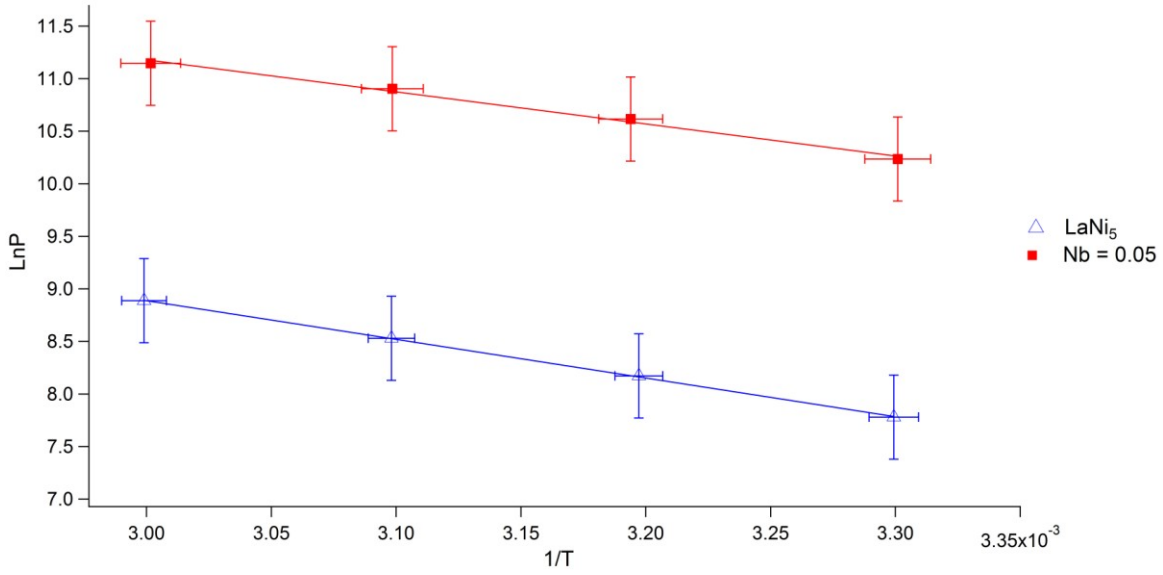

Figure 11.2 Van't hoff data for $LaNi_5$ and Nb = 0.05 showing desorption with associated errors.

The reversible capacity of $LaNi_5$ and Nb = 0.05 at 303 K under 100 bar H_2 was 1.42 wt% and 1.21 wt%, respectively. Measurement errors for capacity are estimated to be ± 0.05 wt% based on 3 PCT measurements using a Pd standard (see Appendix A).

In $LaNi_5$, the plateau in the absorption isotherm is present at 2.5 bar and for desorption is at 2 bar at 303 K. In Nb = 0.05, the plateau pressure for absorption is between 35 - 50 bar and for desorption is between 35 – 23 bar at 303 K up to 100 bar H_2.

Table 11.1 summarises the PCT properties of the two metal hydrides used for the compressor.

Table 11.1 PCT properties showing plateau pressure and enthalpy/entropy values for LaNi5 and Nb = 0.05 for desorption. Note for hysteresis factor 0 = no hysteresis and 1 = large hysteresis.

Alloy	Plateau Pressure Absorption @ 303 K (bar)	Plateau Pressure Desorption @ 303 K (bar)	ΔH (kJ/mol H^2)	ΔS (J/mol H^2)	Hysteresis Factor $Log(P_{Abs}/P_{Des})$
$LaNi_5$	2.92	2.39	-30.63	165.807	0.008
Nb = 0.05	52	35	-25.71	167.97	0.172

It is this difference in the PCT properties of the two alloys, in particular the difference in plateau pressure that helps to cascade the pressure in the stages to achieve a high line out pressure.

Figure 11.3 shows a schematic of the design of the compressor. It includes heating provided by two 250 W band heaters per stage and flowing oil and cooling of the stages is provided by flowing water to enable thermal cycling between 303 and 473 K. The system is operated by a computer program that links to the control unit and is attached in series to the pressure transducers and valves.

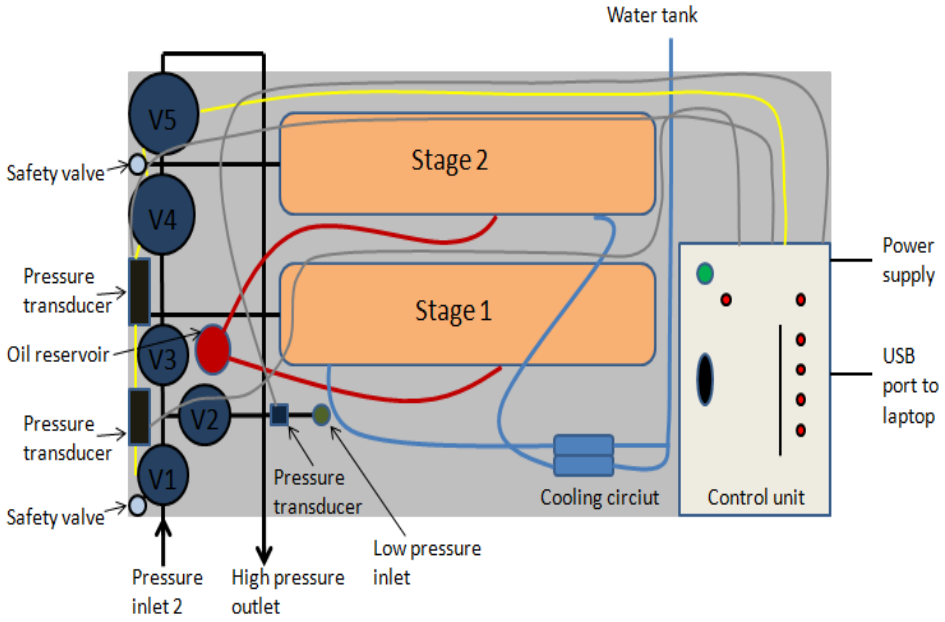

Figure 11.3 Schematic showing the two stages along with the control unit and connecting valves of the compressor.

The hydride beds were loaded in ½" tubes contained within an oil heating / cooling jacket. This oil jacket was heated by resistive heating elements or cooled by circulating tap water through a ¼" copper spiral tube within the oil jacket. Care was taken to ensure that the tubing was rated at the temperatures and pressures designed for operation. In addition, a thermal cut-out safety switch was placed in line with the resistive heating controller.

From measuring the dimensions of the two stages, the internal volumes were calculated to establish the required quantity of metal hydride required. Metal hydrides are subject to expansion on charging with hydrogen so to accommodate this it was decided to only load 60% of the volume with the metal hydride, the rest was dead space. To calculate how much this equates to in terms of weight, the density of the metal hydrides was calculated and multiplied by the volume which could be filled. Subsequently, the first (low pressure) stage

was filled with 164.33 g of $LaNi_5$ and the second (high pressure) stage was filled with 66.87 g of Nb = 0.05.

The system is automated using a custom-built control unit, which utilises a USB data acquisition and *Microsoft Visual Basic 6* software. The experimental sequences are programmed through batch files and the measurements are saved as text files for data analysis.

The constructed compressor can be seen in Figure 11.4.

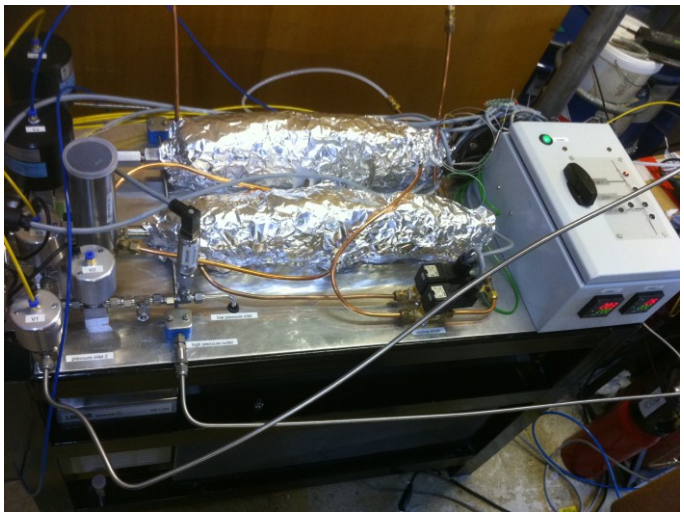

Figure 11.4 The assembled hydride compressor with both stages connected.

11.3 Initial Testing

Initial testing was carried out to investigate how well the compressor operates under normal cycling conditions.

11.3.1 Single-Stage Compression Mode

The testing sequence involved running stage one and two independently to determine whether the storage material was fully activated and readily absorbing-desorbing hydrogen. This is shown in Figure 11.5, where independent stages were used to compress hydrogen into a 2 litre cylinder.

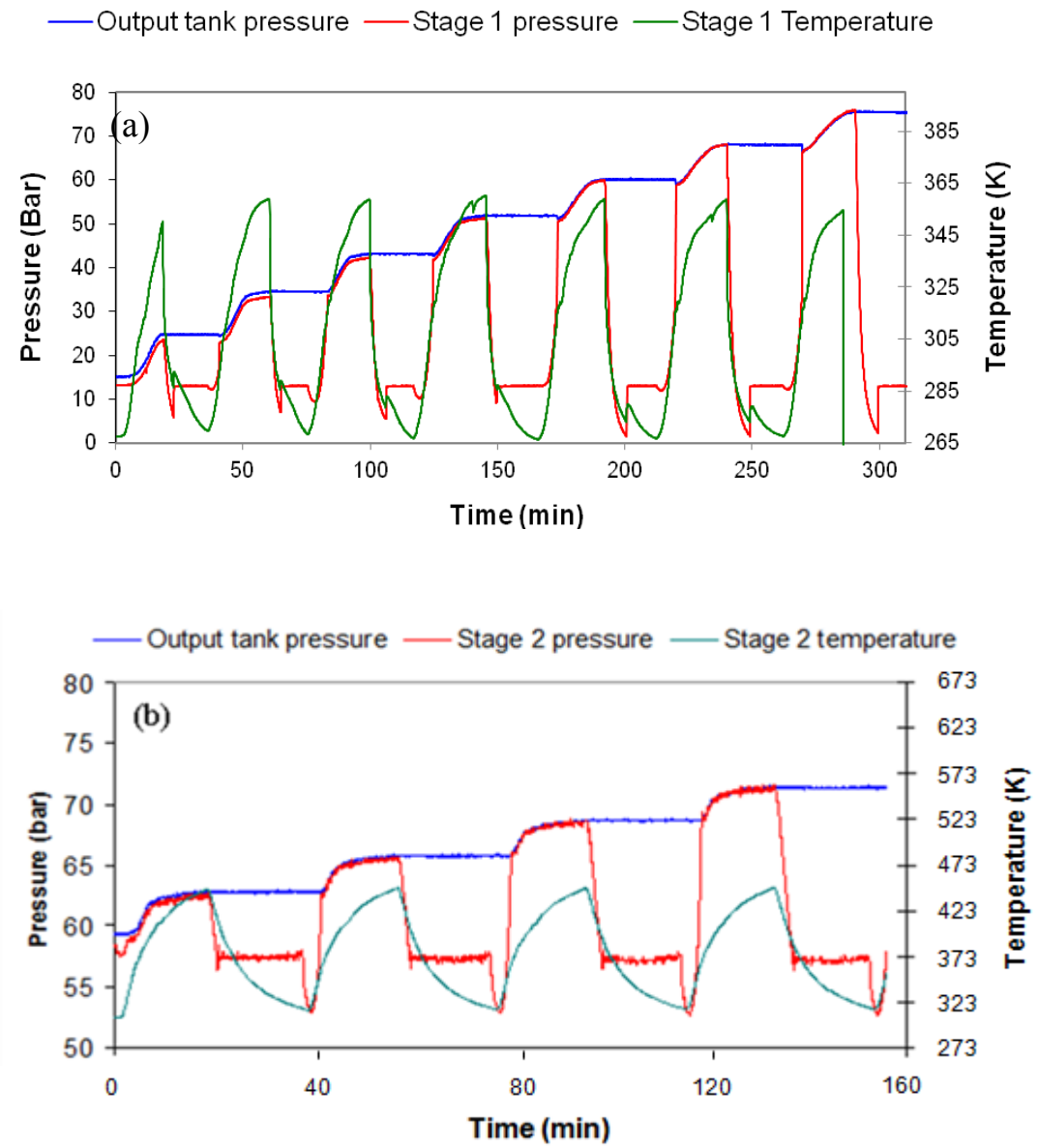

Figure 11.5 Results from initial testing showing (a) the first stage and (b) the second stage in operation.

From Figure 11.5 it can be seen that the increase in temperature from 303 to 473 K drives the stage pressure and subsequent tank output pressure up for both stages. The output pressure value is then shut while the temperature is cooled back down to 303 K. The temperature decrease causes the stage pressure to rapidly fall. The process is then repeated and the output pressure valve is only opened once the pressure within the system is above the pressure in the output tank pressure.

In stage one, shown in Figure 11.5(a), with an initial input pressure of 15 bar an output pressure of 75 bar is achieved after 7 cycles. In stage two, shown in Figure 11.5(b), with an initial input pressure of 59.5 bar an output pressure of 72 bar is achieved in 4 cycles.

11.3.2 Multi-Stage Compression Mode

As previously discussed, to achieve a high line out pressure from a low input pressure it is necessary to run both stages in sequence. This is shown in Figure 11.6. A line input pressure of atmospheric (1 bar) in stage one is boosted above 60 bar whilst filling a 2 litre cylinder. The sequence of events is to cool the low-pressure stage one whilst charging with hydrogen from the 1 bar source, then after charging, close the valve to the supply source and heat stage one. As the pressure in stage one reaches the pressure in stage two, stage one is then opened to stage two (whilst stage two is being cooled). This allows the system to reach higher pressures than can be achieved by stage one alone. The system is designed so that if the pressure within the system is higher than the output tank pressure then the system is open to the tank pressure to increase this as quickly as possible. This can be seen clearly in cycle 1 & 2 where both stages directly contribute to the tank pressure. When cycle three is reached, the

tank pressure is above the pressure generated from stage one so further increases in tank pressure come from thermally heating stage two.

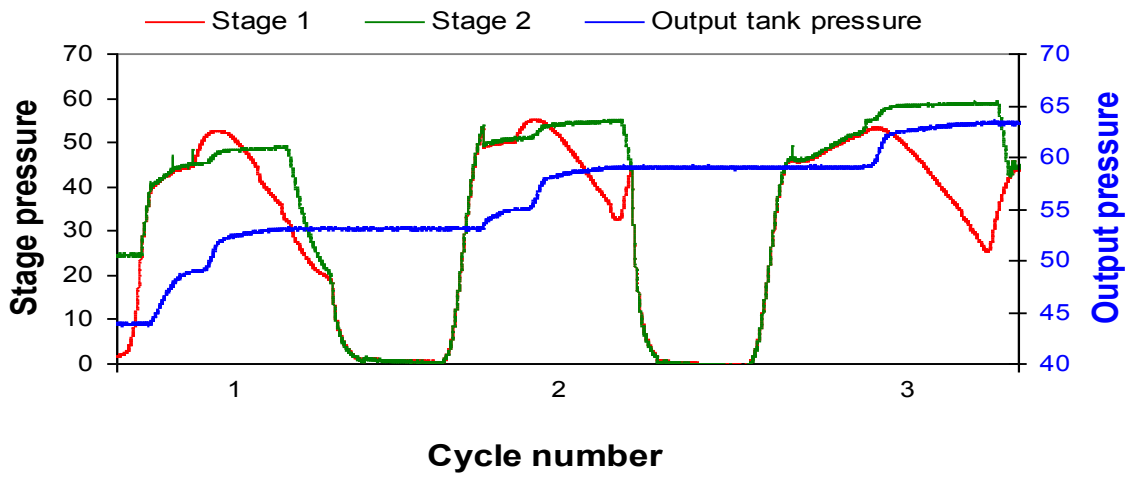

Figure 11.6 Multi-stage gas compression mode.

11.4 Discussion

Initial testing of the two stages, working both independently and in sequence, has highlighted some research issues that should be addressed in the future to improve the performance of the compressor. These can be broken down into three main areas: thermal management and heat transfer, system flexibility and end applications.

11.4.1 Thermal Management and Transfer

Several strategies could be adopted to improve thermal management between the metal hydride bed and heating/cooling system to increase the efficiency of the compressor both in terms of power requirements and productivity by shortening cycle time:

1) Enhance the design to allow the use of a thermal management circuit coupled to an electrolyser or a redundant heat source to decrease heating energy requirements.

2) Develop the use and integration of phase change materials to store and effectively regulate heat flow into the compressor.

11.4.2 System Flexibility

To increase the flexibility of a range of external heat sources and supply pressures, multiple stages could be integrated to the current design using a range of newly developed alloys to operate over a greater range of temperatures and pressures. These multiple stages would provide additional redundancy in the event of a malfunction (e.g. contamination). In this case, the unit could still operate and deliver high pressure hydrogen but at a reduced flow until storage material within the defective stage is replaced.

Additional thermal energy could also be supplied by internal electrical heating elements. Although this would reduce the overall efficiency of the compressor, it would allow for more rapid delivery of high pressure hydrogen.

11.4.3 End Applications

A refuelling station, incorporating a metal hydrogen compressor such as the one developed in the current study, could easily be integrated into existing refuelling stations with the use of numerous buffer tanks for cascade refuelling of high pressure tanks. However, the small scale of this particular system means it would not be practical for automotive applications because the compressor is limited to filling times of 0.5 g H_2/min.

In the short term, one of the applications of the developed compressor to date has been attaching it to various pieces of equipment within the Hydrogen Materials Group laboratories at the University of Birmingham, such as a high pressure hydrogenation cell. This is because it is capable of delivering high purity hydrogen at higher pressures than that achievable from standard hydrogen cylinders which enables testing and characterisation of new hydrogen storage materials.

Table 11.2 shows a comparison of the developed compressor with mechanical and thermal compressors developed by Ergenics.

Although it has not been possible to quantify the heat energy required, annual power and maintenance costs, it can be seen that in comparison to Ergenics metal hydride compressor, the developed compressor does offer significant advantages in terms of the estimated capital cost. In addition higher output pressures are possible even though it is a significantly smaller unit (weighing only a fifth of the weight of the Ergenics compressor).

Table 11.2 Comparison of developed two-stage metal hydride compressor with compressors developed by Ergenics. Note Table adapted from data from Da Costa (2000).

Parameter	Metal Hydride Compressor (Ergenics)	Developed Two-Stage Metal Hydride Compressor
Hydrogen Flow	944000 cc/min	25 cc/min (stage 1)
Inlet Pressure	6.9 bar	5 bar
Outlet Pressure	248 bar	up to 650 bar
Number of Stages	5	2
Weight	100 kg	20 kg
Volume	400 L	144 L
Hot Water Flow (waste heat)	189250 cc/min @ 90 ^{o}C	N/A
Heat Energy Required	240 kBTU/h	TBC
Cooling Water Flow	189250 cc/min @ 303 K	2500 cc/min @ 298 K
Electrical Power	500 W	500 W (peak power)
Estimated Capital Cost	£80,000	£10,000
Annual Power (2,000 h/y, £0.064/kWh)	£60	TBC
Annual Maintenance Cost	£625	TBC

11.5 Summary

Safe and efficient hydrogen compression is required for the transition over to a hydrogen economy. Despite the advantages metal hydride compressors offer over conventional diaphragm compression - namely no moving parts, silent operation and high purity hydrogen -

cost and efficiency need to be improved upon before the use of metal hydride compressors can be fully realised.

The current project has been successful in developing a working two-stage metal hydride compressor which has, so far, shown very reliable operation during both independent and multi-stage cycling.

The computer control system is capable of controlling the two stages independently to maximise the pressure output with a wide pressure input range. Initial testing has shown output pressures of 650 bar are obtainable with an input line pressure of less than 10 bar at 0.5 g H_2/min. This was the limit of the second stage pressure transducer.

Chapter 12

CONCLUSIONS AND FUTURE WORK

12.1 Conclusions

This overall aim of this work was to investigate the synthesis of Laves phase-related BCC solid solution Ti-V-Mn based alloys for use in hydrogen storage and hydrogen compression applications. In particular, for $Ti_{0.5}V_{0.5}Mn$-based alloys, the effect of composition, microstructure, and crystallography on the hydrogen sorption properties were examined using SEM-EDS, XRD and Sievert's-type PCT measurements.

Seven novel compositions based on Ti-V-Mn, (i.e. $Ti_{0.5}V_{0.4}TM_{0.1}Mn$, where TM = Nb, Cr, Mo, Ta and $Ti_{0.5}V_{0.5-x}Nb_xMn$, where x = 0.05, 0.2 and 0.5) were synthesised by arc melting, after which a heat treatment was performed at 1233 K for 6 hours in a vacuum furnace ($< 10^{-6}$ mbar). It was found that small amounts (0.05 - 0.1 at%) of Nb substituted for V resulted in smaller hysteresis between absorption and desorption as well as higher hydrogen dissociation pressures. This finding led to the successful development of a two-stage metal hydride compressor utilising one of the produced Ti-V-Nb-Mn alloys (Nb = 0.05). Trials on the compressor system have shown that output pressures of 650 bar can be achieved from an input pressure of less than 10 bar, at a filling rate of 0.5 g H_2/min.

In addition, by examining the relationship between the unit cell volume and enthalpy of hydride decomposition it was found that Nb substitutions stabilise the C14 Laves phase hydride and transition metal substitutions (0.1 at%) destabilise the BCC phase. These findings indicate that the enthalpy of desorption in Ti-V-TM-Mn and Ti-V-Nb-Mn alloys is

influenced by more factors than unit cell and interstitial volume, such a diffusion mechanisms. This provides evidence for similar relationships existing in other Laves phase related BCC solid solution alloys.

12.1.1 The $Ti_{0.5}V_{0.5}Mn$ System

The $Ti_{0.5}V_{0.5}Mn$ system was investigated around the structural and morphological differences observed due to small deviations in desired stoichiometry in three alloys and the subsequent influence on their hydrogen storage properties.

The small compositional variations, $Ti_{0.5}V_{0.5\pm x}Mn$ (x = -0.04 and 0.01), resulted in differing C14 Laves phase unit cell volumes. PCT measurements showed that the alloys demonstrated reversible hydrogen sorption capacities of 1.53, 1.08 and 1.56 +/- 0.05 wt%, up to 120 bar H_2 at 303 K. Variations in the C14 Laves phase unit cell volume resulted in a small change in the enthalpy of hydride decomposition, however, there was a significant change in the plateau pressure and hysteresis between the alloys: compositional variation of 0.05 at% resulted in a shift of the plateau pressure by almost a third: from 42 – 52 bar to 60 – 70 bar for absorption and 40 – 30 to 25 – 15 for desorption.

It is therefore concluded that this variation in plateau pressure is due to the change in unit cell volume. This has been observed in previous studies investigating AB_5 type alloys, such as $LaNi_5$ (Mendelsohn & Gruen, 1977; Reilly et al., 1999) and AB_2 C14 Laves type alloys (Nakano et al., 1997; Nakano & Wakao, 1995) but provides evidence for this relationship in the $Ti_{0.5}V_{0.5}Mn$ system.

12.1.2 The Ti-V-TM-Mn System

In the Ti-V-Mn system, the effect of small (0.1 at%) transition metal substitutions into the B-site (V-Mn) was investigated, in an attempt to manipulate the hydrogen storage properties (as shown by PCT measurements).

All the alloys showed different behaviour during hydrogen PCT measurements. Nb = 0.1 showed the greatest uptake with a reversible capacity of 1.51 (+/- 0.05) wt% up to 120 bar H_2 at 303 K and small hysteresis between absorption and desorption.

Sloping plateaus were present in isotherms of Nb = 0.1, Cr = 0.1 and Mo = 0.1 which indicates that the alloys were not fully homogenous. Coring could also be seen in the heat treated micrographs of these three alloys which confirms that longer heat treatment times are required to fully homogenise the alloys.

The isotherm for the addition of Ta = 0.1 at% did not exhibit a clear plateau during hydrogen absorption and desorption. This behaviour is not typically observed for interstitial metal hydrides; a discrete solid solution and thermodynamic plateau are usually seen. Plateau pressure is very sensitive to unit cell volumes so this can be explained by the large unit cell volume of the C14 Laves phase in the alloy within this alloy system.

A linear correlation was found between C14 Laves and BCC phase unit cell volume and desorption plateau pressure in Nb = 0.1, Cr = 0.1 and Mo = 0.1: an increase in unit cell volume resulted in decrease in desorption plateau pressure. This relationship has never been investigated in these novel transition metal hydrides but provides further evidence for this correlation in other interstitial alloy systems.

12.1.3 The Ti-V-Nb-Mn System

Following on from the results obtained from the Ti-V-TM-Mn system, it was decided to examine the Ti-V-Nb-Mn system as Nb was substituted for V in the B site, in greater depth. Analysis of the XRD patterns found that increasing Nb-content resulted in an increase in both the unit cell volume and abundance of the C14 Laves phase. This can be attributed to Nb having a larger metallic radius than V, i.e. 1.46 and 1.35 Å, respectively. There was no significant relationship between the amounts of the Nb and the BCC phase, which may indicate that the BCC is not as sensitive to changes in Nb content as the C14 Laves phase.

All four alloys displayed different hydrogen sorption properties as a result of their elemental substitutions. In particular, in the alloys where Nb $\geq$ 0.2 at% significant differences in uptake were observed. Nb = 0.1 showed the greatest reversible uptake of 1.51 (+/- 0.05) wt% at 303 K under 120 bar H_2.

For compression applications, where small hysteresis, large H/M and tuneable plateau pressures are necessary, Nb = 0.05 was highlighted as a promising candidate.

The isotherms of Nb = 0.2 and Nb = 0.5 showed single step uptake with no clearly defined plateau between absorption and desorption which is not typical for interstitial hydrides. This suggests that different mechanisms of uptake have occurred within these alloys and further work would be required to examine this behaviour.

12.1.4 Relationship Between Unit Cell Volume and Enthalpy of Hydride Decomposition in Ti-V-Mn Based Alloys

By examining the relationships between unit cell volumes and enthalpy of hydride decomposition several correlations were observed. Firstly, niobium substitutions appear to stabilise the C14 Laves phase hydride, thereby allowing the hydride to occur at lower pressures. Furthermore, this stabilisation is coupled with a reduction in hysteresis. Secondly, transition substitutions destabilise the BCC phase. As a result of this, the plateau pressure increases when 0.1 at% V is substituted for Mo.

These findings indicate that the enthalpy of desorption in Ti-V-TM-Mn and Ti-V-Nb-Mn alloys is influenced by more factors than unit cell and interstitial volume. This provides evidence for similar relationships existing in other Laves phase related BCC solid solution alloys.

12.1.5 Design and Development of Two-Stage Metal Hydride Compressor

A two-stage metal hydride compressor has been successfully designed and developed using metal hydrides based on $LaNi_5$ for the low-pressure stage and $Ti_{0.5}V_{0.45}Nb_{0.05}Mn$ (Nb = 0.05) for the high-pressure stage.

Trials on the system have shown that it is capable of pressurising a cylinder up to 650 bar from an input pressure of less than 10 bar at 0.5 g H_2/min.

From an application perspective, a metal hydride compressor such as the one developed during this work, could be integrated into an existing refuelling stations relatively easily with

the use of buffer tanks. However, the small scale of this particular system means that it would not be practical for automotive applications.

To date, the compressor has successfully been used within the Hydrogen Materials Group laboratories at the University of Birmingham enabling the high pressure hydrogenation of samples with ultra pure hydrogen.

12.2 Future Work

Findings from this work has provided evidence for Ti-V-Mn based laves phase related BCC solid solution alloys being suitable for applications including metal hydride compressors. There is, however, the need for further research and development on these alloys before their commercial application can be fully realised.

Whilst efforts have been made to investigate the crystallographic changes upon hydriding, it has not been possible using lab based facilities. Due to the size of the unit cells relative to hydrogen it may be possible to discern which interstitial sites hydrogen resides. It is therefore suggested that neutron diffraction measurements be performed (e.g. GEM at ISIS) to take advantage of hydrogen's large scattering cross section relative to Ti, V and Mn facilitating a greater understanding of the hydriding process (Nakamura et al., 2001).

This work has identified that unit cell volume is not the only influence on the enthalpy of sorption. Further investigations into the mechanisms of hydrogen sorption are recommended. Spectroscopic studies such as Raman could offer an insight into the bonding within the alloys, however, atomic hydrogen may be difficult to observe. If Raman spectroscopy yields

inconclusive, inelastic neutron scattering (TOSCA/MAPS ISIS) could be used due to the large neutron scattering properties of hydrogen (Nakamura et al., 2011).

As solid state diffusion is believed to influence the sorption enthalpy, hydrogen - deuterium exchange mechanisms should be investigated, to allow computational models for diffusion mechanisms to be tested.

All the developed alloys showed significantly different microstructures as a result of their compositional variations. The use of transmission electron microscopy (TEM) would allow for examination of the microstructural effects of hydrogen absorption and desorption on the developed alloys (Matsuda et al., 2011). This could also be used to provide information on the structural stability of the alloys during cycling.

Coring was observed in several of the micrographs of the heat treated alloys, in particular in the alloys in which vanadium was substituted for other transition metals. This indicates that longer heat treatment times are required to ensure the alloys are fully homogenous.

Finally, for the metal hydride compressor future work will investigate the durability of the metal hydrides in a cycling environment to determine the life expectancy of the system. In addition, it would be useful to quantify the overall energy efficiency of the system by taking into consideration the electrical energy required and the output pressure achieved during constant use.

Appendix A

HTP-S CALIBRATION ON Pd STANDARD

PCT measurements were performed on a Pd standard prior to measuring the alloys developed in the project to check the calibration of the equipment. This was carried out to ensure consistency of the results obtained on the Hiden Isochema HTPS-2 and used to determine the errors associated with uptake values.

This involved testing a Pd sample on several systems within the Hydrogen Materials Group, including a second Hiden Isochema HTP-S (HTP2) which has lower pressure capabilities, and a Hiden Intelligent Gravimetric Analyser (IGA).

Isotherms were performed over a range of temperatures on each system to check for consistency and repeatability.

Figure B.1 shows absorption isotherms for Pd on the IGA at 298, 323, 348 and 373 K up to 10 bar H_2. Two measurements were performed at each temperature to check for consistency.

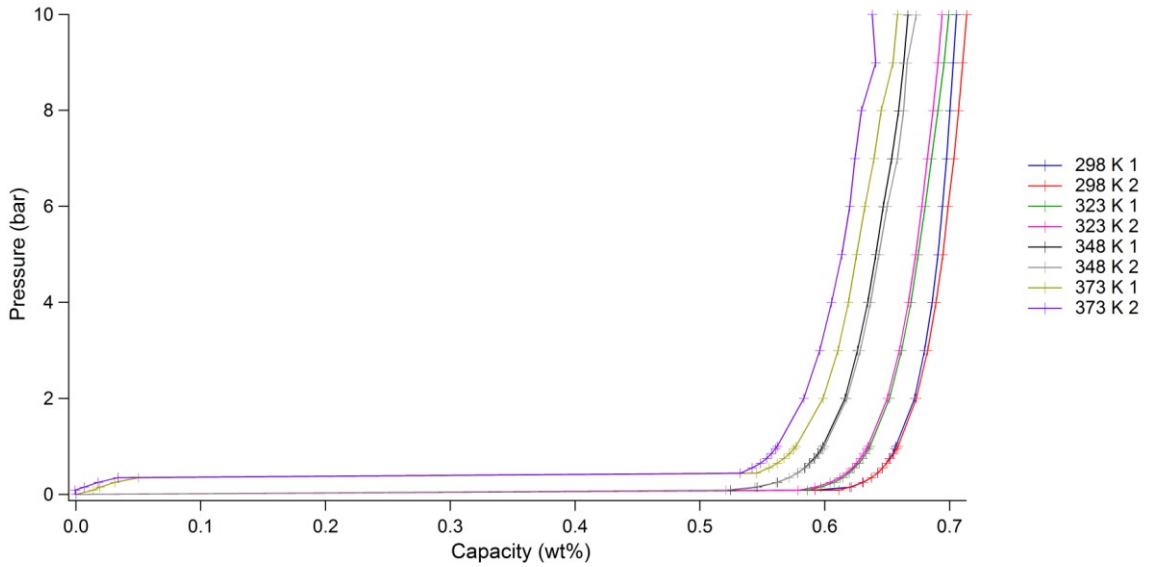

Figure B.1 PCT curves showing absorption for Pd standard on IGA between 298 and 373 K up to 10 bar H_2.

This shows very little deviation (< 0.01 wt%) during repeat absorption measurements.

Figure B.3 shows absorption isotherms for Pd on the HTP at 298, 323, 393 and 473 K up to 10 bar H_2.

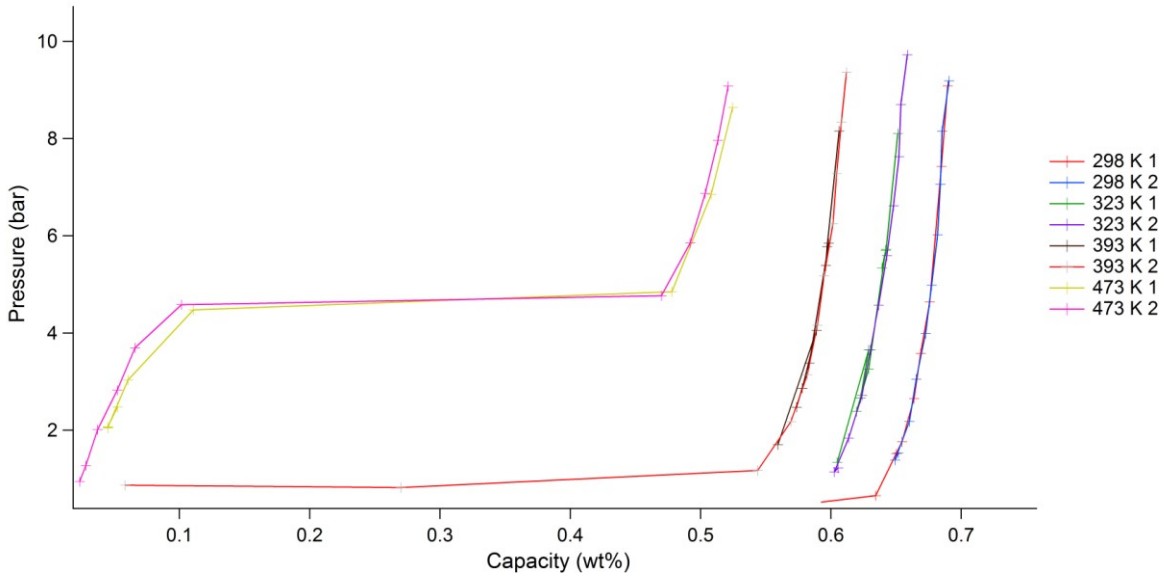

Figure B.2 PCT curves showing absorption for Pd standard on HTP between 298 and 473 K up to 10 bar H_2.

Again, this shows very little deviation (< 0.01 wt%) during repeat absorption measurements.

Finally, Figure B.3 shows absorption isotherms for Pd on the HTP2 at 298, 343, 393 and 473 K up to 10 bar H_2.

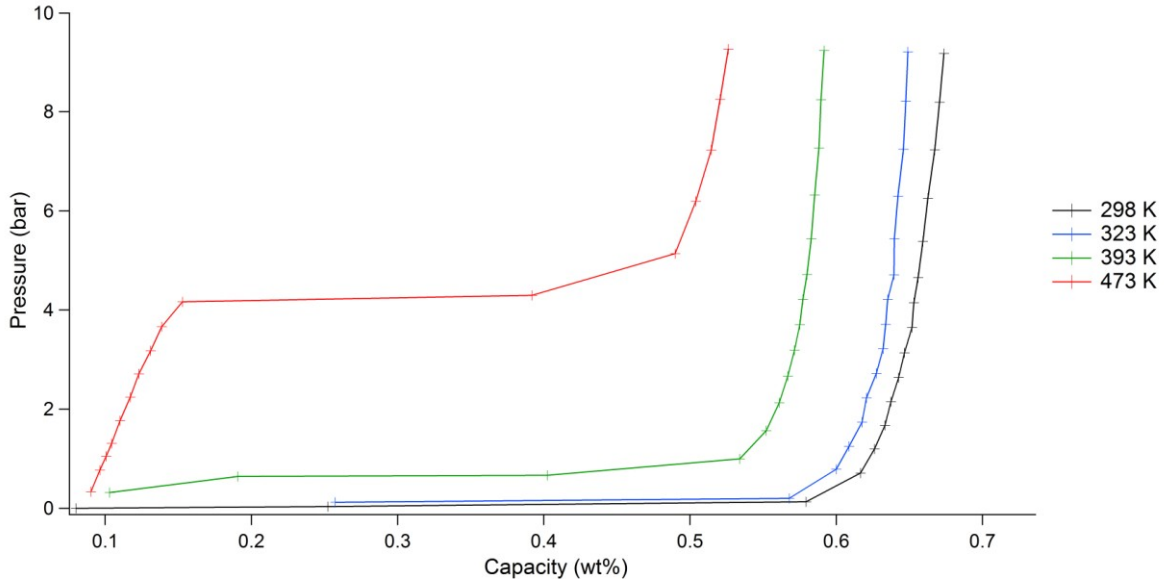

Figure B.3 PCT curves showing absorption for Pd standard on HTP2 between 298 and 473 K up to 10 bar H_2.

In Figure B.3 only 1 measurement was performed at each temperature due to time limitations but the shape of the isotherms on HTP2 appear similar to that of the HTP.

Figure B.4 shows the isotherm for Pd at 323 K (50 ^{o}C) on all three systems up to 10 bar H_2. A comparison of the PCT properties of the Pd standard on all three systems at 298 and 323 K is shown in Table B.1.

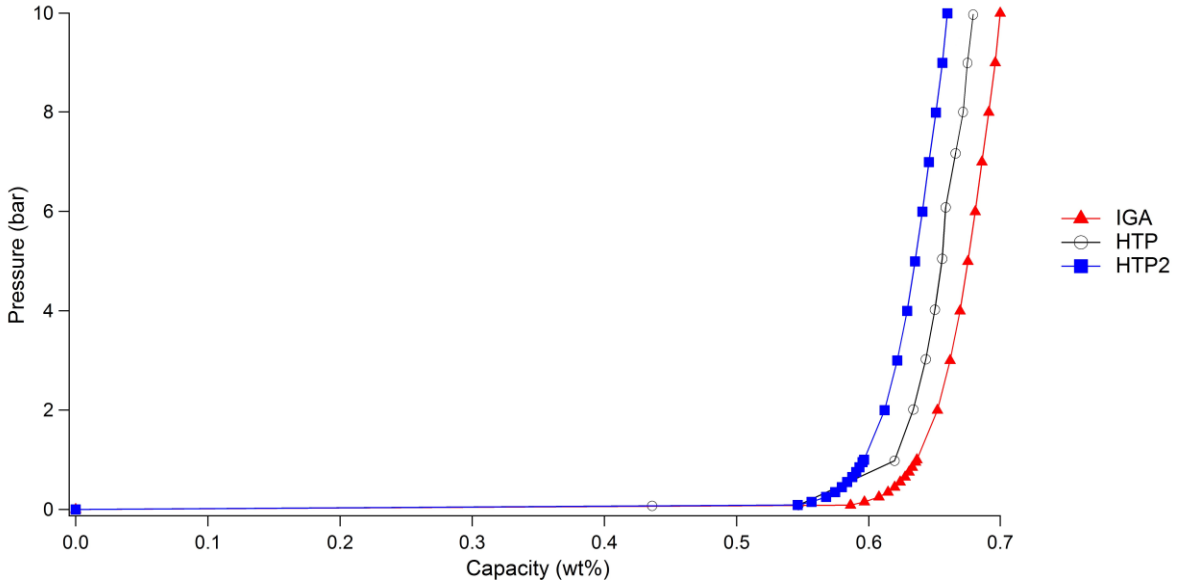

Figure B.4 PCT curve showing absorption for Pd standard on IGA (black circle), HTP (red triangle) and HTP2 (blue square) at 323 K up to 10 bar H_2.

Table B.1 Comparison of PCT properties of Pd standard on IGA, HTP and HTP2.

System	298 K		323 K	
	Capacity	Pressure	Capacity	Pressure
IGA	0.69	9.986	0.67	9.987
HTP	0.66	9.876	0.65	9.886
HTP2	0.64	9.946	0.62	9.952

Although there are small variations in the pressures during the measurements, the variation between the capacity on all three system is 0.05 wt% for absorption and desorption. The calculated for error for uptake measurements will therefore be 0.05 wt%.

Appendix B

B.1 Individual XRD Traces of Ti-V-Mn Alloys

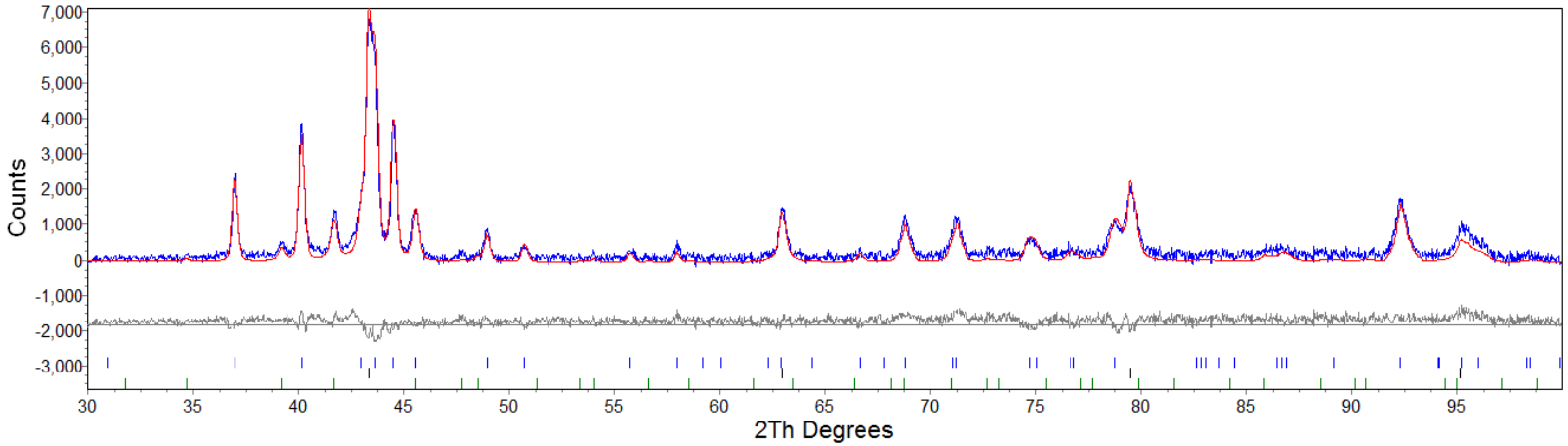

Figure B.1 XRD pattern of as-cast alloy 1 showing observed pattern (blue) and calculated fit after pseudo-Rietveld refinement (red).

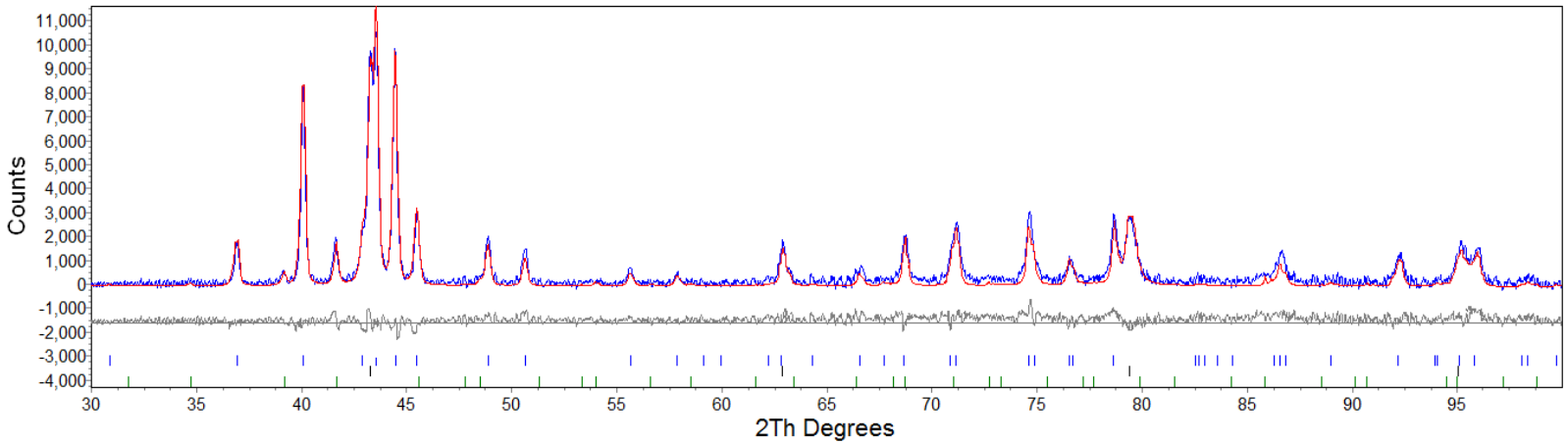

Figure B.2 XRD pattern of as-cast alloy 2 showing observed pattern (blue) and calculated fit after pseudo-Rietveld refinement (red).

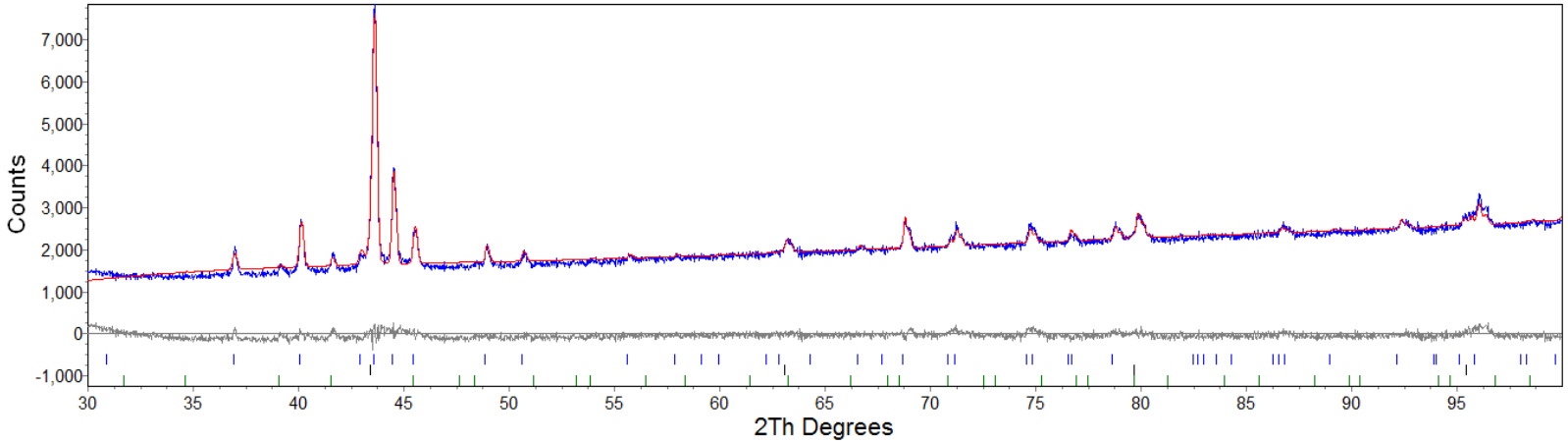

Figure B.3 XRD pattern of as-cast alloy 3 showing observed pattern (blue) and calculated fit after pseudo-Rietveld refinement (red).

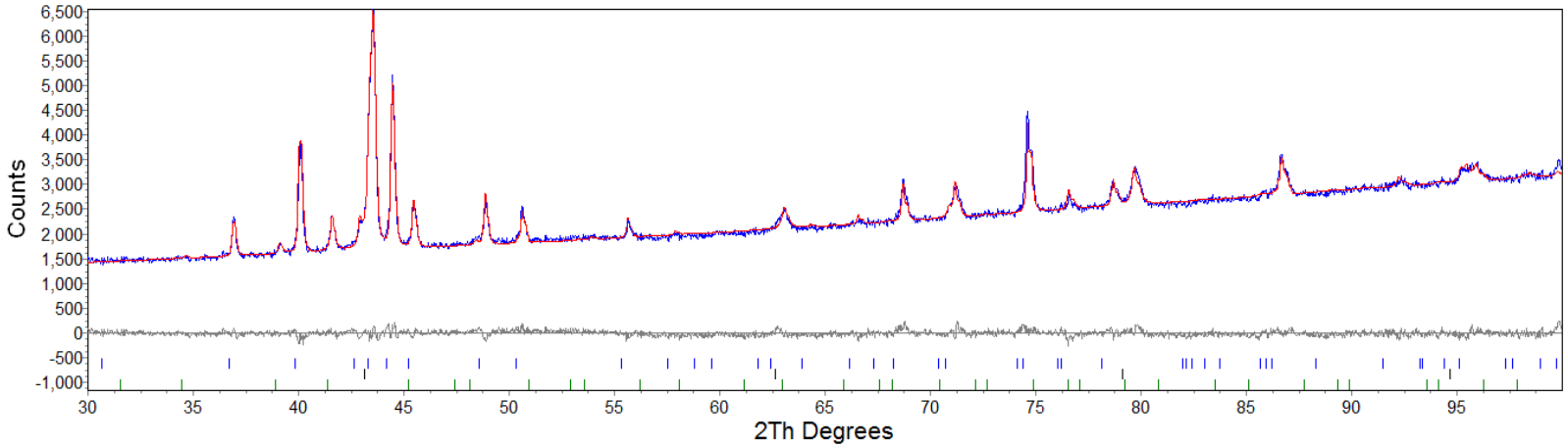

Figure B.4 XRD pattern of heat treated alloy 1 showing observed pattern (blue) and calculated fit after pseudo-Rietveld refinement (red).

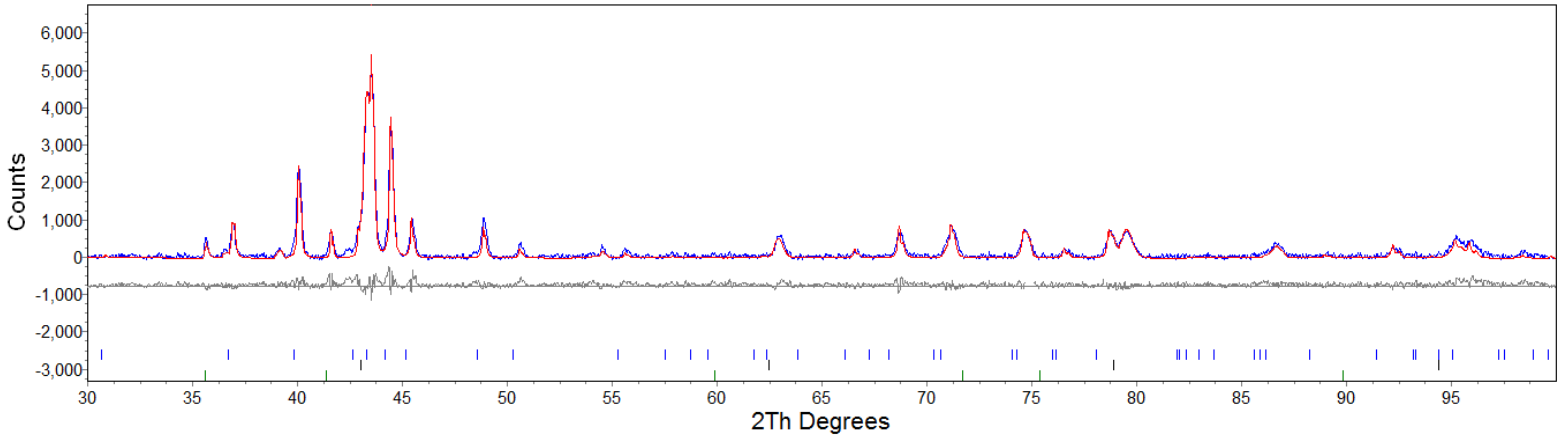

Figure B.5 XRD pattern of heat treated alloy 2 showing observed pattern (blue) and calculated fit after pseudo-Rietveld refinement (red).

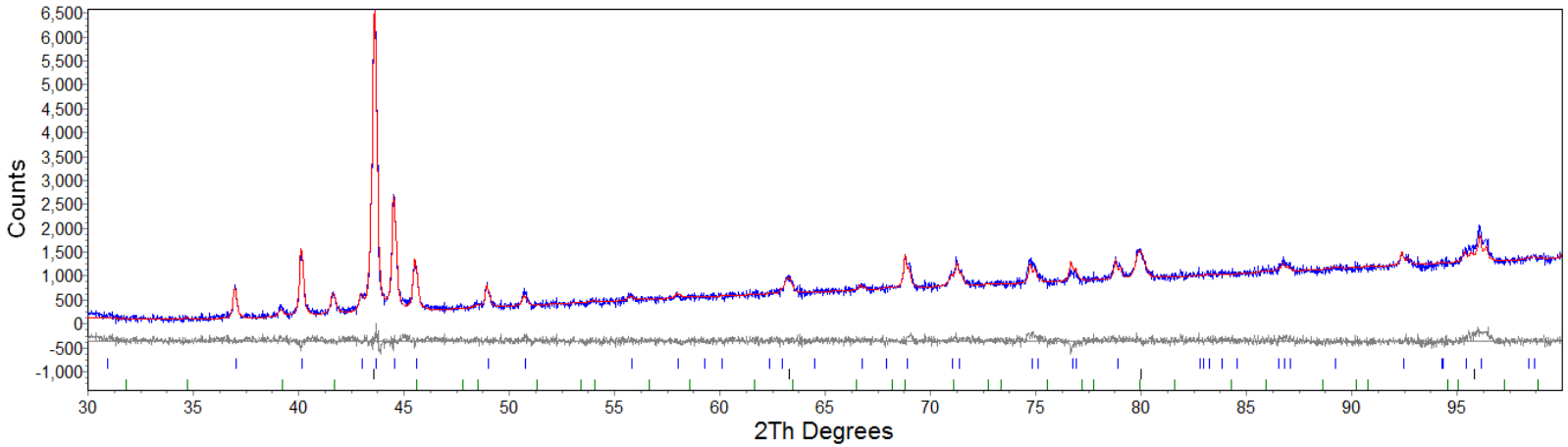

Figure B.6 XRD pattern of heat treated alloy 3 showing observed pattern (blue) and calculated fit after pseudo-Rietveld refinement (red).

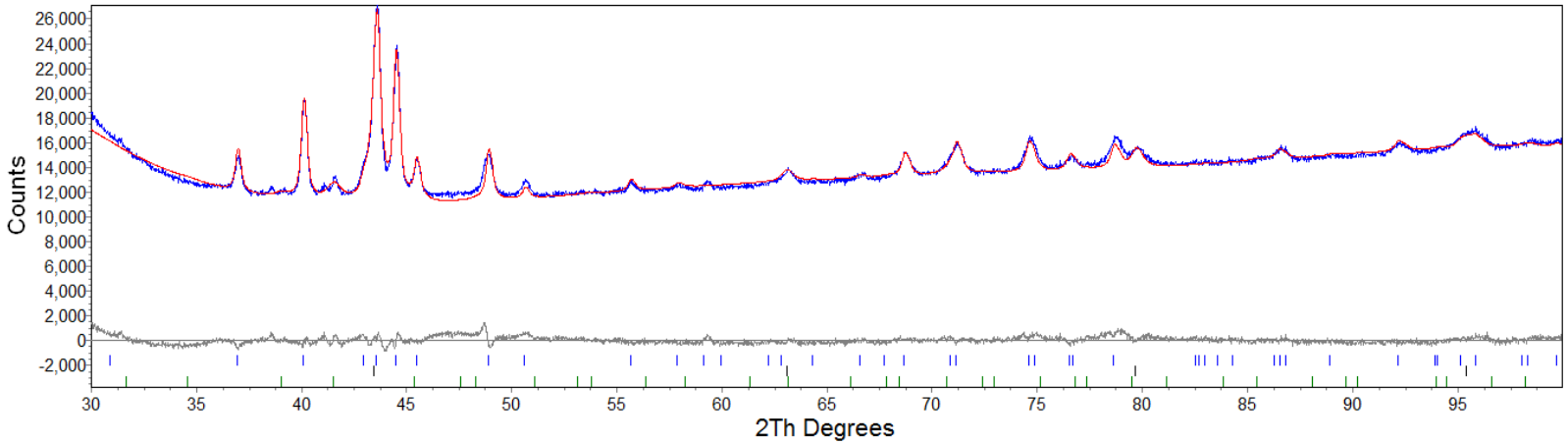

Figure B.7 XRD pattern of hydrogen cycled alloy 1 showing observed pattern (blue) and calculated fit after pseudo-Rietveld refinement (red).

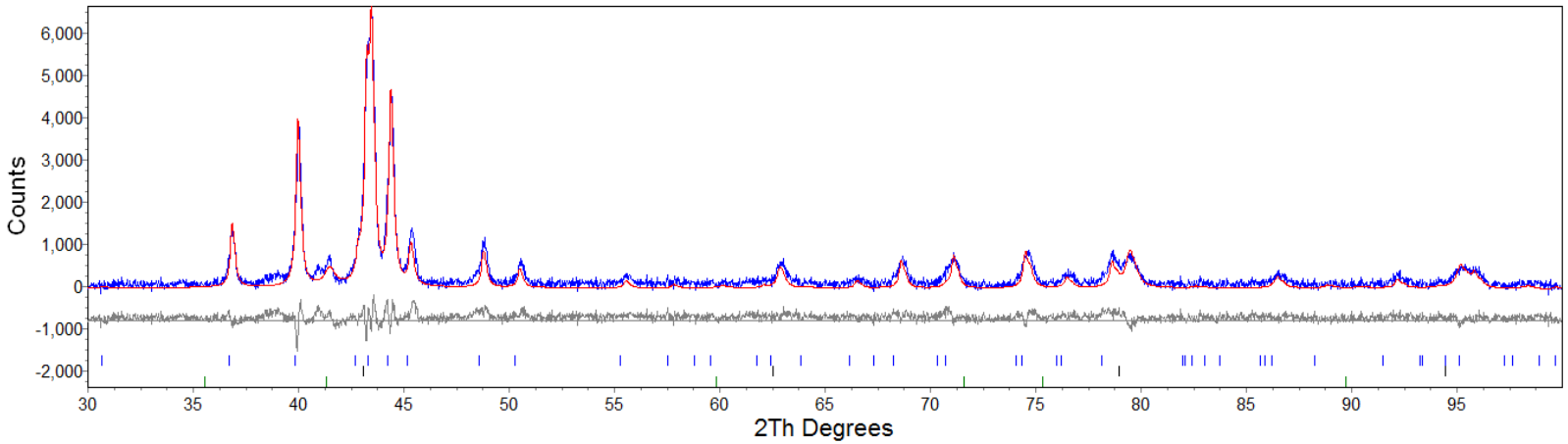

Figure B.8 XRD pattern of hydrogen cycled alloy 2 showing observed pattern (blue) and calculated fit after pseudo-Rietveld refinement (red).

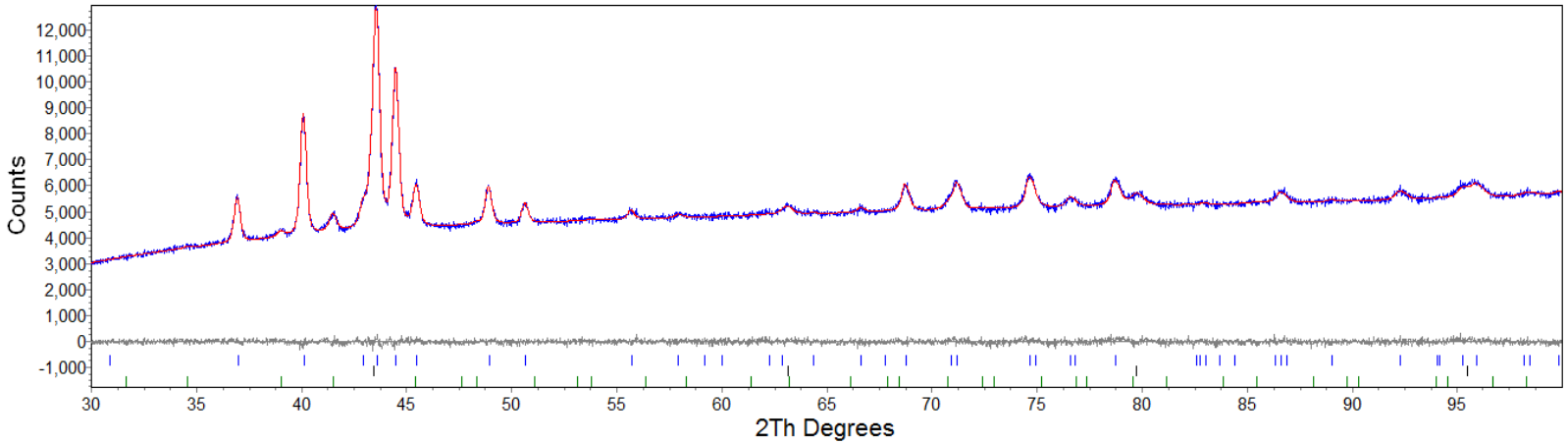

Figure B.9 XRD pattern of hydrogen cycled alloy 3 showing observed pattern (blue) and calculated fit after pseudo-Rietveld refinement (red).

B.2 Calculations for Unit Cell Volumes in Ti-V-Mn Alloys

The following tables show the calculations involved in determining what causes expansion or reduction in the unit cell volume of the C14 Laves and BCC phases between the as-cast and heat treated Ti-V-Mn alloys. This is done by calculating which elemental substitutions have taken place based on the EDS data.

Table B.1 Composition (at%) of C14 Laves phase for as-cast and heat treated Ti-V-Mn alloys.

Alloy	Phase Location	As-Cast EDS			Heat Treated EDS		
		Ti	V	Mn	Ti	V	Mn
1	Light	27.71	21.57	50.76	28.2	17.8	50.4
	% of Overall Composition	27.70	21.56	50.74	28.08	17.79	54.02
2	Light	27.19	18.21	54.6	28.08	16.95	54.98
	% of Overall Composition	27.19	18.21	54.60	28.08	16.95	54.97
3	Light	28.47	15.54	56	27.64	16.12	56.25
	% of Overall Composition	28.47	15.54	55.99	27.64	16.12	56.24

Table B.2 Difference between at% composition of as-cast and heat treated alloys and elemental substitution in Ti-V-Mn alloys.

Alloy	Overall Difference (as cast – heat treated)			
		Ti	V	Mn
1	Difference	0.49	- 3.77	3.28
	% Difference	0.49	- 3.77	3.28
	Elemental Substitution	0	4	- 4
2	Difference	0.89	- 1.26	0.37
	% Difference	0.89	- 1.26	0.37
	Elemental Substitution	1	- 1	0
3	Difference	- 0.83	0.58	0.25
	% Difference	- 0.83	0.58	0.25
	Elemental Substitution	1	- 1	0

Table B.3 Composition (at%) of BCC phase for as-cast and heat treated Ti-V-Mn alloys.

Alloy	Phase Location	As-Cast EDS			Heat Treated EDS		
		Ti	V	Mn	Ti	V	Mn
1	Grey	18.24	33.46	45.53	17.85	33.49	48.67
	% of Overall Composition	18.78	34.41	46.83	17.85	33.49	48.67
2	Grey	17.56	33.32	49.12	19.96	30.49	50.55
	% of Overall Composition	17.56	33.32	49.12	19.96	30.49	50.55
3	Grey	17.52	34.99	47.49	16.3	35.14	48.55
	% of Overall Composition	17.52	34.99	47.49	16.3	35.14	48.55

Table B.4 Difference between at% composition of as-cast and heat treated alloys and elemental substitution in Ti-V-Mn alloys.

Alloy	Overall Difference (as cast – heat treated)			
		Ti	V	Mn
1	Difference	- 0.39	- 0.03	3.84
	% Difference	- 0.91	- 0.93	1.84
	Elemental Substitution	- 1	- 1	2
2	Difference	0.89	-1.26	0.37
	% Difference	0.89	-1.26	0.37
	Elemental Substitution	1	- 1	0
3	Difference	-0.83	0.58	0.25
	% Difference	-0.83	0.58	0.25
	Elemental Substitution	1	- 1	0

B.3 Van't Hoff Data for Ti-V-Mn Alloys

Table B.5 Van't hoff data for absorption and desorption in alloy 1, 2 and 3.

Alloy	Absorption				Desorption			
	T (K)	P	1/T	LnP	T (K)	P	1/T	LnP
	303.141	46.0319	0.003299	3.829335	303.152	24.7752	0.003299	3.209888
	313.163	50.951	0.003194	3.930864	313.149	34.5099	0.003193	3.541252
1	323.147	75.5523	0.003095	4.324825	323.162	46.1614	0.003094	3.832144
	303.217	53.4472	0.003298	3.978694	302.936	28.5043	0.003298	3.350055
	313.176	67.3854	0.003193	4.210428	313.031	42.8345	0.003194	3.757344
2	323.202	84.6116	0.003094	4.438071	323.065	56.6529	0.003095	4.036932
	303.166	48.8951	0.003299	3.889677	303.174	26.3073	0.003298	3.269846
	313.154	62.2661	0.003193	4.131417	313.265	36.5414	0.003193	3.598446
3	323.142	79.2933	0.003095	4.373154	323.12	50.5036	0.003095	3.922045

Appendix C

C.1 Individual XRD Traces of Ti-V-TM-Mn Alloys

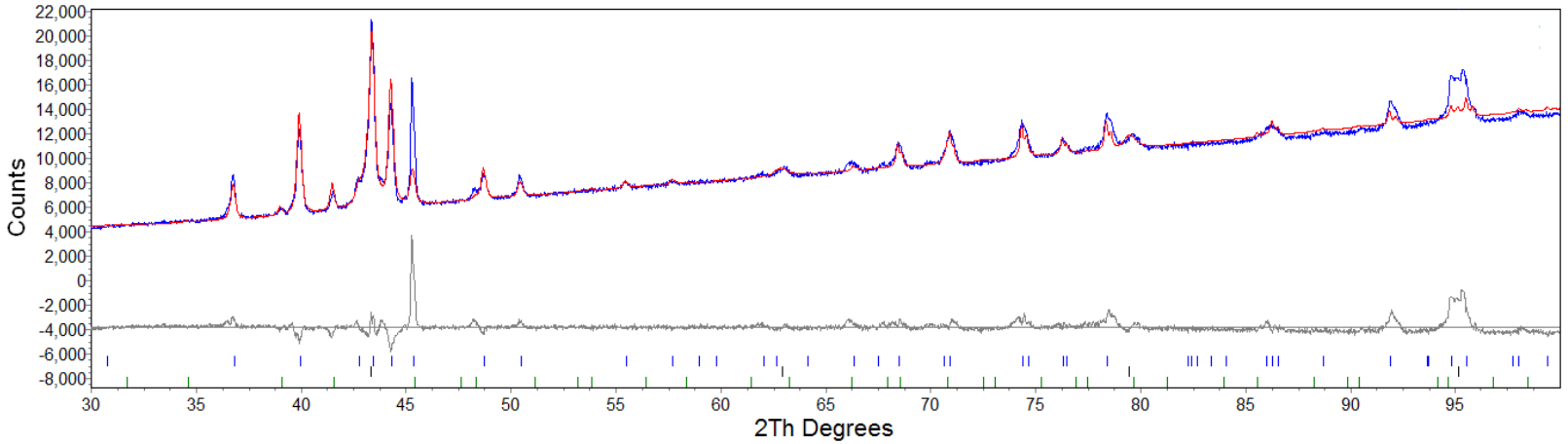

Figure C.1 XRD pattern of as-cast Nb = 0.1 showing observed pattern (blue) and calculated fit after pseudo-Rietveld refinement (red).

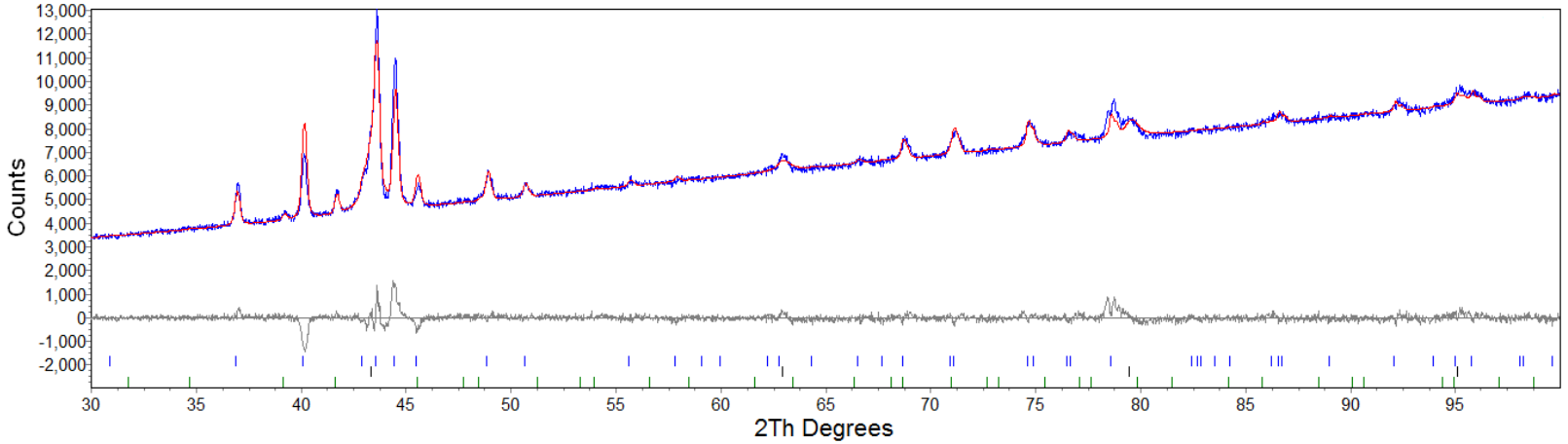

Figure C.2 As-cast Cr = 0.1 showing observed pattern (blue) and calculated fit after pseudo-Rietveld refinement (red).

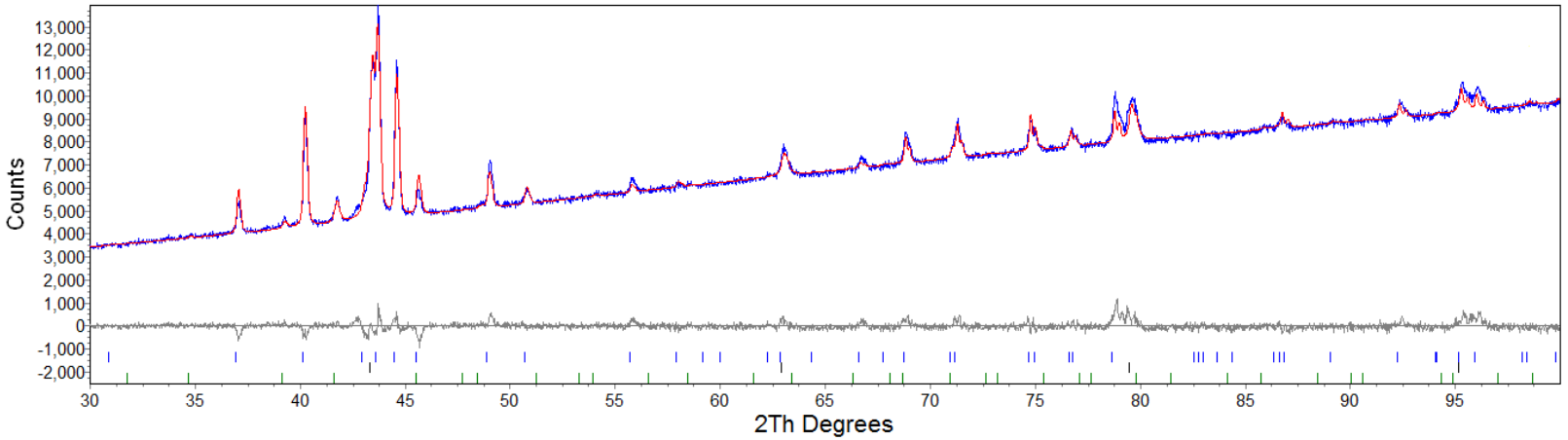

Figure C.3 As-cast Mo = 0.1 showing observed pattern (blue) and calculated fit after pseudo-Rietveld refinement (red).

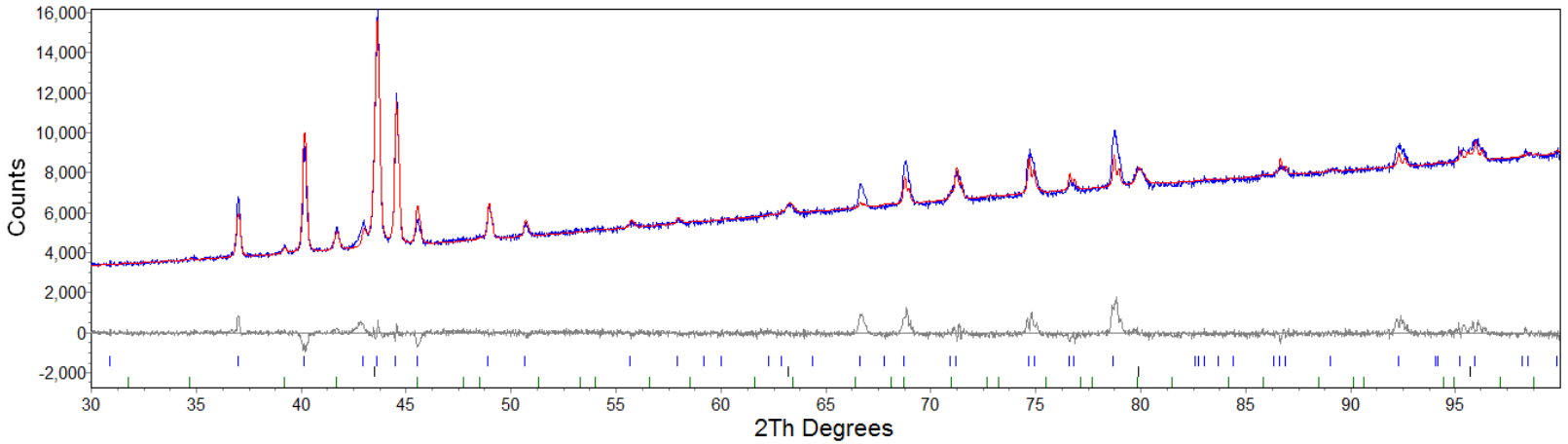

Figure C.4 As-cast Ta = 0.1 showing observed pattern (blue) and calculated fit after pseudo-Rietveld refinement (red).

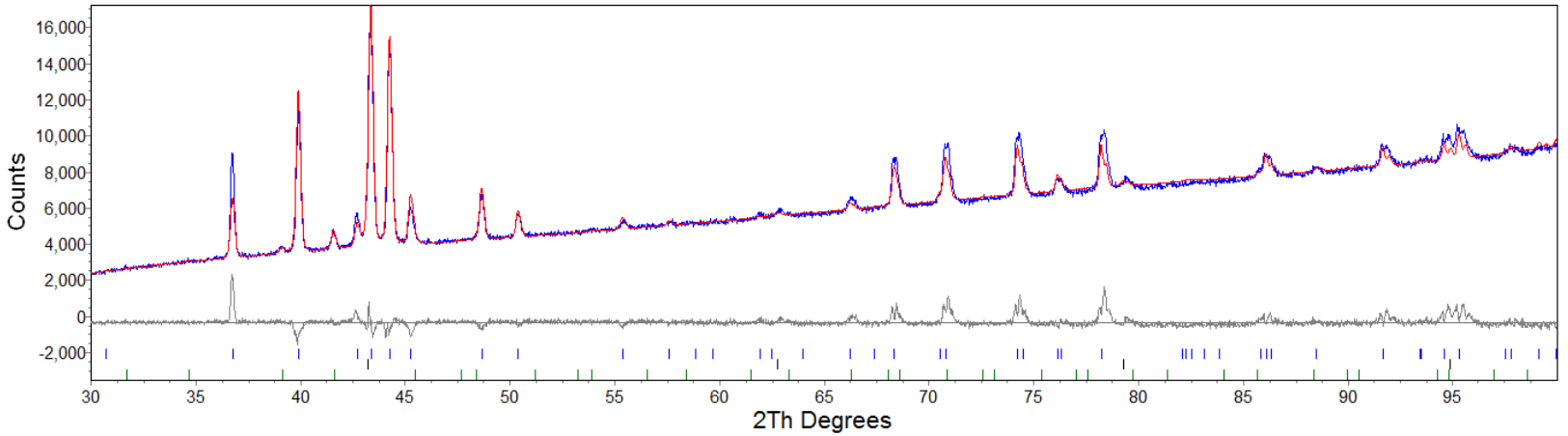

Figure C.5 Heat Treated Nb = 0.1 showing observed pattern (blue) and calculated fit after pseudo-Rietveld refinement (red).

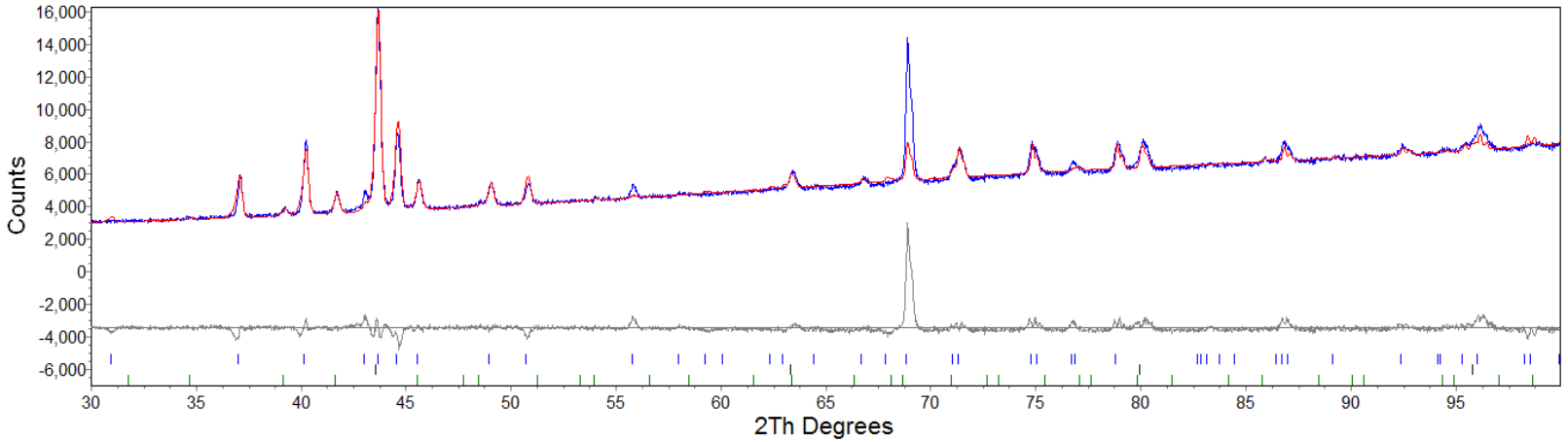

Figure C.6 Heat Treated Cr = 0.1 showing observed pattern (blue) and calculated fit after pseudo-Rietveld refinement (red).

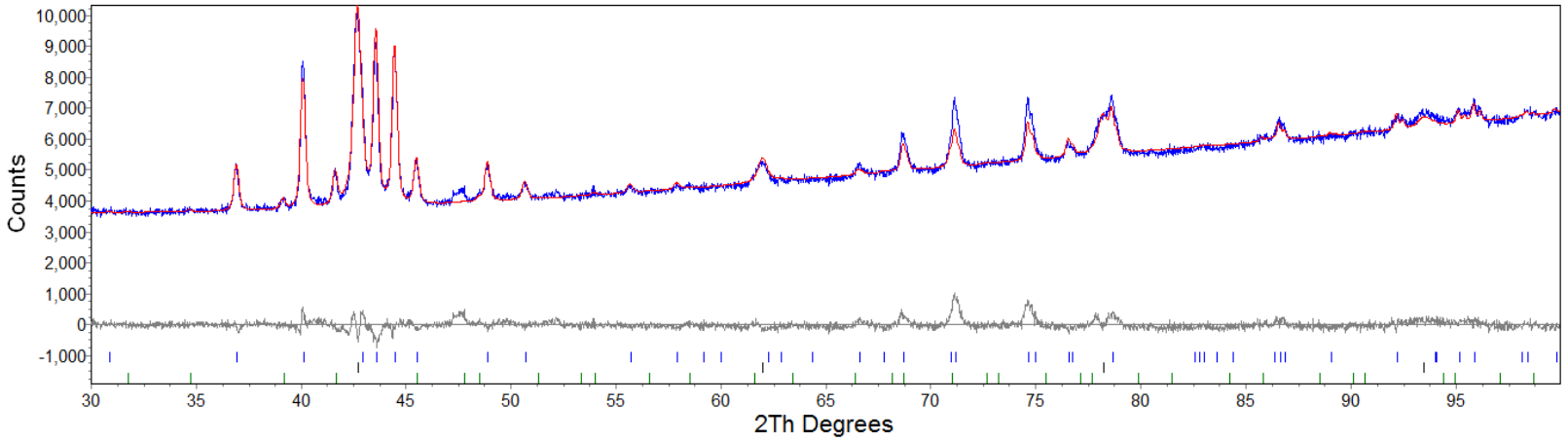

Figure C.7 Heat Treated Mo = 0.1 showing observed pattern (blue) and calculated fit after pseudo-Rietveld refinement (red).

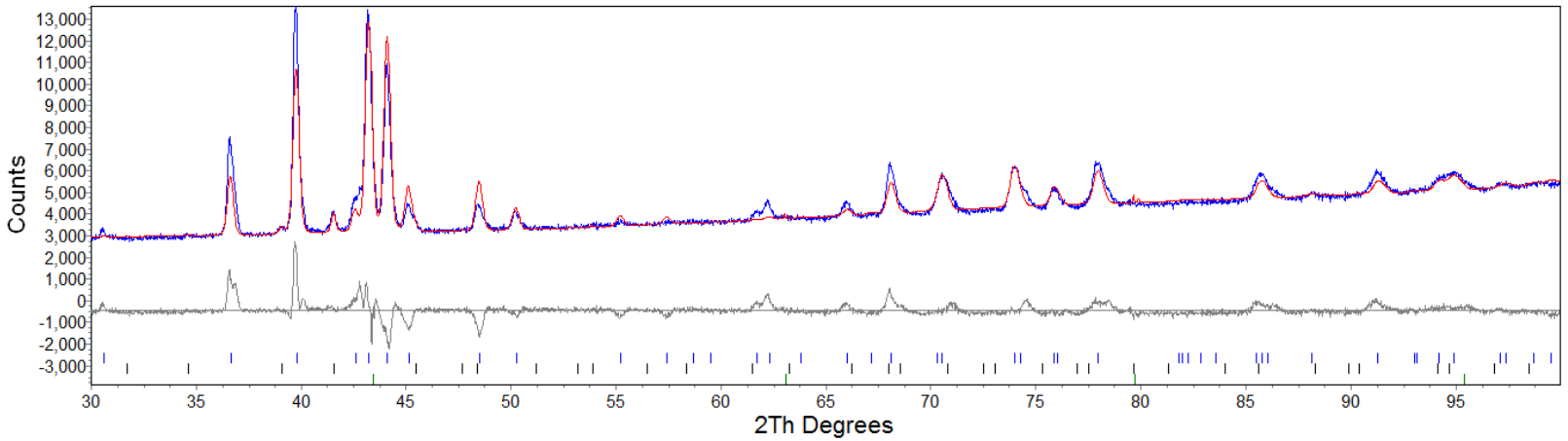

Figure C.8 Heat Treated Ta = 0.1 showing observed pattern (blue) and calculated fit after pseudo-Rietveld refinement (red).

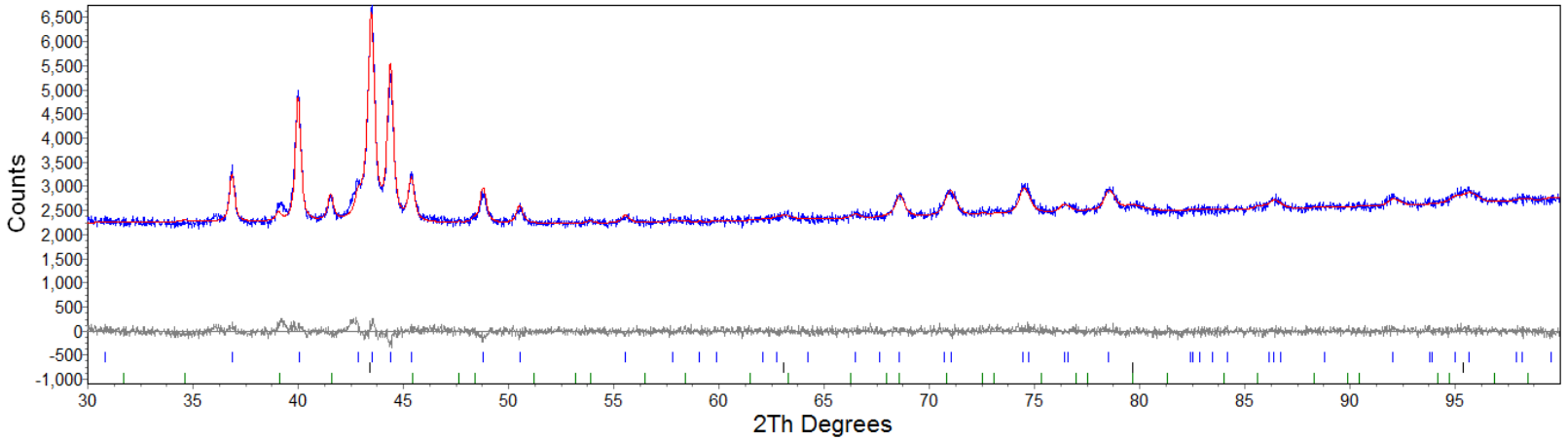

Figure C.9 Hydrogen Cycled Nb = 0.1 showing observed pattern (blue) and calculated fit after pseudo-Rietveld refinement (red).

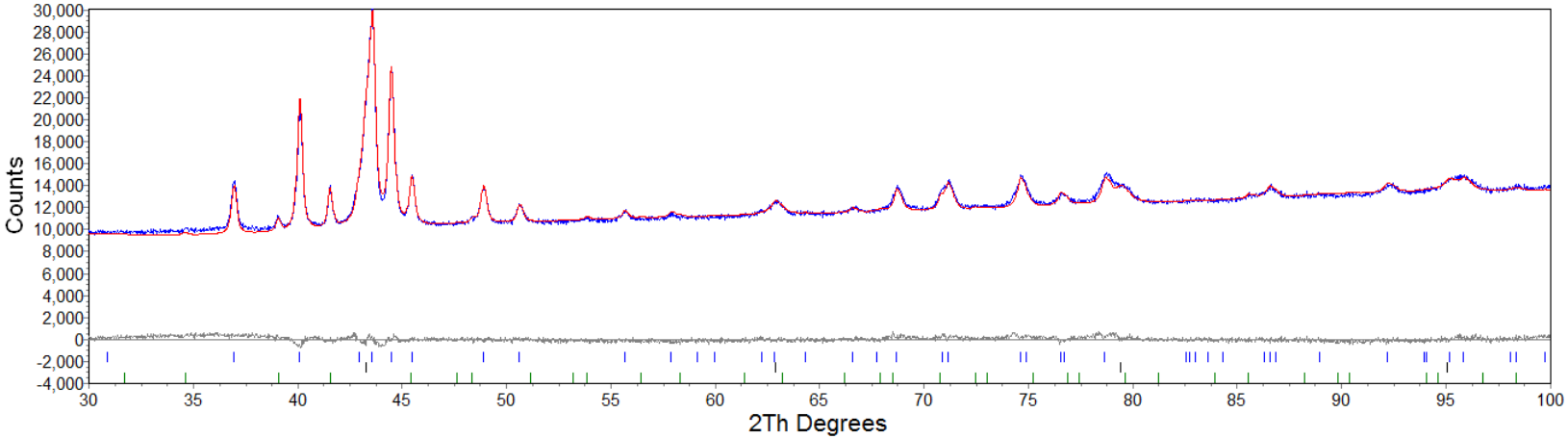

Figure C.10 Hydrogen Cycled Cr = 0.1 showing observed pattern (blue) and calculated fit after pseudo-Rietveld refinement (red).

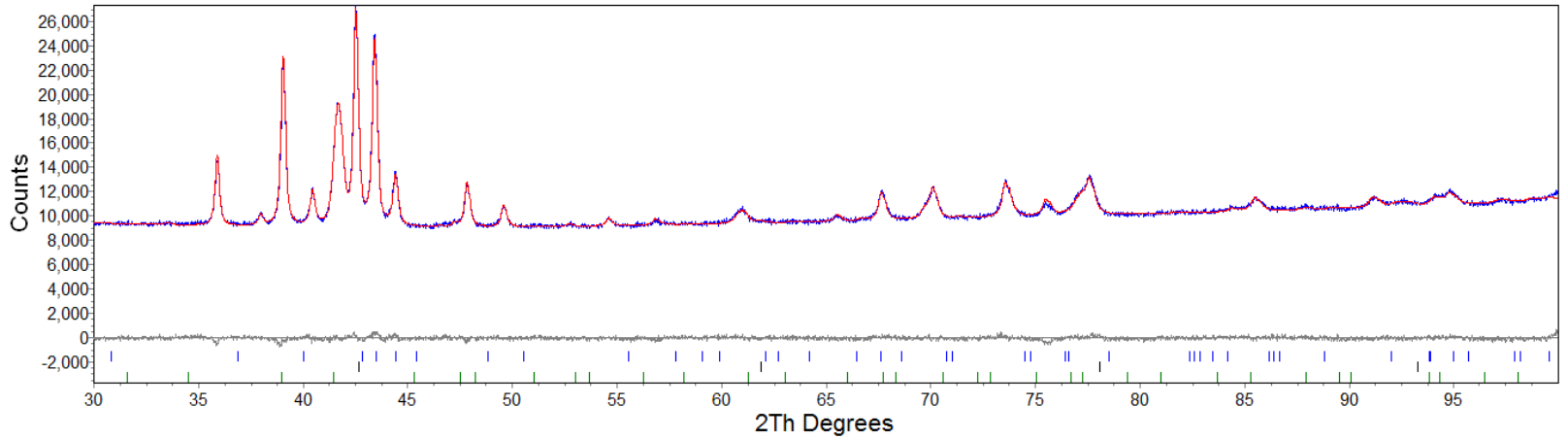

Figure C.11 Hydrogen Cycled Mo = 0.1 showing observed pattern (blue) and calculated fit after pseudo-Rietveld refinement (red).

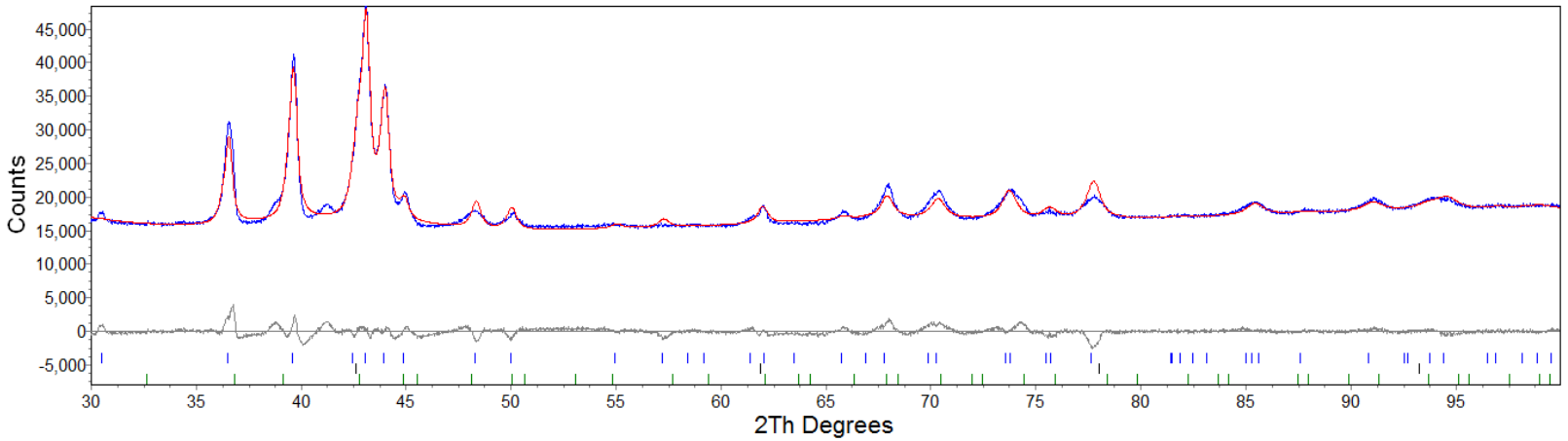

Figure C.12 Hydrogen Cycled Ta = 0.1 showing observed pattern (blue) and calculated fit after pseudo-Rietveld refinement (red).

C.2 Calculations for Unit Cell Volumes in Ti-V-TM-Mn Alloys

The following tables show the calculations involved in determining what causes expansion or reduction in the unit cell volume of the C14 Laves and BCC phases between the as-cast and heat treated Ti-V-Mn alloys. This is done by calculating which elemental substitutions have taken place based on the EDS data.

Table C.1 Composition (at%) of C14 Laves phase for as-cast and heat treated Ti-V-TM-Mn alloys.

Alloy	Phase Location	As-Cast EDS			Heat Treated EDS		
		V	TM	Mn	V	TM	Mn
Nb = 0.1	Light	18.87	5.26	51.52	18.3	7.67	50.27
	% of Overall Composition	24.94	6.95	68.10	24	10.67	54.94
Cr = 0.1	Light	13.42	4.87	51.68	13.86	4.61	51.98
	% of Overall Composition	19.18	6.96	73.86	19.67	6.54	73.78
Mo = 0.1	Light	29.16	7.54	41.41	29.95	8.37	40.18
	% of Overall Composition	37.33	9.65	53.01	38.15	10.66	51.18
Ta = 0.1	Light	20.52	11.85	49.96	21.27	13.05	48.96
	% of Overall Composition	24.92	14.39	60.68	25.54	15.67	58.79

Table C.2 Difference between at% composition of as-cast and heat treated alloys and elemental substitution in Ti-V-TM-Mn alloys.

Alloy	Overall Difference (as cast – heat treated)			
		V	TM	Mn
Nb = 0.1	Difference	- 0.57	2.41	- 1.25
	% Difference	- 0.94	3.11	- 2.17
	Elemental Substitution	- 1	3	- 2
Cr = 0.1	Difference	0.44	- 0.26	0.3
	% Difference	0.49	- 0.42	- 0.08
	Elemental Substitution	0	0	0
Mo = 0.1	Difference	0.79	0.86	- 1.23
	% Difference	0.82	1.01	-1.83
	Elemental Substitution	1	1	-2
Ta = 0.1	Difference	0.75	1.2	- 1
	% Difference	0.62	1.28	- 1.89
	Elemental Substitution	1	1	- 2

Table C.3 Composition (at%) of BCC phase for as-cast and heat treated Ti-V-TM-Mn alloys.

Alloy	Phase Location	As-Cast EDS			Heat Treated EDS		
		V	TM	Mn	V	TM	Mn
Nb = 0.1	Grey	35.24	0.98	41.91	35.81	1.01	43.04
	% of Overall Composition	45.1	1.25	53.64	44.84	1.26	53.89
Cr = 0.1	Grey	30.67	6.3	45.62	30.33	6.29	45.53
	% of Overall Composition	37.14	7.63	55.24	36.92	7.66	55.42
Mo = 0.1	Grey	14.22	1.21	52.4	14.45	1.56	52.42
	% of Overall Composition	20.96	1.78	77.25	21.12	2.28	76.60
Ta = 0.1	Grey	30.81	0.48	46	29.49	0.59	46.44
	% of Overall Composition	39.86	0.62	59.52	38.54	0.77	60.69

Table C.4 Difference between at% composition of as-cast and heat treated alloys and elemental substitution in Ti-V-TM-Mn alloys.

Alloy	Overall Difference (as cast – heat treated)			
		V	TM	Mn
Nb = 0.1	Difference	0.57	0.03	1.13
	% Difference	- 0.26	0.01	0.25
	Elemental Substitution	0	0	0
Cr = 0.1	Difference	- 0.34	- 0.01	- 0.09
	% Difference	- 0.21	0.03	0.19
	Elemental Substitution	0	0	0
Mo = 0.1	Difference	0.23	0.35	0.02
	% Difference	0.15	0.5	- 0.65
	Elemental Substitution	0	0	0
Ta = 0.1	Difference	- 0.22	0.11	0.24
	% Difference	- 0.32	0.15	0.39
	Elemental Substitution	0	0	0

C.3. Van't Hoff Data for Ti-V-TM-Mn Alloys

Table C.5 Van't hoff data for absorption and desorption in Nb = 0.1, Cr = 0.1 and Mo = 0.1

Alloy	Absorption				Desorption			
	T (K)	P	1/T	LnP	T (K)	P	1/T	LnP
Nb = 0.1	303.16	28.6007	0.003299	3.353431	303.15	23.7523	0.003299	3.167679
	313.14	37.4653	0.003193	3.623415	313.11	32.1661	0.003194	3.470913
	323.15	49.7871	0.003095	3.907756	323.17	42.6927	0.003094	3.754028
	333.15	57.7486	0.003002	4.056099	333.17	55.3823	0.003001	4.014260
Cr = 0.1	303.02	54.5291	0.0033	3.998735	303.14	33.3959	0.003299	3.508433
	313.46	69.5753	0.00319	4.242410	312.88	43.1639	0.003196	3.765004
	323.38	85.0082	0.003092	4.442748	322.88	57.9303	0.003097	4.059240
	333.12	93.9659	0.003002	4.542932	333.13	74.5272	0.003002	4.311164
Mo = 0.1	303.19	49.7109	0.003298	3.906225	303.16	29.6052	0.003299	3.387951
	313.18	60.6044	0.003193	4.104367	313.14	38.1448	0.003194	3.641389
	323.12	73.4118	0.003095	4.296085	323.15	49.7159	0.003095	3.906324
	333.15	83.6027	0.003002	4.426078	333.14	59.4201	0.003002	4.084633

Appendix D

D.1 Individual XRD Traces of Ti-V-TM-Mn Alloys

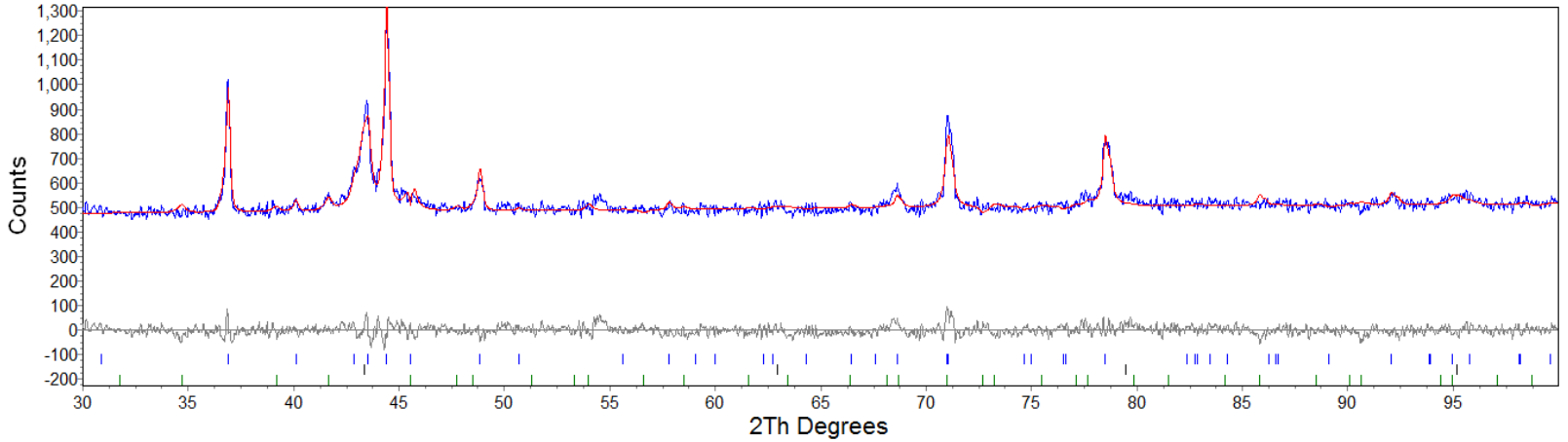

Figure D.1 XRD pattern of as-cast Nb = 0.05 showing observed pattern (blue) and calculated fit after pseudo-Rietveld refinement (red).

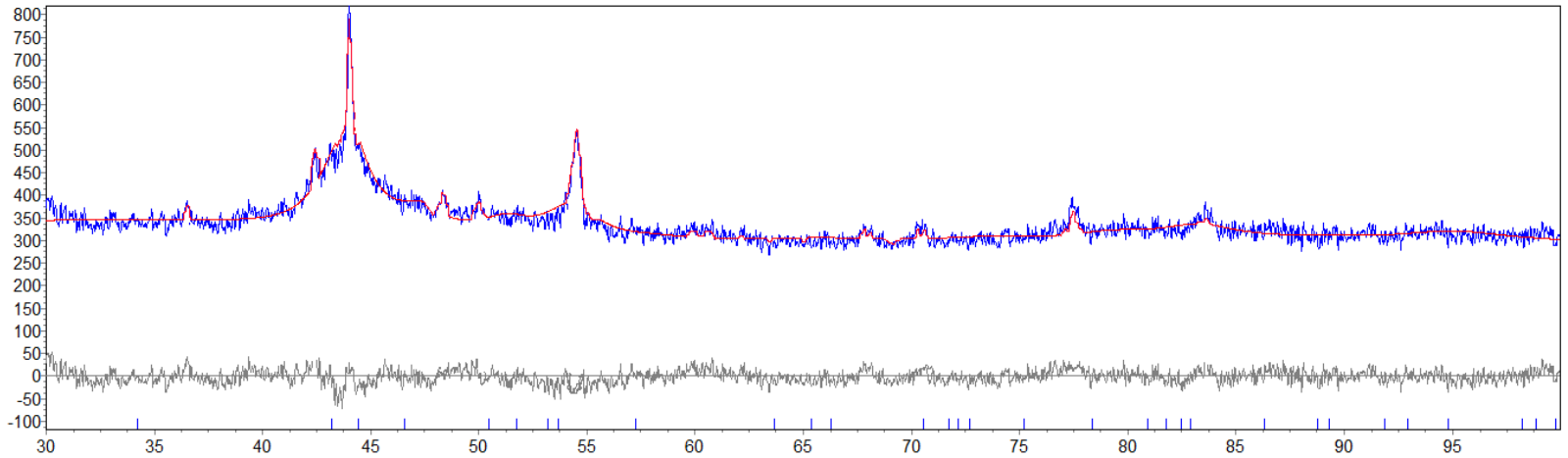

Figure D.2 XRD pattern of as-cast Nb = 0.2 showing observed pattern (blue) and calculated fit after pseudo-Rietveld refinement (red).

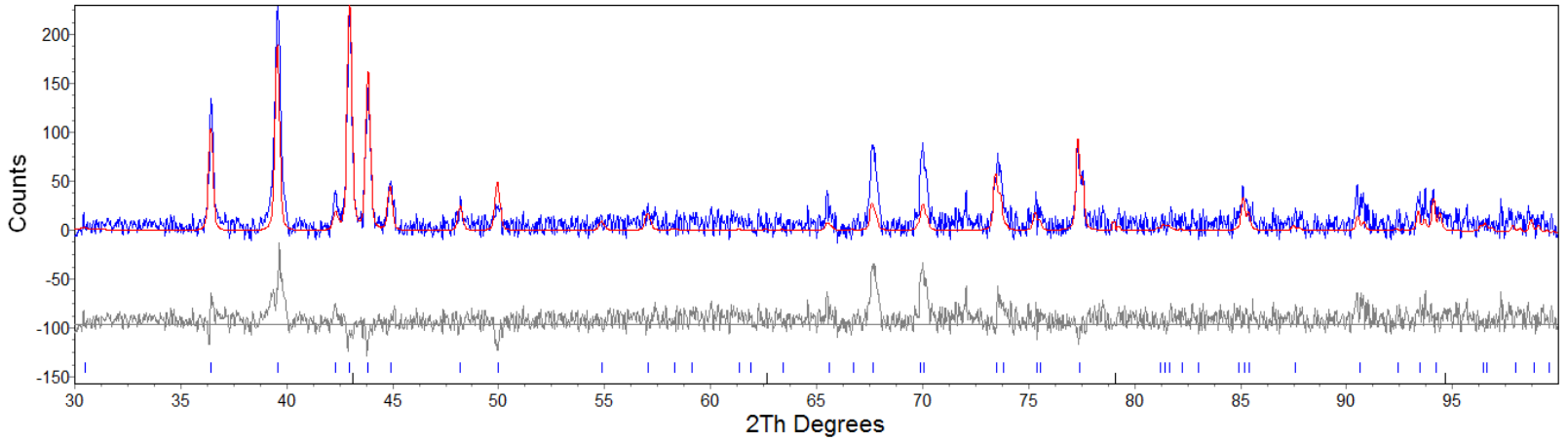

Figure D.3 XRD pattern of as-cast Nb = 0.5 showing observed pattern (blue) and calculated fit after pseudo-Rietveld refinement (red).

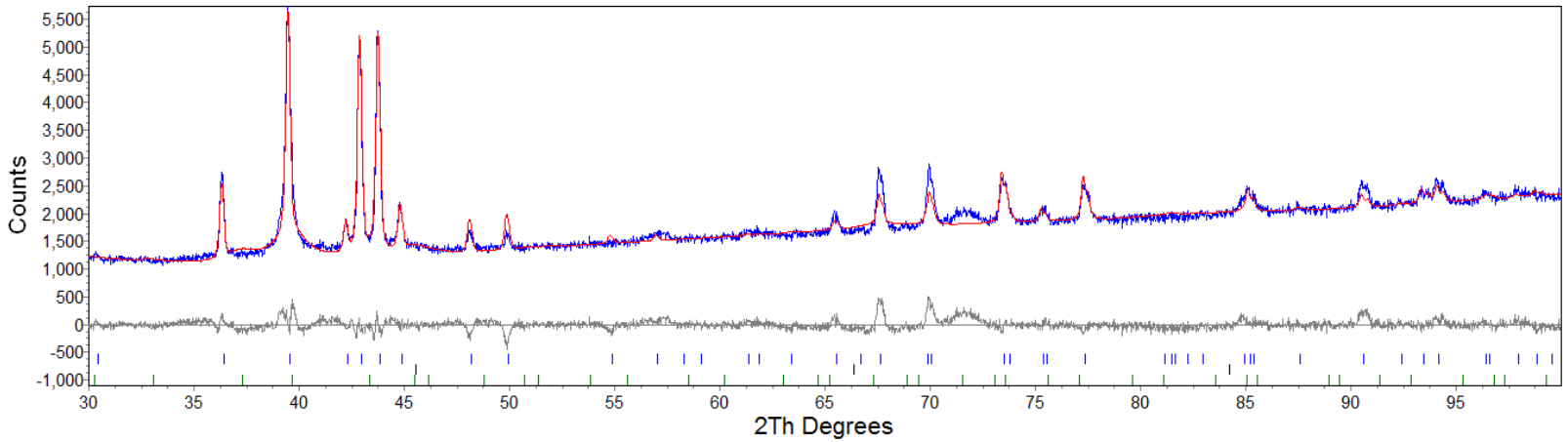

Figure D.4 XRD pattern of heat treated Nb = 0.05 showing observed pattern (blue) and calculated fit after pseudo-Rietveld refinement (red).

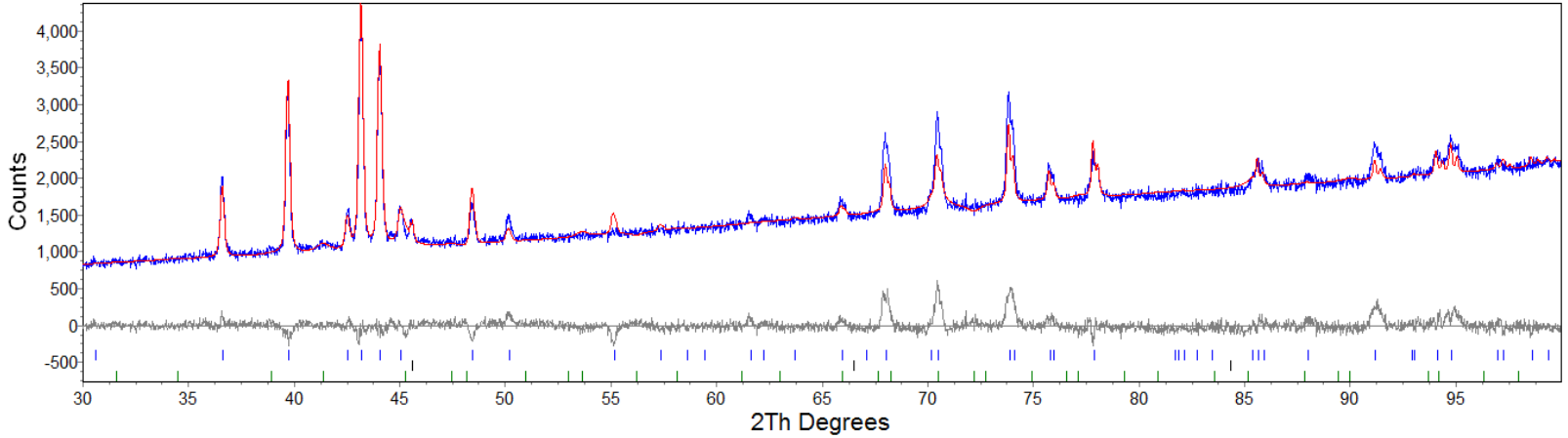

Figure D.5 XRD pattern of heat treated Nb = 0.2 showing observed pattern (blue) and calculated fit after pseudo-Rietveld refinement (red).

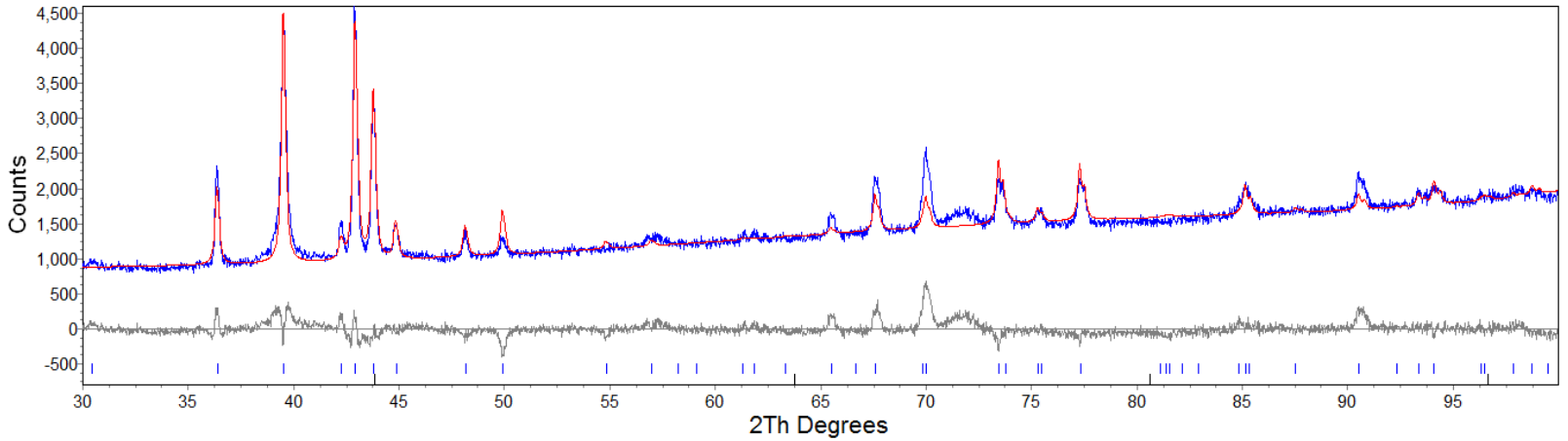

Figure D.6 XRD pattern of heat treated Nb = 0.5 showing observed pattern (blue) and calculated fit after pseudo-Rietveld refinement (red).

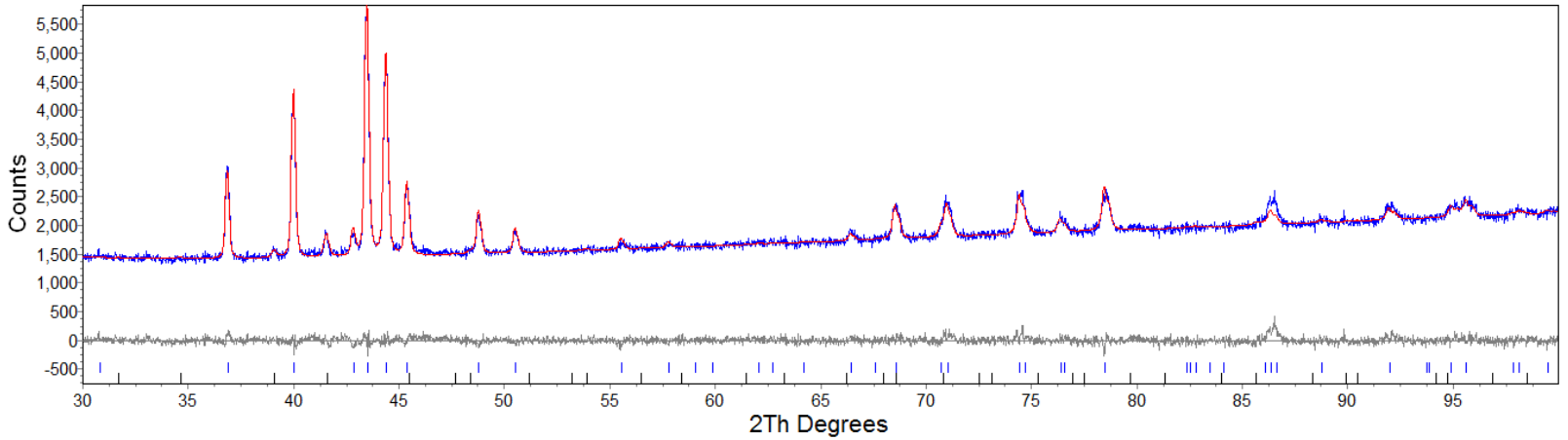

Figure D.7 XRD pattern of hydrogen cycled Nb = 0.05 showing observed pattern (blue) and calculated fit after pseudo-Rietveld refinement (red).

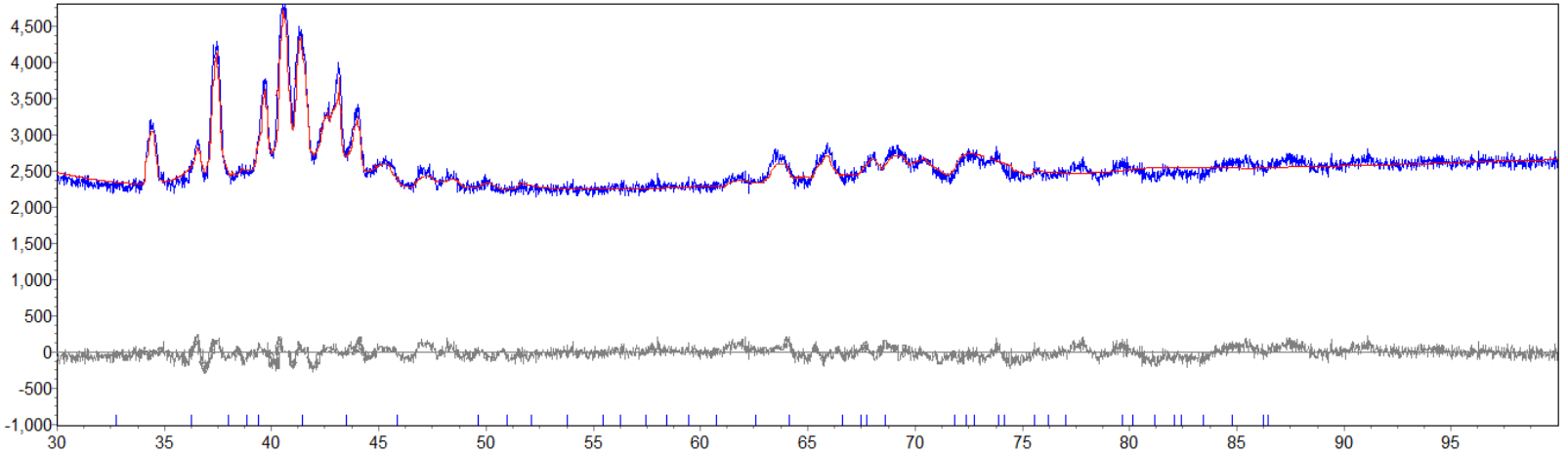

Figure D.8 XRD pattern of hydrogen cycled Nb = 0.2 showing observed pattern (blue) and calculated fit after pseudo-Rietveld refinement (red).

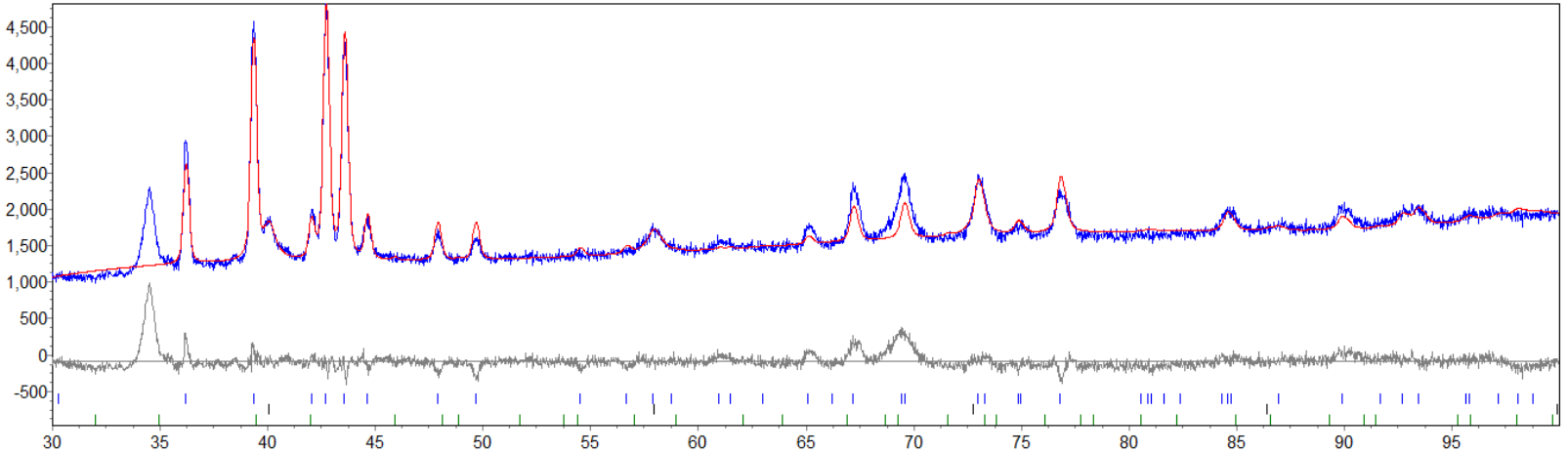

Figure D.9 XRD pattern of hydrogen cycled Nb = 0.5 showing observed pattern (blue) and calculated fit after pseudo-Rietveld refinement (red).

D.2 Calculations for Unit Cell Volumes

The following tables show the calculations involved in determining what causes expansion or reduction in the unit cell volume of the C14 Laves and BCC phases between the as-cast and heat treated Ti-V-Nb-Mn alloys. This is done by calculating which elemental substitutions have taken place based on the EDS data.

Table D.1 Composition (at%) of C14 Laves phase for as-cast and heat treated Ti-V-Nb-Mn alloys.

Alloy	Phase Location	As-Cast EDS			Heat Treated EDS		
		V	Nb	Mn	V	Nb	Mn
Nb = 0.05	Light	17.85	4.76	52.87	18.36	4.59	51.03
	% of Overall Composition	23.65	6.31	70.07	24.82	6.2	68.98
Nb = 0.1	Light	18.87	5.26	51.52	18.3	7.67	50.27
	% of Overall Composition	24.94	6.95	68.10	24	10.67	54.94
Nb = 0.2	Light	15.7	12.25	50.87	14.96	12.83	51.46
	% of Overall Composition	19.92	15.54	64.54	18.88	16.19	64.93
Nb = 0.5	Grey	0	22.77	59.51	0	23.86	58.76
	% of Overall Composition	0	27.8	72.2	0	28.88	71.12

Table D.2 Difference between at% composition of as-cast and heat treated alloys and elemental substitution in Ti-V-Nb-Mn alloys.

Alloy	Overall Difference (as cast – heat treated)			
		V	Nb	Mn
Nb = 0.05	Difference	0.51	- 0.24	- 1.84
	% Difference	0.97	- 0.10	- 0.63
	Elemental Substitution	1	0	- 1
Nb = 0.1	Difference	- 0.57	2.41	- 1.25
	% Difference	- 0.94	3.11	- 2.17
	Elemental Substitution	- 1	3	- 2
Nb = 0.2	Difference	- 0.74	0.58	- 0.59
	% Difference	- 1.04	0.65	0.13
	Elemental Substitution	- 1	1	0
Nb = 0.5	Difference	0	1.09	- 0.75
	% Difference	0	1.08	- 0.97
	Elemental Substitution	0	1	- 1

Table D.3 Composition (at%) of BCC phase for as-cast and heat treated Ti-V-Nb-Mn alloys.

Alloy	Phase Location	As-Cast EDS			Heat Treated EDS		
		V	Nb	Mn	V	Nb	Mn
Nb = 0.05	Grey	33.84	0.86	45.33	34.63	0.8	44.87
	% of Overall Composition	42.28	1.07	56.64	43.13	1	55.88
Nb = 0.1	Grey	35.24	0.98	41.91	35.81	1.01	43.04
	% of Overall Composition	45.1	1.25	53.64	44.84	1.26	53.89
Nb = 0.2	Grey	17.54	3.64	46.89	16.78	4.48	47.7
	% of Overall Composition	25.77	5.35	68.88	24.33	6.50	69.17
Nb = 0.5	Light	0	36.91	26.14	0	37.17	24.82
	% of Overall Composition	0	58.54	41.46	0	59.96	40.04

Table D.4 Difference between at% composition of as-cast and heat treated alloys and elemental substitution in Ti-V-Nb-Mn alloys.

Alloy	Overall Difference (as cast – heat treated)			
		V	Nb	Mn
Nb = 0.05	Difference	0.79	- 0.06	- 0.46
	% Difference	0.84	- 0.08	- 0.78
	Elemental Substitution	1	0	-1
Nb = 0.1	Difference	0.57	0.03	1.13
	% Difference	- 0.26	0.01	0.25
	Elemental Substitution	0	0	0
Nb = 0.2	Difference	- 0.76	0.84	0.81
	% Difference	- 1.43	1.15	0.29
	Elemental Substitution	- 1	1	0
Nb = 0.5	Difference	0	0.26	- 1.32
	% Difference	0	1.42	- 1.03
	Elemental Substitution	0	1	- 1

D.3 Van't Hoff Data for Ti-V-Nb-Mn Alloys

Table D.5 Van't hoff data for absorption and desorption in Nb = 0.05, Nb = 0.1, Nb = 0.2 and Nb = 0.5.

Alloy	Absorption				Desorption			
	T (K)	P	1/T	LnP	T (K)	P	1/T	LnP
Nb = 0.05	303.36	43.2565	0.003296	3.767148	302.94	27.8632	0.003301	3.327307
	313.18	55.4887	0.003193	4.016179	313.1	40.7742	0.003194	3.708049
	323.56	71.9837	0.003091	4.276440	322.74	54.3802	0.003098	3.996000
	333.18	85.745	0.003001	4.451378	333.15	70.3331	0.003002	4.253243
Nb = 0.1	303.16	28.6007	0.003299	3.353431	303.15	23.7523	0.003299	3.167679
	313.14	37.4653	0.003193	3.623415	313.11	32.1661	0.003194	3.470913
	323.15	49.7871	0.003095	3.907756	323.17	42.6927	0.003094	3.754028
	333.15	57.7486	0.003002	4.056099	333.17	55.3823	0.003001	4.014260
Nb = 0.2	303.44	13.3385	0.003296	2.590655	302.76	10.0558	0.003303	2.308150
	313.5	17.6199	0.00319	2.869029	313.23	14.846	0.003193	2.697730
	323.54	21.9417	0.003091	3.088389	322.78	17.8895	0.003098	2.884213
	333.57	31.3487	0.002998	3.445173	332.78	23.8203	0.003005	3.170538
Nb = 0.5	303.20	15.3446	0.003298	2.730764	303.16	8.49308	0.003299	2.139252
	313.15	22.6084	0.003193	3.118322	313.15	10.7661	0.003193	2.376426
	323.15	59.3103	0.003095	4.082783	323.17	15.6881	0.003094	2.752903
	333.16	68.887	0.003001	4.232467	333.16	23.8194	0.003002	3.170524

Publications

Ti-V-Mn based metal hydrides for hydrogen storage

Pickering, L., Li, Jing., Reed, D., Bevan, A., and Book, D.

Journal of Alloys and Compounds, (2013). *580,* S233 - S237.

Design and development of a two-stage metal hydride compressor

Pickering, L., Bevan, A., and Book, D.

To be submitted to Journal of Hydrogen Energy (2014).

Poster Presentations

Ti-V based Metal Hydrides for Hydrogen Storage

Pickering, L., Bevan, A., and Book, D.

Faraday Discussion 151: Hydrogen Storage Materials, Oxford, UK. (2011)

Two-Stage Metal Hydride Compressor

Pickering, L., Bevan, A., and Book, D.

International Hydrogen Research Showcase, Birmingham, UK (2011)

Ti-V-Mn based Metal Hydrides for Hydrogen Storage

Pickering, L., Li, Jing., Reed, D., and Book, D.

MH2012, International Symposium on Metal-Hydrogen Systems , Kyoto, Japan (2012)

List of References

Ahluwalia, R. K., Hua, T. Q., & Peng, J. K. (2012). On-board and Off-board performance of hydrogen storage options for light-duty vehicles. *International Journal of Hydrogen Energy*, *37*(3), 2891–2910.

Ahluwalia, R. K., Hua, T. Q., Peng, J.-K., Lasher, S., McKenney, K., Sinha, J., & Gardiner, M. (2010). Technical assessment of cryo-compressed hydrogen storage tank systems for automotive applications. *International Journal of Hydrogen Energy*, *35*(9), 4171–4184.

Akiba, E. (1999). Hydrogen-absorbing alloys. *Current Opinion in Solid State and Materials Science*, *4*(3), 267–272.

Akiba, E, & Iba, H. (1998). Hydrogen absorption by Laves phase related BCC solid solution. *Intermetallics*, *6*(6), 461–470.

Akiba, Etsuo, Huot, J., & Iba, H. (1994). Laves phase related multiphase alloys. In P. Bannett & T. Sakai (Eds.), *The Electrochemical Society Proceedings Volume 94-27: Hydrogen and Metal Hydride Batteries* (pp. 165–171). Pennington, NJ.

Alternative Energy. (2009). New Advances in Hydrogen Fuel Catalysts. [online]. Available from: http://www.alternative-energy-news.info/new-advances-in-hydrogen-fuel-catalysts [Accessed 15 March, 2012]

American Society for Metals. National Bureau of Standards., U. S. (1980). Bulletin of alloy phase diagrams. *Bulletin of alloy phase diagrams.* Metals Park, Ohio: American Society for Metals.

Armaroli, N., & Balzani, V. (2010). The Energy Challenge. In *Energy for a Sustainable World: From the Oil Age to a Sun-Powered Future* (pp. 1–10). Weinheim, Germany: Wiley-VCH Verlag GmbH & Co. KGaA.

Barrett, C. S. (1973). Crystal Structures of Metals. In T. Lyman (Ed.), *Metals Handbook, Vol. 8: Metallography, Structures, and Phase Diagrams* (8th ed.). Ohio: American Society for Metals.

Bauen, A. (2006). Future energy sources and systems—Acting on climate change and energy security. *Journal of Power Sources*, *157*(2), 893–901.

Benham, M., & Ross, D. (1989). Experimental Determination of Absorption-Desorption Isotherms by Computer-Controlled Gravimetric Analysis. *Zeitschrift für Physikalische Chemie*, *32*, 25–32.

Bevan, A. I., Züttel, A., Book, D., & Harris, I. R. (2011). Performance of a metal hydride store on the "Ross Barlow" hydrogen powered canal boat. *Faraday Discussions*, *151*, 353.

Bjørnar, K., Sondre, G., & Cato, B. (2002). *Hydrogen - Status and Possibilities* [online]. Available from: http://bellona.org/reports/hydrogen [Accessed 19 Januray, 2012].

Bohmhammel, K., Christ, B., Reiser, A., Schlichte, K., Bogdanovic, B., Vehlen, R., & Wolf, U. (1999). Thermodynamic investigation of the magnesium–hydrogen system, *Journal of Alloys and Compounds, 282*, 84–92.

Bououdina, M., Enoki, H., & Akiba, E. (1998). The investigation of the $Zr_{1-y}Ti_y(Cr_{1-x}Ni_x)_2$-$H_2$ system $0.0 \leq y \leq 1.0$ and $0.0 \leq x \leq 1.0$ phase composition analysis and thermodynamic properties. *Journal of Alloys and Compounds*, *281*(2), 290–300.

Bowman, R., & Fultz, B. (2002). Metallic hydrides I: Hydrogen storage and other gas-phase applications. *MRS Bulletin-Materials Research Society*, (September), 688–693.

Broom, D. (2007). The accuracy of hydrogen sorption measurements on potential storage materials. *International Journal of Hydrogen Energy*, *32*(18), 4871–4888.

Burke, K. (2003). Fuel cells for space science applications. *1st International Energy Conversion Engineering Conference*, 1-10.

Burns, L. D., McCormick, J. B., & Borroni-Bird, C. E. (2002). Vehicle of change. *Scientific American*, *287*(4), 64–73.

Callister, W. D. (2003). Imperfections in Solids. In *Materials Science and Engineering: An Introduction* (6th ed., pp. 68–70). New York: John Wiley & Sons, Ltd.

Chandra, D., Reilly, J., & Chellappa, R. (2006). Metal hydrides for vehicular applications: the state of the art. *JOM Journal of the Minerals,Metals & Materials Society*. (February). 26-32.

Checchetto, R., Trettel, G., & Miotello, A. (2004). Sievert-type apparatus for the study of hydrogen storage in solids. *Measurement Science and Technology*, *15*(1), 127–130.

Coelho, A. (2007). TOPAS-Academic, Version 4.1, Coelho Software, Brisbane, Australia.

Crabtree, G. W., Dresselhaus, M. S., & Buchanan, M. V. (2004). The Hydrogen Economy. *Physics Today*, (December), 39–45.

Da Costa, D. H. (2000). Advanced Hydrogen Thermal Compression. In *2000 U.S. DOE Hydrogen Program Review* (pp. 720–727). San Ramon, CA.

Dehouche, Z., Savard, M., Laurencelle, F., & Goyette, J. (2005). Ti–V–Mn based alloys for hydrogen compression system. *Journal of Alloys and Compounds*, *400*(1-2), 276–280.

DfT. (2010). Transport Statistics Great Britain. *Statistics*, (November), 1–5. [online] Available from: http://www.dft.gov.uk/pgr/statistics/datatablespublications/tsgb/edition2008.pdf [Accessed 20 March 2012].

Dillon, A., Jones, K., & Bekkedahl, T. (1997). Storage of hydrogen in single-walled carbon nanotubes. *Nature*, *386*, 377–379.

Dodds, P. E., & Demoullin, S. (2013). Conversion of the UK gas system to transport hydrogen. *International Journal of Hydrogen Energy*, *38*(18), 7189–7200.

Department of Energy, U.S (2010). Targets for Onboard Hydrogen Storage Systems for Light-Duty Vehicles. [online] Available from: http://www1.eere.energy.gov/hydrogenandfuelcells/storage/pdf. [Accessed 23 March 2012]

Dornheim, M. (2011). Thermodynamics of Metal Hydrides: Tailoring Reaction Enthalpies of Hydrogen Storage Materials. In PirajÃ¡n, J. C. M. (Ed.), *Thermodynamics - Interaction Studies- Solids, Liquids and Gases*. InTech.

Dou, T., Wu, Z., Mao, J., & Xu, N. (2008). Application of commercial ferrovanadium to reduce cost of Ti–V-based BCC phase hydrogen storage alloys. *Materials Science and Engineering: A*, *476*(1-2), 34–38.

Eberle, U., Felderhoff, M., & Schüth, F. (2009). Chemical and Physical Solutions for Hydrogen Storage. *Angewandte Chemie International Edition*, *48*(36), 6608–6630.

Edwards, A. (1972). The lattice dimensions of the AB_2 Laves phases. *Metallurgical and Materials Transactions B*, *3* (June), 1365-1372.

Fletcher, D. A., McMeeking, R. F., & Parkin, D. (1996). The United Kingdom Chemical Database Service. *Journal of Chemical Information and Computer Sciences*, *2338*(96), 746–749.

Fruchart, D., Soubeyroux, J. L., & Hempelmann, R. (1984). Neutron diffraction in $Ti_{1.2}Mn_{1.8}$ deuteride: Structural and magnetic aspects. *Journal of the Less Common Metals*, *99*, 307–319.

Graham, T. (1866). On the absorption and dialytic separation of gases by colloid septa. *Philosophical Transactions of the Royal Society of London*, *156*(1866), 399–439.

Gross, K., Züttel, A., & Schlapbach, L. (1998). On the possibility of metal hydride formation: Part I. The synthesis of $MgNi_3B_2$ by mechanical milling and sintering. *Journal of Alloys and Compounds*, *274*, 234–238.

Grove, W. R. (1839). On Voltaic Series and the Combination of Gases by Platinum. *The London and Edinburgh Philosophical Magazine and Journal of Science*, *14*(series 3), 127–130.

Guo, X., Wang, S., Liu, X., Li, Z., Lü, F., Mi, J., Hao, L and Jiang, L. (2011). Laves phase hydrogen storage alloys for super-high-pressure metal hydride hydrogen compressors. *Rare Metals*, *30*(3), 227–231.

Hagström, M., Vanhanen, J., & Lund, P. (1998). AB_2 metal hydrides for high-pressure and narrow temperature interval applications. *Journal of Alloys and Compounds*, *269*, 288–293.

Harris, R., Book, D., Anderson, P., & Edwards, P. (2004). Hydrogen storage: the grand challenge. *The Fuel Cell Review*, *1*, 17–23.

Hawkes, F., Dinsdale, R., Hawkes, D., & Hussy, I. (2002). Sustainable fermentative hydrogen production: challenges for process optimisation. *Internation Journal of Hydrogen Energy*, *27*, 1339–1347.

Hirose, K. (2010). Materials towards carbon-free, emission-free and oil-free mobility: hydrogen fuel-cell vehicles--now and in the future. *Philosophical transactions. Series A, Mathematical, Physical, and Engineering Sciences*, *368*(1923), 3365–77.

Honda. (2013). FCX Clarity. [online] Available from: http://automobiles.honda.com/fcx-clarity [Accessed 15 May 2013].

Hout, J., Akiba, E., & Iba, H. (1995). Crystal structure and phase composition of alloys $Zr_{1-x}Ti_x(Mn_{l-y}V_y)_2$. *Journal of Alloys and Compounds*, *228*, 181–187.

Howarth, R. W., Santoro, R., & Ingraffea, A. (2011). Methane and the greenhouse-gas footprint of natural gas from shale formations. *Climatic Change*, *106*(4), 679–690.

Huot, J., Akiba, E., & Ishido, Y. (1995). Crystal structure of multiphase alloys $(ZrTi)(MnV)_2$. *Journal of Alloys and Compounds*, *231*, 85–89.

Iba, H., & Akiba, E. (1995). The relation between microstructure and hydrogen absorbing property in Laves phase-solid solution multiphase alloys. *Journal of Alloys and Compounds*, *231*, 508–512.

International Energy Agency. (2012). *World Energy Outlook 2012: Executive Summary* [online]. Available from: www.worldenergyoutlook.org [Accessed September 15, 2012].

International Transport Forum. (2010). Reducing Transport Greenhouse Gas Emissions: Trends and Data 2010. [online] Available from: www.internationaltransportforum.org [Accessed 23 May, 2012].

Jorgensen, S. W. (2011). Hydrogen storage tanks for vehicles: Recent progress and current status. *Current Opinion in Solid State and Materials Science*, *15*(2), 39–43.

Kehr, K. W. (1978). Theory of the diffusion of hydrogen in metals. In Alefeld, G. & Völkl, J. (Eds.), *Hydrogen in Metals I. Topics in Applied Physics,* 28, 197–226. Springer Berlin Heidelberg.

Kojima, Y., Kawai, Y., Towata, S., Matsunaga, T., Shinozawa, T., & Kimbara, M. (2006). Development of metal hydride with high dissociation pressure. *Journal of Alloys and Compounds*, *419*(1-2), 256–261.

Krainz, G. (2004). Development of Automotive Liquid Hydrogen Storage Systems. *AIP Conference Proceedings*, *710*(1), 35–40.

Laurencelle, F., Dehouche, Z., Goyette, J., & Bose, T. (2006). Integrated electrolyser—metal hydride compression system. *International Journal of Hydrogen Energy*, *31*(6), 762–768.

Lennard-Jones, J. E. (1932). Processes of adsorption and diffusion on solid surfaces. *Transactions of the Faraday Society*, *28*, 333.

Li, H., Wang, X., Dong, Z., Xu, L., & Chen, C. (2010). A study on 70 MPa metal hydride hydrogen compressor. *Journal of Alloys and Compounds*, *502*(2), 503–507.

Lide, D. R. (2004). *CRC Handbook of Chemistry and Physics*, 85th Edition. Florida: CRC Press.

Lototskyy, M., Klochko, Y., Linkov, V., Lawrie, P., & Pollet, B. G. (2012). Thermally Driven Metal Hydride Hydrogen Compressor for Medium-Scale Applications. *Energy Procedia*, *29*, 347–356.

Lundin, C., Lynch, F., & Magee, C. (1977). A correlation between the interstitial hole sizes in intermetallic compounds and the thermodynamic properties of the hydrides formed from those compounds. *Journal of the Less Common Metals*, *56*, 19–37.

Lynch, J. F., Maeland, A. J., & Libowitz, G. G. (1985). Lattice Parameter Variation and Thermodynamics of Dihydride Formation in the Vanadium-Rich V-Ti-Fe/H_2 System. *Zeitschrift für Physikalische Chemie*, *145*(1_2), 51–59.

Maeland, A. (1964). Investigation of the Vanadium-Hydrogen System by X-Ray Diffraction Techniques1, 2. *The Journal of Physical Chemistry*, *68*(8), 2197–2200.

Maeland, A., Libowitz, G., & Lynch, J. (1984). Hydride formation rates of titanium-based BCC solid solution alloys. *Journal of the Less Common Metals*, *104*(2), 361–364.

Maeland, A., Libowitz, G., Lynch, J., & Rak, G. (1984). Hydride formation rates of BCC group V metals. *Journal of the Less Common Metals*, *104*, 133–139.

Mal, H. Van, Buschow, K., & Miedema, A. (1974). Hydrogen absorption in $LaNi_5$ and related compounds: Experimental observations and their explanation. *Journal of the Less Common Metals*, *35*, 65–76.

Martínez, A., & Dos Santos, D. S. (2012). Influence of the substitution of V by Nb in the structure and properties of hydrogen absorption/desorption of $TiCr_{1.1}V_{0.9}$ alloy. *Journal of Alloys and Compounds*, *536*, S231–S235.

Matsuda, J., Nakamura, Y., & Akiba, E. (2011). Microstructure of Ti–V–Mn BCC alloys before and after hydrogen absorption–desorption. *Journal of Alloys and Compounds*, *509*(11), 4352–4356.

Matsunaga, T., Kon, M., Washio, K., Shinozawa, T., & Ishikiriyama, M. (2009). TiCrVMo alloys with high dissociation pressure for high-pressure MH tank. *International Journal of Hydrogen Energy*, *34*(3), 1458–1462.

Maus, S., Hapke, J., Ranong, C. N., Wüchner, E., Friedlmeier, G., & Wenger, D. (2008). Filling procedure for vehicles with compressed hydrogen tanks. *International Journal of Hydrogen Energy*, *33*(17), 4612–4621.

Mayer, H., Alasafi, K., & Bernauer, O. (1982). Strukturuntersuchungen an $TiMe_{1.87}$ und $TiMe_{1.87}D_{2.36}$ (Me = $V_{0.40}Mn_{0.60}$) mittels Neutronenbeugung. *Journal of the Less Common Metals*, *88*(2), 7 – 10.

Mendelsohn, M. H., & Gruen, D. M. (1977). $LaNi_{5-x}Al_x$ is a versatile alloy system for metal hydride applications. *Nature*, *269*, 45–47.

Miedema, A. (1973). The electronegativity parameter for transition metals: heat of formation and charge transfer in alloys. *Journal of the Less Common Metals*, *32*, 117–136.

Mitrokhin, S., Zotov, T., Movlaev, E., & Verbetsky, V. (2013). Hydrogen interaction with intermetallic compounds and alloys at high pressure. *Journal of Alloys and Compounds*.

Mitrokhin, S. V. (2005). Regularities of hydrogen interaction with multicomponent Ti(Zr)–Mn–V Laves phase alloys. *Journal of Alloys and Compounds*, *404-406*(1), 384–387.

Mitrokhin, S. V, Smirnova, T. N., Somenkov, V. A., Glazkov, V. P., & Verbetsky, V. N. (2003). Structure of (Ti,Zr)–Mn–V nonstoichiometric Laves phases and $(Ti_{0.9}Zr_{0.1})(Mn_{0.75}V_{0.15}Ti_{0.1})_2D_{2.8}$ deuteride. *Journal of Alloys and Compounds*, *356-357*, 80–83.

Mori, D, & Hirose, K. (2009). Recent challenges of hydrogen storage technologies for fuel cell vehicles. *International Journal of Hydrogen Energy*, *34*(10), 4569–4574.

Mori, Daigoro, Kobayashi, N., Shinozawa, T., Matsunaga, T., Kuba, H., Toh, K., & Tsuzuki, M. (2005). Hydrogen storage materials for fuel cell vehicles high-pressure MH system. *Journal of the Japan Institute of Metals,* 308–311.

Mouri, T., & Iba, H. (2002). Hydrogen-absorbing alloys with a large capacity for a new energy carrier. *Materials Science and Engineering: A*, *329-331*, 346–350.

Muthukumar, P., Prakashmaiya, M., & Srinivasamurthy, S. (2005). Experiments on a metal hydride based hydrogen compressor. *International Journal of Hydrogen Energy*, *30*(8), 879–892.

Nakamura, Y., & Akiba, E. (2000). New hydride phase with a deformed FCC structure in the Ti-V-Mn solid solution-hydrogen system. *Journal of Alloys and Compounds*, *311*(2), 317–321.

Nakamura, Y., & Akiba, E. (2002). Hydriding properties and crystal structure of NaCl-type mono-hydrides formed from Ti–V–Mn BCC solid solutions. *Journal of Alloys and Compounds*, *345*, 175–182.

Nakamura, Y., Kamiyama, T., & Akiba, E. (2011). Hydrogen Vibrational Excitation Spectra of CaF_2-Type Metal Hydrides Synthesized from Ti-Based BCC Solid Solution Alloys. *Materials Transactions*, *52*(4), 591–594.

Nakamura, Y., Oikawa, K., Kamiyama, T., & Akiba, E. (2001). Crystal structure of two hydrides formed from a Ti–V–Mn BCC solid solution alloy studied by time-of-flight neutron powder diffraction - a NaCl structure and a CaF structure. *Journal of Alloys and Compounds*, *316*, 284–289.

Nakano, H., & Wakao, S. (1995). Substitution effect of elements in Zr-based alloys with Laves phase for nickel-hydride battery. *Journal of Alloys and Compounds*, *231*(1-2), 587–593.

Nakano, H., Wakao, S., & Shimizu, T. (1997). Correlation between crystal structure and electrochemical properties of C14 Laves-phase alloys. *Journal of Alloys and Compounds*, *254*, 609–612.

Nellis, W. J., Louis, a. a., & Ashcroft, N. W. (1998). Metallization of fluid hydrogen. *Philosophical Transactions of the Royal Society A: Mathematical, Physical and Engineering Sciences*, *356*(1735), 119–138.

Nomura, K., & Akiba, E. (1995). H_2 Absorbing-desorbing characterization of the Ti-V-Fe alloy system. *Journal of Alloys and Compounds*, *231*, 513–517.

Ono, S., Nomura, K., & Ikeda, Y. (1980). The reaction of hydrogen with alloys of vanadium and titanium. *Journal of the Less Common Metals*, *72*, 159–165.

Papathanassopoulos, K., & Wenzl, H. (1982). Pressure-composition isotherms of hydrogen and deuterium in vanadium films measured with a vibrating quartz microbalance. *Journal of Physics F: Metal Physics, 12*, 1369–1382.

Park, J.-G., Jang, H.-Y., Han, S.-C., Lee, P. S., & Lee, J.-Y. (2002). Hydrogen storage properties of $TiMn_2$-based alloys for metal hydride heat pump. *Materials Science and Engineering: A*, *329-331*, 351–355.

Pebler, A., & Gulbransen, E. A. (1967). Equilibrium studies on the systems $ZrCr_2$-H_2, ZrV_2-H_2 and $ZrMo_2$-H_2 between 0°C and 900°C. *Transactions of the Metallurgical Society of AIME*, *239*(10), 1593–1600.

Pickering, L., Li, J., Reed, D., Bevan, A. I., & Book, D. (2013). Ti–V–Mn based metal hydrides for hydrogen storage. *Journal of Alloys and Compounds*, *580,* S233-S237.

Pollet, B. G., Staffell, I., & Shang, J. L. (2012). Current status of hybrid, battery and fuel cell electric vehicles: From electrochemistry to market prospects. *Electrochimica Acta*, *84*, 235–249.

Popeneciu, G., Coldea, I., Lupu, D., Misan, I., & Ardelean, O. (2009). Metal hydrides reactors with improved dynamic characteristics for a fast cycling hydrogen compressor. *Journal of Physics: Conference Series*, *182*(012054), 1–5.

Prasath, B., Leelakrishnan, E., & Lokesh, N. (2012). Hydrogen Operated Internal Combustion Engines–A New Generation Fuel. *International Journal of Emerging Technology and Advanced Engineering*, *2*(4), 52–57.

Reilly, J., & Wiswall, R. (1974). Formation and properties of iron titanium hydride. *Inorganic Chemistry*, *13*(1), 218–222.

Reilly, J.J., Adzic, G. D., Johnson, J. R., Vogt, T., Mukerjee, S., & McBreen, J. (1999). The correlation between composition and electrochemical properties of metal hydride electrodes. *Journal of Alloys and Compounds*, *293-295*, 569–582.

Reilly, James J., & Wiswall, R. H. (1970). Higher hydrides of vanadium and niobium. *Inorganic Chemistry*, *9*(7), 1678–1682.

Rosi, N. L., Eckert, J., Eddaoudi, M., Vodak, D. T., Kim, J., O'Keeffe, M., & Yaghi, O. M. (2003). Hydrogen Storage in Microporous Metal-Organic Frameworks. *Science*, *300*(5622), 1127–9.

Sakintuna, B., Lamari-Darkrim, F., & Hirscher, M. (2007). Metal hydride materials for solid hydrogen storage: A review. *International Journal of Hydrogen Energy*, *32*(9), 1121–1140.

Sandrock, G. (1999). A panoramic overview of hydrogen storage alloys from a gas reaction point of view. *Journal of Alloys and Compounds*, *293-295*, 877–888.

Sandrock, G., & Goodell, P. (1984). Cyclic life of metal hydrides with impure hydrogen: overview and engineering considerations. *Journal of the Less Common Metals*, *104*, 159–173.

Sandrock, G., & Bowman, R. (2003). Gas-based hydride applications: recent progress and future needs. *Journal of Alloys and Compounds*, (356-357), 794–799.

Satyapal, S., Petrovic, J., Read, C., Thomas, G., & Ordaz, G. (2007). The U.S. Department of Energy's National Hydrogen Storage Project: Progress towards meeting hydrogen-powered vehicle requirements. *Catalysis Today*, *120*(3-4), 246–256.

Schlapbach, L., & Züttel, A. (2001). Hydrogen-storage materials for mobile applications. *Nature*, *414*(November), 353–358.

Shibuya, M., Nakamura, J., & Akiba, E. (2008). Hydrogenation properties and microstructure of Ti-Mn-based alloys for hybrid hydrogen storage vessel. *Journal of Alloys and Compounds*, *466*(1-2), 558–562.

Shibuya, M., Nakamura, J., Enoki, H., & Akiba, E. (2009). High-pressure hydrogenation properties of Ti-V-Mn alloy for hybrid hydrogen storage vessel. *Journal of Alloys and Compounds*, *475*(1-2), 543–545.

Shriver, D. F., & Atkins, P. W. (1999). *Inorganic Chemistry* (3rd ed.). London: W. H. Freeman and Co.

Sirdeshmukh, D. B., Sirdeshmukh, L., & Subhadra, K. G. (2011). Crystallography. In *Atomistic Properties of Solids SE - 3* (Vol. 147, pp. 65–114). Springer Berlin Heidelberg.

Stevens, P. (2012). The "Shale Gas Revolution": Developments and Changes. [online] Available from: www.chathamhouse.org [Accessed 25 April, 2013].

Symes, D., Al-Duri, B., Dhir, A., Bujalski, W., Green, B., Shields, A., & Lees, M. (2012). Design for On-Site Hydrogen Production for Hydrogen Fuel Cell Vehicle Refueling Station at University of Birmingham, U.K. *Energy Procedia*, *29*(0), 606–615.

Takeichi, N., Senoh, H., Yokota, T., Tsuruta, H., Hamada, K., Takeshita, H. T., Tanaka, H., Kiyobayashi, T., Takano, T., and Kuriyama, N. (2003). "Hybrid hydrogen storage vessel", a novel high-pressure hydrogen storage vessel combined with hydrogen storage material. *International Journal of Hydrogen Energy*, *28*(10), 1121–1129.

Towata, S., Noritake, T., Itoh, A., Aoki, M., & Miwa, K. (2013). Effect of partial niobium and iron substitution on short-term cycle durability of hydrogen storage Ti–Cr–V alloys. *International Journal of Hydrogen Energy*, *38*(7), 3024–3029.

Tsukahara, M, Takahashi, K., & Mishima, T. (1995). Metal hydride electrodes based on solid solution type alloy $TiV_3Ni_x(0< x<0.75)$. *Journal of Alloys and Compounds*, *226*, 203–207.

Tsukahara, M., Takahashi, K., Mishima, T., Isomura, A., & Sakai, T. (1996). V-based solid solution alloys with Laves phase network: Hydrogen absorption properties and microstructure. *Journal of Alloys and Compounds*, *236*(1-2), 151–155.

Tsukahara, Makoto, Takahashi, K., Mishima, T., Sakai, T., Miyamura, H., Kuriyama, N., & Uehara, I. (1995). Phase structure of V-based solid solutions containing Ti and Ni and their hydrogen absorption-desorption properties. *Journal of Alloys and Compounds*, *224*(1), 162–167.

Turner, J. (2004). Sustainable hydrogen production. *Science*, *305*(5686), 972–4.

Vajo, J. J., Skeith, S. L., & Mertens, F. (2005). Reversible storage of hydrogen in destabilized $LiBH_4$. *The Journal of Physical Chemistry. B*, *109*(9), 3719–22.

Vanmal, H. (1973). A LaNi5 Hydride Thermal Absorption Compressor for a Hydrogen Refrigerator. *Chemie Ingenur Technik*, (2), 80–83.

Visaria, M., & Mudawar, I. (2012). Experimental investigation and theoretical modeling of dehydriding process in high-pressure metal hydride hydrogen storage systems. *International Journal of Hydrogen Energy*, *37*(7), 5735–5749.

Wang, X., Chen, R., Zhang, Y., Chen, C., & Wang, Q. (2006). Hydrogen storage alloys for high-pressure suprapure hydrogen compressor. *Journal of Alloys and Compounds*, *420*(1-2), 322–325.

Wernik, J. H. (1967). *Intermetallic Compounds*. (Westbrook, J. Ed.) (pp. 197–216). New York: John Wiley & Sons, Ltd.

Westerwaal, R. J., & Haije, W. G. (2008). Evaluation of solid-state hydrogen storage systems : Current status. Report ECN-E-08-043.

Winter, C.-J. (2009). Hydrogen energy — Abundant, efficient, clean: A debate over the energy-system-of-change. *International Journal of Hydrogen Energy*, *34*(14), S1–S52.

Winter, M., & Brodd, R. J. (2004). What are batteries, fuel cells, and supercapacitors? *Chemical reviews*, *104*(10), 4245–69.

Wolf, J. (2002). Liquid hydrogen technology for vehicles. *MRS Bulletin*, *27*(9), 684–687.

Wong-Foy, A. G., Matzger, A. J., & Yaghi, O. M. (2006). Exceptional H2 saturation uptake in microporous metal-organic frameworks. *Journal of the American Chemical Society*, *128*(11), 3494–5.

Xu, J., & Froment, G. F. (1989). Methane steam reforming, methanation and water-gas shift: I. Intrinsic kinetics. *AIChE Journal*, *35*(1), 88–96.

Yang, J., Sudik, A., Wolverton, C., & Siegel, D. J. (2010). High capacity hydrogen storage materials: attributes for automotive applications and techniques for materials discovery. *Chemical Society reviews*, *39*(2), 656–75.

Yu, X. (2004). Enhancement of hydrogen storage capacity of Ti-V-Cr-Mn BCC phase alloys. *Journal of Alloys and Compounds*, *372*(1-2), 272–277.

Zhang, J., Huang, Y. N., Peng, P., Mao, C., Shao, Y. M., & Zhou, D. W. (2011). First-principles study on the dehydrogenation properties and mechanism of Al-doped Mg_2NiH_4. *International Journal of Hydrogen Energy*, *36*(9), 5375–5382.

Zhu, M., Wang, H., Ouyang, L., & Zeng, M. (2006). Composite structure and hydrogen storage properties in Mg-base alloys. *International Journal of Hydrogen Energy*, *31*(2), 251–257.

Züttel, A. (2003). Materials for hydrogen storage. *Materials today*, (September), 24–33.

Züttel, A., Rentsch, S., Fischer, P., Wenger, P., Sudan, P., Mauron, P., & Emmenegger, C. (2003). Hydrogen storage properties of $LiBH_4$. *Journal of Alloys and Compounds*, *356-357*, 515–520.

Züttel, A. (2004). Hydrogen storage methods. *Naturwissenschaften*, *91*(4), 157–72.